ISBN 978-82-326-7536-4 (printed ver.)
ISBN 978-82-326-7535-7 (electronic ver.)
ISSN 1503-8181 (printed ver.)
ISSN 2703-8084 (electronic ver.)

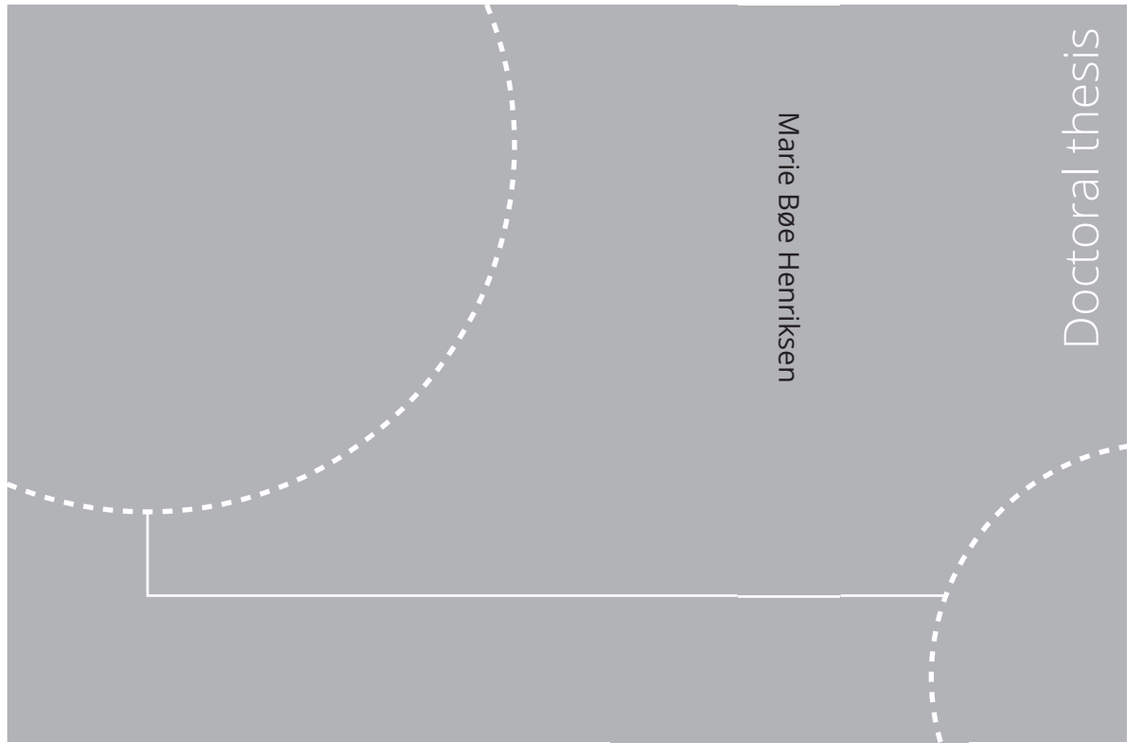

Doctoral theses at NTNU, 2023:418

Marie Bøe Henriksen

On the Calibration and Optical Performance of a Hyperspectral Imager for Drones and Small Satellites

From First Prototypes to In-Orbit Results

Doctoral theses at NTNU, 2023:418

NTNU
Norwegian University of
Science and Technology
Thesis for the degree of
Philosophiae Doctor
Faculty of Information Technology
and Electrical Engineering
Department of Engineering Cybernetics

NTNU
Norwegian University of
Science and Technology

UNIS
The University Centre in Svalbard

NTNU
Norwegian University of
Science and Technology

Marie Bøe Henriksen

On the Calibration and Optical Performance of a Hyperspectral Imager for Drones and Small Satellites

From First Prototypes to In-Orbit Results

Thesis for the degree of Philosophiae Doctor

Trondheim, December 2023

Norwegian University of Science and Technology
Faculty of Information Technology
and Electrical Engineering
Department of Engineering Cybernetics

NTNU
Norwegian University of Science and Technology

Thesis for the degree of Philosophiae Doctor

Faculty of Information Technology
and Electrical Engineering
Department of Engineering Cybernetics

ISBN 978-82-326-7536-4 (printed ver.)
ISBN 978-82-326-7535-7 (electronic ver.)
ISSN 1503-8181 (printed ver.)
ISSN 2703-8084 (electronic ver.)

ITK-report: 2023-26 -W

Doctoral theses at NTNU, 2023:418

Printed by Skipnes Kommunikasjon AS

Abstract

Hyperspectral Imagers (HSIs) are currently being developed for a range of applications. Among these are various forms of Earth observation from airborne platforms such as drones and small satellites. In this thesis, algal blooms, and especially observation of Harmful Algal Blooms (HABs), is the scientific use case in question. The Hyperspectral Small Satellite for Ocean Observation (HYPSO) mission aims to assist oceanographic observations, including observation of algal blooms, with the use of hyperspectral instruments. Since the quality of the collected data affects its usefulness, the instrument calibration and optical performance, as well as understanding the limitations of the instrument, is of high importance. This thesis, therefore, focuses on the calibration and optical performance of HSIs, such as the ones developed for the HYPSO mission, both in terms of the methods used and their results.

First, a prototype based on a pushbroom, grating-based design in the 400 nm to 800 nm range with a 5 nm spectral resolution was developed. It was thoroughly investigated in the lab by measuring characteristics such as the Full-Width at Half-Maximum (FWHM), the spatial Point Spread Function (PSF), and smile and keystone distortions. The results showed that a spectral resolution of 5 nm was achieved, but that the spatial focus was highly dependent on wavelength, which leads to poorer spatial resolution for the shorter and longer wavelengths. The prototype was also used in experiments to improve the wavelength calibration technique with spectral lamps, and to develop and investigate correction schemes for second order diffraction effects.

The HYPSO-1 and HYPSO-2 HSIs were then developed, built, tested, and calibrated. Thermal vacuum tests revealed that spectral characteristics varies slightly with temperature due to expansion of the slit tube component which affects the instrument focus. Besides that, pre-launch calibration showed that all main requirements were fulfilled. HYPSO-1 launched in January 2022, while HYPSO-2 is scheduled for launch in 2024. Investigations of the HYPSO-1 in-orbit data was further performed, showing that the instrument works as expected. The radiometric calibration coefficients have been updated due to a small spatial shift that occurred during launch. Additional in-orbit calibration and final validation of the data is still ongoing. Finally, examples of algal bloom detection by HYPSO-1 and algae spectral signatures with the prototype attached to a microscope are shown, confirming that the instruments work in a real-life setting.

Sammendrag

Hyperspektrale kameraer utvikles for bruk i flere fagfelt, som blant annet jordobservasjon fra droner og småsatellitter. I denne avhandlingen er algeoppblomstring, med særlig fokus på observasjon av farlige algeoppblomstringer, i søkelyset på forskningssiden. Satellittprosjektet *Hyperspectral Small Satellite for Ocean Observation* (HYPSO) har som mål å bistå med havobservasjon ved hjelp av hyperspektrale kameraer. Kvaliteten på de innsamlede dataene er viktig da den direkte påvirker dataenes nytteverdi. Kalibreringen av instrumentet, samt forståelse av instrumentets begrensninger, er derfor svært viktig for å kunne sikre gode dataprodukter. Denne avhandlingen fokuserer derfor på prestasjonen til de hyperspektrale kameraene utviklet for bruk i HYPSO-prosjektet ved ulike optiske tester, både ved å se på metodene som blir brukt og resultatene de gir, samt metoder for å forbedre instrumentet både under utvikling og i dataprosesseringen som følger.

Først ble en prototype, basert på et *pushbroom* gitter-basert design i det spektrale området fra 400 nm til 800 nm med en spektral oppløsning på 5 nm, utviklet. Den ble grundig karakterisert på lab ved å måle full bredde ved halv maksimum, den romlige punktspredefunksjonen og forvrengninger fra *smile* og *keystone*. Resultatene viste at den spektrale oppløsningen på 5 nm var oppnådd, men at det romlige fokuset varierte med bølgelengde. Dette medfører at den romlige oppløsningen ved kortere og lengre bølgelengder i det spektrale området forverres. Prototypen ble også brukt i eksperimenter for å forbedre metoden for bølgelengdekalibrering med spektrale lamper, og til å utforske korreksjon av andre ordens diffraksjonseffekter.

Videre ble hyperspektrale kameraer for HYPSO-1 og HYPSO-2 utviklet, bygget, testet og kalibrert. Miljøtesting i et termisk vakuumkammer viste at den spektrale responsen varier svakt med temperatur fordi spalterøret utvider seg ved varmere temperaturer, noe som gjør at fokuset til instrumentet endres. Utenom det viste lab-kalibreringen at alle hovedkravene til instrumentene var oppnådd. HYPSO-1 ble skutt opp i januar 2022, mens HYPSO-2 har planlagt oppskytning i 2024. Dataene fra HYPSO-1 i bane har blitt analysert og viser at instrumentet fungerer som det skal. De radiometriske kalibreringskoeffisientene har blitt oppdatert da det ble oppdaget et lite romlig skift som følge av oppskytningen. Videre kalibrering og validering av instrumentet i bane pågår fremdeles. Til slutt vises eksempler på deteksjon av algeoppblomstring med HYPSO-1, i tillegg til spektrale signaturer av ulike alger med prototypen festet til et mikroskop, for å vise at instrumentene fungerer med data fra den virkelige verden.

Preface

This thesis is submitted in partial fulfillment of the requirements for the degree of Philosophiae Doctor (Ph.D.) at the Norwegian University of Science and Technology (NTNU). The presented work is the result of the doctoral studies carried out at the Department of Engineering Cybernetics (ITK), NTNU. I have also been a guest Ph.D. student at the University Centre in Svalbard (UNIS), meaning that I have had the pleasure of staying at UNIS for a shorter period of time to perform field- and laboratory work. My main supervisor has been Professor Tor Arne Johansen at ITK at NTNU, and my co-supervisor Fred Sigernes at the Department of Arctic Geophysics at UNIS.

With this thesis, my years as a student are (finally) coming to an end. I joined the HYPSO project in 2018 when I started working on the pre-project for my master's thesis. Little did I know that choosing the topic of calibration over satellite control mechanisms would change my life forever. It led me on an amazing journey, first working with HYPSO HSIs during my master's thesis, then over to the Netherlands for a year working as a Young Graduate Trainee (YGT) in the optics section at the European Space Agency (ESA) - the European Space Research and Technology Centre (ESTEC). This gave me invaluable experiences, knowledge and motivation (I'm forever grateful for this adventure), before traveling back to NTNU to continue working on this Ph.D. project, leading me to where I stand today.

I have learned more than I could ever have imagined over the last couple of years, about hyperspectral imaging, optics in general, optical design, difficulties with optical design, satellite development, removing epoxy, phytoplankton pigments, how cold the water in the Arctic is, planning experiments, planning test campaigns, writing reports, writing reports, writing papers, writing reports, and how much caffeine my body needs (need is a strong word, let's say accepts) before it works better by drinking just water instead. I hope this work can be useful for anyone building their own hyperspectral instruments, or developing satellite payloads in general, and that the HYPSO data is useful for the community as we have worked hard to make it so.

This has been a long journey. Enjoy the read.

Marie Bøe Henriksen,
Tønsberg, 2023-09-01.

Acknowledgements

This PhD journey has been quite an adventure, and I could never have completed it all on my own.

First and foremost I would like to thank my supervisors, Tor Arne Johansen and Fred Sigernes, for supporting me along the way and letting me explore all these different projects. The opportunity of going to Svalbard to use the optics lab and attend classes have been highly appreciated, and the feedback on all projects and publications have been invaluable. I must also thank everyone contributing to field work and campaigns, especially Geir Johnsen, Asgeir Sørensen, Torkild Bakken and, of course, Natalie Summers (I still picture you on the boat trip to Ny-Ålesund with wind in your face), you have all inspired me more than you know.

A large part of this PhD project has been related to the HYPSO mission. I must thank the full HYPSO-team, both current and previous members, for all the work that has been done. I mean come on guys, we launched a satellite! The largest of thanks goes to you, Elizabeth, I have no idea how the payloads would ever have been completed without you. Thank you for all the hours in the lab, for all the testing and documentation, and all discussions both HYPSO-related and others. A big thanks also to you, Gara - going to the US would not have been the same without the two of you. I must also add you in here, Petter, even though you're not officially a part of the HYPSO-team. Our Oslo-gatherings are always fun, I'm really glad you all are not too far away. And also thank you, Evelyn, for all the support and for leading us to the launch of HYPSO-1 (you have been sorely missed after you left). Thank you so much Roger and Sivert for everything from technical help to motivational support, and all the work you have done with HYPSO-2. All the credit in the world to the two of you for making the second satellite payloads ready. Thank you so much, Esmée, for joining in during my last years, working with you is always a pleasure. I don't know if you've realized it, but you spread so much joy I can't even describe it. I would also like to thank Lise Lyngsnes Randeberg for access to the calibration lab which made my life a lot easier during this PhD (easily noticed the times the access had expired).

In addition to spending time at NTNU and UNIS, I got to collaborate on a set-up at UiO as well. Thank you so much for this opportunity, Torbjørn Skauli, and for teaching me along the way. Also thanks to you, Gard, for all the work on the set-up and setting up all the measurements. I'm so glad we could work on this set-up together. In addition, I

must send a thanks to my previous colleagues at ESTEC. Especially you, Volker, thank you so much for taking me under your wing, for showing interest in my work and for answering any questions I've had along the way. And thank you, Simon, for the help, all updates, and discussions during our coffee chats, I've really appreciated it.

Last but not least, a huge thanks to my family and friends that have supported me in so many ways during these years. Kristina, Sofie and Guro, I don't even know how to begin thanking the three of you. I'm so glad I have you, and that we find time for cabin trips and celebrations even in busy times. Please let it never end. And Kristina, our writing days and conversations in general have helped so much. Thank you for being here through it all. I'm so glad we could go through the PhD life together, even we've been at different universities. Same goes to you, Elise. Thank you so much for our writing retreat, I have no idea how I got so much done in 10 days. I must also thank you for your bottomless enthusiasm and never-ending energy (even though you might not feel like it yourself, you keep on going like no one else I know). You're a source of inspiration, that's for sure. Thank you Jostein and Marko for listening to me whenever I need to talk. I don't know how you always have the answers I need to hear. Ann-Helen, thank you for always (and I mean always) being there, since our very first steps. I always enjoy a cup of tea or coffee, a glass of wine, or anything else with you. And Kjetil, thank you for putting up with me, specially these last couple of months. Your support and help with all the tiny stupid things (and the big ones too) means so much to me. I don't know what I would do without you.

Finally, I also want to give an extra shout-out to Lykke, Foss, Java, Kvante, Magnus, Pheobe, Alexa and Ipa (now the last weeks) for comforting cuddles, relaxing walks and ~~some~~ quite a lot of chaos throughout these years.

Funding information:
This Ph.D. project was mainly funded by the Research Council of Norway (NRC) through the Centre of Excellence funding scheme with the Centre for Autonomous Marine Operations and Systems (AMOS) program (grant no. 223254), and have in addition been supported by the IKTPLUSS Mission-oriented Autonomous Systems with Small Satellites for Maritime Sensing, Surveillance and Communication (MASSIVE) project (grant no. 270959) and by the Norwegian Space Agency (NoSA) and ESA through the Programme de Développement d'Expériences Scientifiques (PRODEX) project (grant no. 400132515).

Table of Contents

1 Introduction

The oceans are a vital part of life on Earth, and it is more important than ever to monitor its health and the changes occurring due to climate change. It is, however, extremely difficult to monitor something so vast with only in-situ measurements. Remote sensing is therefore key to observe this great extent of liquid that colors our planet blue. There are many methods and instruments that can be used to measure different aspects of the oceans. In this thesis, the main focus will be on ocean color remote sensing using hyperspectral imaging from drones and small satellites. This limits the area of study to only the top of the water column. However, focusing on the surface of the water means that larger areas can be monitored over time with satellite platforms, giving indispensable time-series to observe these ever-changing oceans.

1.1 Monitoring the oceans

To monitor the oceans is a complex task. Their vast areas cover more than 70% of the Earth's surface, and their movements, content and colors are continuously changing. In-situ measurements are valuable both for local monitoring and calibration and validation of large scale measurements, but it is impossible to monitor the oceans on a global scale using only in-situ measurements. Different models are currently being used to further understand and predict both ocean and Earth dynamics. Remote sensing data of the oceans are input to many of these models, such as models of the ocean carbon cycle, ecosystem models (growth and decay of phytoplankton for example), and biogeochemical models, which are further used to explain other oceanographic processes and how these may impact the Earth.

Observation of ocean color also provides a unique window to monitor large scale marine ecosystems by detecting and estimating Chlorophyll-a (Chl-a) concentrations, as the state of these ecosystems can be estimated from Chl-a data [1]. Chl-a is also commonly used as an indication of phytoplankton biomass, providing valuable information about phytoplankton systems. As phytoplankton is estimated to be responsible for half of the global carbon fixation on an annual scale [2], understanding and monitoring phytoplankton is extremely important, also in regards to climate change.

1.1.1 Monitoring the oceans from space

The first satellite sensor to monitor ocean color was the Coastal Zone Color Scanner (CZCS), launched by National Aeronautics and Space Administration (NASA) in 1978. Its main goal was to measure the water-leaving radiance at selected bands in the visible spectral range to estimate concentrations of phytoplankton pigments in the top layers of the water column in Case 1 waters (open ocean) [3].

CZCS has been followed by a list of others since then. Among these are the Polarization and Directionality of the Earth's Reflectance (POLDER) instrument, the Sea-viewing Wide Field-of-view Sensor (SeaWiFS), the Moderate Resolution Imaging Spectroradiometer (MODIS), the Medium Resolution Imaging Spectrometer (MERIS) onboard Envisat, the Hyperspectral Imager for the Coastal Ocean (HICO) mounted on the International Space Station (ISS), the Ocean and Land Colour Instrument (OLCI) onboard Sentinel-3, the Hyperspectral Precursor of the Application Mission (PRISMA) instrument, the Hyperspectral Imager (HSI) for the Environmental Mapping and Analysis Program

(EnMAP), the Ocean Color Instrument (OCI) for the Plankton, Aerosol, Cloud, ocean Ecosystem (PACE) mission and the instrument for the Copernicus Hyperspectral Imaging Mission for the Environment (CHIME) mission. Table 1.1 shows their launch date (for time perspective) and some of their key specifications.

Table 1.1: Examples of ocean color satellite instruments.

Launch year	Instrument	Spectral range [nm]	No. bands	Spatial resolution [m]
1978	CZCS [3]	433-12500	6	825
1996, 2002	POLDER [4]	443-910	8	6000
1997	SeaWiFS [5, 6]	402-885	8	1100
1999, 2002	MODIS [7, 8]	405-14385	36	250, 500, 1000
2002	MERIS [9]	390-1050	15	300, 1200
2009	HICO[10]	380-1000	124	90
2016, 2018	OLCI [11]	390-1040	21	300, 1200
2019	PRISMA [12]	400-2505	237	30
2022	EnMAP [13, 14]	420-2450	242	30
(2024)	OCI [15]	340-2260	117	1000
(2028)	CHIME [16]	400-2500	>200	30

There are several parameters that are important to consider when comparing the different instruments. Among these are factors concerning the spatial domain (the spatial resolution and swath width), the spectral domain (number of bands, spectral resolution and spectral range), radiometric domain (Signal-to-Noise Ratio (SNR) and dynamic range) and the temporal domain (revisit time and data latency). The older instruments are typically larger in physical size, with varying spatial resolution, low spectral resolution, and a low number of spectral bands. They typically also have a revisit time of several days. Newer instruments however are getting smaller and more compact so that they can fit on Cube Satellite (CubeSat) platforms, as discussed further in Section 2.2.3. These often have shorter revisit times, sometimes accomplished by the possibility of having multiple CubeSats in a constellation. With the technology steadily developing, the performance of the instruments are also being continuously improved, racing towards the performance of the older and larger instruments.

There are many applications for ocean color remote sensing data. Some of these include estimation of phytoplankton pigments such as Chl-a (as done with CZCS), atmospheric variations (using the dark ocean as a background), oil spill detection, monitoring water quality, ice cover changes, and ocean pollution. There are different requirements needed

for the different applications. A more detailed list of suggested requirements will follow in Section 2.1.5. Some main parameters to think about for ocean color applications are the spatial resolution to detect and map features close to the coast, the spectral resolution which determines to which accuracy some components can be determined, and high SNR to make sure enough ocean signal is received through the atmosphere.

One of the primary concerns regarding remote sensing data is the accuracy of the data products [1], both due to many uncertainties in the signal chain and due to most of the remote sensing instruments being different from each other, for example in terms of specifications and performance. This makes it harder to ensure continuous time series of the same data products with sufficient accuracies to follow the development of oceanographic phenomena. Calibration and characterization, in addition to good instrument design, is therefore of high importance for the satellite remote sensing instruments.

1.1.2 Monitoring algal blooms

One important phenomenon that can be detected and studied by monitoring ocean color is algal blooms. An algal bloom is an event where the number of microalgal cells grow rapidly, and they can last for days, weeks or even months. They can be caused by an increase in nutrients or light, or a change in temperature, all making favorable conditions for a bloom. They typically occur on a seasonal basis during the spring and later in the summer, depending on geographical location [17]. The blooms vary in color from the pigments of the blooming species, and can be turquoise, green, red, or brown in color. An example of a bloom in the Barents Sea captured by MERIS onboard Envisat can be seen in Figure 1.1.

During a bloom, the phytoplankton use nutrients in the water for photosynthesis, and the bloom will eventually stop when the system is saturated. The increase of phytoplankton cells during the bloom leads to an increase in zooplankton grazing on the phytoplankton. The zooplankton are in turn a food source for fish, which further can be eaten by marine mammals such as seals and whales, and are therefore important to the marine ecosystems. Some phytoplankton, like the coccolithophores, form calcium carbonate plates (coccoliths) around their cells. The process of making these plates changes the seawater alkalinity, which leads to changes in the solubility of carbon dioxide in the water, which in turn leads to an impact on the carbon cycle [19]. Since phytoplankton binds carbon and produce oxygen through photosynthesis and is

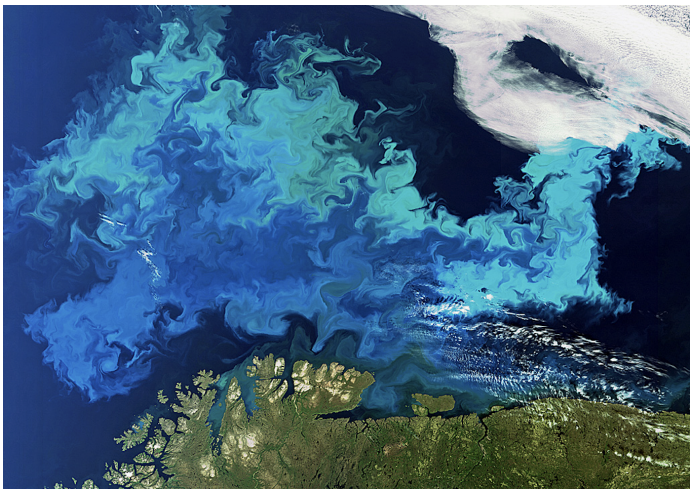

Figure 1.1: Phytoplankton bloom in the Barents Sea, captured by the MERIS instrument onboard Envisat in August 2011. Image credit: ESA, available at [18].

estimated to be responsible for more than half of the Earth's oxygen production, increased knowledge of the dynamics of algal blooms is also important to understand one of our main sources for oxygen.

Some blooms can be harmless. Others, however, may be harmful in different ways to other species staying in the same waters. Some algal species can produce toxins which are poisonous to other organisms. As an example, some dinoflagellate and diatom blooms may cause paralytic shellfish poisoning [20, 21]. Another example is cyanobacterial blooms which can contaminate drinking water [22]. Algal blooms can also be harmful if the biomass grows so large that it harms the surrounding ecosystem by blocking out light, clogging gills of fish, or causing anoxia (depletion of oxygen) affecting all the oxygen-dependent organisms. Harmful Algal Blooms (HABs) can also have a significant impact on local economy, as the harmful bloom can cause massive fish deaths, harming fisheries and the aquaculture industry [23]. As other algal blooms, HABs can occur in perfectly healthy ecosystems on a regular, seasonal basis. However, they may also occur unexpectedly due to reasons such as sudden nutrient inputs [20]. And the detection of toxic blooms is complicated, not only just to detect the harmful species itself, but also due to some species only being harmful under certain growth conditions [19]. As both algal blooms in general and HABs may increase both in frequency and intensity with climate change, they are important to detect, monitor, understand and predict to ensure minimal harm to the society.

The concentration of Chl-a is often used to estimate phytoplankton biomass [2] and thereby detect algal blooms, as Chl-a is the main phytoplankton pigment and present in all species [24]. Distinguishing different phytoplankton functional types from remote sensing data is a more complex task, and requires high spectral resolution to determine different pigments [19]. Nevertheless, it has been shown that it is possible to detect certain groups. One example is given in Sathyendranath et al. [25], where diatoms are separated from other phytoplankton species in remote sensing data. More on the different phytoplankton pigments, groups and algorithms for detection is presented in Section 2.1

There are several challenges to consider when using remote sensing data for ocean color observation. Atmospheric disturbances is one, due to the optical path through the atmosphere being long, and the ocean being a relatively dark target. This leads to only around 10% of the received signal strength on the sensor to be reflectance from close to the ocean surface, with the rest being atmospheric effects caused by absorption and scattering in the atmosphere [20]. High SNR and good atmospheric correction is therefore important to be able to obtain usable data from the water surface, as further discussed in Section 2.1.3.

Typically, the phytoplankton biomass also resides 10 to 15 m below the water surface. The received signal consists of a mix of the signal reflected from different depths, where the maximum depth depends on the turbidity of the water. It can still be possible to detect phytoplankton below the surface, but the signal is then weaker and might be disturbed by other particles higher up in the water column. This makes the task of retrieving the phytoplankton spectral signatures more difficult. The same holds for distinguishing phytoplankton from other constituents in the water [26]. Hyperspectral data with high spectral resolution may therefore be beneficial, making the full spectra in the spectral range available, thereby opening up possibilities for trying to distinguish the different constituents and species in the water.

1.1.3 AMOS and the observational pyramid

From 2013 to 2022, the Centre for Autonomous Marine Operations and Systems (AMOS) at the Norwegian University of Science and Technology (NTNU) was a research program established for, among other things, mapping and monitoring of the seabed and the oceans [27]. Much of the AMOS activities were related to underwater mapping. However, combining data from different platforms to obtain an overview and a greater understanding of the whole ocean space was also in focus. Aerial platforms such as

drones and finally spaceborne platforms such as small satellites for larger spatial and temporal coverage of the observations were therefore also involved. This concept, named the observational pyramid, is illustrated in Figure 1.2.

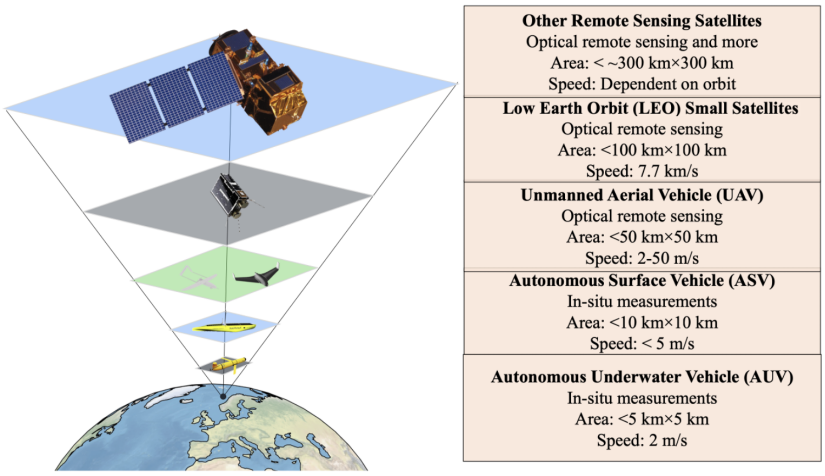

Figure 1.2: The observational pyramid with all the different autonomous data-collecting robotic agents developed at NTNU AMOS. The right-hand side of the figure gives typical values for speeds, area coverage and data collection methods [28].

As a part of NTNU AMOS, the Hyperspectral Small Satellite for Ocean Observation (HYPSO) small satellite mission was developed for ocean color observation, as described in the next section. With this mission, AMOS and NTNU aimed to contribute to the complex world of ocean color observation, as the introduction has described.

1.2 The HYPSO mission

The main objective of the HYPSO mission is to provide low latency hyperspectral data products to support marine environmental monitoring [29]. This way, the HYPSO satellites will be close to the top of the observational pyramid (Figure 1.2), interacting with other platforms in their investigations of the oceans. Much of the mission design is based on detecting, classifying and monitoring algal blooms, especially HABs , but the hyperspectral data collected can also be useful for other applications.

The main concept of operations (at least for HYPSO-1 and HYPSO-2) is illustrated in Figure 1.3 (from Grøtte et al. [29]). First, commands are uploaded from the ground

station with a prioritized list of targets, pointing mode and other acquisition parameters to the satellite. The satellite can then capture data of a selected target. For this, different scanning schemes can be used. Among these is a slewing maneuver where the satellite rotates during the acquisition so that it captures overlapping frames over the same area. The overlapping frames can be used to enhance the spatial resolution or SNR depending on application, as described in [29]. On-board data processing can then be performed before downlinking the data to a nearby ground station. The downlinked data can further be used to send alerts to the other platforms in the observational pyramid, to be investigated in more detail by scientists or used as input to different models.

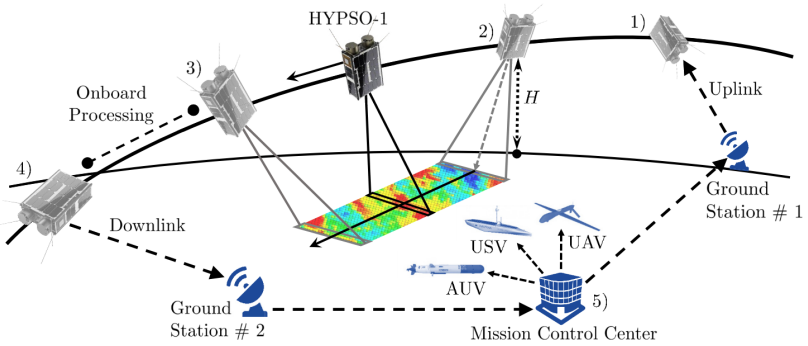

Figure 1.3: HYPSO-1 main concept of operations. (1) Commands uplinked from ground station to the satellite, (2) image acquisition of a target (here using the slew maneouver), (3) on-board processing, (4) downlinking the data to a nearby ground station, (5) distribution and use of the data. Figure from [29].

In addition to important parameters and challenges discussed in the previous sections, the data size and downlink capacity is of high importance for hyperspectral sensors. The hyperspectral data captured is typically large in size, while the data downlink is limited by speed and access (both in time and availability) of ground stations. On-board processing is therefore also an important aspect to consider, as discussed in Langer et al. [30]. The HYPSO satellites focus on on-board processing to reduce the latency from observation to possible HAB detection. Standard processing steps such as georeferencing and radiometric calibration can be applied on-board the satellite. Further, cloud detection and classification algorithms can be applied, reducing the size of the data that is downlinked during nominal operation (keeping the possibility of downlinking full or raw datasets if desired as well). If for example HABs are imaged, they can be detected by the on-board processing, flagged and then downlinked on the next pass, giving a very short response time from detection to alerting other platforms in the observational pyramid.

That the HYPSO satellites will be able to process data on-board gives them a unique position at the top of the pyramid, with the possibility of assisting oceanographic observations in close to real-time [28]. The fact that the satellites are operated by students and team members at the university makes it easier to coordinate missions with other platforms such as drones, Unmanned Surface Vehicles (USVs), and Autonomous Underwater Vehicles (AUVs). This is of huge benefit in a real-life setting where planning and coordinating missions can take up a lot of time and resources.

At the time of writing, the first satellite (HYPSO-1) is operational in orbit, and the second satellite (HYPSO-2) is under development and scheduled for launch in 2024. The third satellite (HYPSO-3) is in its planning-phase. Both HYPSO-1 and HYPSO-2 are based on the Multipurpose 6U Platform (M6P) CubeSat bus from Kongsberg NanoAvionics (KNA), see illustrations shown in Figure 1.4, while the size and form of HYPSO-3 is still to be decided. For the rest of this thesis, only HYPSO-1 and HYPSO-2 are in focus.

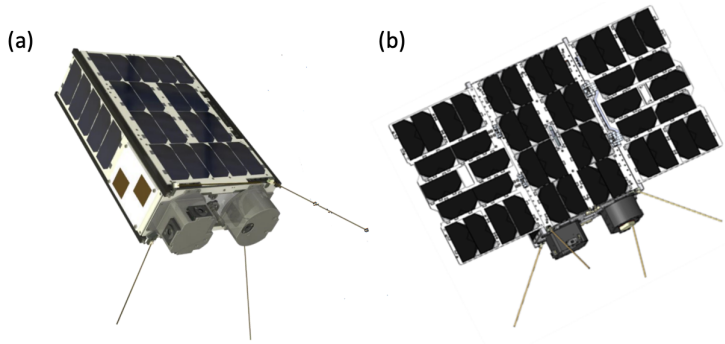

Figure 1.4: Illustrations of the HYPSO-1 and HYPSO-2 satellite buses. (a) HYPSO-1 , (b) HYPSO-2 (with additional solar panels). Image credits: KNA.

1.2.1 HYPSO-1

The HYPSO-1 CubeSat is a 6U CubeSat, making it a relatively small satellite compared to many others used for ocean color. It has one payload onboard, the hyperspectral payload, which consists of an HSI, a Red-Green-Blue (RGB) camera, and an electronics stack that controls the cameras. The HSI is the main instrument and will be in focus in this thesis, while the RGB camera is an additional instrument meant to support the HSI observations. The HYPSO-1 HSI will be described in more detail throughout the thesis, especially in Chapter 6 and Chapter 7, and the hyperspectral payload in general in Section 1.2.3. This section focuses more on the satellite and mission details.

On 13 January 2022, HYPSO-1 was launched into space with the SpaceX Transporter-3 mission into a sun-synchronous 540 km (morning) Low Earth Orbit (LEO) with an orbital period of about 96 minutes. A picture of the fully assembled satellite before launch can be seen in Figure 1.5. At the end of February 2022 the payload commissioning phase began, and was continued to be carried out in parallel with development and advances in the satellite operations scheme, imaging campaigns and data acquisitions for calibration and validation of the hyperspectral payload. The satellite operations are run by students and researchers in an academic environment, which provides both limitations and flexibility in terms of operating the satellite [31]. For example, there is a low threshold to explore new operational scenarios, but the team is less experienced and time is needed to both develop and understand the systems and procedures. More details on the first months of operations and the first data captured by HYPSO-1 is presented in Bakken et al. [28], and data from the HYPSO-1 HSI in-orbit is presented in Chapter 8 and Chapter 9.

An overview of the satellite bus and its components is shown in Figure 1.6. The blue components belong to the payload and are provided by NTNU, while the green components are provided by KNA. An image showing the hyperspectral payload inside the satellite bus is shown in Figure 1.7, showing the different subsystems in real life.

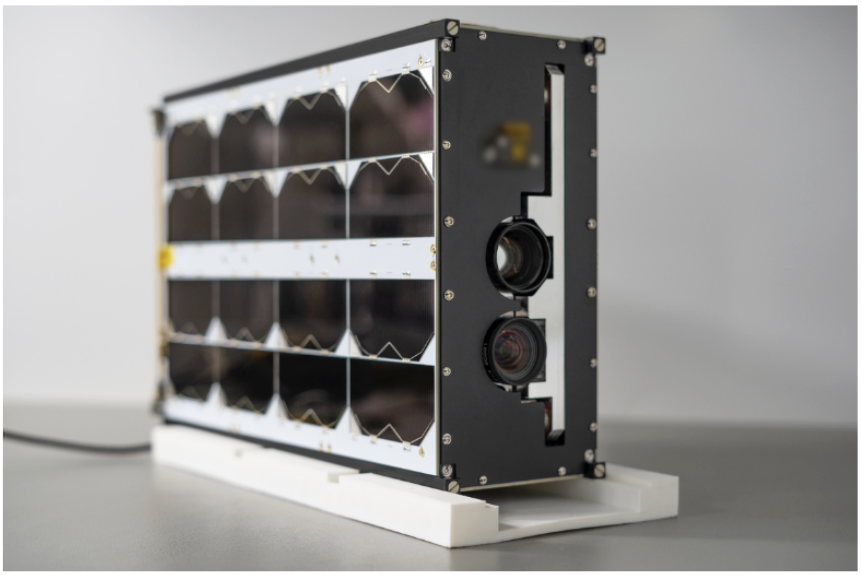

Figure 1.5: The fully assembled HYPSO-1 satellite before launch. Image credit: KNA.

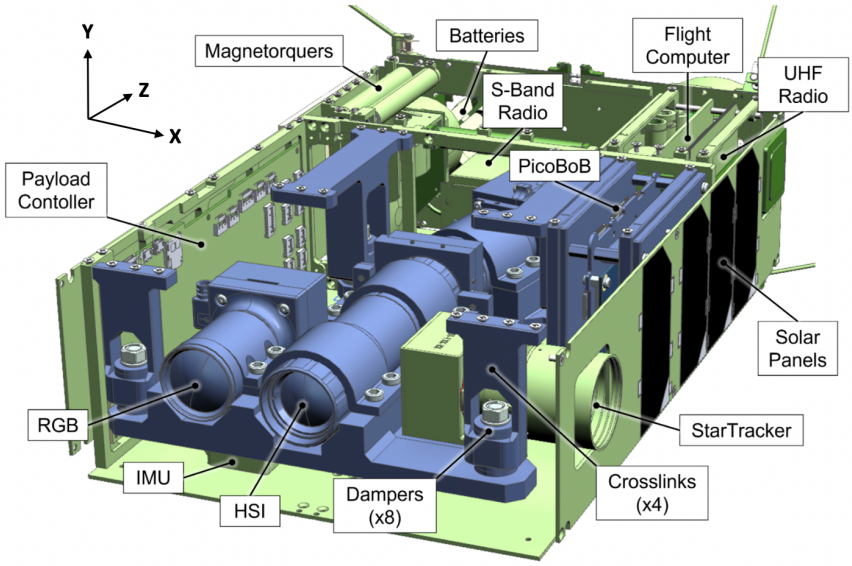

Figure 1.6: Overview of the HYPSO-1 satellite components inside the bus. Components from the bus provider KNA are shown in green, and the NTNU components shown in blue [32].

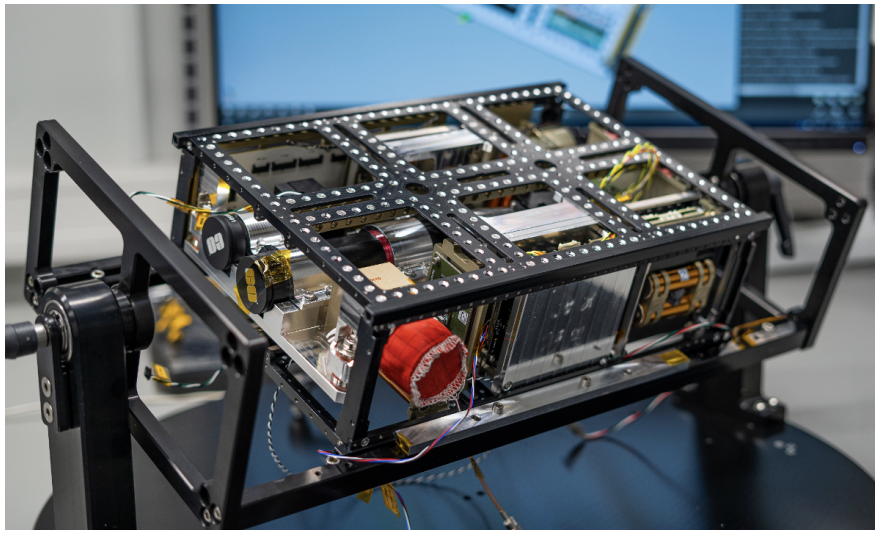

Figure 1.7: The HYPSO-1 hyperspectral payload inside the satellite bus, together with the other subsystems, during the satellite integration phase. Image credit: KNA.

1.2.2 HYPSO-2

HYPSO-2 will in many ways be a twin of HYPSO-1, with some noticeable changes. First of all, there will be two payloads onboard compared to only one payload in HYPSO-1. The first payload is a hyperspectral payload, similar to that of HYPSO-1, with the differences described in Section 6.1.2. The second payload is a Software Defined Radio (SDR), which is described in Birkeland et al. [33], and is not further discussed in this thesis. The HYPSO-2 satellite bus will also be similar to that of HYPSO-1, but with additional (and deployable) solar panels, additional X-band radio for communication, and a 530 km sun-synchronous orbit in the afternoon (compared to a 540 km morning orbit for HYPSO-1). It is scheduled for launch in 2024, and the payloads were delivered to KNA for integration into the satellite bus at the end of summer 2023.

1.2.3 The HYPSO hyperspectral imager payload

The HYPSO hyperspectral payload consists of an HSI, an RGB and the electronics stack called Pico Breakout Board (PicoBoB), as seen in Figure 1.8. The HSI is based on a Commercial-Off-The-Shelf (COTS) design [34, 35] originally made for drones, which is described in further detail in Chapter 3. The modifications needed for use in space are

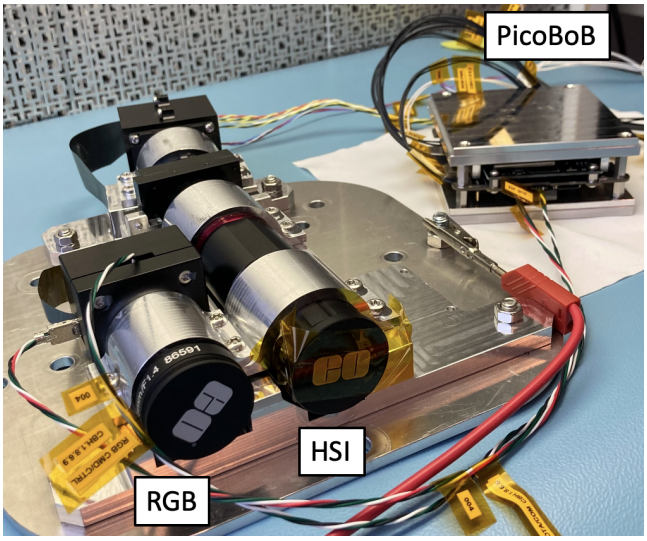

Figure 1.8: Picture of the HYPSO-1 HSI payload, also described in Section 6.1, showing the HSI, RGB camera, and the electronics stack PicoBoB.

described in Prentice et al. [36]. These changes mainly consist of exchanging plastic parts with metal, removing grease from the lens objectives and designing a more robust payload platform for the payload to endure the shock and vibrations occurring during launch.

The main specifications of the HSI are shown in Table 1.2. It is a pushbroom hyperspectral instrument based on a transmission grating design in the visible to Near-Infrared (NIR) (400 nm to 800 nm) spectral range, with a spectral resolution of about 5 nm (with the theoretical limit being 3.3 nm). When used on the satellite, only a selected Area of Interest (AoI) on the sensor is used. This is mostly due to data storage and downlink capabilities, as the data files grow fast in size. The AoI is placed in the center of the sensor, as this is where the optical quality is best, but can also be reprogrammed after launch. It is also possible to acquire data with the full sensor, later referred to as full frame captures.

Table 1.2: Specifications of the HYPSO hyperspectral imager design.

Parameter	**Specification**
Sensor	Sony IMX249
Image size	(1936, 1216) pixels
Pixel size	5.86 μm
Area of interest[1]	Pixel (428:1508, 266:950)
Bit depth	12-bit
Spectral range	400-800 nm
Grating	300 grooves/mm, transmission
Slit dimensions	7 mm x 50 μm
Theoretical FWHM	3.33 nm

[1] Pre-selected AoI, can be changed if needed.

Recommendations and requirements for ocean color instruments are described in more detail in Section 2.1.5. In summary, there are a handful of bands that should be included, high spatial and spectral resolution is desirable, and high SNR necessary to retrieve phytoplankton signatures. Some requirements are easy to ensure, such as a high dynamic range by choosing a sensor with 12- or 14-bit resolution. Other parameters are more complex. Important characteristics that affect the final data product such as Full-Width at Half-Maximum (FWHM), smile, and keystone are described further in Section 2.3, together with calibration and characterization methods to measure and understand the performance of the hyperspectral instrument. However, to already summarize some of the important requirements set for the HYPSO HSI, where some of them will be validated through the work in this thesis, a selection of the HSI requirements are shown in Table 1.3.

Table 1.3: Set of hyperspectral imager requirements.

Parameter	Requirement
Sensor response	Linear
Spectral range	400-800 nm
FWHM	< 5 nm
Spatial resolution	< 100 m
Smile after correction	< 1 pixel
Keystone after correction	< 1 pixel
SNR	> 400
Polarization sensitivity	$< 5\%$
Uncertainty of polarization sensitivity	$< 0.2\%$
Stray light	Minimized

The performance of the HSI is important, and relies heavily on the calibration and characterization. This should be a priority in the development of future hyperspectral imagers, as argued in [26]. Since the HYPSO satellites do not have any dedicated calibration equipment onboard (like larger satellites might have), the pre-launch calibration and characterization is especially important. In-orbit calibration techniques, as described in Section 2.3.8 may still be used, but it is desired to have as much knowledge about the instrument as possible prior to launch. This thesis therefore focuses on the calibration and characterization of the HSIs used in the HYPSO missions. Ensuring good performance when the instrument is assembled, investigating the performance before, during and after environmental tests of the payload, and investigating techniques to improve the acquired data in post-processing are all topics discussed in this thesis.

1.3 Aim of this work

From what is described above, it is clear that observing the oceans is an important task, and remote sensing data is needed to monitor phenomenon such as algal blooms on a global scale. The aim of this work is therefore to contribute to building, testing, calibrating and characterizing the HSIs that are used in the HYPSO mission. The focus in this thesis is to ensure good quality of the HSI data captured by the HYPSO satellites. This will be done by investigating the HSI design in detail, looking into the details of the calibration procedures, developing correction algorithms to improve the captured data, and finally to connect real observations with the biological signatures from algal blooms, which is the main motivation for the whole project and what ties it all together.

1.3.1 Research questions

From everything presented above, the following research questions have been identified:

Research Question 1 (RQ1):
What is a simple yet trustworthy method of performing wavelength calibration, and what must be taken into account to make sure it yields sufficient results?

Research Question 2 (RQ2):
Which calibration and characterization procedures are needed to describe the performance of a low-cost HSI for ocean color applications?

Research Question 3 (RQ3):
Which steps should be a part of the pre- and post-processing pipeline for the HYPSO-1 HSI?

Research Question 4 (RQ4):
Can a small HSI built out of COTS components be used to detect algae in the ocean?

RQ1 goes into the details of wavelength calibration. What is the best practice with the equipment we have available? What gives the best results, both in terms of which spectral lamps to use during measurements and which mathematical terms that should be used to describe the pixel to wavelength relationship? Answering these questions are useful also for others performing wavelength calibration with spectral lamps. Which calibration and characterization procedures that should be prioritized and performed for an instrument before use is also an important question to answer. RQ2 is therefore about looking into the possibilities, recommendations in the literature and results from experiments in the lab to figure out which procedures is more important for a low-cost ocean color HSI.

For RQ3, a question related to the HYPSO-1 HSI is formulated specifically, as it must be figured out what exact steps that are needed in the processing pipeline of the HYPSO-1 data. An answer to this question is needed so that users can use the HYPSO-1 data. Finally, RQ4 sums up the ultimate question for the HYPSO HSI: Can we actually use these HSIs to detect algae in the ocean? This is a tough question to answer, but an important one since the whole HYPSO mission is based on using these instruments for exactly this purpose.

1.3.2 Main contributions to the field

From the work presented in this thesis , the main contributions can be listed as follows:

- **A detailed description of how to build the HSI V6 instrument**, and details on its optical performance. Including a parts list, instructions on how to assemble the instrument and tips and tricks related to focusing the instrument. A comparison to the previous version, the HSI V4, focusing on improvements in throughput and overall data quality has also been shown.

- **A study of wavelength calibration**, focusing on wavelength calibration of grating-based spectrometers using spectral lamps. From this it was found that measurement points at the edges of the spectrogram are desirable, and excluding known double peaks from the dataset is advised as long as enough data points are available.

- **A detailed description of calibration and correction methods applied to the HYPSO-1 HSI**, giving calibrated data products to the users/scientists. This includes discussions, explanations and recommendations from investigations of the in-orbit data, as well as all calculated calibration coefficients and correction matrices needed for the operations that are suggested.

- **Pre-launch calibration of the HYPSO-2 HSI**, which can be used to create calibrated products for the HYPSO-2 HSI after launch, as well as be compared to in-orbit data once the satellite is operational in space.

1.3.3 List of contributing papers

This thesis is mainly built on the publications that were published during the project period, together with some extra experiments and analysis that were also performed but not published. In addition, some publications (here referred to as Supporting Paper (SP)) have used results from these thesis. The SPs will be referred to, but the content from these papers are not directly included in the thesis. An overview of where the different papers have been used in the thesis is shown in Figure 1.9. This is followed by a brief overview of the papers, their content and what is included in this thesis from each paper.

	Chapters						
	Part 1			Part 2			
SP 1		4.3.2					
Paper 1	3	4.4	5.4				
Paper 2					7		
Paper 3				6.2.2			
Paper 4				6			
Paper 5		4.5					
SP 2							9.1
Paper 6						8	
Paper 7						8.1.5	9.2.2
Paper 8							9.3
SP 3				6.2.2			
Paper 9		4.3.3					
SP 4				6.2.2			
Paper 10			5				
Paper 11		4.4.4					
SP 5							9.1

Figure 1.9: Overview of publications, in chronological order, and where they are included in the thesis. Gray marks publications that are only referred to in the thesis.

List of main publications in chronological order:

Paper 1: **M. B. Henriksen**, E. F. Prentice, C. M. van Hazendonk, F. Sigernes, and T. A. Johansen, "A do-it-yourself VIS/NIR pushbroom hyperspectral imager with C-mount optics" in Optics Continuum, Vol. 1, No. 2, (2022).

This paper describes the development of HSI Version 6 (V6), further developed from the HSI Version 4 (V4). It includes theoretical calculations on the improvements, a list of components, detailed instructions for assembly, proof of concept, comparisons of the HSI V4/V6 performance and initial results from second order light correction.

Adapted results can be found in Chapter 3, Section 4.3 and Section 5.4. All authors conceptualized the paper. M.B.H. wrote and prepared the initial outline, and finalized the submission. F.S. did the initial design of the instrument. M.B.H., E.F.P. and F.S.

built and assembled the instrument. M.B.H., C.M.H. and F.S. acquired the data and performed calculations and analysis. All authors reviewed the draft and contributed to the final submission. The main work of M.B.H. for this publication was the calibration and comparison of HSI V6 to HSI V4 (throughput, smile and keystone).

Paper 2: **M. B. Henriksen**, E. F. Prentice, F. Sigernes, and T. A. Johansen, "Pre-Launch Calibration of the HYPSO-1 Cubesat Hyperspectral Imager" in Proc. IEEE Aerospace Conference, (2022).

This paper describes the methods and results from the pre-launch calibration campaign of the HYPSO-1 HSI, including wavelength and radiometric calibration, investigations of sensor characteristics, FWHM, smile, keystone, polarization sensitivity and spatial focus of the instrument.

Adapted results can be found in Chapter 7. M.B.H. wrote and prepared the initial outline, and finalized the submission. M.B.H. and E.F.P. acquired the data. M.B.H. performed the analysis. All authors reviewed the draft and contributed to the final submission. The main work of M.B.H. for this publication was the calibration of the HYPSO-1 HSI, as presented in the paper. This includes setting up the calibration procedures, acquiring the data and analyzing the data.

Paper 3: E. F. Prentice, **M. B. Henriksen**, T. A. Johansen, F. N. Medina, and A. G. S. Juan, "Characterizing Spectral Response in Thermal Environments, the HYPSO-1 Hyperspectral Imager" in Proc. IEEE Aerospace Conference, (2022).

This paper describes investigations of the HSI response with changing temperature, with experiments using the HYPSO-1 engineering model in a thermal chamber.

Adapted results from selected parts of the paper can be found in Section 6.2.2. E.F.P. wrote and prepared the initial outline, and finalized the submission. E.F.P. acquired the data. E.F.P. and M.B.H. performed the analysis. All authors reviewed the draft and contributed to the final submission. The main work of M.B.H. For this publication was helping E.F.P. with the data analysis and discussion of the results.

Paper 4: E. F. Prentice, E. Honoré-Livermore, S. Bakken, **M. B. Henriksen**, R. Birkeland, M. Hjertenæs, A. Gjersvik, T. A. Johansen, F. Aguado-Agelet, F. Navarro-Medina, "Pre-Launch Assembly, Integration, and Testing Strategy of a Hyperspectral Imaging CubeSat, HYPSO-1" in Remote Sensing, Vol. 14, No. 18, (2022).

This paper describes the Assembly, Integration, and Testing (AIT) process of the HYPSO-1 HSI payload, including timelines, details of the assembly process, overview and results from tests and a summary of lessons from the process.

Adapted results from selected parts of the paper (test overview, radiation test and Thermal Vacuum (TVAC) test) can be found in Chapter 6. Author contributions are as follows: Conceptualization, E.F.P. and T.A.J.; methodology, E.F.P., E.H.-L. and F.A.- A.; software, S.B. and R.B.; investigation, E.F.P., M.H. and M.B.H.; resources, M.B.H., A.G., F.A.-A. and F.N.-M.; writing—original draft preparation, E.F.P., E.H.-L., S.B. and R.B.; writing—review and editing, all; visualization, E.F.P., M.H. and E.H.-L.; supervision, T.A.J.; project administration, E.H.-L.; funding acquisition, T.A.J., R.B. and E.H.-L. All authors have read and agreed to the published version of the manuscript. The main contributions of M.B.H. for this publication was acquiring and analyzing data from the radiation test, and helping with analysis and discussion of the results regarding the optical data (images) acquired during the other environmental tests.

Paper 5: **M. B. Henriksen**, F. Sigernes, T. A. Johansen, "A Closer Look at a Spectrographic Wavelength Calibration" in Proc. 12th Workshop on Hyperspectral Image and Signal Processing: Evolution in Remote Sensing (WHISPERS), (2022).

This paper describes an investigation of wavelength calibration using spectral lamps, focusing on the algorithms used to calculate and apply the calibration coefficients to provide the most accurate result with a simple set-up.

Adapted results can be found in Section 4.4. M.B.H. wrote and prepared the initial outline, and finalized the submission. M.B.H. acquired the data and performed the analysis, with input from F.S. and T.A.J. All authors reviewed the draft and contributed to the final submission.

Paper 6: **M. B. Henriksen**, J. L. Garrett, T. A. Johansen, F. Sigernes, "Comparing pre- and post-launch images from the HYPSO-1 cubesat hyperspectral imager" in Proc. 73rd International Astronautical Congress (IAC), (2022).

This paper describes an initial look at the HYPSO-1 in-orbit data, focusing on comparing the HSI performance from the pre-launch calibration campaign to the data captured in-orbit. Several datasets were captured in-orbit to estimate noise, spectrogram artifacts, spectral shift and spatial shift. In addition, a method for destriping to correct the images was proposed.

Adapted results can be found in Chapter 8. M.B.H. wrote and prepared the initial outline, and finalized the submission. Data was acquired by the HYPSO team. M.B.H. and J.L.G. performed the analysis. All authors reviewed the draft and contributed to the final submission. The main work of M.B.H. for this publication was requesting in-orbit data from the HYPSO-team and comparing this data with the pre-launch calibration data to assess the performance of HYPSO-1 in-orbit.

Paper 7: S. Bakken, **M. B. Henriksen**, R. Birkeland, D. D. Langer, A. E. Oudijk, S. Berg, Y. Pursley, J. L. Garrett, F. Gran-Jansen, E. Honoré-Livermore, M. E. Grøtte, B. A. Kristiansen, M. Orlandic, A. J. Sørensen, F. Sigernes, G. Johnsen, T. A. Johansen, "HYPSO-1 CubeSat: First Images and In-Orbit Characterization" in Remote Sensing, Vol. 15, No. 3, (2023).

This paper describes the first in-orbit images and analysis of the HYPSO-1 CubeSat hyperspectral imager. The development and current status of the mission and payload operations is described, and the in-orbit performance of the HSI investigated, including the spatial and spectral resolution, radiometric performance and SNR.

Adapted results from selected parts of the paper (spectral resolution and the Kongsfjorden campaign) can be found in Section 8.1.5 and Section 9.2.1, respectively. Author contributions are as follows: Conceptualization, T.A.J.; Data curation, S.Bakken., M.B.H., R.B., D.D.L., S.B. and M.E.G.; Formal analysis, S.Bakken., M.B.H., D.D.L., Y.P., J.L.G., M.O. and G.J.; Funding acquisition, A.J.S. and T.A.J.; Investigation, S.Bakken., M.B.H., D.D.L., S.Berg., Y.P., M.E.G. and F.S.; Methodology, S.Bakken., M.B.H., D.D.L., A.E.O., S.Berg., J.L.G., M.E.G. and F.S.; Project administration, S.Bakken., E.H.-L., M.O., A.J.S. and T.A.J.; Resources, S.Bakken., R.B., A.E.O., S.Berg., E.H.-L. and T.A.J.; Software, S.Bakken., M.B.H., D.D.L., S.Berg., Y.P. and J.L.G.; Supervision, E.H.-L., M.O., A.J.S., G.J. and T.A.J.; Visualization, S.Bakken., M.B.H., D.D.L., Y. P. and J.L.G.; Writing – original draft, S.Bakken., M.B.H., R.B., D.D.L., A.E.O., S.Berg., Y.P., J.L.G., E.H.-L., G.J. and T.A.J.; Writing – review & editing, S.Bakken., M.B.H., R.B., D.D.L., A.E.O., S.Berg., F.G.-J., Y.P., J.L.G., E.H.-L., M.E.G., B.A.K., M.O., P.G., A.J.S., F.S., G.J. and T.A.J. The main contributions of M.B.H. for this publication was estimating and presenting the spectral resolution from the in-orbit data and presenting data from the Kongsfjorden campaign, as well as drafting and helping with the organization of the full paper.

Paper 8: M. Haugum, G. M. Fragoso, **M. B. Henriksen**, A. Zolich and T. A. Johansen, "Autonomous Flow-Through RGB and Hyperspectral Imaging for Unmanned Surface Vehicles" in Proc. OCEANS Limerick, (2023).

This paper describes the construction of an autonomous flow-through imaging system (microscope) with, among others, a hyperspectral camera attached. This system can be used to scan water samples in-situ, and the hyperspectral data can be useful for classification of the particles (such as algae).

Adapted results from selected parts of the paper can be found in Section 9.3, mostly focusing on the hyperspectral data samples and analysis of these samples. M.H. wrote and prepared the initial outline, and finalized the submission. M.H. and A.P.Z. built the system. M.H. acquired the data. M.H., G.M.F. and M.B.H. performed the analysis. All authors reviewed the draft and contributed to the final submission. The main contributions of M.B.H. for this publication was calibration and analysis of the hyperspectral data acquired.

Paper 9: G. M. Selnesaunet, **M. B. Henriksen** and T. Skauli, "Imaging the point spread function of hyperspectral cameras - the full truth about coregistration error and resolution" in Proc. SPIE Optics+Photonics, (2023).

This paper describes a set-up and method that can be used to measure the spatial Point Spread Function (PSF) for characterization of cameras (including hyperspectral imagers).

Adapted results from selected parts of the paper can be found in Section 4.1.3 and Section 4.2.5. G.M.S. wrote and prepared the initial outline.G.M.S. and T.S. made the set-up, M.B.H. supported with SW control of the cameras. G.M.S. and M.B.H. acquired the data. G.M.S. performed the analysis, with input from M.B.H. and T.S. All authors reviewed the draft and contributed to the final submission. The main contributions of M.B.H. for this publication was the development of the SW controlling the hyperspectral cameras, and help with the analysis of the results.

Paper 10: **M. B. Henriksen**, F. Sigernes, T. A. Johansen, "Comparing filters for correction of second order diffraction effects in hyperspectral imagers" in Proc. 13th Workshop on Hyperspectral Image and Signal Processing: Evolution in Remote Sensing (WHISPERS), (2023).

This paper describes how second order diffraction effects can be corrected by the use of filters, and compares four different filters in combination with three different light sources to assess which set-up is better to use to characterize the second order effects.

Adapted results can be found in Chapter 5. M.B.H. wrote and prepared the initial outline, and finalized the submission. M.B.H. acquired the data and performed the analysis. All authors reviewed the draft and contributed to the final submission.

Paper 11: **M. B. Henriksen**, G. M. Selnesaunet, T. Skauli, "Using spatial PSF measurements to compare the performance of two DIY hyperspectral imagers" (in preparation).

This paper describes the comparison of the measured spatial PSF for HSI V4 and HSI V6, as well as other metrics measured by the measurement system such as keystone and coregistration error.

Adapted results can be found in Section 4.3.4. All authors wrote and prepared the initial outline. Measurement set-up was prepared by G.M.S. and T.S., instruments were prepared by M.B.H. Data acquisition and analysis was performed by M.B.H. and G.M.S. All authors reviewed the draft and contributed to the final submission. The main contributions of M.B.H. for this publication was the development of the SW controlling the hyperspectral cameras, and analysis and discussions of the comparison of the cameras.

A list of SPs follows, in chronological order. These publications use the work presented in this thesis. They are referred to and included in the list of publications, but the content from these publications are not included in the thesis.

SP 1: **M. B. Henriksen**, J. L. Garrett, E. F. Prentice, A. Stahl, T. A. Johansen, and F. Sigernes, "Real-time Corrections for a Low-cost Hyperspectral Instrument" in Proc. 10th Workshop on Hyperspectral Image and Signal Processing: Evolution in Remote Sensing (WHISPERS), (2019).

This paper describes a method for smile and keystone characterization and software correction in the HSI V4 instrument.

The paper is referred to in Section 4.2.4. M.B.H. wrote and prepared the initial outline, and finalized the submission. M.B.H. and E.F.P. acquired the data. M.B.H. and J.L.G. performed the analysis. All authors reviewed the draft and contributed to the

final submission. The main work of M.B.H. for this publication was the calibration (procedures, measurements and analysis) of the hyperspectral imager, and making the set-up and testing the method for smile and keystone detection.

SP 2: A. E. Oudijk, H. Øveraas, S. Marty, D. R. Williamson, T. Svendsen, S. Berg, R. Birkeland, D. Ø. Halvorsen, S. Bakken, **M. B. Henriksen**, M. O. Alver, G. Johnsen, T. A. Johansen, A. Stahl, P. Kvaløy, A. Dallolio, S. Majaneva, G. M. Fragoso, J. L. Garrett, "Campaign for Hyperspectral Data Validation in North Atlantic Coastal Waters" in Proc. 12th Workshop on Hyperspectral Image and Signal Processing: Evolution in Remote Sensing (WHISPERS), (2022).

This paper describes a joint research campaign in Frohavet outside of Mausund in April 2022, focusing on the technology, sensor and platforms used and the data gathered during the campaign.

The paper is referred to in Section 9.1. A.E.O. wrote and prepared the initial outline, and finalized the submission. A.E.O, H.Ø., S.M., D.R.W, T.S., S.B., R.B., D.Ø.H., S.B., P.K. A.D., S.M., G.M.F. and J.L.G. acquired the data. All authors contributed to the analysis. All authors reviewed the draft and contributed to the final submission. The main contributions of M.B.H. for this publication was helping with the calibration of the HYPSO-1 data used in the campaign.

SP 3: F. Navarro-Medina, A. E. Oudijk, **M. B. Henriksen**, A. Gjersvik, F. S. Grønvold, T. A. Johansen, "Experimental set-up of a thermal-vacuum chamber for thermal model in-house correlation and characterization of the HYPSO hyperspectral imager" in CEAS Space Journal, (2023).

This paper describes additional thermoelastic experiments performed with the HYPSO-1 qualification model, to investigate how different temperatures in affects the HSI performance in vacuum. The focus is on the experimental set-up and the method of comparing experimental results with models and simulation results.

The paper is referred to in Section 6.2.2. All authors contributed to the study conception and design. F.N.-M. and A.E.O. prepared the first draft of the manuscript. F.S.G. made the initial vacuum chamber set-up. F.N.-M., A.E.O. and A.G. adapted the vacuum chamber for thermoelastic measurements and performed the initial tests. F.N.-M., A.E.O. and M.B.H. collected the data and performed the analysis. All authors reviewed the draft and contributed to the final submission. The main contributions of M.B.H.

for this publication was help with acquisition of the hyperspectral data and analysis of these hyperspectral images from the test.

SP 4: F. Navarro-Medina, A. E. Oudijk, **M. B. Henriksen**, U. Garcia-Luis, A. Gomez-San Juan and T. A. Johansen, "Structural Thermal Optical Performance (STOP) analysis and experimental verification of an hyperspectral imager for the HYPSO CubeSat" in Optics and Lasers in Engineering, Vol. 173, (2024).

This paper describes a structural thermal optical performance (STOP) analysis of the HYPSO HSI, which is further compared with experimental results from thermoelastic experiments.

The paper is referred to in Section 6.2.2. All authors contributed to the study conception and design. Material preparation, data collection and analysis were performed by A.E.O. and F.N.-M. The thermal model and analysis and the thermal-structural interface were performed by U.G.-L. and F.N.-M. The structural model and analysis and the structural-optical interface were performed by A.G.-S.J. and F.N.-M The optical model and analysis, and the experiments were performed by A.E.O., T.A.J., F.N.-M. and M.B.H. The first draft of the manuscript was written by F.N.-M. and A.E.O. and all authors commented on previous versions of the manuscript. The final edition of the text and of all figures was done by U.G.-L. All authors read and approved the final manuscript. The main contributions of M.B.H. for this publication was help with acquisition of the hyperspectral data and analysis of these hyperspectral images from the test.

SP 5: J. A. Justo, D. D. Langer, J. L. Garrett, **M. B. Henriksen**, R. T. Ionescu, and T. A. Johansen, "An Open Hyperspectral Dataset with Sea-Land-Cloud Ground-Truth from the HYPSO-1 Satellite" in Proc. 13th Workshop on Hyperspectral Image and Signal Processing: Evolution in Remote Sensing (WHISPERS), (2023).

This paper describes an open dataset of HYPSO-1 data, calibrated and labeled so that it is ready to be used for classification, testing new algorithms and other applications for external users.

The paper is referred to in Section 9.1. The main contributions of M.B.H. for this publication was on the calibration of the HYPSO-1 data.

1.3.4 Other contributions and responsibilities

During these years I have been a part of the HYPSO project and the Small Satellite (SmallSat) lab at NTNU. This has given me additional tasks and responsibilities on the way, including:

- Leading the mechanical team for development of the HYPSO hyperspectral payloads since the beginning of 2021.
- Supporting and supervising a number of students (both on bachelor's and master's level) within the HYPSO project.
- Leading the activities within the Programme de Développement d'Expériences Scientifiques (PRODEX) project since the beginning of 2022.
- Lecturing in TTK4265 (one semester) and helping out with the course lab work.
- Providing input for the development of a new optics lab at the Department of Engineering Cybernetics (ITK), NTNU.

In addition to the publications listed in the previous section, the following presentations based on work in this thesis have also been presented at different events:

- "HYPSO-1 Cubesat with Hyperspectral Imager over Ny-Ålesund, Svalbard" at the Svalbard Integrated Arctic Earth Observing System (SIOS) online conference, 12-14 October 2022.
- "HYPSO-1 Cubesat with Hyperspectral Imager over Ny-Ålesund, Svalbard" at the Polar Night Week (PNW) at the University Centre in Svalbard (UNIS) in Longyearbyen, Svalbard, 23-27 January 2023.
- "Pre-Launch Calibration of the HYPSO-2 Cubesat Hyperspectral Imager" at the the Workshop on Innovative Technologies for Space Optics (WITSO), at the European Space Research and Technology Centre (ESTEC) in Noordwijk, the Netherlands, 6-10 November 2023.

It can also be mentioned that the publication "A Closer Look at a Spectrographic Wavelength Calibration" won the *Outstanding Paper Award* at the the Workshop on Hyperspectral Image and Signal Processing: Evolution in Remote Sensing (WHISPERS) conference in 2022, and that the presentation "HYPSO-1 Cubesat with Hyperspectral Imager over Ny-Ålesund, Svalbard" won a place at the SIOS PNW in 2023 being one of the top presentations presented at the SIOS online conference in 2022.

1.3.5 Thesis outline

This thesis is built up as follows. This chapter, Chapter 1, introduces the HYPSO mission and the main motivation for both the mission and thereby also the work presented in this thesis. Research questions are defined, and publications related to this thesis are described. Next, relevant background theory is presented in Chapter 2. First, theory related to ocean color is described to get a better understanding of what is required of the instrument to observe oceanographic features such as algal blooms. This is followed by details on hyperspectral imaging, discussing different techniques and giving examples of other HSIs used on small satellites. Then, selected calibration and characterization techniques are presented to provide some background theory on how these procedures can be performed and which set-ups are typically used.

The following content of the thesis is divided into two main parts. The first part describes the development of the hyperspectral imager used in this thesis (Chapter 3), the general methods of calibration procedures that are used (Chapter 4), details on the wavelength calibration (Section 4.4) and methods for second order correction (Chapter 5). The second part discusses all work related to the HYPSO missions, starting off by describing the AIT process of both HYPSO-1 and HYPSO-2 in Chapter 6. The pre-launch calibration of the HYPSO-1 HSI is then presented in Chapter 7, and in-orbit data from HYPSO-1 after launch is presented and discussed in Chapter 8. This is followed by a description of some research campaigns supported by HYPSO-1 in Section 9.1 and Section 9.2.1. On-ground signatures which can be useful for validation is found in Section 9.3. Finally, discussion and conclusion of the full thesis can be found in Chapter 10 and Chapter 11, respectively, where the work presented in this thesis will be discussed in context of the research questions and main goals.

2 | Background theory

First, an introduction to ocean color and phytoplankton pigments is presented. Secondly the concepts of hyperspectral imaging are introduced. Some small and compact HSI designs and small satellite missions are then presented, and finally some previous research and methods for HSI calibration and characterization are discussed.

2.1 Ocean color

Most of us consider the ocean blue. There are, however, many phenomena that can give the water hints of other colors such as turquoise, green, red, orange and brown. The visible color depends on the Inherent Optical Properties (IOPs) of the water (properties of the water that do not change with light) such as absorption and scattering (typically determined by the concentration of different particles and dissolved matter in the water), and the spectral composition and angular distribution of the incoming light [2]. The optical properties of the water that do change with light, such as its color, are called Apparent Optical Properties (AOPs). When measuring ocean color, information about the light field is therefore important to be able to retrieve IOPs such as Chl-a concentration. Light from the Sun is reflected both at and below the water surface, as illustrated in Figure 2.1, giving the water the color as we see it. Light is also scattered and reflected by gases and aerosols in the atmosphere, which affects the recorded light seen by the sensor. This can also make the observations hazy unless atmospheric correction is applied, as described further in Section 2.1.3.

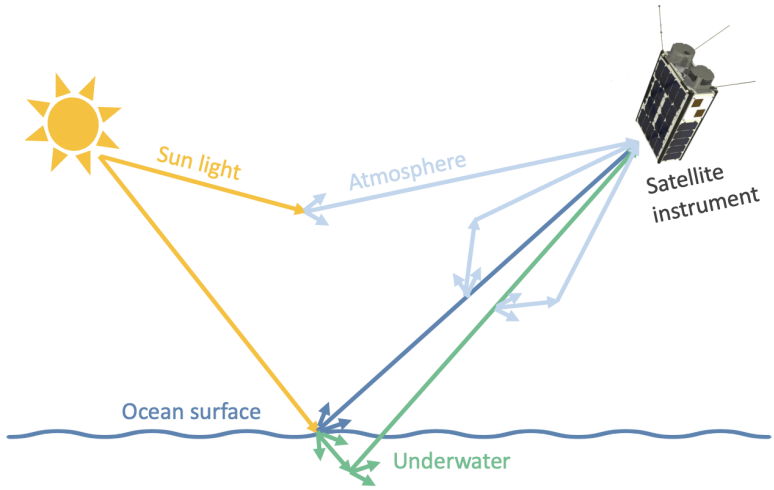

Figure 2.1: Illustration of sunlight being scattered and reflected on its path between the Sun and the sensor of an ocean color remote sensing satellite.

2.1.1 Case 1 and Case 2 waters

Productive and turbid waters, in contrast to "clear ocean", can be divided into two main types: Case 1 and Case 2 waters [37]. In Case 1 waters, phytoplankton is the dominating

optically significant constituent and it is mainly the absorption of phyoplankton pigments that affects the reflected spectral signature. In Case 2 waters, on the other hand, other optically significant constituent such as Colored Dissolved Organic Matter (CDOM) and non-algal Total Suspended Matter (TSM) are also present, and the reflected light will be a mix of the spectral signatures of the all the particles present. Coastal areas are typically Case 2 waters. Here, the sea floor might also be visible in shallow areas, adding another component affecting the reflected signal.

Chl-a retrival in Case 2 waters is therefore more complex than for Case 1 waters, and different algorithms are needed for the two cases [2]. In Case 1 waters, band ratio algorithms or other algorithms focusing on the phytoplankton pigments can be used to estimate the Chl-a concentration. In Case 2 waters, on the other hand, multivariate data analysis techniques might be needed to separate the concentrations of the different components.

2.1.2 Phytoplankton pigments and groups

Phytoplankton are unicellular microscopic marine algae (and some bacteria) utilizing photosynthesis. They contain different pigments, which vary with species. Common for all phytoplankton is the pigment Chl-a. This is useful in the sense that the Chl-a concentration can be (and often is) used to estimate phytoplankton biomass, in combination with information about other parameters such as Sea Surface Temperature (SST) and salinity [19, 24]. But it also means that Chl-a can not be used as a discriminator between different species. In other words, it does not provide much information about biodiversity.

Phytoplankton can be divided and grouped in different ways. One of them is by dividing into Chlorophyll-c (Chl-c) containing algae, Chlorophyll-b (Chl-b) containing algae, and phycobiliprotein phytoplankton, as done in Berge et al. [38]. Within these groups are, among others, diatoms, dinoflagellates and haptophytes examples of Chl-c containing algae, prasinophytes and chlorophytes examples of Chl-b containing algae, and crytpophytes and cyanobacteria examples of phycobiliprotein phytoplankton. Each of these classes have marker pigments, belonging to either chlorophylls, carotenoids or phycobiliproteins, which can be used for classification.

An overview of some marker pigments is given in [19] where, among others, fucoxanthin is mentioned as a major marker for diatoms (even though it is also present in prymnesiophytes, chrysophytes and dinoflagellates), peridinin a marker for

dinoflagellates, and Chl-b a marker for chlorophytes (and also present in prasinophytes). An extensive overview and examples of detecting different phytoplankton types is also given in [19].

It is, however, worth noting that the pigment content, and thereby the spectral signature, can vary within the same species, such as with the physiological state of the population [2]. The same species in different environments, such as Case 1 and Case 2 waters, can also have different pigment composition, as shown in Stuart et al. [39].

Nevertheless, an example of the absorbance spectra of some of the different pigment groups is shown in Figure 2.2. This shows that hyperspectral data collecting the full spectral signatures can be useful when trying to separate signal from the different pigments, as they are somewhat overlapping, but with different shapes and intensities in different parts of the spectrum.

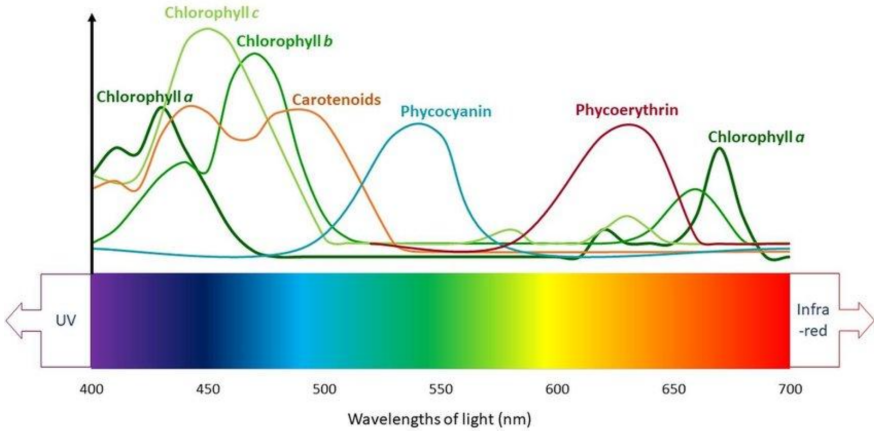

Figure 2.2: Example of absorbance spectra of some pigments that are typical in phytoplankton [24].

2.1.3 Satellite data products, atmospheric correction and reflectance

Satellite data is often processed to different pre-defined levels, as listed in Table 2.1. Most relevant for this thesis are levels 1a, 1b and 2. This is from the unprocessed data (with metadata attached) to calibrated data, and further to calculated data products such as reflectance and Chl-a concentration.

Table 2.1: Levels of satellite data products [40].

Data product	Description
Level 0	Unprocessed instrument data at full resolution, in raw units such as volts or digital counts.
Level 1a	Unprocessed instrument data at full resolution, with additional metadata such as calibration coefficients and georeference parameters attached, but not applied, to the data.
Level 1b	Calibrated instrument data, in calibrated units such as radiance.
Level 2	Data products such as normalized reflectance (by applying atmospheric correction) and geophysical variables (such as Chl-a concentration), at same resolution and location as Level 1 data.
Level 3	Variables mapped onto uniform space-time grid, with missing points interpolated or masked, and regions from several data sets mosaicked together.
Level 4	Results from combination of satellite data and model output, or results from other analysis.

The calibrated data product in level 1b is typically Top-of-Atmosphere (ToA) radiance, which is the radiance recorded at the sensor consisting of both reflected light from the ocean and light affected by absorption and scattering in the atmosphere. For ocean color applications, the signal from the atmosphere is an undesired part of the measured signal and is removed with atmospheric correction algorithms to retrieve the water-leaving radiance. As mentioned, only about 10% of the received signal is from the ocean, which makes the atmospheric correction of utmost importance for the quality of the further derived data products.

Atmospheric correction for Case 1 waters typically use the fact that the water-leaving radiance in the NIR domain (above 700 nm) is close to zero. Signal in this spectral range can therefore be used to estimate the optical properties in the atmosphere, which can be extrapolated to the visible spectral range through atmospheric models to obtain the water-leaving radiance [2]. Other effects such as white caps or sun glints might also disturb the signal, but are harder to correct for. In Gordon et al. [41], examples of atmospheric correction algorithms for SeaWiFS and MODIS are given. Further details on atmospheric corrections are, however, out of scope of this thesis, and will not be described here in more detail.

The spectral remote sensing reflectance, R_{rs}, is one of the more typical data products and can be defined as

$$R_{rs}(\theta, \phi, \lambda) = \frac{L_w(\theta, \phi, \lambda)}{E_d(\lambda)}, \tag{2.1}$$

where L_w is the water-leaving radiance (referring to the upwelling light that has been reflected from all depths in the water and can be observed just at the water surface), E_d is the downwelling irradiance (incoming light from the Sun), λ is wavelength (as it is spectrally dependent), θ is the observer zenith angle and ϕ the observer azimuth angle. L_w can be measured by remote sensing platforms (with atmospheric corrections applied to the data), while E_d is the known Solar irradiance [40]. Also often used is the normalized marine reflectance ρ_{wN}, which is defined as π times the remote sensing reflectance [42].

2.1.4 Algorithms for chl-a retrieval

Standard algorithms to retrieve Chl-a concentrations typically use spectral band ratios of water-leaving radiance or reflectance with bands in the blue and green part of the visible spectrum [19, 43, 44]. It can, for example, be estimated from a fourth-order polynomial equation such as

$$\log_{10}([\text{chl-a}]) = a_0 + a_1 X + a_2 X^2 + a_3 X^3 + a_4 X^4, \tag{2.2}$$

where a_0 to a_4 are the polynomial fit coefficients and X calculated as

$$X = \log_{10}\Big(\frac{R_{rs}(\lambda_{blue})}{R_{rs}(\lambda_{green})}\Big), \tag{2.3}$$

where λ_{blue} and λ_{green} refers to a wavelength in the blue and green part of the spectrum, respectively [43].

An example of this is the Ocean Chlorophyll (OC) algorithms OC2 and OC4 developed for SeaWiFS. OC2 uses the bands 490 nm (blue) and 555 nm (green) in Equation (2.3), while OC4 uses four bands where one of 443 nm, 490 nm and 510 nm are used as the blue band and 555 nm is used as the green band [45]. The reason OC4 uses four bands is that the different blue bands may cause over or underestimation of Chl-a based on there being high or low Chl-a concentration in the water. The band used is therefore selected based on which band has the strongest response (which is related to the amount of Chl-a). These algorithms are then tuned (finding values for a_0 to a_4) by comparing the results with in-situ measurements.

Acquisition of in-situ data is therefore very important, and it also important for validation of the final data products once the algorithm is established.

2.1.5 Recommendations for ocean color remote sensing

There are several reports with recommendations for ocean color remote sensing, such as [42, 46, 47, 48]. Some focus on mission requirements, while others focus more on sensor and instrument specific requirements. Some of the recommendations concerning remote sensing missions and instruments focusing on Chl-a and phytoplankton detection and classification are presented here. At the end of this section, a summary of the requirements presented here is given in Table 2.2.

In Case 1 waters, the visible spectrum can be divided into two main parts; the blue part (below 590 nm) and the red part (above 590 nm). Ideally, one wavelength from each of these parts is enough to calculate a ratio to detect changes in Chl-a concentration. In real life, however, the process is more complex, with atmospheric effects affecting the signal and other constituents being present in the water.

For atmospheric correction, at least two bands in the NIR, sufficiently distant from each other, should be used (due to aerosol scattering varying spectrally, but in a smooth manner). They should also be close to the visible domain to ensure reliable extrapolation to the visible part of the spectrum. The NIR channels should be selected to avoid prominent absorption bands, such as water vapor and oxygen bands. Suggested "safe windows" from the International Ocean Colour Coordinating Group (IOCCG) report no. 1 [46] are 704-713 nm, 744-757 nm, 772-786 nm, 855-890 nm and 1025-1064 nm, where the higher wavelengths provide the safest windows.

Retrieving more pigments than just Chl-a also increases the wavelength requirements even further. From the IOCCG report no. 13 [42], the recommended wavelengths for Chl-a detection are 360 nm, 385 nm, 400 nm, 412 nm, 425 nm, 443 nm, 490 nm, 510 nm, 555 nm, 565 nm, 670 nm, 710 nm and 748 nm (in addition to bands for atmospheric correction). For detection of other phytoplankton pigments, 655 nm is recommended for Chl-b, 470 nm for carotenoids, 490 nm and 550 nm for phycoerythrin and 620 nm for phycocyanin. To identify phytoplankton taxonomic groups, 710 nm is suggested in addition. Identifying CDOM and TSM in Case 2 waters requires information from additional spectral bands, which increases the number of bands needed. Signal from phytoplankton and CDOM diverges at shorter wavelengths (around 380 nm to 440 nm) where the phytoplankon absorption tends to decrease while the absorption from CDOM

Table 2.2: Summary of recommended requirements for ocean color remote sensing, focusing on missions and instruments used for phytoplankton detection and classification.

Parameter	Requirement	Comment
Wavelengths, Chl-a	360 nm, 385 nm, 400 nm, 412 nm, 425 nm, 443 nm, 490 nm, 510 nm, 555 nm, 565 nm, 670 nm, 710 nm, 748 nm	Main bands are 412 nm, 443 nm and 555 nm.
Wavelengths, other pigments	470 nm, 490 nm, 550 nm, 620 nm, 655 nm	For Chl-b, carotenoids, phycoerythrin and phycocyanin.
Wavelength, taxonomic groups	710 nm	
Wavelengths, CDOM and TSM	410 nm	Other bands close to UV can also be used.
Wavelengths, atmospheric correction	704-713 nm, 744-757 nm, 772-786 nm, 855-890 nm, 1025-1064 nm	Minimum two bands within the suggested spectral windows.
Spectral resolution	< 5 nm	
SNR	400-1000, (> 800 preferred)	Before atmospheric correction (after it should be 40-100).
Bit depth of sensor	12- or 14-bit	For sufficient dynamic range.
Radiometric accuracy of radiance product	2-5%	Accuracy of ToA radiance should be 0.5%.
Polarization sensitivity	$< 1\%$	
Spatial resolution	50-1000 m	Varies with application (and Case 1 or Case 2 waters).
Temporal resolution	1 hour - 3 days	

increases exponentially [46]. A band closer to UV such as at 410 nm can therefore be beneficial to distinguish phytoplankton and CDOM. A hyperspectral sensor in the visible to NIR domain is therefore beneficial, as it will cover all the bands in the selected spectral range. Trying to identify small changes in the pigment composition from different phytoplanktonic species increases the spectral resolution requirement, since narrow bands are required to observe these shifts [46]. A spectral resolution of at least 5 nm

is recommended, and even less than 1 nm for certain biophysical signatures such as fluorescent lines. For atmospheric bands closer to NIR, a spectral resolution of 10 nm might be sufficient [42, 47, 48].

Further, high SNR is recommended for both Case 1 and Case 2 waters. From [49], an SNR of minimum 400 is recommended, Turpie et al. [47] suggests an SNR of 500-1000, while in Muller-Karger et al. [48] an SNR above 800 is preferred. These requirements are based on the definition of SNR found in Gordon et al. [50], using the total signal and noise at the sensor (ToA). The corresponding atmospherically corrected SNR should be about 40-100 [51]. There is often higher concentrations of Chl-a and CDOM in Case 2 waters, giving low signal in the 380 nm to 440 nm range. However, for coastal areas, features such as clouds and sand should not be saturated, which means that the sensitivity, or dynamic range, must be greater than when observing only Case 1 waters. A dynamic range of 12- or 14-bit would typically be required for Case 2 waters [2], where 14-bit is the preferred choice [47, 48]. To ensure an accuracy of around 30% of the derived Chl-a products, a water-leaving radiance accuracy of 5% (at 443 nm) is required, which translates to a goal of 0.5% accuracy of the ToA radiance [42, 52]. To achieve this, effects from stray light (unwanted light in the system) should be reduced as much as possible in the instrument design, and polarization sensitivity should be kept below 1%. The radiometric accuracy requirements for SeaWiFS and MODIS (for the visible range) were 5% for absolute radiance values and 2% for relative reflectance values, and it is advised to keep these requirements for future missions. For high calibration standards like this, on-board calibration systems are typically used. Vicarious calibration techniques can also be used, but might not achieve the same accuracy [46]. Even stricter values were suggested in Muller-Karger et al. [48], with an absolute radiometric calibration accuracy less than 2%, and relative calibration accuracy of 0.2%.

For Case 1 waters, a spatial resolution of at least 1 km is recommended. For coastal waters, a spatial resolution of about 250 to 300 m is suggested, while a higher resolution closer to 50 m is recommended for some specific applications such as HAB detection [42, 47, 53]. A temporal resolution of hours to days are recommended, depending on application. For algal bloom detection, 1 hour to 3 days is suggested [47, 48].

Finally, the IOCCG report no. 1 [46] points out that simple and cheap sensors would be desirable. They must, however, fulfill the scientific requirements for their applications. A constellation of satellites can also be beneficial, as it allows observations of the same target from different angles, and increases the temporal resolution.

2.2 Hyperspectral remote sensing

Hyperspectral imaging, also called imaging spectroscopy, can be useful in many fields. A hyperspectral image essentially holds an additional dimension of spectral information in each pixel. Any application that can benefit from spectral signatures in more than one point can therefore find hyperspectral imaging useful. For remote sensing purposes, hyperspectral instruments can be used to map and classify different components in larger areas, whether it be forests, fields, mountains or oceans. It can also be used to study ecosystems, natural cycles such as the water cycle, carbon cycle and nutrition cycles, or monitor status of areas and events such forest fires, change in ice coverage, and vegetation health, are some examples.

In this thesis the focus is on small pushbroom hyperspectral imagers used in remote sensing applications (from drones and satellite platforms) for ocean color Earth observation. Hyperspectral imaging with pushbroom grating-based instruments are therefore first described. Some other small and compact HSI designs are then presented, followed by a description of other small and compact hyperspectral satellite payloads.

2.2.1 Hyperspectral imaging with a pushbroom grating-based design

When acquiring hyperspectral data with a pushbroom grating-based hyperspectral imager, a continuous part of the electromagnetic spectrum is imaged for each pixel in the spatial image. The dispersive element, here the grating, disperses the light so that different wavelength reach different parts of the camera sensor. Other dispersive element configurations, such as using a prism or prism and grating together (grism) can also be used, as described in the next section.

The instrument typically consists of front optics focusing the light onto an entrance slit, followed by optics collimating the light towards the grating. From here, imaging optics focuses the light again onto the image sensor which records the final signal. The optical diagram illustrating this concept is shown in Figure 3.1 in Chapter 3. The image captured by the sensor can be referred to as a spectrogram. It has one spatial dimension (along the slit), and one spectral dimension containing the spectral signature of each spatial pixel. When used in a pushbroom configuration, the instrument scans an area while capturing images, and these are combined into a hyperspectral datacube with two spatial dimensions and one spectral dimension.

2.2.2 Other hyperspectral imaging techniques

In addition to pure grating-based designs, configurations with prisms or both gratings and prisms can also be used. In Herrala et al. [54], an HSI using a prism-grating-prism configuration was presented, and in Sigernes et al. [55] a grating-prism instrument was used. Both of these design are examples of small, compact and lightweight HSIs. Volent et al. [56] shows an example on how the grating-prism HSI can be used for remote sensing purposes for example, by using it for kelp forest mapping in Ny-Ålesund from an aerial platform.

Other methods to capture hyperspectral data includes spectral filters, Fourier transform imaging interferometers and snapshot hyperspectral imagers. An overview describing these methods, as well as their advantages and disadvantages, can be found in Qian et al. [57]. The spectral filter based approach uses filters to block and transmit the desired wavelengths. For example can tunable filters or Linear Variable Filters (LVFs) be used. Fabry-Pérot Interferometer (FPI) based filters, transmitting only the selected bands of interest, are also an option. The Fabry-Pérot filters can also be placed on-chip on top of a detector. It is then referred to as an On-Chip Stepped Filter (OCSF). The Fourier transform approach is based on imaging interferometers. The interferograms that are obtained by the interferometer then goes through a Fourier transform algorithm to extract the spectral signature for each pixel.

With the snapshot approach, no scanning is necessary as the full hyperspectral datacube is generated in one single capture (as the name suggests). This requires a more complex design, but can be achieved by several imaging technologies. Some of these include multi-aperture filtered camera, coded aperture snapshot spectral imager and image mapping spectrometry. FPIs can also be used. An example of a piezo actuated Fabry-Pérot interferometer used as a snapshot HSI is presented in Saari et al. [58], and is small and light weight enough to fit on a Unmanned Aerial Vehicle (UAV) platform as shown in Saari et al. [59] and Honkavaara et al. [60]. Another example of a snapshot HSI is the instrument presented in Dwight et al. [61], which is based on the image mapping principle [62]. Multispectral imaging is also a similar technique utilizing more than the standard three RGB bands. The number of bands are, however, limited, and normally not continuous such as for a hyperspectral imager. For ocean color remote sensing, both multi- and hyperspectral instruments are and have been used. Here, the pushbroom hyperspectral instruments are in focus, but comparisons to multispectral imagers are used when applicable.

2.2.3 Examples of small HSIs used in space

The number of new satellites is increasing, and with smaller satellite platforms such as CubeSats, the satellite instruments developed are both increasing in number and decreasing in size. A larger portion of these instruments are now also becoming hyperspectral. A comprehensive overview over hyperspectral satellites, their history and their evolution can be found in Qian et al. [57]. Another overview over hyperspectral instruments for aquatic remote sensing can be found in Dierssen et al. [26]. Here, some selected (multi- and) hyperspectral instruments onboard (or planned to be onboard) satellite platforms are presented, as seen in Table 2.3.

Table 2.3: Examples of other small multi- and hyperspectral instruments used for space.

Name	Type	Spectral range	Spectral resolution	Spatial resolution	SNR
HICO	Grating	380-1000 nm	5.7 nm	90 m	200
AaSI	Fabry-Pérot	500-900 nm	10 nm	200 m	(unknown)
Hyperscout	LVF	450-900 nm	10 nm	80 m	50 @ 300 km
NACHOS	Grating	290-500 nm	1.3 nm	400 m	(unknown)
CSIMBA	Interference filter	475-900 nm	5 nm	20 m	15-300
ASPECT	Fabry-Pérot	500-900 nm	10 nm	1 m @ 3 km	(unknown)
Hawkeye	Linear filter	412-865 nm[a]	20 nm	120 m	120-400
ELOIS	Freeform grating	400-2450 nm	10 nm	35 m	> 400
CHIMA	Freeform grating	600-800 nm	0.5 nm	1 km	> 1000

[a] Only 8 bands in the 412-865 nm range.

HICO was, as it names suggest, designed specifically for the coastal ocean, focusing on the littoral, estuarial, riverine and other shallow-water areas. It was not launched on a satellite, but mounted on ISS from 2009 until its end of life in 2014. The instrument was a pushbroom grating-based HSI in the 400 nm to 900 nm spectral range with an Offner configuration in front of the slit. The laboratory calibration of the instrument is presented in Korwan et al. [63], showing details of the performance of the instrument prior to launch, including the measured smile and keystone distortions. The first images and initial in-orbit results were presented in Lucke et al. [10], while vicarious calibration

techniques applied to the HICO data have been presented in Gao et al. [64]. They show that a spectral shift was detected after launch, how second order correction can be applied following the method presented in Li et al. [65] and perform in-orbit radiometric calibration to achieve level 1b data. Even though HICO is slightly larger than HYPSO-1, weighing 41 kg compared to 7 kg for HYPSO-1, it is interesting to compare the two both in terms of performance and development process.

In 2017, the Finnish Aalto-1 3U CubeSat launched with, among others, the Aalto Spectral Imager (AaSI) onboard. AaSI was developed based on the Fabry-Pérot HSIs presented by Saari et al. in [58], with its main goal being a technology demonstrator of these instruments in space [66]. It can record 2D spatial images at one to three selected wavelengths simultaneously, using multiple orders of the FPI transmission function with the RGB Bayer pattern on the image sensor. Within seconds it can also capture images in the other channels. The design of the Aalto-1 CubeSat is presented in Praks et al. [67], while some of the first images from the AaSI in-orbit are presented in Mughal et al. [68]. Hyperscout, on the other hand, was first launched in 2018, and was developed to be a commercially available product for Earth observation. It has been followed by a second generation, Hyperscout-2, which has a second Infrared (IR) channel and was launched in 2020. The Hyperscout instrument is a pushbroom HSI with a Three-Mirror Anastigmat (TMA) telescope at the front, and a LVF separating the wavelengths on the sensor. It is designed to be extremely compact, with a size of only 1U and weighs less than 2 kg [69, 70]. Hyperscout also focuses on onboard data processing, which is further described in Soukup et al. [71].

In 2022, the Nano-satellite Atmospheric Chemistry Hyperspectral Observation System (NACHOS) was launched on a 3U cubesat. The instrument uses a grating based Offner design, making it compact. The imager itself is only 1U in size, with an additional 0.5U for the electronics stack. NACHOS focuses more on anthropogenic and volcanic gas-phase emissions, and is designed closer to the Ultraviolet (UV) with a spectral range of 290 nm to 500 nm and a spectral resolution of 1.3 nm with a 0.57 nm spectral sampling interval. To ensure low noise (as high SNR is needed for gas detection), a simple on-board calibration system was also included. Four Light Emitting Diodes (LEDs) was placed inside the instrument right in front of the sensor so that they provide even illumination when turned on. Bright images are then captured in-orbit by turning on these LEDs, while dark frames are captured by pointing the satellite towards deep space. This is used to remove pixel-to-pixel non-uniformities in the sensor response, which reduces noise and increases the SNR [72]. The laboratory calibration and field performance tests can be found in Post et al. [73].

In addition to the ones already launched, several small hyperspectral payloads are currently under development. The Compact Smartspectral Imager for Monitoring Bio-agricultural Areas (CSIMBA) is a pushframe HSI with a TMA telescope and a thin film interference filter directly deposited onto the image sensor [74, 75]. The instrument is made for a 12U CubeSat, and is planned to be launched in 2023 [76]. The spectral range is 475 nm to 900 nm, and the spectral resolution 5 nm. Its main use case is monitoring vegetation, agricultural fields and biodiversity status.

Based on the AaSI design (among others) is also the Asteroid Spectral Imaging Mission (ASPECT) spectral imager payload. This aims to use the hyperspectral imager for deep space exploration of small Solar system bodies, and is planned to be of a 1-3U size [77, 78]. The Hawkeye instrument is another small ocean color instrument, only 1U in size. It is, however, multispectral rather than hyperspectral, capturing only up to 8 bands at the time, similar to SeaWiFS [79].

Another larger instrument (40 kg class) is the Enhanced Light Offner Imaging Spectrometer (ELOIS). This uses a freeform grating design which offers increased flexibility and throughput performances, reduced offsets due to smile and keystone and allows reduction of about a factor 4 in volume with respect to classical Offner-spectrometer designs. It is developed to cover the 400 nm to 2450 nm range with a spectral resolution of 10 nm, where a resolution of 2.5 nm is available in the unbinned mode [80]. It targets land observation and will provide a spatial resolution of 35 m [81].

Inspired by ELOIS, the Compact Hyperspectral Instrument for Monitoring the Atmosphere (CHIMA) is also being developed. CHIMA focuses on higher spectral resolution and higher SNR, targeting atmospheric applications. The spectral range was reduced to 600 nm to 800 nm, and the spectral resolution increased to 0.5 nm. Low smile and keystone distortions are still in focus, and high SNR will be achieved by binning 3x3 pixels. To keep the high spectral resolution even when binning is applied the original spectroscope layout is folded, making a complex yet high-performing design [80, 81].

A common factor for the smaller satellite instruments is that there is rarely space to include calibration equipment onboard the satellite. This results in the pre-launch calibration to be extremely important. In addition, vicarious calibration methods and in-orbit calibration using natural targets is commonly used for these smaller satellites, as further described in Section 2.3.8.

2.3 Calibration and instrument performance

Calibration is the process of converting sensor specific units, such as pixel number or sensor count, to physical units, such as wavelength or radiance. This way, measurements and derived data products from different sensors can be compared, and the amount of measured light can for example be used to estimate Chl-a concentration in the ocean. In addition to the calibration, characterization of the instrument response is important to understand how the measurements are obtained, what kind of disturbances that may arise in the data and why. For space instruments, the calibration and characterization can be divided into pre-launch and post-launch (in-orbit) measurements. The pre-launch calibration and characterization should be extensive and characterize as many aspects of the instrument as possible [42]. The in-orbit calibration and characterization is often more limited since measurement set-ups in a controlled environment no are no longer available. There are, however, some methods for in-orbit calibration and characterization, as described further in Section 2.3.8.

In Datla et al. [82], a guideline for best practice when it comes to the instrument calibration can be found. They state that first, the mission and calibration requirements should be determined. The components and subsystem should then be characterized and the sensor performance modeled, and finally the full system should be calibrated towards the International System of Units (SI) traceable standards. The sensor response should also be monitored and continued to be updated after launch. A comprehensive list of suggested specifications that should be measured and characterized to describe the performance of a hyperspectral instrument can be found in Skauli *et-al.* [83]. Further, an overview over calibration and validation strategies from the European Space Agency (ESA) can be found in Niro et al. [84]. It is, however, important to keep in mind the balance between the price (including both time and money) of the calibration and the price of the instrument. As stated in Bowles et al. [85], the calibration cost should be consistent with the cost of the instrument. When working with COTS instruments, a calibration campaign on the level of a full ESA satellite instrument should not necessarily be expected.

2.3.1 Wavelength calibration

Wavelength calibration, also known as spectral calibration, determines the relationship between spectral pixel index and wavelength so that pixels on the detector can be mapped to their corresponding wavelength. Knowledge of this pixel to wavelength function is

important as even minor spectral deviations can affect the detection of spectral features significantly [86].

There are several ways to accomplish wavelength calibration. Among these are calibration using spectral lamps, a monochromator, a tunable laser or gas cells [87]. Monochromators and tunable lasers require more expensive and complex equipment, but give the opportunity to measure line responses of different wavelengths in small steps. The use of spectral lamps is a simpler option where only the spectral lines of the selected lamps are used as measurement points. Since the pixel to wavelength relationship is often a somewhat well-behaved function, using spectral lamps instead of a monochromator or tunable laser is often deemed sufficient [88]. Measuring the response in each band is, however, still wanted to derive an accurate instrument model [42].

As some examples, wavelength calibration was performed using first a monochromator to establish the approximate wavelength positions, then 20 selected lines from helium, argon and mercury gas emission lamps with a second or third order polynomial fit to describe the pixel to wavelength relationship in Bowles et al. [85]. Lenhard et al. [89] used a monochromator for the wavelength calibration, with a second order polynomial to describe the pixel to wavelength relationship. As the monochromator was used, they measured the Spectral Response Functions (SRFs) which also incorporates the FWHM in the spectral response model of the instrument. In Bruegge et al. [90] they performed wavelength calibration for the Multi-Angle Imaging Spectroradiometer (MISR) instrument under thermal vacuum conditions. Calibration in thermal vacuum conditions is beneficial for space instruments if possible, but requires a more complex set-up.

2.3.2 Radiometric calibration

Radiometric calibration, sometimes referred to as sensitivity calibration, converts from digital counts registered by the sensor to radiance. This is commonly done by letting the instrument measure the signal of an SI traceable standard (calibrated light source). Integrating spheres, coated with a highly reflective material such as Spectralon on the inside, illuminated by tungsten lamps are often used. They assure high degree of spatial uniformity of the output light. A radiometric calibration gain is then calculated for each pixel of the sensor. This way, effects such as vignetting are also evened out (flat-field correction). Deviations such as darker patches from dust in the system can also be corrected for [91].

A standard equation for a sensor measuring radiance in digital units can be written as

$$DN_{i,j} = G \cdot A_{i,j} \cdot \Omega \cdot L(\lambda) \cdot \Delta\lambda \cdot \eta \cdot t \cdot \tau, \tag{2.4}$$

where $DN_{i,j}$ is the digital counts recorded by the sensor in spatial pixel i and spectral pixel j, G is the instrument detector and digitization gain, $A_{i,j}$ is the area of the detector, Ω is the instrument solid angle, $L(\lambda)$ is the spectral radiance at the instrument entrance aperture, $\Delta\lambda$ is the bandwidth, η is the Quantum Efficiency (QE) of the detector, t is the integration time and τ the instrument optical transmission [82]. When performing radiometric calibration, Equation (2.4) can be rewritten as

$$L(\lambda) = DN_{i,j} \cdot g, \tag{2.5}$$

where

$$g = \frac{1}{G \cdot A_{i,j} \cdot \Omega \cdot \Delta\lambda \cdot \eta \cdot t \cdot \tau}, \tag{2.6}$$

where g then is the gain found during the calibration [82]. Since the reference radiance is wavelength dependent, wavelength calibration must first be applied, and errors in the wavelength calibration (including errors from smile) may lead to errors in the radiometric calibration results.

Not apparent in these equations are also the dark background signal (the signal recorded when there is no light), or offset, which must be subtracted from the measured signal ($DN_{i,j}$) before the calibration gains are calculated. The dark background signal can come from thermal emissions within the optics, or leakage current in the photodetector [83], and can vary with both exposure time and temperature [42].

One disadvantage with using the tungsten lamps for calibration is that they have a very different spectrum than that of the Sun, which is what illuminates most of the targets for remote sensing instruments for Earth observation. This leads to potential errors if the instrument has strong out-of-band responses, for example, such as seen in Barnes et al. [92]. The on-ground calibration should therefore also be done with a light source similar to that of the Sun, such as a Sun simulator, to minimize the error from out-of-band contributions [42].

An example of radiometric calibration performed with an integrating sphere at 5 different lamp levels can be found in Bowles et al. [85]. 20 images were captured at each lamp level, and dark images acquired frequently. A linear least-squares fit of the averaged instrument

response was used to compute the gains for each sensor element. The main sources of uncertainty were those related to the integrating sphere, those from random variations in the repeated measurements and those from the spectral calibration (smile).

2.3.3 Resolution and full width at half maximum

The resolution of a system gives information about how fine measurements are sampled or resolved, and is an important measure when trying to understand the quality of the measurements. As discussed in Dekker et al. [94] it is, however, not always well defined.

For optical instruments, there is a limit on the resolution both from an optical point of view (such as diffraction limit) and from the sensor point of view (sampling). For hyperspectral instruments, both the spectral and spatial resolutions are important. For a pushbroom system, the along track spatial resolution depends on parameters such as exposure time, frame rate, movement of the platform/target etc., while the spectral and across track spatial resolution depend on the imaging optics and sensor sampling. The spatial resolution of the collected data product must also not be mistaken for the spatial resolution of the instrument. The final spatial resolution of the data product depends on the distance to the target, viewing angle etc., and may also be affected by operations such as resampling and/or binning [42].

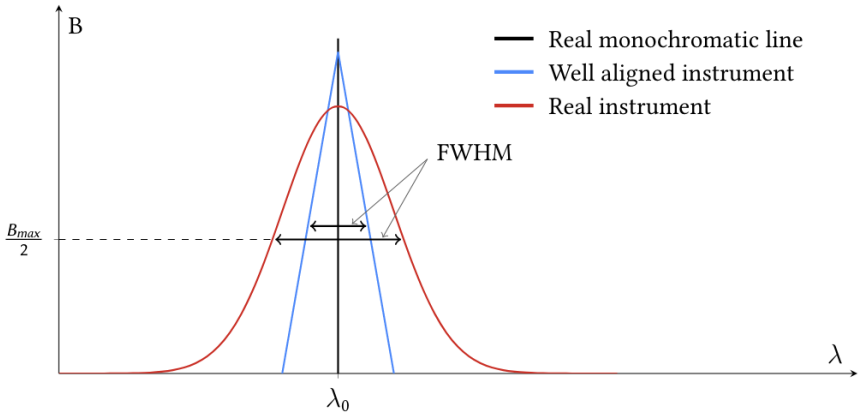

Figure 2.3: Illustration of the full width at half maximum, where B is intensity, λ is wavelength and λ_0 the center wavelength. Illustration from Henriksen [93].

For the spectral and across track spatial resolution, FWHM is often used as a measure of the resolution [95]. The FWHM is the measured width of a peak at the height of half of the peak maximum value, as seen in Figure 2.3. For spectral resolution, spectral lines from spectral calibration lamps or a monochromator are typically used to get estimates of the FWHM at different wavelengths. For across track resolution, thin stripes (typically 1/10 of a pixel) can be used as targets.

2.3.4 Smile and keystone

Smile and keystone are two common optical distortions affecting pushbroom hyperspectral instruments. Smile is a spectral misregistration, and can be seen as bent spectral lines as a function of slit height (spatial axis), while keystone is a spatial misregistration which typically appears as skewed lines as a function of wavelength (spectral axis). These kind of distortions may for example lead to classification errors and should therefore be minimized before the data is used [96, 97]. An example of how spatial misregistrations like keystone can affect the data quality is also given in Høye et al. [98]. Ideally, smile and keystone should be minimized in the design. Smile can for example be reduced by introducing a spherical grating or curved prism [99, 100]. For COTS instruments it is, however, beneficial to not require tailored components. Another solution can therefore be to correct for smile and keystone in software. Fridman et al. [101] even argues that for high resolution sensors it is better to correct keystone in software using resampling than trying to correct in hardware by changing the design.

Before correction of smile and keystone can take place, the distortions must be detected and characterized. In Mouroulis et al. [102], smile and keystone are measured separately. Smile is measured using spectral lines from a monochromator, while keystone is measured by imaging a pinhole illuminated by a white source. Feng et al. [103] focuses on only smile correction with resampling. Doing separate measurements simplifies the measurement set-ups needed, but as both smile and keystone warp the image in different ways they also affect each other. If possible, they should therefore be measured and corrected simultaneously.

One method for simultaneous detection and correction is presented in Lawrence *et al.* [104] using Ground Control Points (GCPs) [105]. GCPs were created in the spectrogram by using spectral calibration lamps (mercury-argon and krypton) to produce stripes in the spectral domain, in combination with thin vertical lines to produce stripes in the spatial domain. In total, 36 GCPs were created. The position of

the points in the image were detected and mapped to a straight reference grid using a two-dimensional quadratic polynomial distortion model, described as

$$x = a_{00} + a_{10}x_{ref} + a_{01}y_{ref} + a_{11}x_{ref}y_{ref} + a_{20}x_{ref}^2 + a_{02}y_{ref}^2, \tag{2.7}$$

$$y = b_{00} + b_{10}x_{ref} + b_{01}y_{ref} + b_{11}x_{ref}y_{ref} + b_{20}x_{ref}^2 + b_{02}y_{ref}^2, \tag{2.8}$$

where x and y are the measured coordinates and x_{ref} and y_{ref} the reference coordinates, and a and b the model coefficients. On matrix form, this can be written as

$$\mathbf{X} = \mathbf{WA} + \varepsilon_x, \tag{2.9}$$

$$\mathbf{Y} = \mathbf{WB} + \varepsilon_y, \tag{2.10}$$

where $\mathbf{W}$ holds the terms with the reference coordinates, and ε_x and ε_y are error terms for the measured coordinates. The pseudo-inverse solutions for the model coefficient matrices are then given as

$$\hat{\mathbf{A}} = (\mathbf{W}^T\mathbf{W})^{-1}\mathbf{W}^T\mathbf{X} \tag{2.11}$$

$$\hat{\mathbf{B}} = (\mathbf{W}^T\mathbf{W})^{-1}\mathbf{W}^T\mathbf{Y}. \tag{2.12}$$

These calculated model coefficients matrices, $\hat{\mathbf{A}}$ and $\hat{\mathbf{B}}$, are then used to transform the image coordinates to the reference coordinates (which may be non-integer values) by resampling and interpolation. This method is further used in this thesis, as described in Section 4.2.4.

Another example on smile and keystone correction can be found in Yokoya et al. [97], where phase correlation and cubic spline interpolation was used. The method is also tested on post-launch data from various scenes showing that the method is robust, making it promising as an in-orbit characterization method. It is worth noting, however, that resampling and software correction does not always solve every problem. As mentioned in Bowles et al. [85], resampling produces its own errors, and for some applications the errors from smile might be less problematic than those from resampling. One should therefore be careful with software corrections, and make estimates on the accuracies of any corrections applied to the data.

2.3.5 Point spread function

The PSF describes how a point source is imaged by an instrument. When discussing the PSF for spectrometers, it is important to distinguish between the PSF describing the

system response in one spatial and one spectral dimension (a point in the spectrogram), and what is here referred to as the spatial PSF which describes how a point source is imaged in spatial-spatial domain of the hyperspectral datacube. A 3D PSF describing how the light from a point source is distributed in the hyperspectral datacube can also be measured.

Measurements of the PSF are not always done directly. Line Spread Functions (LSFs), describing the instrument response in one direction are often used, and then later combined to form a final estimate of the PSF. In the spectral dimension, the SRF can be measured using a narrow spectral source. In the spatial domain, a thin slit can be imaged instead of a point source, to produce the Cross-Track Response Function (CRF) (sometimes also referred to as the Spatial Response Function (SiRF), in the across-track direction), and similarly the Along-Track Response Function (ARF) in the along-track direction [106]. These 1D response functions can then be combined to create 2D or 3D PSFs. Some examples of SRF, ARF and CRF measurements are given in Bender et al. [107] and Mouroulis et al. [108], and an example of reconstructing a 2D spatial-spectral PSF from the measured SRF and SiRF can be found in Kosec et al. [109].

A set-up to measure the spatial PSF is presented in Torkildsen and Skauli [110]. They use a collimator and a slit mounted on a rotational and translational stage, which allows the slit to scan (translational motion) to measure LSFs at different angles (rotational motion). The spatial PSF is then reconstructed by tomographic reconstruction for every band. Measurements of a HySpex camera and a Specim camera are used as examples in the paper. A similar set-up can be found at the Calibration Home Base (CHB) at the German Aerospace Center (DLR). A collimator set-up with target slits mounted in a turnable wheel are used to measure LSFs in along- and across-track directions. The CHB set-up used to characterize a HySpex camera is described in Lenhard et al. [111].

In Jemec et al. [112], a method to measure the 3D PSF directly is suggested. They combine a monochromatic source with a 2D PSF set-up from Jemec et al. [113]. This results in a virtual point-like source being imaged at different wavelengths. They also suggest that the set-up can be improved even further by extending to sub-pixel 3D PSF measurements by moving the mirror in the set-up in sub-pixel steps and using a scanning monochromator for spectral sub-pixel measurements.

PSF measurements can also be used to compare instrument performance. In Skauli [114], a metric characterizing coregistration errors from PSF measurements was proposed. Coregistration errors are errors arising from differences in the instrument response

in different parts of the image. Smile and keystone are, as mentioned, examples of distortions from spectral and spatial coregistration errors. These errors can also be seen as changes in the center position, shape and/or size of the PSF varying with wavelength (spectral axis) or along the slit (spatial axis), as visualized in Figure 2.4. The metric looks at the integrated difference between two PSFs, and corresponds to an upper bound of the error in the image data. An example of how this metric can be used to compare cameras is presented in Torkildsen et al. [110].

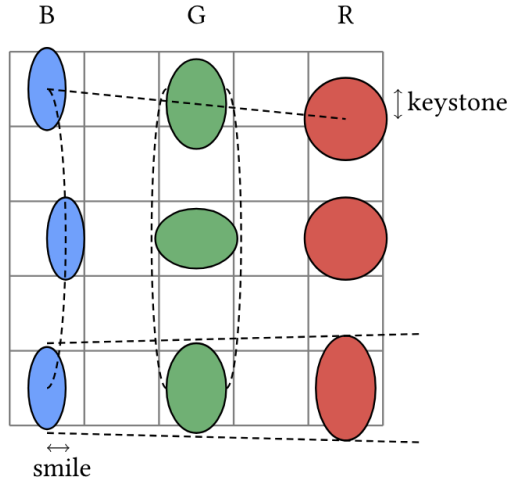

Figure 2.4: Differences in PSF shape, size and center position that may occur in pushbroom HSIs. Illustration from Henriksen [93], modified from Mouroulis et al. [96].

2.3.6 Stray light

Stray light can be described as all unwanted light in an optical system. There are several categories of stray light. A simple way to divide it is into spectral and spatial stray light. Spectral stray light is unwanted light in the spectral channel from other spectral bands, which can also be referred to as out-of-band contributions [42]. One case of spectral stray light common in grating spectrometers is second order diffraction effects, which is caused by higher order diffractions from the grating overlapping with the desired first order signal, thereby contaminating the result. This is described and discussed further in Chapter 5. Spatial stray light is related to reflections and scattering of light inside the optical train. Reflections such as ghosts may appear, for example, such as seen for the Hawkeye instrument in Holmes et al. [79]. In addition, light from external sources due to light leakage can also contaminate the measurements.

Stray light often have signal levels well below a factor of 10^{-5} of the maximum signal value (with exceptions such as ghosts or second order light etc. which typically have a stronger signal). High dynamic range is therefore needed to measure these levels of stray light. To achieve higher dynamic range in the measurement, a bracketing technique can be used. This is commonly done by acquiring several images at different light levels or exposure times, and combining them to a high dynamic range image.

For remote sensing instrument, and especially ocean color instruments, it is important to characterize how dark regions are affected in high contrast scenes, such as the dark ocean close to a bright cloud [42]. An important stray light criterion is therefore how many pixels away from a bright target stray light is observed, and at which levels. An example of this is the Fluorescence Imaging Spectrometer (FLORIS) instrument for the Fluorescence Explorer (FLEX) mission, where signal at a distance from the edge of a transition from a bright to dark area larger than 40 Spatial Sampling Distance (SSD) shall be less than 0.2 mW/(m^2 sr nm) before correction and 0.04 mW/(m^2 sr nm) after correction [115]. Since the FLEX mission attempts to measure solar induced chlorophyll fluorescence in the narrow oxygen bands, low stray light levels are extremely important to avoid contamination of the signal.

To achieve low levels of stray light, stray light is often reduced in the design by introducing components such as baffles and light traps. In addition, stray light can be characterized, and correction algorithms applied to improve the captured data. One example of stray light correction is the simple spectral stray light correction method presented in Zong-et al. [116]. The spectral LSF (SRF) is measured for each band, the in-band contributions removed and the remaining stray light signal used to create a spectral stray light correction matrix. This method was further developed in Zong-et al. [117], using PSF measurements to create a spatial stray light correction matrix as well. Uncertainties of this correction method are further discussed in Zong-et al. [118] and Schinke et al. [119]. Stray light correction can also be done by using PSF measurements and deconvolution, such as used for the Tropospheric Monitoring Instrument (TROPOMI) instrument in Tol et al. [120]. Finally, Lenhard et al. [89] shows an example on how stray light correction impacted their derived data products when using a HySpex instrument to measure Secchi depth. They found that applying stray light correction gave an improvement of up to 19% in the systematic errors. Stray light correction is therefore worth considering if strict requirements on the data products must be met.

2.3.7 Signal-to-noise ratio

The SNR is defined as the ratio between signal and noise. The definition of signal is typically quite simple, as it is most often simply the signal measured by the instrument. For ocean color remote sensing instruments, the ToA signal received at the sensor is often used to calculate the SNR at ToA. The SNR can also be calculated based on the received water leaving radiance, which is the signal detected after corrections such as atmospheric correction has been applied. For simulations or in the lab, the SNR is also often found for different light levels.

The definition of noise, however, is more complex. The noise level can either be defined by the fluctuation of the retrieved signal for different observations of the same area, or as the fluctuation of the retrieved signal from within the same area. At instrument level, the temporal fluctuation calculated as the root-mean-square of a large number of measurements of the same target is often used [42]. Noise contributions can come from natural fluctuations in the signal (photon noise), quantification noise, read noise or dark current (dark signal measured in electrons per second), among others [83]. For the final data product, noise can also come from the compression, resampling, imperfections and uncertainties in the calibration, stray light, polarization and other effects that are not perfectly corrected.

Since the received signal varies with wavelength, so does the SNR, and it should therefore be estimated for each band. It is also recommended to calculate the SNR for different light levels, which can be done during the calibration of the instrument [42].

An example of SNR calculations for the MISR instrument can be found in Bruegge et al. [90], where SNR was estimated for each pixel as a function of light level using the radiometric calibration data. They also estimated the expected SNR in-orbit by using a radiometric model. Kudela et al. [51] gives another example of calculation of SNR, where it is estimated as the mean signal divided by the nugget variance (the small-scale variability of the data).

2.3.8 In-orbit calibration

Ideally, the calibration and characterization done prior to launch should be checked and updated in-orbit [42], but this is not necessarily an easy task. Larger satellites may have some calibration equipment onboard, while smaller satellites typically do not have room for this kind of equipment. There are, however, other methods that can be

used such as vicarious calibration techniques [121]. Vicarious calibration techniques are typically used for missions that do not have calibration equipment onboard, and refers to techniques that use natural or artificial sites for post-launch calibration. Typical targets are the Earth and planetary targets whose radiometric signal can be modeled with a high degree of confidence, are temporally stable, and are spatially and spectrally uniform. The most common vicarious targets used are Pseudo-Invariant Calibration Sites (PICS). These are desert sites that have been carefully selected due to their low cloud coverage, high reflectance, good stability and uniform response in terms of temporal, spatial and spectral characteristics [122]. Algeria-3, Algeria-5, Libya-1, Libya-4, Maurtania-1 and Maurtania-2 are all examples of PICS sites. Earth targets typically also rely on a Radiative Transfer Model (RTM) used to simulate the sensor signal over a test site [84].

For in-orbit radiometric calibration, the RadCalNet network [123] provides free and open access to ToA reflectances over four selected sites across the globe (Gobabeb in Namibia, La Crau in France, Railroad Valley Playa in USA and Baotou in China) every 30 minutes with a 10 nm resolution in the 400 nm to 1000 nm range. For ocean color instruments, it is also possible to use data from radiometers mounted to buoys giving a measure of the water-leaving radiance. For this, stations such as the Marine Optical Buoy (MOBY) near Hawaii [124] and the Buoy for the Acquisition of a Long-Term Optical Series (BOUSSOLE) site in the Mediterranean Sea [125] can be used. Other vicarious calibration targets are Deep Convective Clouds (DCCs), the Moon and stars. DCCs are very thick clouds with a bright and uniform spectrum with a high SNR [121, 126]. The Moon is a good target for stability monitoring (lunar trending), as it is illuminated by the Sun and can be observed by satellites without looking through the Earth's atmosphere, removing the uncertainties from atmospheric variations. One of the models widely used for lunar calibration is the Robotic Lunar Observatory (ROLO) model [127]. One of the disadvantages using the Moon is that it is a small source that normally does not fill the full Field of View (FOV) of the sensor. It can therefore only be used to assess parts of the sensor. Stars can also be useful for radiometric calibration. In Meygret et al. [128] stars are also used to calculate the Modulation Transfer Function (MTF) (normalized Fourier transform of the PSF) in-orbit.

The wavelength calibration should also be checked post launch to make sure that the spectral characteristics of the bands stay the same, and that no spectral shifts have occurred after launch [42]. Absorption lines in the atmosphere such as the solar Fraunhofer lines and the absorption line from the oxygen and water vapor can be used for spectral calibration or to detect spectral shifts by comparing with results from the pre-launch calibration [121, 74].

Cross-sensor calibration is also an option, where two instruments observe the same target on ground at the same time (ideally), and their responses compared. This is especially useful if comparing a CubeSat instrument (with no room for calibration equipment onboard) with a larger well-calibrated satellite instrument. Cross-calibration can be done over PICS sites, for example [121]. The Moon can also be used as a target, such as shown in Eplee et al. [129], where they cross-calibrate the SeaWiFS and MODIS instruments. An advantage with lunar cross-calibration is that temporal overlap of the measurements is not necessarily needed as there is no atmosphere to consider.

As mentioned in the IOCCG report no. 14 [121], the required accuracy of the water-leaving radiance can be around $\pm 5\%$ for some ocean biogeochemistry studies. This is extremely demanding in terms of the radiometric calibration accuracy. The recorded signal at ToA is typically 10 times larger than the water-leaving radiance, meaning that the radiometric calibration of the instrument must be accurate to a fraction of one percent even with a perfect atmospheric correction applied. Current vicarious calibration methods are accurate to a few percent at best, making it difficult to achieve high accuracy on the water-leaving radiance products without comparing the data products with in-situ measurements.

The process of comparing and adjusting the calibration coefficients based on in-situ measurements can be referred to as system absolute calibration or system vicarious calibration, and also includes the atmospheric correction scheme (as atmospheric correction must be applied to obtain the water-leaving radiance estimate). Performing a full system calibration is also recommended before releasing the final data products.

2.3.9 Validation

While calibration can be defined as the process of converting sensor specific units to physical units, validation can be defined as the process of assessing the quality (uncertainty) of the data products derived from the calibrated data [130]. Validation can be done by comparing the calibrated data products, such as ToA radiance, water-leaving radiance or chlorophyll concentration to independent measurements of the same quantity (reference value, ground truth). This is done to ensure that the user's requirements are met for the data are actually delivered. A comprehensive and accurate set of validation reference data is as a consequence very important to ensure that the mission is successful [84].

For ocean color sensors, the water-leaving radiance is of importance. The in-situ reference can be measured directly by above the water surface or indirectly using interpolated values of underwater measurements of the upwelling radiance just below the surface (such as for the MOBY and BOUSSOLE buoys). In addition, the downwelling solar irradiance above the water must be measured. This can be done by a well calibrated radiometer on a stable platform [42]. To assess the quality of the data products, validation metrics can be used [84, 131]. A common test essentially checking the consistency between the difference of two measurements (from the satellite and the reference value) and their uncertainties can be written on the form [132]

$$|x - y| < k\sqrt{u_x^2 + u_y^2 + \Sigma^2}, \tag{2.13}$$

where x and y are the satellite and in-situ measurements respectively, u_x and u_y their uncertainties, Σ an additional variance of the differences due to co-location mismatch and k the coverage factor. If $k = 1$, the measurements are said to be consistent as the combined uncertainties are consistent with 1 standard deviation. If $k = 2$ they are said to be in statistical agreement to a 4.5% significance level. This test does, however, assume that the uncertainty estimates of the measurements are available. If not, other methods such as calculating the correlation coefficient, bias and Root Mean Square Error (RMSE) can be used [84, 131].

Part I

The Hyperspectral Imager

From optical design to characterization of the final instrument

3 | Redesigning and building a hyperspectral imager

In 2018, Sigernes et al. presented a small and lightweight design of a pushbroom hyperspectral imager with S-mount optics [34]. This prototype was primarily designed for drone applications, where weight and size are highly restricted. The components were all COTS components, and the housing 3D printed, making the HSI both cheap and easy to produce. A redesign of the HSI V4 was needed to provide an instrument achieving high enough SNR for ocean observation from both airborne drones and satellite platforms. This led to the development of the HSI V6, which is presented in this chapter. This chapter is based on parts of **Paper 1**: "A do-it-yourself VIS/NIR pushbroom hyperspectral imager with C-mount optics" [35], including the supplement describing how to assemble the HSI in detail.

3.1 Optical design

The HSI V4 is, as mentioned, a pushbroom HSI with a transmissive grating and S-mount optics, built with COTS components and 3D printed parts. The design consists of front optics, a slit, collimating optics, a transmissive grating, detector optics and an imaging sensor. The specific components used are summarized in Table 3.1.

Table 3.1: Main components of the HSI V4 and HSI V6.

Component	HSI V4	HSI V6
Front optics	16 mm focal length, F/4, from Edmund Optics (#83-107)	50 mm focal length, F/2.8, from Edmund Optics (#67-717)
Slit	25 μm wide, 3 mm high, from Edmund Optics (#38-558)	50 μm wide, 7 mm high, from Thorlabs (S50RD)
Collimating optics	10 mm focal length, from Edmund Optics (#63-519) and 30 mm focal length, from Edmund Optics (#63-523)[a]	50 mm focal length, F/2.8, from Edmund Optics (#67-717)
Transmission grating	600 grooves/mm, from Edmund Optics (#49-580)	300 lines/mm , from Edmund Optics (#49-579)
Detector optics	25 mm focal length, F/2.5, from Edmund optics (#56-776),	50 mm focal length, F/2, from Edmund Optics (#67-717)
Imaging sensor	iDS camera head (UI-3060CP Rev. 2) with Sony IMX174 sensor	iDS camera head (UI-3060CP Rev. 2) with Sony IMX174 sensor

[a] For the HSI V4 used here, a 25 mm focal length lens was used instead.

The main design goal of both the HSI V4 and HSI V6 was a small instrument covering the spectral range of 400 to 800 nm, with a FWHM less than 5 nm. The design of HSI V6 would in addition need to follow many requirements set by the HYPSO mission, as it would be a prototype for the hyperspectral instrument used for HYPSO-1. Requirements for spatial resolution and SNR, as presented in [29], in addition to size and weight requirements when later modified to be used in space, were therefore taken into consideration when the instrument was developed. The primary goal when redesigning the HSI V6 was to increase the throughput to comply with the SNR needed to observe ocean color.

The basic optical design of HSI V4 could easily be reused for the HSI V6. The overall layout of the optical diagram was not changed, and a transmissive grating design was still used. However, the main components such as the lens objectives, slit and grating were changed to larger components to fit C-mount lens apertures. The optical diagram of the HSI V6 is shown in Figure 3.1, and illustrates the general idea of the design. The main parts are the front objective (L_0), slit (S), collimating objective (L_1), grating (G), detector objective (L_2), and finally the detector with the imaging sensor. The center wavelength used was $\lambda_c = 600$ nm, mainly meaning that the detector objective is placed at an angle of 10.37° (the diffraction angle of 600 nm) from the grating.

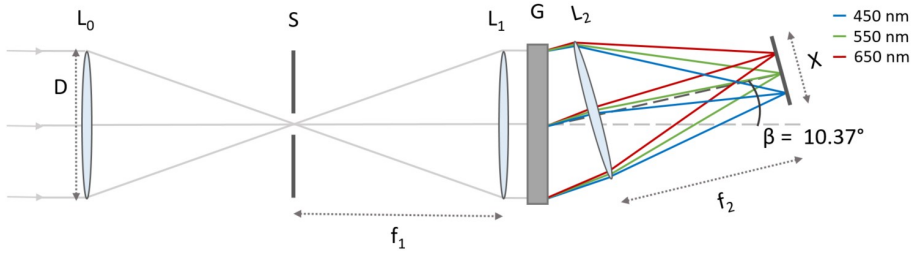

Figure 3.1: Optical diagram of the HSI V6 showing the front objective (L_0), slit (S), collimating objective (L_1), grating (G), detector objective (L_2), and the sensor with length X in spectral direction. The diameter of the lenses is $D = 18.4$ mm and the diffraction angle is $\beta = 10.37°$. L_0 and L_1 are set to F/2.8, while L_2 is set to F/2.

The focal lengths of the new objectives are $f_0 = f_1 = f_2 = 50$ mm and the back flange focal distances are 17.526 mm, typical for C-mount objectives. Three equal objectives were used, with L_0 and L_1 set to F/2.8, while L_2 set to F/2 to collect as much light as possible after it is dispersed by the grating. Imaging at F/2.8 increases the amount of light collected by the system as the aperture is larger, compared to the HSI V4 design imaging at F/4. Using two identical objectives facing the entrance slit makes the use of baffles or field lenses to collimate the light before reaching the grating superfluous, since the optical properties of the objectives are the same.

The grating was changed from a 600 grooves/mm in the HSI V4 to a 300 grooves/mm transmission grating in the HSI V6, since the 300 grooves/mm grating has an overall higher efficiency. It is blazed at $17.5°$ and has above 50% efficiency for the wavelength range of 400 to 800 nm, peaking at 75% around 500 nm. The diffraction angle is calculated for the center wavelength $\lambda_c = 600$ nm, as

$$\beta = \arcsin\left(\frac{k\lambda_c}{a}\right) = 10.37°, \tag{3.1}$$

where $a = 3.33$ μm is the spacing between the grooves in the grating and $k = 1$ represents the first spectral order.

3.1.1 Theoretical throughput

The theoretical spectral throughput can be calculated as

$$\Phi_\lambda = B_\lambda E_\lambda T_\lambda G, \tag{3.2}$$

where B_λ is the spectral radiance, E_λ is the grating efficiency at the first spectral order for each wavelength, T_λ represents the geometric losses and transmission factors of the optical elements, and G is the etendue. The etendue G is further defined as

$$G = \frac{G_A \cos\beta}{f_2^2} w' h', \tag{3.3}$$

where $G_A \cos\beta$ is the illuminated area of the grating, f_2 is the focal length of the detector objective, w' is the slit width magnification and h' is the slit height magnification. The slit width- and height magnifications can be calculated as

$$w' = \frac{f_2}{f_1} \frac{\cos\alpha}{\cos\beta} w \tag{3.4}$$

and

$$h' = \frac{f_2}{f_1} h, \tag{3.5}$$

respectively, where w is the slit width, h is the slit height, α is the incident angle of the incoming light, β is the diffraction angle of the grating, and f_1 and f_2 are the focal lengths of the collimating and detector objectives, respectively [133].

By using the parameters presented here, and assuming the same spectral radiance (E_λ) and geometric losses and transmission factors of the optical elements (T_λ), the theoretical spectral throughput for the center wavelength $\lambda_c = 600$ nm of the HSI V4 and HSI V6 can be compared. This gives

$$\frac{\Phi_{\lambda,V6}}{\Phi_{\lambda,V4}} = 9.75, \tag{3.6}$$

meaning that the HSI V6 is expected to have about 10 times more throughput than the original HSI V4 at 600 nm.

The HSI V4 used in here for measuring and comparing optical performance, however, has been modified with a collimator lens with $f_1 = 25$ mm, instead of $f_1 = 30$ mm. This gives the theoretical throughput ratio to be 6.77 at 600 nm instead. Repeating these calculations for different wavelengths shows that the ratio ranges from about 4.6 at 400 nm to about 7.8 at 800 nm (for the HSI V4 used here). The values vary mostly due to differences in grating efficiencies of the two gratings.

3.1.2 Theoretical full width at half maximum

The theoretical FWHM is calculated as

$$\text{FWHM} = \frac{wa\cos\alpha}{kf_1} = 3.33 \text{ nm}, \tag{3.7}$$

where $w = 50$ μm is the slit width, $\alpha = 0^\circ$ is the incident angle of the incoming light and $f_1 = 50$ mm is the focal length of the collimating objective [134, 135]. Both changing the grating to one with more grooves/mm and increasing the slit width from 25 μm to 50 μm widens the theoretical FWHM. On the other hand, longer focal length on the objectives reduces the FWHM, so that the final theoretical FWHM is 3.33 nm, compared to 1.4 nm for the HSI V4.

Many ocean color phenomena require a spectral resolution of less than 5 nm, as discussed in Section 2.1.5. The increase in FWHM was therefore seen as an acceptable trade-off as it is still within the typical requirement for ocean color applications, and since the HSI V6 is primarily developed for observing the ocean (hence the importance of increasing the throughput). The wider slit, larger lens apertures and higher efficiency in the grating increases the theoretical throughput[29, 36], which is the primary goal for the HSI V6 design.

3.1.3 Instantaneous field of view

The Instantaneous Field of View (IFOV) of the instrument is defined as

$$\text{IFOV} = 2\arctan\left(\frac{w}{2f_0}\right), \tag{3.8}$$

where w is the slit width or slit height depending on along-track or cross-track direction, respectively, and f_0 the focal length [105]. The IFOV is calculated to be 0.057° in along-track direction, and 8.008° in cross-track direction. For example, when used on

a satellite platform in an orbit with altitude about 500 km, this gives a spatial resolution of about 500 m, and a swath width to be 70 km [29, 36], which is within the requirements of the HYPSO mission.

3.2 Components

A list of the all parts used are shown in Table 3.2. How the parts fit together is shown in an exploded view of the instrument in Figure 3.2. Most parts are COTS components from Thorlabs and EO. In addition to the COTS components, two 3D printed parts are needed (the grating holder and the detector holder, parts 11 and 14 in Figure 3.2, respectively).

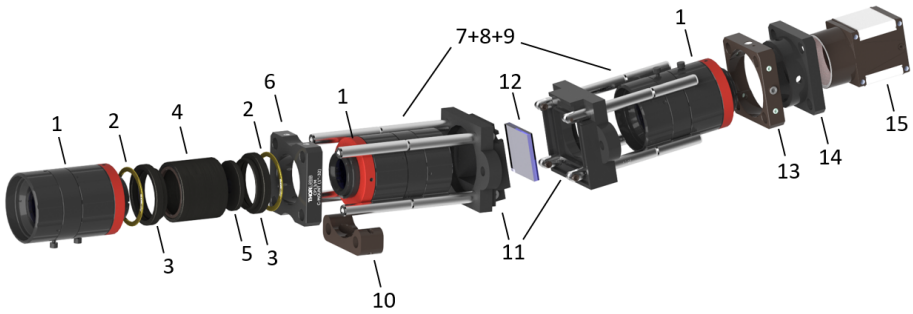

Figure 3.2: Exploded view showing the components of HSI V6 in CAD. (1) Objective, (2) spacer ring, (3) adapter ring, (4) lens tube, (5) slit, (6) cage plate for lens tube, (7+8+9) steel rods and swivels, (10) mounting bracket, (11) grating holder, (12) grating, (13) cage plate for detector mount, (14) detector mount, (15) detector. Numbers coincide with item numbers in Table 3.2.

Since the front objective back focal flange distance is 17.526 mm, any standard C-mount objective may be used as front optics. The instrument can, for example, be mounted on a microscope as in Volent et al. [136] and Haugum et al. [137] (**Paper 8**). The camera head is also easily exchangeable, making it possible to customize the instrument to the intended application.

The detector used here is an industrial global shutter camera from Imaging Development Systems (iDS) with a Sony IMX174 Complementary Metal Oxide Semiconductor (CMOS) image sensor. It is mainly chosen as it has high QE in the visible range, and fulfills resolution and SNR requirements for the HYPSO mission [36, 29]. Other sensors, such as detector heads with Sony IMX249, Sony IMX252 and CMOSIS CMV2000 sensors were also tested during the development of the HSI V6. The Sony IMX249 is a less expensive version of the IMX174, with similar optical performance but a lower frame rate. The Sony

Table 3.2: HSI V6 detailed list of parts (1 inch = 2.54 cm).

Item	Part	Description	Qty	Cost[a] [€]
1	EO #67-717	50 mm Visible (VIS)-NIR objective (front, collimator and detector)	3	1353.00
2	Thorlabs CMSP-KIT	C-mount 0.25 - 2 mm spacer ring kit	1	81.13
3	Thorlabs SM1A10	Adapter ring SM1 to C-mount internal	2	32.11
4	Thorlabs SM1M10	SM1 lens tube 1 inch long with internal threads and two internal retaining rings	1	11.37
5	Thorlabs S50RD	Fixed high precision mounted slit, customized height 7 mm	1	78.52
6	Thorlabs CP12	30 mm cage plate - SM1 tubes	1	17.06
7	Thorlabs ER1.5-P4	4 x steel rods 1.5 inch long	1	18.22
8	Thorlabs ER1-P4	4 x steel rods 1.0 inch long	1	15.74
9	Thorlabs C3A	4 x rod end swivels	1	48.36
10	Thorlabs CP02B	30 mm cage mounting bracket	1	12.25
11	Grating holder	3D printed grating holder	1	
12	Edmund Optics (EO) #49-579	25 mm square, 17.5 degree blazed transmission grating (300 lines/mm)	1	86.10
13	Thorlabs CP03/M	30 mm cage plate - 35 mm aperture (for iDS-mount)	1	15.39
14	iDS mount	3D printed iDS mount	1	
15	UI-3060CP Rev. 2	iDS camera head with Sony IMX174 sensor	1	820.00
16		4 mm bolts, M3 set screws, spacers and lock nuts		
		Total cost		**2,589.25 €**

[a] Cost at time of purchase.

IMX252 has smaller pixels than IMX174/249, and a smaller sensor area. Both IMX252 and CMV2000 are more sensitive in the NIR wavelengths, at the cost of having lower QE in the VIS range. Other parameters to consider when choosing the detector include the size of the sensor, number of pixels, pixel size, well depth and bit depth, among others.

3.2.1 3D printed parts

The parts needing to be 3D printed are the grating holder and the iDS detector mount. Both are constructed for use with the 30 mm cage system from Thorlabs. The Computer Aided Drafting (CAD) files are available online: `http://kho.unis.no/doc/Gratingholder.zip` for the grating holder and `http://kho.unis.no/doc/IDSinsert.zip` for the detector mount. The grating holder consists of two parts that are held together by two 4 mm bolts, spacers and lock nuts, as seen in Figure 3.3.

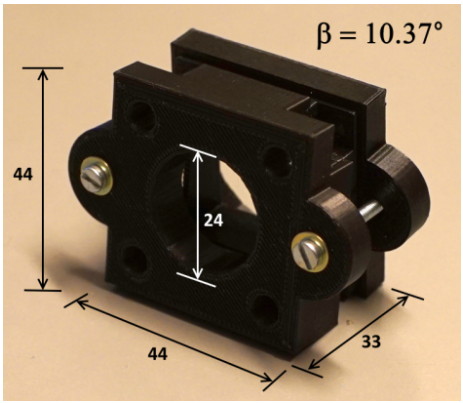

Figure 3.3: Assembled 3D printed grating holder. All measurements are in units of mm.

3.3 Assembly

Before the full instrument is assembled, focus of the objectives must be set. For remote sensing applications from drones and satellites, focus on all objectives should be set to infinity. For other applications imaging at closer distances, the front objective focus may be adjusted accordingly. The slit tube, grating and detector subassemblies are then assembled separately. Finally, spacer rings and screws are added at the end.

Assembling the parts in a flowbench is recommended in order to minimize dust and contaminants from entering the optical system. The parts are assembled using hex key sets. A full list of recommended tools is shown in Table 3.3. It is useful to have both the imperial and the metric sets from Thorlabs, CCHK/M and CCHK, respectively, as the optical components switch between both. The spanner wrench, SPW602, is also recommended to more easily twist the internal retaining rings in the lens tube without damaging any parts.

Table 3.3: Recommended tools for assembly.

Part	Description	Reason
Thorlabs CCHK/M	Metric hex key set	
Thorlabs CCHK	Imperial hex key set	
Thorlabs SPW602	Spanner wrench	Mount slit inside tube
EO #46-097	25 mm square window	Practice assembly of grating holder
	Optics cloths	Minimize dust on parts during assembly

3.3.1 Setting the objective focus

There are three identical COTS objectives in the imager. However, due to slight tolerance differences during manufacturing, focus on each must be set individually to ensure optimal performance. Each objective has two adjustable settings: the aperture (F/#) and the focus. The apertures can be set by simply twisting the outer, rear band of the objective to the correctly labeled f-number. The position is locked with a set screw on this band (threadlock can be used for extra security). The focus is set by removing the locking set screw in the center band of the objective and twisting the front band.

The goal is to focus each of the objectives at infinity, since the imager is meant to be used in remote sensing applications observing objects at a great distance. Setting the focus at infinity can, for example, be done by focusing on a distant outdoor target, or by using a collimator and pattern to simulate a distant pattern in the lab. When setting the focus, the objective can be mounted to the detector directly via the standard C-mount. The iDS cameras come with supporting computer software, called uEye Cockpit, that provides a real-time image viewer, which is very handy when manually setting the focus. The detector can then be connected to a computer running the software with a USB 3.0 cable (or other cable, depending on camera model). This gives a visual representation of the image when setting the focus. If switching to a different camera, thought should be given on how to display images during assembly, as this is also needed later to assure that the slit is straight and that the spectral focus is good when adding spacer rings. When viewing the real-time feed, the focus band should be twisted until the objects in the image are clearly in focus. The set screw is then tightened to keep the focus from changing further. Epoxy or threadlock can be used on the set screws to ensure they remain locked. Replacing the set screws with grub screws can also be an option to avoid that the exposed screw head is accidentally bumped.

Figure 3.4a shows a set-up with an objective mounted on the detector, facing out the window to view distant objects with sharp features such as trees and buildings. In Figure 3.4b a set-up using a collimator lens and a pattern, as described in [138] (**SP 1**), with a white paper background is shown. It is best practice to use different kind of set-ups to test that the focus is good, such as one set-up to set the focus and another for validation.

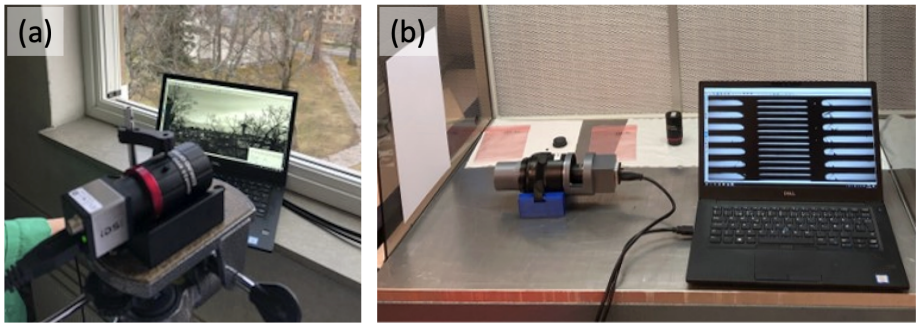

Figure 3.4: Example set-up for setting individual objective focus. (a) Looking out the window to observe distant targets. (b) Using a collimator and reticle pattern in the lab.

3.3.2 Slit tube subassembly

The slit tube subassembly consists of the lens tube, slit, and retaining rings. The retaining rings are needed to mount the slit into the lens tube at the precise location that matches the flange focal distances. In addition, adapter rings are needed on both sides of the tube to mount the objectives. The assembly is made compatible with the 30 mm cage system from Thorlabs, and is held together by the CP12 cage plate and 6 mm diameter steel rods. Making three extra M3 set screw holes in the sides of the CP12 cage plate to secure the lens tube is recommended.

The technical drawing in Figure 3.5 shows the lengths of the components in the slit tube assembly, and the correct position of the slit inside the tube. The goal is to obtain the back focal C-mount flange distance of 17.526 mm from the slit to both objectives. Note that the slit is not positioned in the center (depth-wise) of the slit holder (the case holding the slit), so the slit holder should not be positioned exactly at the center of the lens tube. Normally the slit is blackened on one side. If so, this side should face the front objective to minimize stray light.

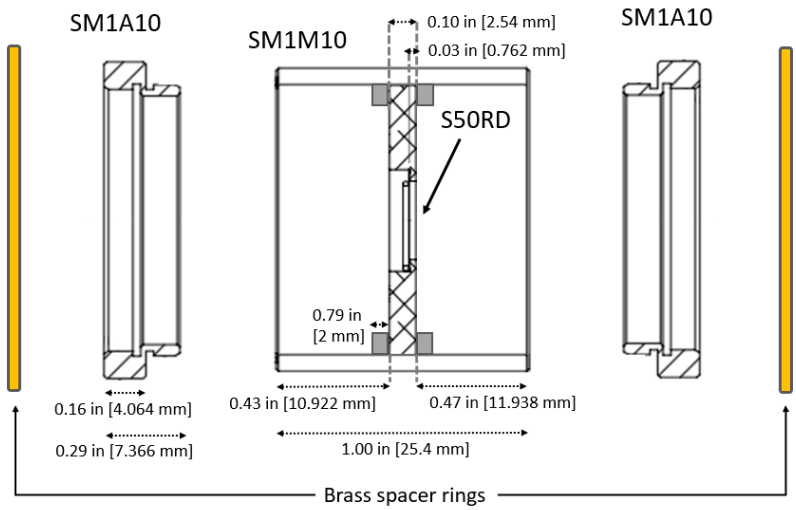

Figure 3.5: Technical drawing of the slit tube assembly, showing the slit inside the lens tube, and adapter rings and spacer rings on each side of the tube.

The front of the slit holder (facing the front objective) should be placed approximately 12 mm into the lens tube, while the distance from the back of the slit holder to the other edge of the lens tube should be about 11 mm. The distance from the slit to the edge of the lens tube is then 12.7 mm on both sides. Adding the adapters gives a distance of 16.764 mm. A spacer ring of about 0.5 mm is then needed to get a distance close to 17.526 mm. Another option is to deliberately not place the slit in the middle of the lens tube, and only use spacer rings on one side. It should be kept in mind, however, that when adding spacer rings less threads of the objective will be engaged with the adapter. A large amount of spacer rings on one objective could result in the objective no longer being able to be fastened. It is therefore better to use spacer rings on both sides.

The slit should then be mounted into the lens tube using two internal retaining rings, following the steps shown in Figure 3.6. The spanner wrench is a helpful tool to get the retaining rings, and the slit, at the right distance into the tube. Once the slit and retaining rings are in place, an adapter ring can be mounted on each side of the tube. Spacer rings between the adapter rings and objectives might be needed, but this is first visible when testing the camera and inspecting the focus of the acquired images. The easiest is therefore to try either without any spacer rings or with one 0.5 mm spacer ring on each side first, assemble the full instrument and later reopen it and adjust the number of spacer rings if needed.

Figure 3.6: Slit tube assembly. (a) Insert slit into the lens tube, (b) adjust retaining rings inside the tube using the spanner wrench, (c) add adapter rings, (d) add objectives (with spacer rings if needed), (e) add cage plate before adding the second objective.

3.3.3 Grating subassembly

The grating is the most brittle component in the optical train. Before assembling the grating holder and the four rod swivels, training should be done using a regular 25 mm square window (ex. #46-097 from EO) in replacement of the grating. The 3D print can be tight, so it is good to practice to test with the glass window first to make sure that there is enough room in the 3D print. If the 3D print is too tight it should be trimmed to fit before adding the actual grating.

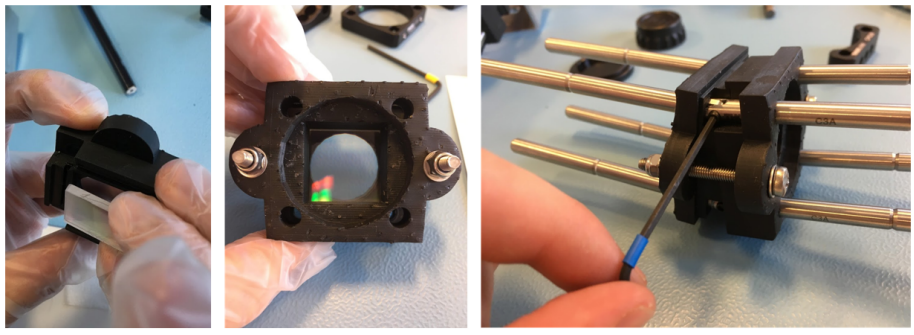

Figure 3.7: Grating holder assembly. (a) Insert the grating in half of the housing, (b) press fit the other half and secure it with bolts, (c) assemble cage rails on each side of the housing independently and join them in the center with the small included screw.

The grating holder can then be assembled by inserting the grating between the two 3D printed grating holder parts. A vector addition of the arrows noted on the grating edges gives the direction of the incoming light path. This will get the blaze angle correctly oriented. The 3D print is then secured with bolts and cage rails are added, as shown in Figure 3.7.

3.3.4 Detector subassembly

As for the detector, the camera head from iDS is fixed to the instrument by the 3D printed insert that fits the 30 mm cage plate. The cage plate is first slid onto the 3D printed detector mount and secured with set screws. The back objective is then screwed into the detector with the standard included threading. One extra M4 set screw is needed to fix the camera head tight. Making two additional M3 set screw holes in the sides of the cage plate is recommended.

3.3.5 Full instrument assembly

The final assembly of the imager includes adding the front and collimating objectives to the slit tube subassembly, and further connecting this to the central grating subassembly. The slit subassembly simply slides into the grating holder. Anti-rotation is controlled by the four supporting cage rails. Once slid into place, set screws on the cage plate lock the slit tube position. Prior to adding the cage plate, the cage mounting bracket can be slid onto any two rails and secured with set screws. This bracket helps with mounting the camera to other platforms or rotational stages after assembly (but is optional). The detector subassembly can then be slid into the back grating holder via the cage rails. Set screws lock the back optics onto the cage rails.

When the instrument is fully assembled, final focusing by adjusting the spacer rings must be done. Again, using a real-time image viewer, such as uEye Cockpit for the iDS cameras, is needed. A pattern, or any sharp lines, can be used to examine the spatial focus. Spectral sources or a fluorescent lamp can be used to investigate the spectral focus. The final focusing is done by adjusting the distances between the front and collimator objectives and the slit tube by adding or removing spacer rings.

Since the objectives are circular, they can be simply twisted, relative to the slit tube, and loosened until the focus is sharp. The gap that then forms between the objective and adapter can be measured and gives the size of the additional spacer ring that is

needed. The twist to loosen approach only works if the distance is too short to begin with. It is therefore recommended to start with fewer spacer rings than expected so that the additional distance needed can be measured accurately. When focus is adjusted, the image viewer can also be used to verify that the slit is aligned. If the spectral lines are skewed, the slit tube should be rotated to obtain straight lines.

The fully assembled instrument can be seen in Figure 3.8. The total volume is about 220 x 65 x 65 mm^3 and the weight is just under 650 g. To ensure that the screws and parts will not move during flight, for instance, epoxy or threadlock can be added to the screws. This will, however, make it harder to reopen the instrument if that should be needed, for example to re-adjust focus with spacer rings. Threadlock is the more forgiving choice and can be applied directly to the threading of the optical components and screws. Be sure not to add excessive amounts so that the threadlock leaks through into the optical train. If using epoxy on screws, only a dot needs to be applied to the head of the screw where it comes in contact with the mating surface. This will make it easier to remove, if desired, but will still show clearly if the screw becomes loosened. Both can be removed with a careful application of heat such as a heat gun or soldering iron, but caution should be used not to damage other parts nor melt the 3D printing.

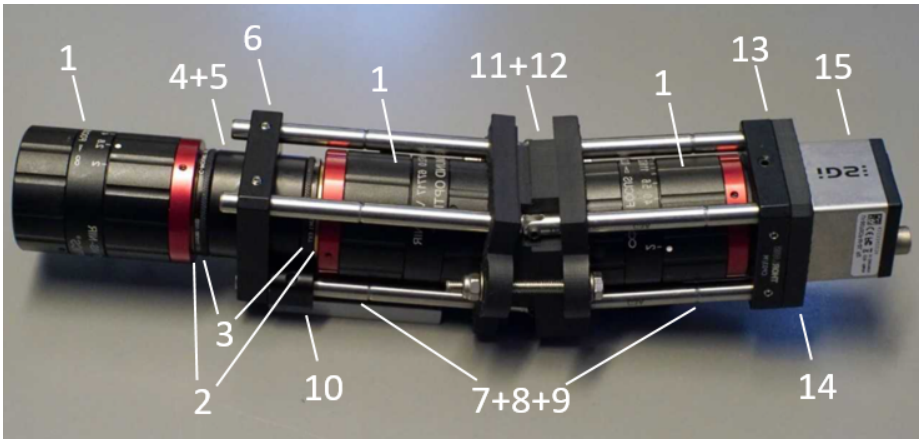

Figure 3.8: HSI V6, fully assembled instrument. (1) Objective, (2) spacer ring, (3) adapter ring, (4+5) slit tube assembly, (6) cage plate for lens tube, (7+8+9) steel rods and swivels, (10) mounting bracket, (11+12) grating in grating holder, (13) cage plate for detector mount, (14) detector mount, (15) detector.

3.4 Proof of concept

The HSI V6 was used to acquire hyperspectral datacubes at UNIS for proof of functionality. The exact setup is described in Hazendonk et al. [139]. A Syrp Genie mini motion control system was used to ensure a smooth rotation when capturing spectrograms. The data was recorded using the iDS software uEye Cockpit, and stored as 8-bit .avi video files to minimize the data size. The settings such as exposure time and frame rate were adjusted according to the light conditions, and the scan duration adjusted to obtain about 3400 frames per datacube for a scan of 30°. Examples on how the hyperspectral image processing pipeline can be implemented can be found in Grøtte et al. [140].

A hyperspectral datacube of the Longyearbyen harbor was recorded on 26-08-2019. For reference, an image of the harbor was taken simultaneously with a mobile phone, as seen in Section 3.4. An RGB image was created from the hyperspectral data using the wavelengths 660 nm, 540 nm and 480 nm for the red, green and blue channels, respectively, as is shown in Section 3.4. This shows a close to "real" RGB image as the wavelengths chosen are similar to those seen by the human eye. Details in the harbor are visible in the generated image, showing that the imager is capable of capturing spatial features. The generated RGB image shown in Figure 3.9 is not gamma corrected, which should be done if comparing the mobile phone reference images with the generated RGB images in more detail.

As the data is hyperspectral, each pixel in Section 3.4 holds spectral information. Point spectra of the sky and ground in the Longyearbyen harbor datacube, pixel positions marked in Section 3.4, are shown in Figure 3.10. The sky spectrum has a high response between 400 nm and 600 nm, while the ground spectrum has a lower response overall, except for around 700 nm to 800 nm. The calibrated values (not shown) show the same trends, with even higher response around 700 nm for the ground spectrum. This coincides with the expected values, as the sky spectrum generally peaks around 550 nm and has low values above 700 nm, while the spectral signature of vegetation, which is present in the ground pixel, has a high signal from 700 nm and up. The reduction from 12-bit data to 8-bit data should, however, be done with care, as it significantly affects the intensity resolution of the data. This is not critical when looking at the spatial performance of the HSI, as done with the created RGB image in Figure 3.9 , but affects the spectral signatures as seen in Figure 3.10. It is recommended to store data as 12-bit if possible, especially if data is collected for scientific use.

Figure 3.9: Longyearbyen harbor, 26-08-2019. (a) Mobile phone image, for reference. (b) RGB image generated from the hyperspectral datacube, using wavelengths 660 nm, 540 nm and 480 nm. Data from [139].

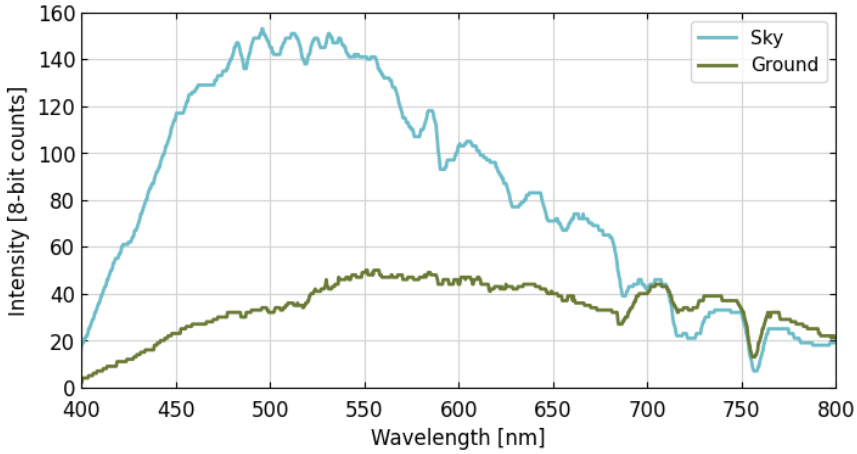

Figure 3.10: Point spectra from the Longyearbyen harbor datacube, showing sky with diffuse clouds (blue) and ground in the mountainside covered in grass (mossy green).

3.4.1 Comparison of measured throughput in HSI V4 and HSI V6

The ratio of the throughput in HSI V6 to HSI V4 was measured experimentally, in addition to the theoretical calculation done in Section 3.1.1. Both instruments were placed in front of a Lambertian screen (Labsphere SRT-99-180) illuminated by a 1000 W tungsten lamp (ORIEL SN7-1275), with a distance of 1 m between the lamp and the screen. The exposure times were adjusted so that the captured images were nearly overexposed to limit the effects of noise. The signal was then scaled by exposure time to obtain comparable values, as shown in Figure 3.11. The measured throughput ratio at 600 nm was found to be 6.77, which is the same as the theoretical value found in Section 3.1.1, and verifies that the throughput is increased in the HSI V6, as expected. The average measured throughput ratio in the spectral range of 400 nm to 800 nm was found to be 6.91.

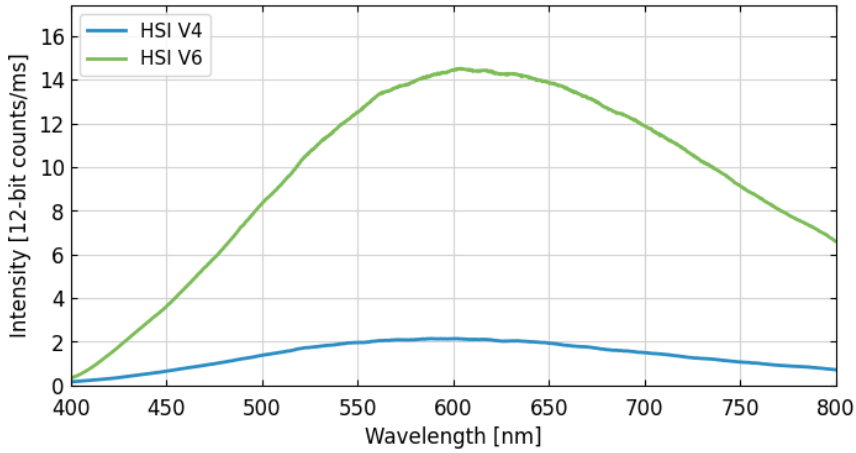

Figure 3.11: Measured radiometric response in HSI V4 and HSI V6 divided exposure time, showing the improved throughput experimentally.

3.5 Conclusions

A new version of the HSI V4 presented in Sigernes et al. [34] was created, with the main goal of increasing the throughput of the system, to further increase the SNR, keeping the spectral and spatial resolution roughly the same. The resulting HSI V6 was also built out of COTS components, still being a pushbroom HSI with a transmissive grating as the dispersive element. The optics, however, were increased in size from S-mount to C-mount components, resulting in a slightly larger instrument of about 220 x 65 x 65 mm^3 in size,

and weighing just under 650 g. The theoretical increase of throughput was calculated to be 9.75 times higher than the original HSI V4 design, and 6.77 times higher for the modified HSI V4 that was further used. The measured increase in throughput was also found to be 6.77, confirming that the throughput in the new design has been increased.

4 | Calibration and optical performance

4.1 Calibration facilities and equipment

For the work presented in this thesis, data has been collected with several hyperspectral instruments (different models) and in different locations based on the type of experiment and measurement set-up needed. The main part of the work was conducted at NTNU. Data for some of the projects, mainly the ones focusing on comparison of the HSI V4 and HSI V6 and second order diffraction effects, were collected at UNIS, while the PSF measurements were performed at the University of Oslo (UiO). The equipment and measurement set-ups that were used are described in detail in this section.

4.1.1 NTNU

At NTNU, mainly two labs were used. Most used was the SmallSat Lab (Figure 4.1a) with an Electrostatic Discharge (ESD) safe area and a flowbench for assembly and initial testing of the HSIs (Figure 4.1b). In addition, an optical calibration lab was used for calibration purposes (Figure 4.1c). In the calibration lab there is an integrating sphere (Model ISS-30VA, Gigahertz Optik) with a certified tungsten halogen lamp with reference radiance from 400 nm to 2500 nm with a 10 nm resolution, that can be used for radiometric calibration. The integrating sphere can also be used in combination with pencil style spectral calibration lamps for wavelength calibration. The lamps available are argon (Ar), krypton (Kr) xenon (Xe) and mercury (Hg) spectral calibration lamps (Newport Models 6030, 6031, 6033 and 6035, respectively). In the SmallSat lab, spectral tubes (Geissler tubes) from Frederiksen Scientific were also available and were used for testing. Neon (Ne, model no. 2850.00), hydrogen (H_2, model no. 2850.20), helium (He, model

Figure 4.1: Labs at NTNU. (a) Entrance to the SmallSat Lab, (b) flowbench in the SmallSat Lab, (c) calibration lab with integrating sphere.

no. 2850.30), oxygen (O_2, model no. 2850.50), nitrogen (N_2, model no. 2850.70, carbon dioxide (CO_2, model no. 2851.20), mercury (Hg, model no. 2550.10), argon (Ar, model no. 2850.40), krypton (Kr, model 2850.60), water (H_2O, model no. 2851.10), xenon (Xe, model no. 2851.30) and natrium and helium (Na and He, model no. 2851.80) were available. These lamps could all be used with the spectral tube holder (model no. 2855.70) with a built in power supply. However, when working with these lamps they were found to emit quite weak light, making it necessary to look straight at the lamp with the HSI to record any signal. This is not desirable as this configuration makes the set-up very sensitive to changes in the orientation between the instrument and the lamp. The Geissler lamps were therefore not used for calibration purposes.

For simple validation set-ups, fluorescent light (for spectral peaks) or a stable Thorlabs QTH10/M lamp (for broadband spectrum) were used in combination with a white sheet of paper. These set-ups were used during initial testing/assembly and environmental tests, and are further described in the report "HYPSO2-TPL-OPT-004 Optical Validation Test Plan" [141], and discussed in Section 6.2.1. For simulating targets at an infinite distance a Zeiss Makro-Planar 100 mm F/2 objective was used as a collimator in combination with 3D printed patterns. The two patterns most used were a striped and a halfmoon pattern, as seen in Figure 4.2. The patterns were fastened to the back of the Zeiss lens objective and the HSI placed in front so that it viewed the collimated light from the pattern through the lens objective. The 3D printer available in the lab was an Original Prusa i3 MK3 with a resolution of 0.2 mm and black PolyLactic Acid (PLA) filament. In addition, optical breadboards, poles, holders, filters and other optical and optomechanical components were available (or ordered) as well, to assemble set-ups when needed.

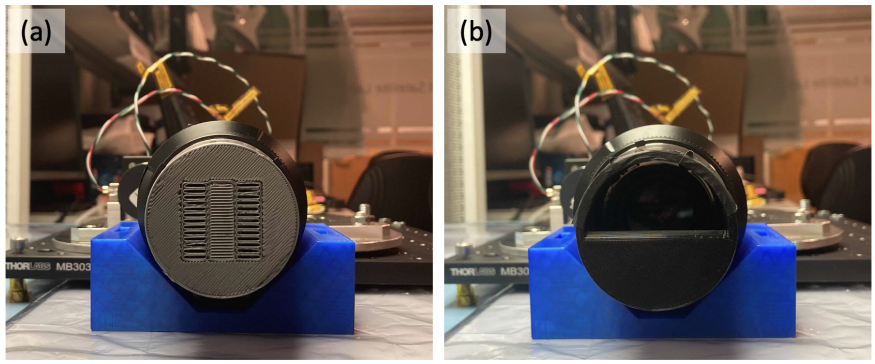

Figure 4.2: 3D-printed patterns. (a) Striped pattern, (b) halfmoon pattern.

4.1.2 UNIS

At UNIS, the radiometric calibration set-up consisted of a Lambertian screen (Labsphere SRT-99-180) illuminated by a 1000 W tungsten lamp (ORIEL SN7-1275) at a set distance, as described in Sigernes et al. [142]. A monochromator set-up was also available, which is described in detail in Sigernes et al [143, 144] and shown in Figure 4.3b. The main components of the monochromator set-up are a fiber illuminator (Leica 150W) connected to the entrance slit of a monochromator (Jobin Yvon HR320), with the exit slit fed into an integrating sphere (Edmund Optics, 6 inches diameter) with a transmitting diffuser (Teflon, 0.5 mm thick) at the output port. The output of the sphere is the target for both the instrument and a FICS spectrograph (Fixed Compact Spectrograph from Oriel SN 7743) which monitors the output wavelength of the monochromator. This set-up was used for the investigations of second order effects in Chapter 5.

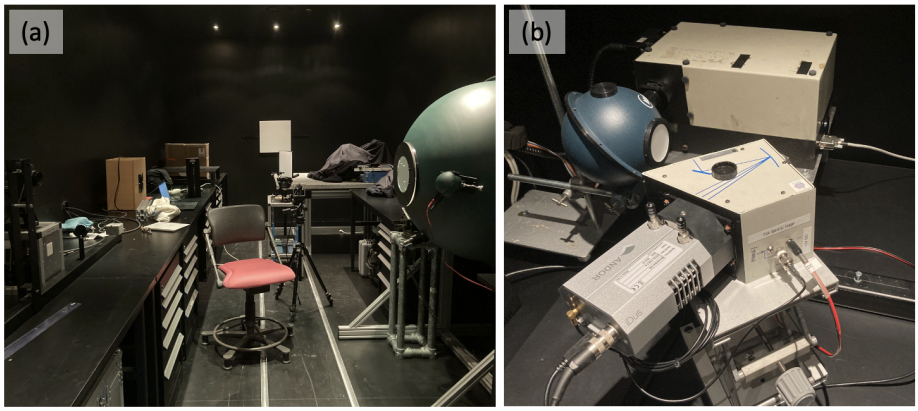

Figure 4.3: Optical lab at UNIS. (a) Lab layout with integrating sphere and reflectance plate on the wall, (b) monochromator equipment.

4.1.3 UiO

At UiO, a set-up to measure the spatial PSF has been developed. The original set-up is described in Torkildsen et al. [110], and further development and improvements in Selnesaunet et al. [145] (**Paper 9**).

The set-up consists of a collimator (Inframet CDT 11100HR off axis collimator), a slit (22 μm $\times$ 25 mm slit, metal film on glass) and a light source (Inframet LS-DAL Multi-channel broadband VIS-NIR with two white LEDs and a 2856K halogen bulb). The

slit is mounted on a turnwheel, and moved across a 25 mm optical port by using a Standa rotational stepper motor which again is mounted on a Standa translational stepper motor, allowing scans in one direction (translation) in 360 ° angles (rotation) to be possible. The light source can be operated with a chosen ratio of the LEDs and halogen bulbs to ensure a uniform spectrum across the VIS-NIR bands. To minimize light contamination, 3D printed parts were used to cover exposed parts of the set-up. The set-up with and without these 3D printed covers is shown in Figure 4.4.

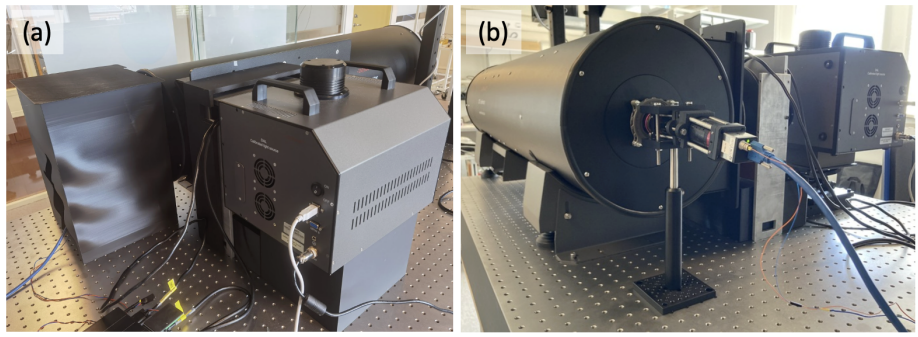

Figure 4.4: Collimator set-up in the optics lab at UiO. (a) With covers and (b) without covers.

4.2 Calibration and characterization methods

Here, the methods on how the wavelength and radiometric calibrations, and how characterizations such as measuring the FWHM, smile, keystone and spatial PSF are performed, are presented. Results from these types of calibrations and characterizations are presented throughout the thesis.

4.2.1 Wavelength calibration

The wavelength calibration presented in this thesis is performed using the spectral lamps available at NTNU. The HSI is placed in front of the integrating sphere with a spectral lamp inserted into the sphere, as seen in Figure 4.5. The data is typically collected with the argon and mercury lamps (unless other is specified), and the spectral lines from these lamps used to find a map between pixel and wavelength. An example of data collected from the argon and mercury lamps, and the wavelengths of the spectral peaks used, is shown in Figure 4.6.

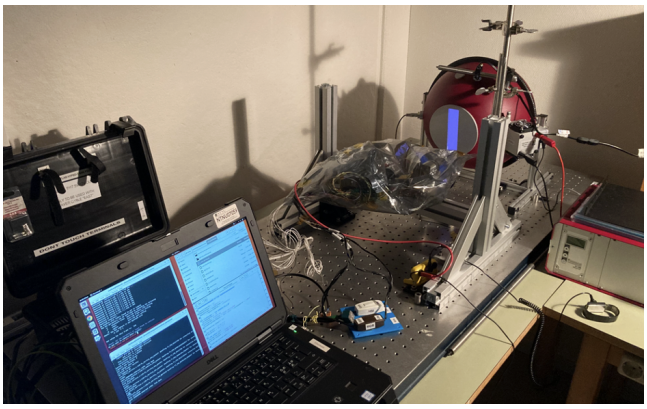

Figure 4.5: Spectral calibration set-up.

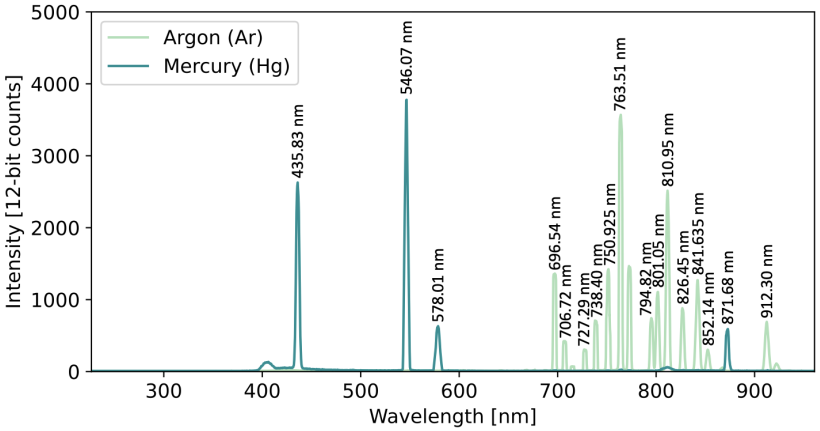

Figure 4.6: Spectral lines from argon (Ar) and mercury (Hg) spectral lamps.

A second or third order polynomial is typically used to describe the pixel to wavelength relationship, such as

$$\lambda \approx a_0 + a_1 \cdot p + a_2 \cdot p^2, \tag{4.1}$$

for a second order fit, where λ is the wavelength, p is the spectral pixel index and a_0, a_1 and a_2 are the spectral calibration coefficients. A study on other ways to describe the pixel to wavelength relationship, and which may be better, is presented in Section 4.4. This calibration can then be repeated for every row (field position) in the image to avoid errors due to the smile effect. Also used later in this thesis is the spectral calibration matrix. This is created by calculating the wavelength for each pixel in the image as

described above, and storing them in a matrix (the same size of the image). This is just an alternative and convenient way to store and apply the wavelength calibration.

4.2.2 Radiometric calibration

For radiometric calibration, only the integrating sphere set-up at NTNU was used. The HSI was placed in front of the inlet of the sphere so that the full FOV of the instrument was illuminated, as seen in Figure 4.7. Settings (such as exposure time) were set so that the images were well exposed (close to the maximum value, but not overexposed at any wavelength). Typically 10 images were acquired and averaged before further use. The reference data, containing the radiance value for each wavelength from the integrating sphere lamp, is shown in Figure 4.8. This data is only sampled at 10 nm resolution, and was therefore interpolated using cubic spline interpolation before use.

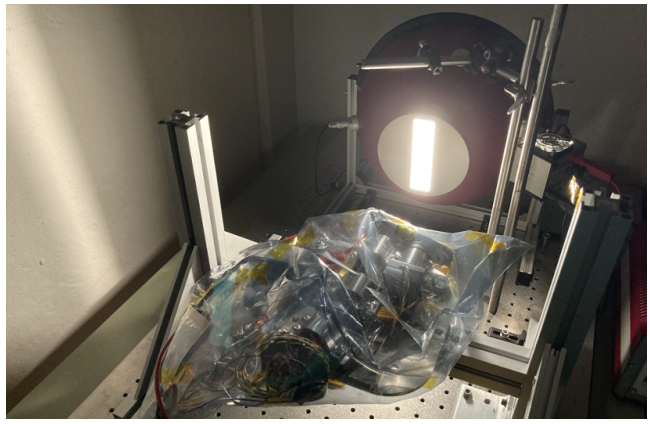

Figure 4.7: Radiometric calibration set-up with integrating sphere at NTNU.

After acquiring the data, the normalized signal captured by the instrument, S [counts/sec] is first estimated by removing the estimated background value (average value in dark image) from the averaged image, and then scaling the pixels values by the exposure time that was used. The radiometric calibration coefficient, K, is then calculated as

$$K = \frac{L}{S}, \tag{4.2}$$

for each pixel, where L is the absolute radiance [mW/(m^2 nm sr)]. As a calibration coefficient is calculated per pixel, it also corrects for unevenness in the light distribution in the image such as from vignetting (flat-field correction).

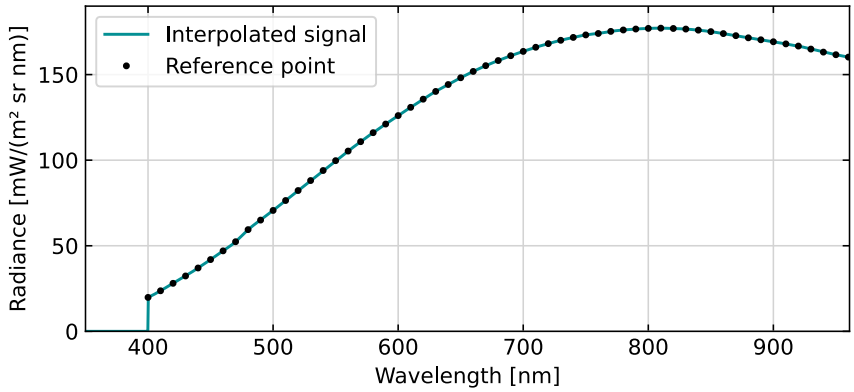

Figure 4.8: Reference spectrum of the integrating sphere at NTNU.

Dark image

One important step during the calibration is to remove any static background value. Background value here means the pixel count recorded by the camera sensor when no light is present. This value was found by acquiring typically 10 images (unless other is specified) in the dark with the lens cap on. The images were then averaged, and the average value out of all 10 images used. It is worth noting that using one background value per pixel is an option if there are patterns or unevenness in the distribution of background values in the image. For the instruments tested here the distribution was uniform, and the average value therefore used for all pixels for simplicity.

4.2.3 Full width at half maximum

The FWHM is estimated from the spectral calibration data. The line spectrum in one row is investigated at the time. In some cases, all rows in the image are used. If not other is specified, it is the center row (middle of the image) that is used for the analysis. In a python script the line spectrum is first smoothed using a bartlett window function. The position of the peaks are then detected using the `scipy.signal.find_peaks()` function, with a distance parameter of 18 and a peak height value of 10% of the maximum value in the line. The width of the peaks at half maximum are then found using `scipy.signal.peak_widths()`, and the units converted from pixels to wavelength using the spectral calibration coefficients.

4.2.4 Smile and keystone

This method is based on the one presented in **SP 1**: "Real-time Corrections for a Low-cost Hyperspectral Instrument" [138]. This was a publication by the author at the end of her master's degree, which also was related to calibration of hyperspectral imagers and acted as a pre-project to the work presented in this thesis. The main idea of the set-up is the same, but the algorithms have been improved throughout this thesis.

When acquiring data for smile and keystone characterization, the spectral calibration lamps were used with the integrating sphere in the calibration lab at NTNU. The collimator lens with the 3D printed striped pattern was placed in front of the HSI pointing towards the integrating sphere, as seen in Figure 4.9. If not other is stated, the argon and mercury lamps were used. The spectral lamps together with the striped pattern create distinct points in the spectrogram that are used in the analysis. Typically 10 images were acquired per spectral calibration lamp and the images combined by summation when performing the analysis so that the spectral lines from both lamps were available in the image, as seen in Figure 4.10.

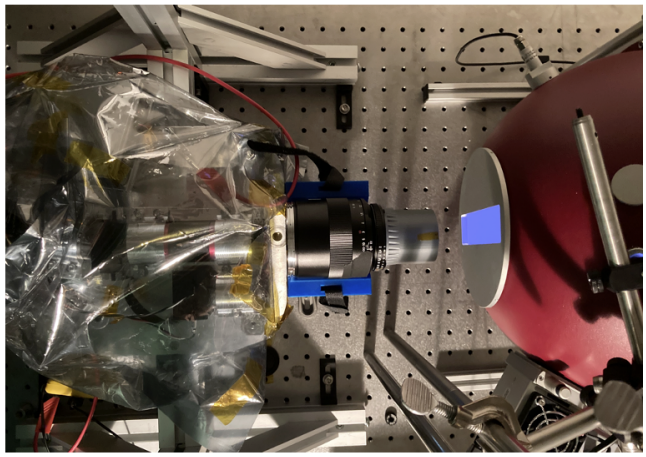

Figure 4.9: Smile and keystone characterization set-up.

The smile and keystone detection and correction follows the method from Lawrence et al. [104] using GCPs and a two-dimensional quadratic polynomial distortion model, as described in Section 2.3.4. The points were detected by first masking the image using a threshold value of 3500 (out of maximum 4095 counts) and detecting the center position of the contours of the points. The points were

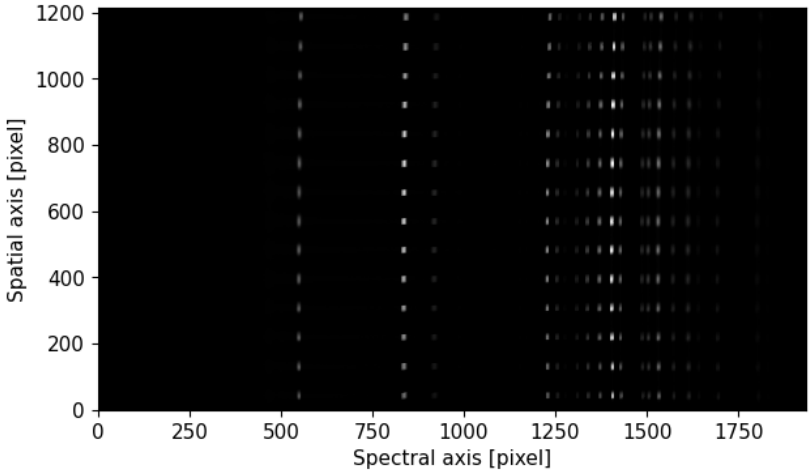

Figure 4.10: Smile and keystone characterization frame.

then sorted onto a grid to create the reference grid, and removing any lines were all points were not detected. The model coefficients to the two-dimensional quadratic polynomial distortion model were then calculated. To get estimates of the smile and keystone distortions a second order polynomial fit was made to the vertical lines to estimate smile and a first order polynomial (linear) fit was made on the horizontal lines to estimate the amount of keystone. For correction, new values were calculated for the reference grid using the calculated model coefficients, and then applied using the `scipy.ndimage.map_coordinates()` function.

Only correcting for smile

An option is also to only correct for the smile effect, as done in Section 8.2.2. Here, the spectral calibration matrix is used. The wavelengths from the center row are used for reference, and the spectra in the other rows are interpolated and resampled onto the same wavelengths. Another option could be to use the spectral calibration data to model the smile effect at different wavelengths and use this for smile correction (only).

4.2.5 Spatial point spread function

The spatial PSF is found by measuring the LSF at several angles (by rotating the slit) with the set-up described in Section 4.1.3. These LSFs are then used to reconstruct

the PSF through tomographic reconstruction, as described in Torkildsen et al. [110] and Selnesaunet et al. [145] (**Paper 9**). This set-up is presented in detail in **Paper 9**: "Imaging the point spread function of hyperspectral cameras - the full truth about coregistration error and resolution" [145], with only the main procedures described here in this section.

Measurements of LSFs

During measurements, the HSI was placed in front of the collimator, and a 3D printed cover placed on top to minimize external light and reflections. The slit, now imaged by the HSI, was adjusted so that it was centered in the spectrogram, and the rotational center was also found. Further, the camera settings such as exposure time, frame rate, pixel clock, gain (if needed) and so on were found so that the captured data was well exposed without any parts being overexposed. A custom made control software was used to control the stepper motors and the instrument so that the HSI captured and stored images on trigger pulses sent from the stepper motors. This way the data acquisition was synced with the motor steps. The slit was set up to scan with a translational motion to measure one LSF. The desired amount of motor steps between each captured image, motor speed and length of the scan were chosen. The scan was then repeated for a selected number of angles.

The resulting data set contains the spatial LSF in both along and across track direction, and several LSFs at different angles as well (depending of the number of angles used during the scan), for all wavelengths. It is worth noting that this set-up does not measure the traditional spectrometer PSF which would use a monochromatic source and measure the PSF in the spectrogram, but a spatial PSF which describes the distribution of the light in the spatial-spatial domain of the hyperspectral datacube, as discussed in Section 2.3.5.

Data processing

Pre-processing of the data consists of correlation correction, averaging by binning every 10 frames, smoothing to reduce noise and finding the number of frames per pixel from the LSF measurements, as described in Selnesaunet et al. [145] (**Paper 9**). The pre-processing steps can be described as follows:

- **Correlation correction**: During measurements, the rotational center of the slit is not necessarily located exactly in the center of the image. This results in an offset in the position of the LSF peak when plotting all LSFs together. To correct for this,

the position of every LSF pairs, a pair being two LSFs with a 180° step between them, are matched up using correlation. The offsets are found and applied to the data, thereby aligning the LSFs.

- **Averaging by binning**: Binning is then applied to reduce noise by averaging the response from 10 frames.

- **Smoothing**: A Savitzky–Golay filter is then applied to the LSFs to reduce the high frequency noise even further.

- **Finding number of frames per pixel**: The number of frames covering one pixel during a scan is estimated by looking at the peak of the along track LSF in each pixel. The number of frames between the peaks gives the number of frames captured per pixel. The average distance (number of frames) between all the detected peaks is used as the conversion factor, and is only used to convert from number of frames to number of pixels on the axes in the plots below.

Finally the PSFs are reconstructed from the measured LSFs through tomographic reconstruction, as described in Hovland et al. [146]. The tomographic reconstruction uses the LSFs as 1D projections at different angles to build up a 2D image of the PSF for each band. The reconstruction assumes the object (here the PSF) to be rotationally symmetric about the axis of rotation. More measurements (LSFs) therefore results in a better representation of the final PSF. Noise can affect the results as some of the noise may be amplified in the reconstruction process. See Selnesaunet et al. [145] (**Paper 9**) for more details on the exact reconstruction process used here. Radial noise appearing as radial streaks from the center of the PSF after reconstruction, is removed in the frequency domain. After transforming back to the spatial domain, residual noise is removed by removing all values below 5% of the total enclosed energy in the PSF.

4.3 Calibration and optical performance of HSI V6

Here, the focus is on the calibration and optical performance of the HSI V6. Results from measurements of the optical performance of HSI V4 is also presented, to compare the two. A quick comparison of the specifications of the instruments are shown in Table 4.1, to give context to the results. This section is based on parts of **Paper 1**: "A do-it-yourself VIS/NIR pushbroom hyperspectral imager with C-mount optics" [35], and is a continuation of the work presented in Chapter 3.

Table 4.1: Summary of some specifications of the HSI V4 and HSI V6. FL = focal length.

Specification	HSI V4	HSI V6
Lenses	Front lens: F/4 FL=16 mm, field lens: FL=10 mm, collimator lens: FL=30 mm, detector lens: F/2.5 FL=25 mm	Front and collimating lens objective: F/2.8 FL=50 mm, imaging lens objective: F/2 FL=50 mm.
Slit height	3 mm	7 mm
Slit width	25 μm	50 μm
IFOV	0.089° (along track), 10.712° (across track)	0.057° (along track), 8.008° (across track)
Magnification	1.2	1
Grating	600 lines/mm	300 lines/mm
Theoretical FWHM	1.4 nm	3.3 nm
Designed center wavelength	552.5 nm	600 nm
Designed spectral range	400 - 800 nm	400 - 800 nm
Full spectral range[a]	200 - 973 nm	260 - 1027 nm
Average spectral sampling distance	0.399 nm per pixel	0.396 nm per pixel
Size	$120\times50\times50$ mm^3	$200\times65\times65$ mm^3
Weight	< 200 g	650 g

[a] The full spectral range available on the sensor denotes the spectral range from the first to the last spectral pixel on the camera sensor, and exceeds the designed spectral range. The exact values varies with each instrument as it depends on the exact placement of the components.

4.3.1 Calibration

Wavelength calibration was done using the argon and mercury-argon spectral lamps in the calibration lab at NTNU. The lines in the center row of the spectrogram are shown in blue in Figure 4.11. The exact spectral range reaching the sensor, which can be referred to as the full spectral range, differs slightly between different individual models as it depends heavily on the exact placement of the components. The full spectral range can easily be found using the spectral calibration data, and is from below 300 nm to above 900 nm for the IMX174 sensor, as seen in Figure 4.11. If using a smaller sensor, such as the IMX252, the full spectral range is shortened and spans from right below 400 nm to about 850 nm. The full spectral range differs from the designed spectral range of 400 nm to 800 nm simply because the sensor is larger than needed.

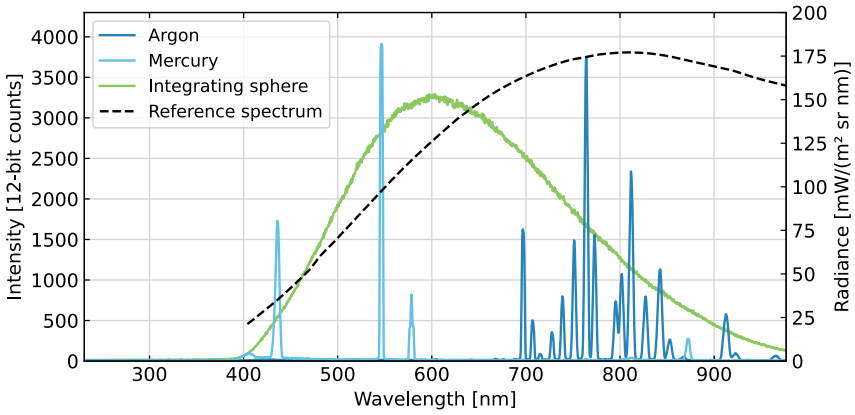

Figure 4.11: HSI V6 calibration data. Blue lines show spectral calibration peaks from the argon (dark blue) and mercury (light blue) lamps. The green line is the uncalibrated measured spectrum from the integrating sphere set-up (radiometric calibration), while the black dashed line is the reference spectrum from the integrating sphere set-up. All recorded values are shown in counts (left axis), while the reference spectrum is given as radiance (right axis). The spectra are sampled from the center horizontal row of the detector.

For radiometric calibration, the integrating sphere with the certified tungsten halogen lamp in the calibration lab at NTNU (described in Section 4.1.1) was used. The recorded spectrum by the HSI V6 is shown in green, while the reference data from the integrating sphere is shown in a black dashed line in Figure 4.11. The measured spectrum (green line) shows that there is almost no light recorded below 400 nm, which is mainly due to the coating on the objectives blocking light below 400 nm. The signal above 800 nm is low due to low QE of the sensor, and contaminated by second order diffraction effects (discussed further in Chapter 5). The usable spectral range is therefore 400 nm to 800 nm, which is the designed spectral range of the instrument. The full spectral range is shown for the calibration data since the wavelengths above 800 nm are used to investigate the second order diffraction effects in Chapter 5.

4.3.2 Full width at half maximum

Spectral resolution, measured as the FWHM, was calculated from the spectral calibration data shown in Figure 4.11. The mercury peak at 546.1 nm was found to be 3.69 nm, which is close to the theoretical value of 3.33 nm. When having a closer look at all detected peaks in the 400 to 800 nm range, and also at different positions in the slit image (different

rows), it is clear that the FWHM varies both with wavelength and field position, as seen in Figure 4.12. For the shorter wavelengths, the FWHM varies only a little with field position, and the calculated values mostly stay below 4 nm. For the longer wavelengths on the other hand, the FWHM is much wider in the center of the image than on the edges, and the overall value reaches 5 nm.

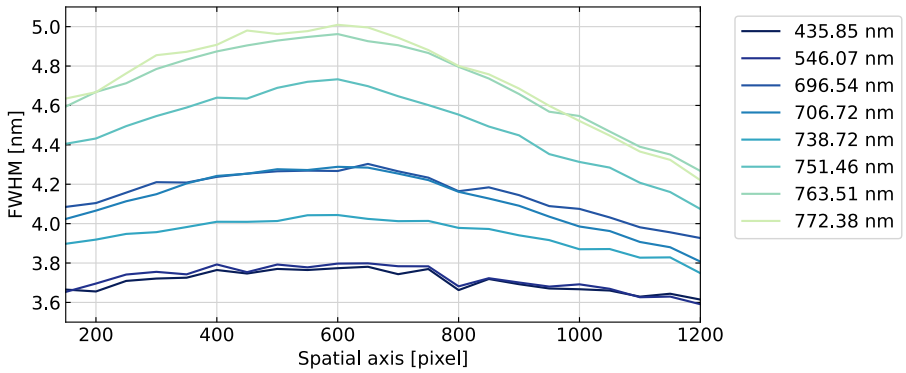

Figure 4.12: Estimated FWHM for the HSI V6 as a function of spatial position (different positions in the slit image) for the detected spectral calibration peaks in the spectral range of 400 to 800 nm.

Achieving a measured FWHM equal to the theoretical FWHM is hard as the focus of the objectives and all distances between the optical elements must be extremely precise in order to obtain the theoretical value. In practice this is hard to accomplish without spending a large amount of time and resources on precision mechanics. However, values close to the theoretical FWHM are possible to achieve, as shown here.

4.3.3 Smile and keystone

Smile and keystone were measured as described in Section 4.2.4. Smile as a function of spatial position (slit height) was estimated as a second order polynomial fit of the position of the spectral calibration wavelengths. Both the average value and the minimum and maximum values are shown in Figure 4.13. The offset in HSI V6 due to smile is close to 5-6 pixels, while for HSI V4 it is closer to 20 pixels on the edges of the image. The HSI V4 uses a 3 mm slit which limits the area of the sensor that is illuminated, represented by the shaded gray area in the Figure 4.13, so the distortions from smile that are observed in the actual image is less than 10 nm. If a 7 mm is used instead, the larger distortions would be seen. The curve for HSI V6 is slightly tilted, causing more pixel shifts for longer

wavelengths (above 600 nm). This spectral tilt is most likely due to the slit not being aligned perfectly vertically. It is clear that the HSI V6 is less affected by the smile effect, which is due to the larger and higher quality optics.

Keystone as a function of wavelength was estimated as a linear fit of the position of stripes (from the striped pattern used when acquiring data) at different wavelength. The maximum shift was found at the edges of the spectrogram, as expected, and is shown

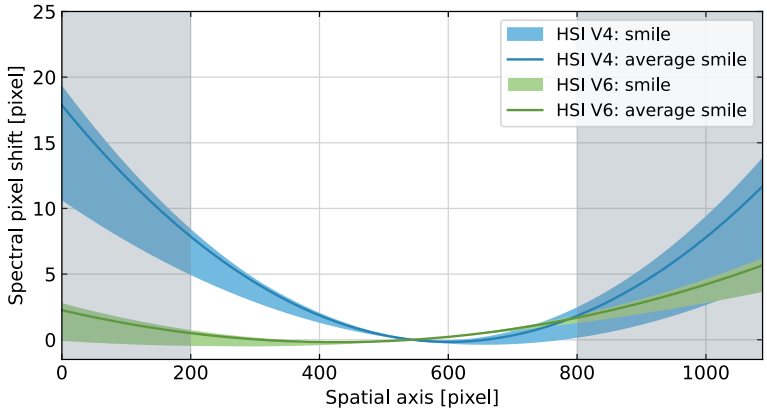

Figure 4.13: Measured pixel shifts due to smile in HSI V4 and HSI V6. The shaded area corresponds to the area where no light is recorded when using a 3 mm long slit (used in the original HSI V4 design) instead of a 7 mm long slit which illuminates the full sensor (used for the HSI V6).

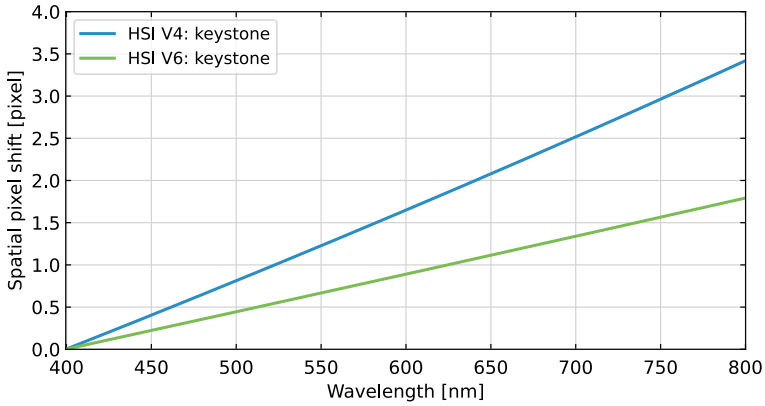

Figure 4.14: Measured pixel shifts due to keystone in the HSI V4 and HSI V6.

in Figure 4.14. It can be seen that the pixel shift due to keystone is less than 2 pixels for the HSI V6, and less than 3.5 nm for the HSI V4. The HSI V6 shows also here better performance.

Both spectral tilt, smile and keystone can be corrected in software [147, 138, 148], to some extent, where smile and keystone can be corrected either separately or simultaneously (where the latter is preferred as they affect each other). Low smile and keystone distortions before correction are still desired to ensure good data quality.

4.3.4 Spatial point spread function

To measure the spatial PSF, LSFs were measured and then used to reconstruct the spatial PSF, as described in Section 4.2.5. This section is based on the results presented in **Paper 11**: "Using spatial PSF measurements to compare the performance of two DIY hyperspectral imagers" [149].

Line spread function

The LSFs in across and along track for a set of wavelengths within the designed spectral range of 400 nm to 800 nm for both HSI V4 and HSI V6 are shown in Figure 4.15. For both imagers, the measurements from the center of FOV were used.

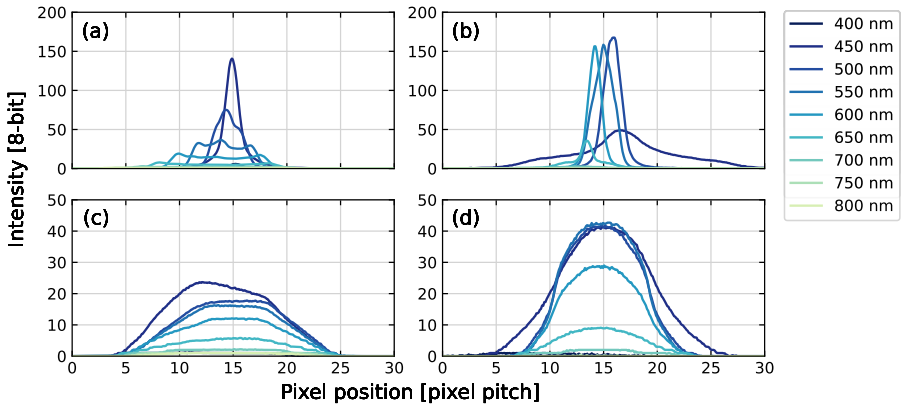

Figure 4.15: LSFs in across track and along track direction for both cameras in the center of FOV. (a) HSI V4 across track, (b) HSI V6 across track, (c) HSI V4 along track, (d) HSI V6 along track. Note difference in y-axis for across and along track LSFs.

The signal below 450 nm and above 650 nm is very low. This is mostly due to the QE of the sensor, and efficiency of the optical components. For HSI V4, 450 nm has the sharpest and strongest peak. This suggest that the focus is set to be best for the shorter wavelengths. Optimally the focus should be set to be best at the center wavelength, and can be fine tuned by the user by twisting the tube on the front lens. The broadening of the peak for longer wavelengths, as well as features like the triple peak for the 550 nm peak in across track direction, all most likely come from chromatic aberrations. For HSI V6, both 450 nm, 500 nm and 550 nm show similar response, closely follows by the 600 nm peak. The optimal focus is set closer to the center wavelength here, but could be set even closer to 600 nm.

It can also be seen that for both instruments, the LSFs are most narrow in the across track direction, and wider in the along track direction. This is due to the measurement slit being more narrow than the pixel height and instrument slit, as illustrated in Figure 4.16. In across track direction, the thin measurement slit creates a narrow stripe on the detector (assuming light at all wavelengths). As the scan progresses, the light from the measurement slit moves up or downwards towards the next pixel. The width of the LSF in this direction therefore depends on how many steps (in the scan) there are for the narrow stripe to cross a pixel.

In the along track direction, the two slits are parallel. The illumination from the measurement slit is now spread over a larger area on the sensor, resulting in less light per pixel. In addition, the fact that the measurement slit is more narrow than the instrument slit means that the width of the LSF now depends on how many steps it takes for the measurement slit to cross the instrument slit. This results in wider LSFs in the plots as

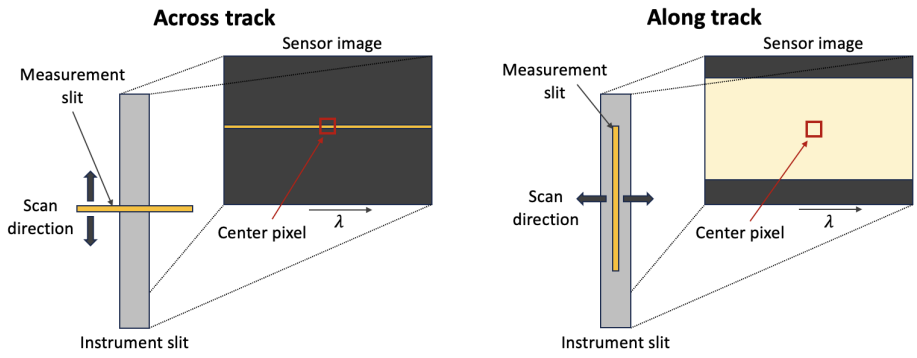

Figure 4.16: Illustration of LSF measurements in across and along track directions.

it takes a bit more than 10 steps for the measurement slit to cross the instrument slit in along track direction, while it only takes a few to around 10 steps for the measurement slit to cross a pixel in across track direction. It is worth noting that for these measurements, 8-bit data was saved instead of 12-bit data. For the dark areas in the images, such as for the shorter and longer wavelengths, the lower intensity resolution makes separating signal and noise much harder than if 12-bit data was stored. For future experiments, 12-bit data should therefore be saved instead.

Spatial point spread function measurements

The full spatial PSFs were reconstructed from the LSF measurements, and are shown for selected wavelengths in Figure 4.17 and Figure 4.18 for HSI V4 and HSI V6 respectively. Wavelengths between 450 nm and 650 nm were chosen as it can be seen from the LSFs in Figure 4.15 that there is very little signal and a lot of noise in the measurements outside of this range. The reconstruction process is very sensitive to noisy data, there is therefore no point in reconstruction the spatial PSF for the noisy wavelengths.

First, it can be pointed out that the x- and y-axes differ between the two plots. The spatial PSFs for HSI V4 are 20-25 pixels high and 2-10 pixels wide, while the PSFs for HSI V6 are about 10 pixels high and 2-5 pixels wide, making them much smaller than for HSI V4. The HSI V4 has a slightly larger FOV, meaning that a pixel from the HSI V4 covers a slightly larger area than for the HSI V6 (assuming the same sensor is used). It is therefore natural that the measured PSFs cover a larger area in the HSI V4. The HSI V4 also has a magnification of 1.4, while HSI V6 has no magnification. There are, however, also other factors that affect the size of the PSFs. The HSI V6 has bigger and better quality optics, which should make the PSF better (smaller). HSI V4 also has a more narrow slit, which should have made the PSF more narrow in the along track direction.

Another factor that should be considered but is not shown in these plots is that the HSI V4 collects a lot less light than HSI V6, as shown in Section 3.4.1 where the improved throughput is discussed. For these measurements, an exposure time of 240 ms was needed for the HSI V4, while only 60 ms was used for the HSI V6. This affects the measurement time a lot, since the frame rate needs to be adjusted accordingly. For the HSI V4 PSFs, the peaks are again broader for the longer wavelengths. The most narrow peak is at 450 nm both in center and at the edge of FOV. The variations with wavelength are again due to chromatic aberrations. Overall, the sharper response is found at the edge of FOV, where also the 500 nm peak is quite sharp, suggesting the the optimal focus has changed slightly towards longer wavelengths. Above 600 nm, however, the signal is very weak and noisy,

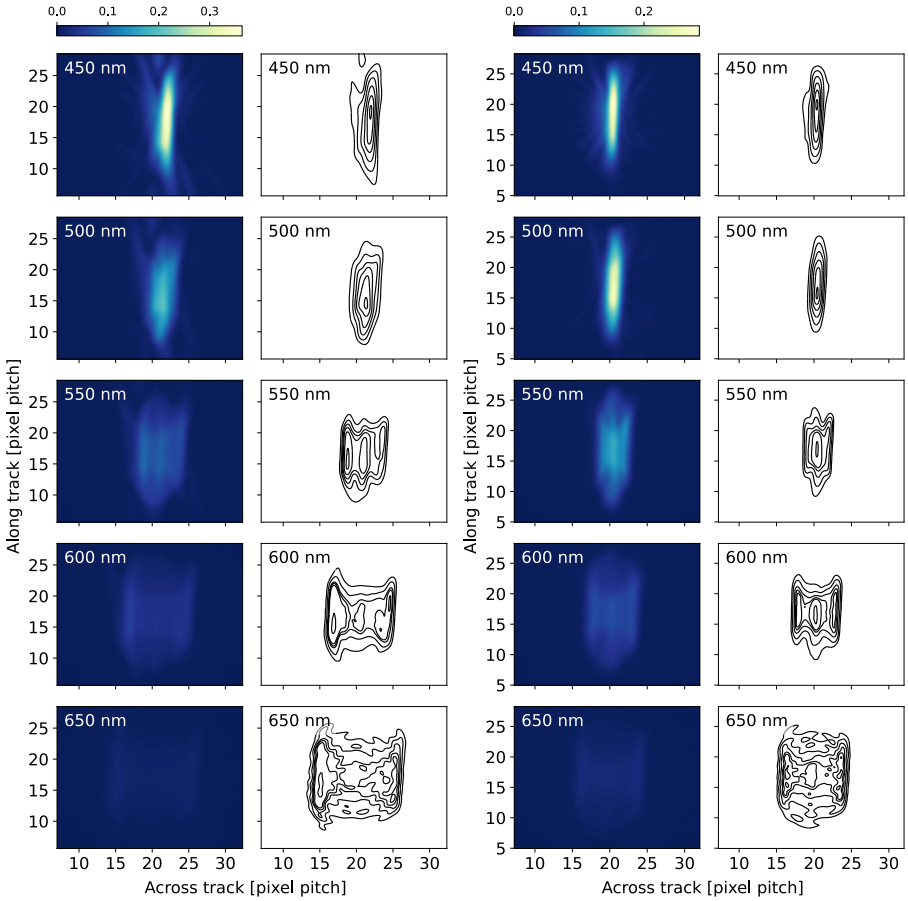

(a) Center of FOV. *(b) Edge of FOV.*

Figure 4.17: Reconstructed spatial PSF for HSI V4.

and the PSF grows wide, suggesting that the performance at these wavelengths are not optimal for this imager. The focus should be adjusted and the measurements repeated for a proper comparison.

For the HSI V6 PSFs, the smaller PSFs are found in the center of FOV. This is more as expected, as the best performance should be in the center of FOV close to the optical axis. It can be seen that the focus depends on the field position, as the most narrow peak in the edge of FOV is found at 650 nm. The center of the PSFs move towards the right for longer wavelengths. This is due to the keystone effect. That keystone is visible in the center of

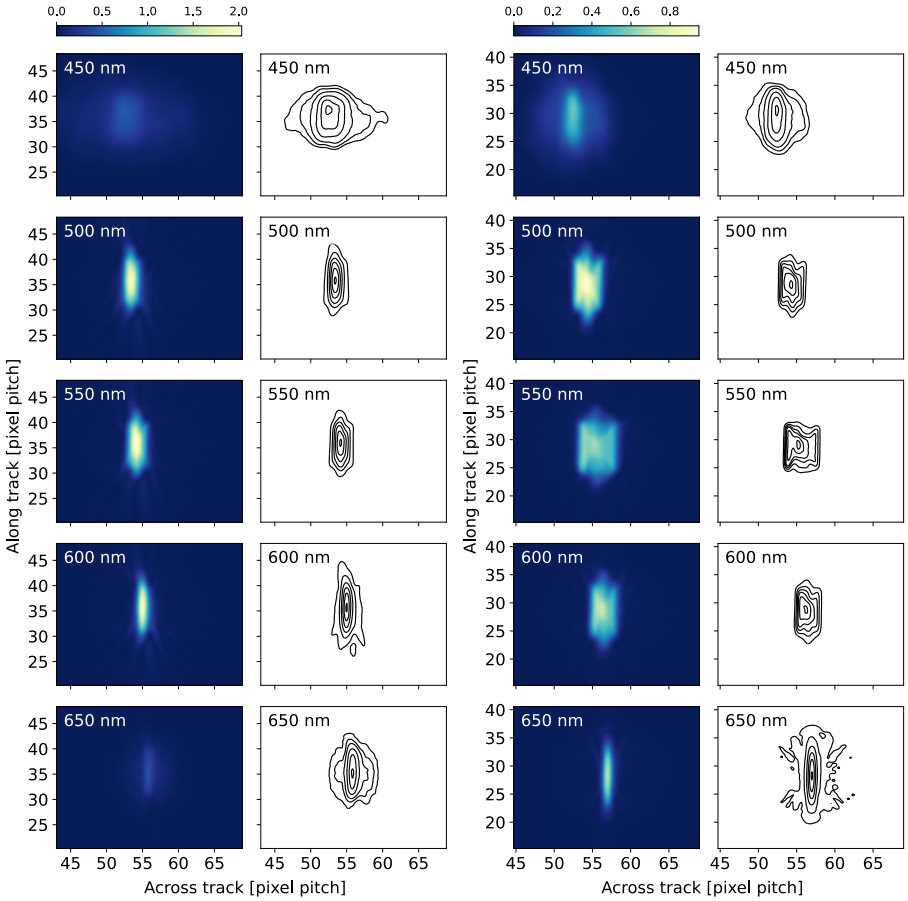

(a) Center of FOV. *(b) Edge of FOV.*

Figure 4.18: Reconstructed spatial PSF for HSI V6.

FOV is most likely to the sensor being tilted compared to the optical train (which can be adjusted when mounting the sensor housing to the optical train).

It should be noted, however, that neither the HSI V4 nor the HSI V6 used in these experiments were perfectly focused and adjusted. This is therefore not a completely fair comparison. The experiments should be repeated for properly focused instruments, and their performance then be compared in more detail. In addition, as already mentioned, future experiments should include storing the 12-bit data for higher dynamic range.

4.4 A closer look at wavelength calibration

Commercial instruments are typically calibrated before being delivered to the customer. When building the instrument in-house, however, one must also perform the calibration and make sure that it is accurate, allowing pixels on the detector to be mapped to their corresponding wavelength. When performing wavelength calibration, there are different ways of both collecting data and analyzing the results. A closer look at wavelength calibration using spectral lamps was therefore done, since this is the equipment available at NTNU. It is also a relatively simple set-up, which makes it easy to use for others that are building their HSIs in-house, or need to perform the calibration themselves for some other reason. This section is based on **Paper 5**: "A Closer Look at a Spectrographic Wavelength Calibration" [150], with results from additional experiments added. Measurements were repeated using a larger selection of spectral lamps, and the analysis improved by acquiring data of multiple exposure times and stacking them to High Dynamic Range (HDR) before continuing the analysis, as suggested in the proposed further work section of the original paper and from feedback after the conference presentation.

4.4.1 The pixel to wavelength relationship

Often, a close to linear relation between the spectral pixel index and wavelength is expected. For instruments with a grating, the light is dispersed following the grating equation

$$m\lambda = d(\sin\alpha + \sin\beta), \tag{4.3}$$

where m is the spectral order, λ is the wavelength, d is the grating groove spacing, α is the angle of the incoming light (incident angle) and β is the angle of the diffracted light (diffraction angle) [134]. The change in β with wavelength is typically small, which leads to a close to linear relationship. However, small deviations from a linear fit are often observed. Solving for the diffraction angle as a function of wavelength, $\beta(\lambda)$, shows that the relationship is follows an $\arcsin$ function

$$\beta(\lambda) = \arcsin\left(\frac{m\lambda}{d} - \sin\alpha\right), \tag{4.4}$$

which indeed can be approximated as linear in areas close to zero, but is not truly linear. Other factors may also affect deviations from a linear fit. Chrien et al. mention that small misalignment in the angular positioning of the grating may introduce deviations [151].

Optical aberrations from the lenses may also affect the incident angles of light rays onto the grating, which again may lead to a nonlinear relation in dispersion of light. Different ways of describing the pixel to wavelength relationship are investigated here to see whether using a standard polynomial curve fit is sufficient, or if including theoretical knowledge from the grating equation and/or trigonometric relations between the diffraction angle and pixel position on the sensor can improve the calibration.

Method 1: Polynomial curve fit of λ

As already mentioned, the pixel to wavelength relationship is expected to behave close to linearly, which would correspond to a first order polynomial fit. A second or third order polynomial fit is, however, often used [148, 151, 152] (**Paper 2**). Here, polynomial fits of different orders are used to investigate the relationship, following

$$\hat{\lambda} = \sum_{i=0}^{n} a_i \cdot p_\lambda^i, \tag{4.5}$$

where $\hat{\lambda}$ is the estimated wavelength, $n \in \{1..3\}$ is the order of the polynomial, p_λ the pixel index of wavelength λ, and a_i the polynomial fit coefficients.

Method 2: Polynomial curve fit of β

The polynomial curve fit can also be used to estimate diffraction angle (instead of wavelength) from the pixel index. The grating equation can then be used to convert from diffraction angle to wavelength. This way, the sine relation in the grating equation is excluded from the polynomial curve fit, but included in the model as the grating equation is used. The polynomial curve fit becomes

$$\hat{\beta} = \sum_{i=0}^{n} b_i \cdot p_\lambda^i, \tag{4.6}$$

where $\hat{\beta}$ is the estimated diffraction angle, and b_i are the polynomial fit coefficients. By assuming $\alpha = 0$ and using spectral order $m = 1$, the grating equation applied becomes

$$\hat{\lambda} = d \cdot \sin \hat{\beta}, \tag{4.7}$$

which completes the map from pixel index to wavelength.

Method 3: Curve fit of β with arctan

The sensor is tilted $10.37°$ from the grating, matching the diffraction angle β_c of the center wavelength. According to simple trigonometry, an offset in diffraction angle, denoted $\Delta\beta = \hat{\beta} - \beta_c$, should result in an offset in pixel position on the sensor, $\Delta p_\lambda = p_\lambda - p_{\lambda_c}$, following

$$\Delta\beta = \arctan\Big(\frac{\Delta p_\lambda \cdot p_{width}}{f_2}\Big), \tag{4.8}$$

where p_{λ_c} is the pixel index of the center wavelength, p_{width} is the width of each pixel, and f_2 is the focal length of the detector lens. A least squares curve fit is then made to the function

$$\hat{\beta} = c_0 + \arctan(c_1 + c_2 \cdot p_\lambda))), \tag{4.9}$$

where $c_0..c_2$ are the coefficients of the fit. Following theory, c_0 corresponds to β_c. The estimated diffraction angle is again used with the simplified grating equation in Equation (4.7) to convert to the estimated wavelength.

Method 4: Curve fit of λ with grating equation

A least squares curve fit is then made to the grating equation in Equation (4.3), in combination with the diffraction angle to pixel position relationship described in Equation (4.9). The function for the fit then becomes

$$\hat{\lambda} = d_0 \cdot (\sin(d_1) + \sin(d_2 + \arctan(d_3 + d_4 \cdot p_\lambda))), \tag{4.10}$$

where $d_0..d_4$ are the coefficients of the fit. Following theory, d_1 corresponds to α, while d_2 corresponds to β_c. An additional version assuming $\alpha = 0$ was also tested by forcing $d_1 = 0$, to reduce the number of coefficients to be estimated.

4.4.2 Leave-one-out cross-validation and RMSE

Leave-one-out cross-validation is used when testing the different methods. For each set of emission lines, all lines except one are used to calculate the fit coefficients. The fit is then tested on the one emission line that was not included in making the fit. $\hat{\lambda}$ is estimated from the pixel index p_λ. The error from the corresponding reference wavelength is calculated as $e = \lambda_{ref} - \hat{\lambda}$. This is done for every emission line in the set, resulting

in a list of errors for each set. The RMSE is further used as a measure on how well different methods describe the pixel to wavelength relation. The RMSE is calculated as

$$RMSE = \sqrt{\frac{1}{m}\sum_{j=0}^{m} e_j^2}, \tag{4.11}$$

where m is the number of emission lines in the set, and e_j is the error for each emission line in the set. The RMSE is calculated for each method with each set.

4.4.3 Experiments using argon and mercury spectral lamps

The HSI V6 was used to acquire images of the emission lines from the argon (Ar) and mercury (Hg) wavelength calibration lamps used in combination with the integrating sphere in the calibration lab at NTNU. The HSI was mounted in front of the integrating sphere, illuminated by one calibration lamp at the time. The exposure time was adjusted so that the image was well lit but not overexposed, and 10 frames were taken for each calibration lamp. Combined images were made by adding one image of each lamp together, as seen in Figure 4.19, to provide a calibration image with both argon and mercury emission lines available.

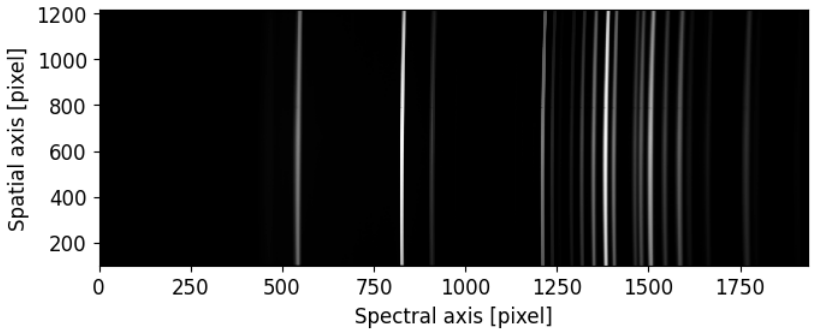

Figure 4.19: Combined calibration image with both argon and mercury emission lines.

The center horizontal line was extracted and used for the analysis to avoid smile effects. For full calibration, the wavelength calibration can be done for each horizontal line as discussed in Section 4.2.1, or smile can be corrected as in Henriksen et al. [138] (**SP 1**) or Riihiaho et al. [147].

Detecting spectral lines

The center line was smoothed, and the spectral peaks detected using Python code and the scipy signal function `find_peaks()`. The detected peaks were manually mapped to the known emission lines of argon and mercury (air wavelengths retrieved from the National Institute of Standards and Technology (NIST) webpages [153, 154]). Doing this manually makes it easy to know which detected lines are double peaks, i.e. two lines so close to each other that they are recorded as a single line within the FWHM of the instrument. Using automated detection and mapping to correct wavelengths is also possible, but it is then important to be certain that the correct wavelengths are being mapped. The detected emission lines are shown in Figure 4.20, and their values in Table 4.2.

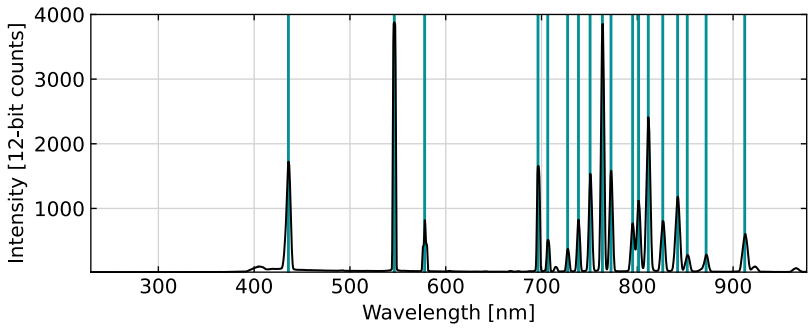

Figure 4.20: Center horizontal line of the combined calibration frame (black spectrum), and the argon and mercury reference wavelengths (blue vertical lines).

It is important to remember that the theoretical FWHM of the HSI is 3.3 nm, while the measured value tends to fall between 3.5 to 4.5 nm for the wavelengths in the desired spectral range [148] (**Paper 2**). This means that emission lines from the calibration lamps that are close to each other (less than 3-4 nm apart) will be seen as one single line by the instrument. The detected emission lines are therefore further divided into sets, also shown in Table 4.2, to investigate the impact of using double peaks and of using only a small selection of emission lines for the calibration. Set 1 contains all the detected wavelengths, set 2 is a subset with the two broadest double peaks removed, set 3 contains only single peaks (except 794.82 nm as this is partly merged with the 800.61/801.48 nm double peak), and set 4 uses only a small selection of the single peaks.

Table 4.2: The argon (Ar) and mercury (Hg) emission lines. The "x" marks emission lines used in each set.

Lamp	Wavelength [nm]	Set 1	Set 2	Set 3	Set 4
Hg	435.83	x	x	x	x
Hg	546.07	x	x	x	
Hg	576.96 / 579.02	x			
Ar	696.54	x	x	x	x
Ar	706.72	x	x	x	
Ar	727.29	x	x	x	
Ar	738.40	x	x	x	
Ar	750.39 / 751.46	x	x		
Ar	763.51	x	x	x	x
Ar	772.37 / 772.42	x	x		
Ar	794.82	x	x		
Ar	800.62 / 801.48	x			
Ar	810.37 / 811.53	x	x		
Ar	826.45	x	x	x	x
Ar	840.81 / 842.46	x	x		
Ar	852.14	x	x	x	x
Hg	871.68	x	x	x	
Ar	912.30	x	x	x	x

Results and discussion

The pixel indices of the detected emission lines form a close to linear relation with the reference wavelengths, as seen in Figure 4.21. This confirms the close to linear relationship that is expected and commonly assumed. There are, however, small deviations from the linear fit, as seen in Figure 4.22.

The deviation between reference wavelengths and estimated wavelengths (as shown for method 1 with $n = 1$ in Figure 4.22) was plotted for the different methods and sets (not shown). For all other methods and sets the highest deviations were found for the shortest wavelengths. Most reference wavelengths are located in the upper part of the spectrum investigated, as seen in Figure 4.20, leaving the lower part of the spectrum thin with measurement points. Lamps providing additional emission lines in the lower part of the spectrum might therefore help to improve the analysis.

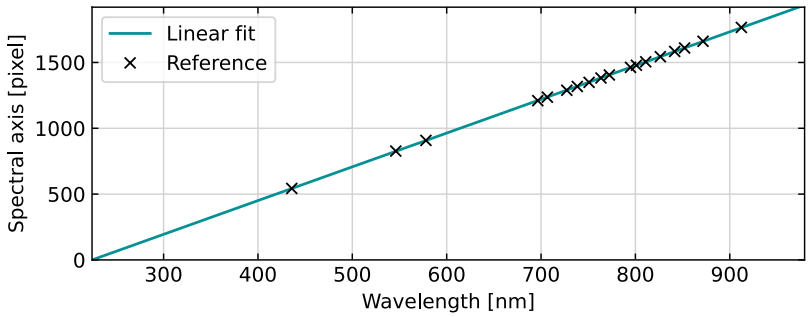

Figure 4.21: Pixel index of the reference wavelengths (crosses) with a linear fit (blue line) showing close to linear relationship between reference wavelength and recorded pixel index.

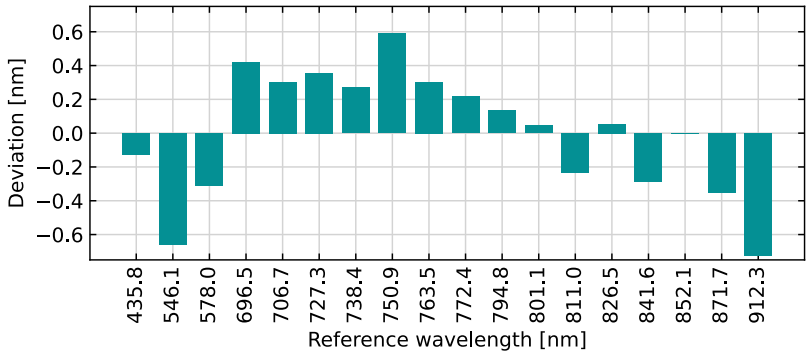

Figure 4.22: Deviation between the reference wavelengths and estimated wavelength of the pixel indices after a linear fit.

The RMSE values for each method with each set are shown in the table shown in Figure 4.23. The values for the curve fits of wavelength via the grating equation (method 4) are shown in cursive as these fits depend heavily on the initial guess values of the coefficients (input parameters to the least squares curve fit function). This is most likely due to few measurement points, as estimating 4-5 coefficients from only 6-18 points gives large uncertainties to the resulting model.

The lowest RMSE values for all sets are found with the curve fit of diffraction angle (method 3). This suggests that including theoretical models such as the grating equation and simple trigonometry can help to explain the pixel to wavelength relationship better than a standard linear fit. The first order polynomial curve fit of wavelength (method 1

Method		Set 1	Set 2	Set 3	Set 4
1	n=1	0.131	0.142	0.155	0.286
	n=2	0.180	0.191	0.231	0.228
	n=3	0.247	0.267	0.233	0.771
2	n=1	0.185	0.201	0.246	0.324
	n=2	0.156	0.168	0.203	0.128
	n=3	0.249	0.269	0.269	0.790
3		0.114	0.125	0.125	0.072
4		0.190	0.218	0.218	1.786
	α=0	0.192	0.209	0.209	0.786

Colours
< 0.1
0.1-0.2
0.2-0.3
0.3-0.5
> 0.5

Figure 4.23: RMSE values for the different methods and sets. n = order of polynomial fit.

with $n = 1$, which corresponds to linear fit) also shows low RMSE values for all sets. This suggests that a linear fit still is a good approximation, even though small deviations can be seen.

For most methods, set 1 has the lowest RMSE values, and the values increase as the number of emission lines in the sets decrease. This suggests that there are too few measurement points (emission lines) to make good fits. The double peaks do not seem to degrade the results, but rather improve the accuracy. This might be different if more points were available.

The RMSE values in Figure 4.23 generally show no clear trends to which method is the better choice, but confirms that the pixel to wavelength relationship is mainly linear and that a linear fit might be sufficient. The low values found with the curve fit of diffraction angle (method 3) shows that there can be a benefit to include theoretical models. More measurement points are needed, however, specially in the lower part of the spectrum (400 to 600 nm), both to improve the methods further and to properly compare the methods and the effect of including double peaks in the analysis.

From this, it is noted that future experiments should include using different calibration techniques or additional spectral lamps to achieve more measurement points across the full spectrum of interest. Different ways of detecting the emission line peaks in the pre-processing should also be tested. Additional experiments using more spectral lamps and improved peak detection was therefore carried out, with the results presented in the next section.

4.4.4 Experiments using a larger selection of spectral lamps

The same HSI V6 was again used together with a larger selection of spectral lamps. The lamps used were argon (Ar), hydrogen (H_2), helium (He), krypton (Kr) spectral lamps from Frederiksen Scientific (models numbers 2850.40, 2850.20, 2850.30 and 2850.60, respectively). The HSI was pointed directly towards the lamp, and kept in the exact same position for every lamp. Exposure times of 10 ms, 20 ms, 50 ms, 100 ms, 200 ms, 500 ms and 1000 nm were used, and 10 images captured at each exposure time which were further averaged before further use. The images captured at different exposure times were combined to an HDR image. Starting with the image captured at the longest exposure time, the overexposed values were masked out. Values from the shorter exposed images were thereby filled in and scaled by the exposure time to create the HDR image.

Only the middle row in the image (center of the slit image) was used to avoid smile effects. The line was normalized by dividing by the maximum value in the line and then smoothed. The normalized peaks are shown in Figure 4.24. It can be seen that the peaks cover most of the spectral range on the sensor, except for the first 500 pixels on the spectral axis. This is due to low QE in the sensor below 400 nm and coating on the lenses blocking light below 400 nm. The first visible peak is at 447.15 nm, while the last peak at the very edge of the spectrogram is at 965.78 nm.

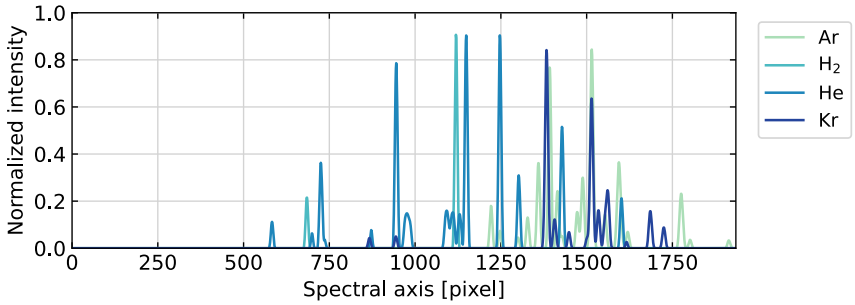

Figure 4.24: The measured line spectra of argon (Ar), hydrogen (H_2), helium (He) and krypton (Kr) spectral lamps.

Detecting spectral lines

The peaks were then first detected using the scipy signal function `find_peaks` in Python. Each peak was then investigated further, by isolating the peak and 4 neighboring pixels on each side. A second order polynomial fit was made to this selection, and the peak

detection (here by finding the maximum value of the peak) repeated on an interpolated line with 100 steps per original pixel, to obtain a subpixel peak position. The detected peaks were then manually mapped to the known emission lines for argon, hydrogen, helium and krypton (air wavelengths retrieved from NIST webpages [153, 155, 156, 157]). Multiple peaks found close to each other were noted down. For strong peaks close together, the average position of the peaks were used.

An overview of the wavelengths and comments about each peak can be found in Table 4.3. The peaks were further divided into sets, also shown in the table. The description of the sets is also summarized in Table 4.4, to provide a quick overview. To easier visualize the location of the peaks in each set, they are also marked as black lines in the spectrum in Figure 4.25. The sets were chosen as follows. Set 1 contains all the detected peaks. Set 2 has the broadest peaks, namely the 801 nm argon peak and 830 nm krypton peak, removed. Set 3 contains none of the broadest peaks or averaged values (as they are averaged due to two/three peaks being very close together), while set 4 has also the peaks with neighboring peaks removed.

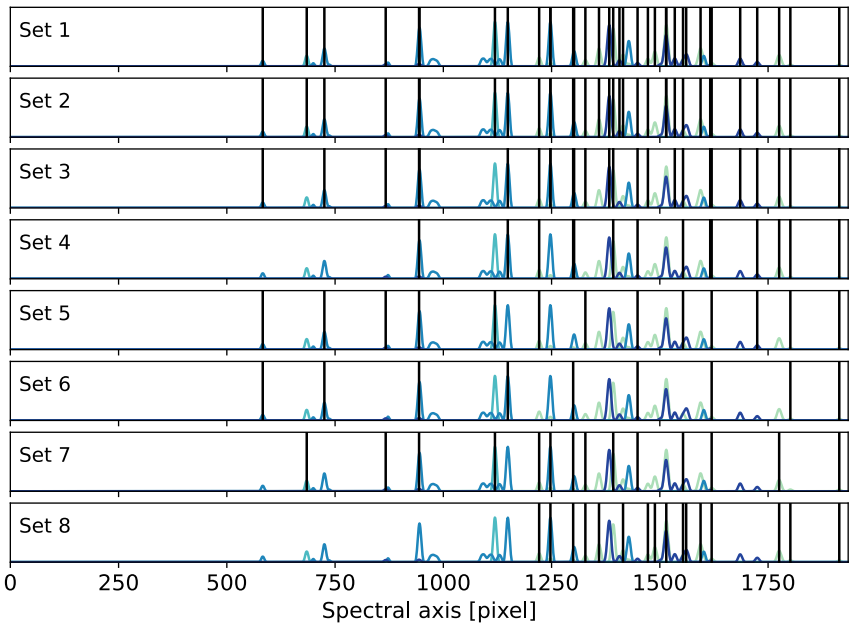

Figure 4.25: Location of the peaks in the spectrogram for each set.

Table 4.3: Overview of the argon (Ar), hydrogen (H_2), helium (He) and krypton (Kr) emission lines divided used, and the sets into which they are divided.

Lamp	Peak [nm]	Set 1	Set 2	Set 3	Set 4	Set 5	Set 6	Set 7	Set 8	Comments
He	447.15	x	x	x		x	x			Weaker peak at 447.19 nm.
H_2	486.13	x	x					x		Average of 486.128, 486.129 and 486.136 nm.
He	501.57	x	x	x		x	x			Small peak on the side.
Kr	557.03	x	x	x		x		x		Weaker peaks at 556.22 and 558.04 nm.
Kr	587.09	x	x	x	x	x	x	x		
He	587.56	x	x	x						Weaker peaks at 587.56 and 587.60 nm.
H_2	656.28	x	x			x		x		Average of 656.271, 656.272 and 656.285 nm.
He	667.82	x	x	x	x		x			
Ar	696.54	x	x	x	x	x		x	x	
He	706.52	x	x	x						Weaker peaks at 706.52 and 706.57 nm.
Ar	706.72	x	x	x				x	x	Weaker peak at 706.87 nm.
Ar	727.29	x	x	x	x		x	x	x	
He	728.14	x	x	x	x					
Ar	738.40	x	x	x		x		x	x	Weaker peaks at 738.04 and 739.30 nm.
Ar	750.93	x	x						x	Average of 750.39 and 751.47 nm.
Kr	760.15	x	x	x						Weaker peaks at 758.74 and 764.12 nm.
Ar	763.51	x	x	x	x			x	x	
Kr	768.99	x	x							Average of 768.52 and 769.45 nm.
Ar	772.40	x	x						x	Average of 772.38 and 772.42 nm. Visible peak on the side.
Kr	785.48	x	x	x	x	x	x	x		
Ar	794.88	x	x	x					x	Visibly part of double peak with 801 nm.
Ar	801.05	x							x	Average of 800.62 and 801.48 nm. Visibly part of double peak with 795 nm.
Kr	810.86	x	x							Average of 810.44 and 811.29 nm. Small peak on the side (at 805.95 nm).
Ar	810.95	x	x						x	Average of 810.37 and 811.53 nm.
Kr	819.01	x	x	x						Weaker peaks at 820.27 and 821.84 nm.
Ar	826.45	x	x	x	x	x		x	x	
Kr	829.81	x								Weaker peaks at 826.32, 827.23 and 828.11 nm. Clear double peak.
Ar	841.64	x	x						x	Average of 840.82 and 842.46 nm.
Kr	850.89	x	x	x	x					
Ar	852.14	x	x	x	x	x	x	x	x	
Kr	877.68	x	x	x						Weaker peak at 876.41 nm.
Kr	882.87	x	x	x	x	x				
Ar	912.30	x	x	x	x			x	x	
Ar	922.45	x	x	x	x	x	x		x	
Ar	965.78	x	x	x	x	x	x	x	x	
		35	33	25	14	13	9	14	16	Total number of peaks used in set

Table 4.4: Summary of the different sets.

Set	Description
Set 1	All peaks
Set 2	Broadest peaks removed
Set 3	Average and broadest peaks removed
Set 4	All peaks with neighboring peaks removed
Set 5	Selection of set 2, evenly distributed
Set 6	Selection of set 5, evenly distributed
Set 7	No helium peaks (selection of other peaks)
Set 8	Only argon lamp (all peaks used)

Set 5 contains a selection of the peaks from set 2, trying to select peaks evenly distributed in the spectrogram. Set 6 does the same using the peaks from set 4, resulting in an even smaller selection evenly distributed. Set 7 does not contain any peaks from the helium lamp, to see the effect of excluding a lamp with peaks in the lower part of the spectrum, while set 8 only contains the peaks from the argon lamp, to see the effect of only using one lamp with peaks concentrated in one part of the spectrum.

A linear fit was applied to all the data points (set 1), and showed a linear fit (not shown here). The deviations from this linear fit, however, can be seen in Figure 4.26. The general trend is negative deviation at the edges and positive deviation in the center, showing hints towards a second order polynomial function. The peaks at the shortest wavelengths, however, does not follow this trend. There does not seem to be any systematic error for any of the lamps.

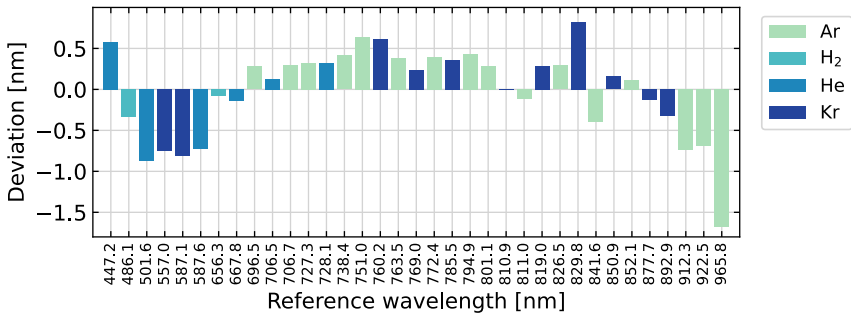

Figure 4.26: Deviations from a linear fit of all detected peaks.

Results and discussion

The RMSE values for each method with each set are shown in a table in Figure 4.27. The colors in the table are used to easier visualize the numbers.

Most noticeable are the many dark green (low) values for set 4, and the dark orange (high) values for method 4 with $\alpha = 0$. The good fit in set 4 can be explained by this set consisting of few (14) and "good" values, as this set contains only peaks that have no close neighboring peaks around. Set 5, 7 and 8 also have few peaks (13, 14 and 16, respectively), but these have higher RMSE values. It was also seen when using the argon and mercury lamp that fewer points gave a worse fit. This suggests that choosing which lines to use based on information about potential neighboring peaks that can introduce uncertainties, and exclude them, can be beneficial. Keeping in mind, however, that one should not use too few lines.

Method 4 has overall the highest RMSE values, and the worst fits are found when there are less points in the set. This indicates that this method is too complex, and not trustworthy with the limited number of measurement points available. The method still depends heavily on the initial guess values, and no attempt was made here to achieve a better fit by tweaking the values. This method will therefore not be in focus for the rest of the discussion.

Method		Set 1	Set 2	Set 3	Set 4	Set 5	Set 6	Set 7	Set 8
1	n=1	0.54	0.53	0.59	0.66	0.70	0.79	0.70	0.42
	n=2	0.52	0.51	0.67	0.15	0.88	1.02	0.61	0.26
	n=3	0.29	0.29	0.34	0.12	0.44	0.44	0.42	0.27
2	n=1	0.58	0.58	0.66	0.11	0.88	1.10	0.50	0.25
	n=2	0.47	0.46	0.60	0.11	0.79	0.92	0.54	0.26
	n=3	0.29	0.29	0.33	0.12	0.43	0.43	0.41	0.27
3		0.38	0.37	0.48	0.07	0.63	0.74	0.40	0.26
4		0.53	0.54	0.58	1.65	0.92	1.40	0.50	0.83
	α=0	1.56	1.55	1.44	1.89	1.66	1.78	2.04	1.74

Colours
< 0.25
0.25-0.5
0.5-0.75
0.75-1
> 1

Figure 4.27: RMSE values for the different methods and sets with peaks from the argon (Ar), hydrogen (H_2), helium (He) and krypton (Kr) spectral lamps.

When looking at set 1 and set 2, it can be seen that the results are quite similar, but that removing the broad peaks as done in set 2 slightly improves the fit for all methods. The worst sets are set 5 and 6, which suggests that trying to distribute the measurement points evenly by excluding potentially good measurements does not help.

Excluding the helium lamp, as done in set 7, does not seem to have any particular effect other than making the fit a bit worse due to less measurement points being included in the fit. Set 8, however, with only points from the argon lamp, shows pretty good results for all methods except method 4. This could either be because there is some difference between the lamps (causing error when using multiple lamps together), or due to the points being focused on only a part of the spectral range, as it only covers the upper part from 697 to 966 nm. When looking at the deviations from a linear fit (Figure 4.26) there does not seem to be any systematic error from the different lamps. Most likely, it is due to the points being grouped in the 700 to 950 nm range that the fit shows good results.

The best methods seem to be method 1 and method 2 (polynomial fits of λ and β), with a third order polynomial fit (n=3). When looking at the deviations from the linear fit in Figure 4.26 this could be due to the dip seen in the lower part of the spectrum. For set 4 and set 8, the lower wavelengths were not included in the analysis, and then the second order fit (n=2) have very similar, and even slightly better, results.

Overall, no clear conclusions can be drawn when it comes to what is the better method. The results hint to more measurement points being better (as expected), and that removing the broadest peaks (or other peaks that should not be trusted) is beneficial. Choosing the best peaks (with no neighbors which introduces uncertainties) gives better results for most methods, but making a selection barely based on an even distribution in the spectrogram does not give better results.

4.4.5 Rerun of analysis with argon and mercury spectral lamps

Some changes were made to the analysis pipeline from the initial experiments with only the argon and mercury lamps:

- 10 images were averaged instead of applying the analysis on each image.
- Images were captured at different exposure times and used to build up an HDR image.
- The lines were normalized by dividing by the maximum value.
- The position of the peaks were detected twice, second time on an interpolated line to provide subpixel peak position.

The analysis was therefore repeated for the argon and mercury lines and sets presented in Table 4.2. The deviations from a linear fit of all the points (set 1) are shown in Figure 4.28. Comparing this to the deviations found previously (Figure 4.22), it can be seen that the wavelengths in the center have similar values, slightly lower in the new analysis, while the wavelengths at the edges have higher deviations. Most noticeable is the peak at 912.3 nm, where the deviation from the linear fit increased from -0.7 to -1. The trend is, however, similar.

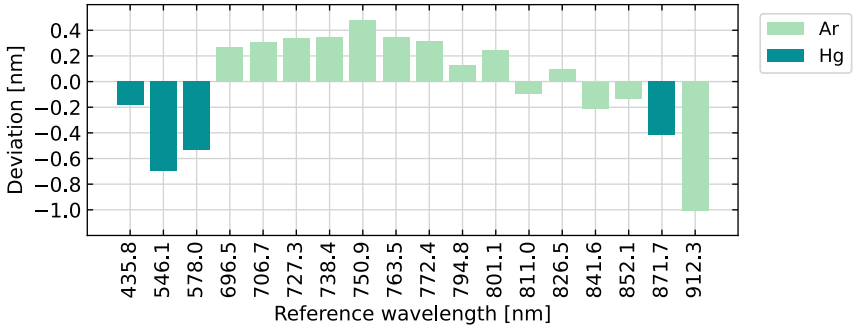

Figure 4.28: Deviations from a linear fit of the detected argon and mercury peaks.

The RMSE results are presented in Figure 4.29. The values themselves are all higher than in the initial experiment, most likely due to the analysis being performed on 1 average image instead of 10 separate images. What will be compared here is therefore the trends, and where the highest and lowest values can be found.

Method		Set 1	Set 2	Set 3	Set 4
1	n=1	0.41	0.43	0.49	0.90
	n=2	0.59	0.57	0.69	1.52
	n=3	0.44	0.49	0.40	0.84
2	n=1	0.58	0.61	0.74	1.05
	n=2	0.51	0.49	0.59	1.22
	n=3	0.43	0.49	0.40	0.83
3		0.36	0.34	0.43	0.59
4		0.55	0.68	0.69	2.98
	α=0	0.82	0.82	3.80	2.43

Colours
< 0.25
0.25-0.5
0.5-0.75
0.75-1
> 1

Figure 4.29: RMSE values for the different methods and sets with peaks from Ar, Hg.

It can be seen that method 4 gives poor results, specially when $\alpha = 0$. Again, this fit depends heavily on the input parameters, and will therefore not be discussed further. In both tables (Figure 4.23 and Figure 4.29) the highest RMSE values are found for set 4, which again suggests that few measurement points results in a poorer fit. The difference between set 1 and set 2, however, is small. If anything, removing the double peaks seems to make the results slightly worse, which coincides with what was seen in the previous analysis.

The best results for set 1, 2 and 3 can again be found with method 3. For method 1, a second order polynomial gives a poorer fit than both first and third order polynomials, which is different than for what was seen in the previous results. For method 2, the best fit is found for the third order polynomial, similar to the results found when using the larger selection of spectral lamps.

The results between the old and new analysis have similar trends. The main difference is that method 4 looks clearly worse with the new analysis, and set 4 performs worse for all methods (also for the methods that gave good results with the previous analysis). It is, however, difficult to make any clear solutions to whether or not the changes in analysis steps matter due to few measurement points that seems to affect the results even more.

4.4.6 Discussions and conclusion

The wavelength to pixel relationship can be hard to model, as aberrations from the lenses and other optical effects may alter the paths of the light rays. Errors from the calibration equipment or from the pre-processing such as the peak detection algorithm may also affect the results. No clear conclusion regarding which method is better to use or which wavelengths should be used is therefore made from these experiments. There are are too many factors in play. However, some observations that should be considered for future experiments and calibration campaigns with these lamps are noted:

- Measurement points at the edges of the spectrogram are desirable, to make sure the fit describes the full spectrum and not just the part where measurements were obtained.
- The points do not need to be evenly distributed over the spectral range.
- Excluding double peaks or other peaks where the exact wavelength is not known is a good idea, as long as enough measurement points are available.

Regarding which method to use, there is no clear winner. However, the method should not be too complex (such as method 4). A polynomial fit of both first, second and third order can be used, but the accuracy of the fit should be investigated. The same holds if using method 3, which also showed promising results.

The deviations from a linear fit for both the argon and mercury set, and the set with argon, hydrogen, helium and krypton, is shown again in Figure 4.30, with the x-axis showing the wavelengths in true scale. The y-axis also uses the same scale here. This makes it easier to visually compare if the deviations are similar or not. It can be seen that the same trend is visible in both sets. The only outlier seems to be the 447 nm helium line in Figure 4.30b, which is positive, while the deviation for the 435 nm mercury line in Figure 4.30a is negative. Both plots show that the deviations from a linear fit seems to look like a sinusoidal function, and the shape visible in the spectral range explains why a third order polynomial fit may cause a good fit. Overall, the response of the instrument

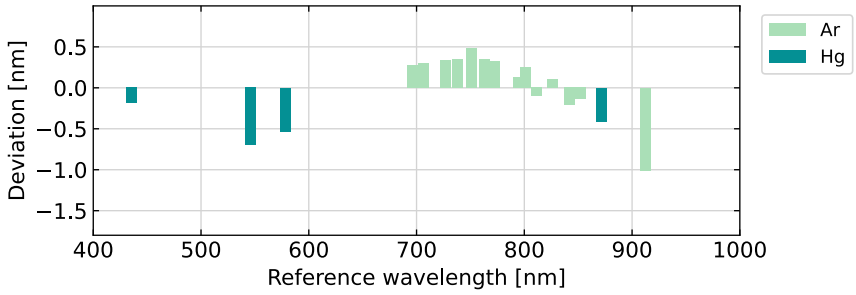

(a) Argon (Ar) and mercury (Hg) spectral lamps.

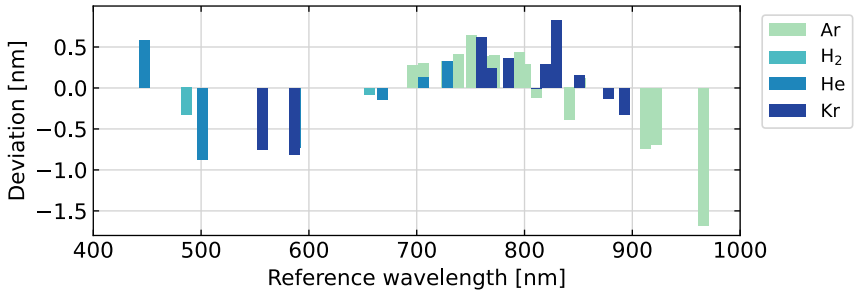

(b) Argon (Ar), hydrogen (H_2), helium (He) and krypton (Kr) spectral lamps.

Figure 4.30: Deviations from linear fits, scaled with correct distance between the peaks on x-axis in terms of wavelength.

should be investigated so that the results from the calibration can be explained. If the deviations from a linear fit are close to zero for all wavelengths, a linear fit should be sufficient to explain the wavelength to pixel relationship.

When using leave-one-out cross-validation and RMSE to evaluate the different methods, the wavelengths tested against the fit are limited to the ones used in that set. This means that for a set using only wavelengths in one part of the spectrum (such as when using only the argon lines), only wavelengths in this part of the spectrum are tested to evaluate the fit. This may give a false indication of a good fit, when in reality the fit in a different part of the spectral range could have huge deviations. A better way to fairly evaluate the methods for each set should therefore be developed, to make sure that the full spectral range is used to evaluate the fit.

For further investigations, even more measurement points in the full spectral range (here especially wavelengths between 400 and 600 nm, and below 400 nm too if possible) should be included. Instead of excluding peaks that have neighboring peaks or trying to evenly distribute measurements over the spectrum, weighting of the peaks could be applied. Trustworthy peaks with no neighbors could be weighted higher than double peaks, and thereby contribute more to the fit. The effect of applying such weighting could be investigated, and could be beneficial when having fewer measurement points available. It could also be worth trying to improve the peak detection even further. A Gaussian fit could be made to each line, as in Mao et al. [158], and the peak decided from this Gaussian fit instead. This would lead to less error from imperfect peaks.

5 | Second order diffraction effects

The full spectral range of both the HSI V4 and the HSI V6 is from about 250 nm to 1000 nm. Due to coating on the objectives and low QE in the detector and grating for shorter wavelengths there is very little signal reaching the sensor below 400 nm, and no signal below 380 nm. This is confirmed by the recorded spectra in Figure 4.11.

Due to the grating theory, second order diffraction effects appear for the longer wavelengths. For a diffraction grating, the relationship between the overlapping orders of light is linear and follows the relation

$$\lambda_k = \frac{(k+1)\lambda_{k+1}}{k}, \tag{5.1}$$

where k denotes the order of the diffracted light so that λ_k is a wavelength at one order lower than λ_{k+1} that reach the same area on the detector [159]. Second order diffraction effects from the wavelengths at 380 nm and up are therefore expected to appear from about 760-800 nm and upwards in both the HSI V4 and the HSI V6.

It is desired to develop a method to remove the second order light present in the upper part of the spectrum so that these wavelengths can be used, thereby expanding the usable range of the instrument. Since wavelengths between 700 nm and 1000 nm are typically used for atmospheric correction purposes, as mentioned in Section 2.1.5, it would be especially useful for the HSI V4 and HSI V6 to be able to use the 800 nm to 1000 nm range that is already recorded by the sensor. To do this, however, second order corrections must be applied.

This chapter is based on **Paper 10**: "Comparing filters for correction of second order diffraction effects in hyperspectral imagers" [149], and parts of **Paper 1**: "A do-it-yourself VIS/NIR pushbroom hyperspectral imager with C-mount optics" [35]. Further, additional experiments were set up at UNIS during a research stay in the fall of 2021 to investigate and compare the filter method with monochromator measurements. The measurements and results from these experiments are also presented here.

5.1 Methods to measure and remove second order light

There are several methods that can be used to measure and remove (or correct for) second order light contributions. Among them are using filters, a monochromator and different targets with real life data. The methods investigated in this chapter are mainly based on the two first, with filter measurements and a monochromator set-up. First, however, some background on all the three different methods is given here.

5.1.1 Filters

One way to measure second order light is by using filters as presented in Stanishev et al. [159] and Lee et al. [160]. The relationship between the first and second orders of the light is found by comparing measurements acquired with and without a filter. This is further used for correction by simply subtracting the estimated amount of second order light from the longer wavelengths based on the amount of incoming first order light.

Estimating the second order contributions using only the intensity differences as done with these filter measurements makes the correction sensitive to the incoming light spectral signature. For the second order diffractions the light spreads out, which both decreases the intensity (peak height) and increases the FWHM (peak width). A significant change in the incoming spectrum will therefore result in a less accurate correction since the signal from neighboring wavelengths changes, which is not captured by the filter measurements.

5.1.2 Monochromator

A monochromator can be used to capture the changes in both intensity and FWHM for several wavelength positions, thereby avoiding the weakness of the filter method. Interpolation can then be used to create a more extensive model of the instrument, as presented in Bruchkouskaya et al. [161]. For each wavelength, both the first and second order of the light emitted from the monochromator are recorded, providing detailed input for this model. This does, however, require a more complex set-up than only using the filters. The acquired data also depends on the efficiency of the optical components in both the monochromator set-up and the instrument, the width of the slits and the light source, and it is important to distinguish effects coming from the measurement set-up itself from the effects coming from the instrument that is being tested.

With a monochromator set-up, a full spectral stray light correction of the instrument can further be achieved, as presented in Zong et al. [116]. Their method allows for not only the undesired second orders of light to be observed, but also other effects or artifacts from scattering, ghosts or other stray light mechanisms. A monochromatic laser source is used to characterize the instrument response for the full spectral range, and this is further used to derive a spectral stray light correction matrix, which in turn is used for the correction.

5.1.3 In-flight data

An empirical method for second order correction for HICO was presented in Li et al. [65]. Instead of using laboratory data, in-flight ocean data with underwater features such as coral reefs was used to characterize the amount of second order light in the data. Since solar radiation at longer wavelengths (800 nm and above) are absorbed by the water, coral reef features present at the longer wavelengths are from second order light. This was used to quantify the second order effects and correct the data during flight. This method

is hard to test in the lab as it uses in-flight data. Using parts of the dataset to characterize the second order effects makes the differences in incoming light for characterization and correction much smaller. However, it requires either a fitting scene (dark ocean) in the image, or an image captured in similar conditions with similar parameters, which puts some constraints on the usability on this method.

A similar method, combining the in-flight and filter method, is using different reflectance standards on ground, as done in Xu et al. [162]. Here, a compensation model to correct a UV-VIS instrument is presented using different colored tiles (UV included and UV excluded standards) to predict the relationship between the first and second order signals. The second order light in the other datasets are then corrected based on the amount of incoming first order light, as for the filter method. Using these standards gives a more controlled set-up than using the filters with the Sun as light source, but the weakness of dependence on incoming light is still present.

5.2 Filter method

To measure second order light with filters, the filter method from Section 5.1.1 was used as a baseline. Cut-off filters were used to estimate the relationship between the first and second order light, mainly focusing on the spectral range between 380 nm to 1000 nm, as this is where light is recorded in the HSI V4 and HSI V6.

5.2.1 Measurements

Longpass (LP) filters which block out the first order light below 500 nm (and therefore contains no second order light below 1000 nm) were used together with data obtained without filters to estimate the amount of second order light. In addition, shortpass (SP) filters, which block out the first order light above 750 nm (and therefore records only the second order light above 750 nm directly) were also used for additional measurements and to compare the use of the different filters.

The method was tested both in front of the integrating sphere in the calibration lab at NTNU (Figure 5.1b) with its stable lamp as light source, and with pointing the HSI out the window towards the sky on a cloudy and a sunny day (Figure 5.1c). Using the Sun as a light source in the measurements could be beneficial since the filter method can be sensitive to changes in spectra when applying the corrections on real data.

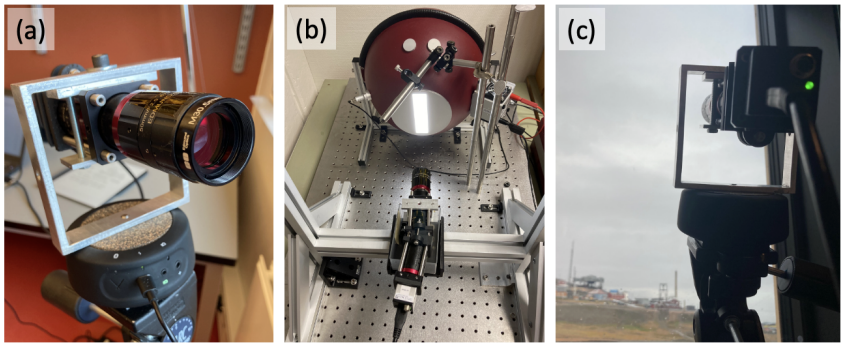

Figure 5.1: Set-up when capturing data with filters. (a) Filter mounted on the HSI front lens. (b) Measurements taken in front of the integrating sphere. (c) HSI pointing towards the sky out the window (set-up was also repeated on a sunny day with blue skies).

Two LP filters with cut-off wavelength at 500 nm (EO #15-224) and 525 nm (EO #64-626) and two SP filters with cut-off wavelength 700 nm (EO #15-261) and 750 nm (EO #15-262) were used. The filter curves from these filters are shown in Figure 5.2a. It can be seen that the curves are not perfect step responses which would have been ideal, but are slightly curved. In addition, the amount of light transmitted varies a bit with wavelength. The latter will be corrected here by dividing the acquired response by the filter curve, as described later. It can also be noted that the 700 nm SP filter does not block all light above 930 nm, which should be kept in mind if using these wavelengths with this filter.

A set of images were captured with the HSI V6 with each of the filters attached onto the front lens in turn (Figure 5.1a). Between each filter measurement, a measurement with no filter was also acquired. The no filter data was also captured to monitor the fluctuation of the light level. An overview of the data is given in Table 5.1. An extra dataset was also acquired for the purpose of testing the corrections on an independent dataset, and is used in the later chapters. For each dataset, 10 images were taken and averaged to reduce noise. Further, only the center line (center of the slit image) was investigated to avoid smile effects.

The measurements in front of the integrating sphere were first used to measure the true filter efficiencies, since the reference transmission plots (Figure 5.2a) are only for the general filter type and not specific for each and every produced filter. The filter efficiency curves were calculated using the recorded signal with the filter divided by the no filter data. The resulting plots are shown in Figure 5.2b. Overall they are similar to the reference curves, but there are some small shifts, differences in the intensity of the

Table 5.1: Filter data for measuring second order light. Data without filter was acquired before, between and after each filter measurement. Data with filter means one filter attached at the time, with filters: LP 500 nm, LP 525 nm, SP 700 nm, SP 750 nm.

Set	Light source	Description
1	Integrating sphere	No filter (5 datasets), with filter (4 datasets)
2	Cloudy sky	No filter (5 datasets), with filter (4 datasets)
3	Sunny sky	No filter (5 datasets), with filter (4 datasets)
4	Test data (cloudy sky)	No filter (5 datasets), with filter (4 datasets)

wobbles, and noisy data below 400 nm and above 800 nm (as expected for the HSI V6). The calculated filter efficiency curves were therefore modified to remove the noise, as seen in Figure 5.2c, which are the curves that are used further in these experiments. It should be noted that in the filter efficiencies used, the peak at 930 nm for the SP 700 nm filter was also not included.

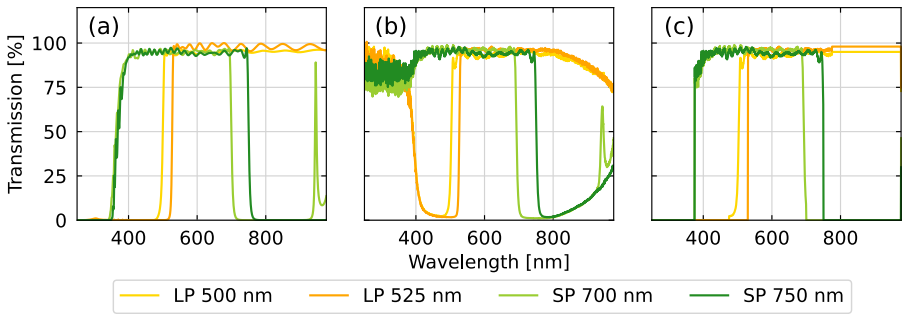

Figure 5.2: Filter transmission curves for the longpass (LP) and shortpass (SP) filters. (a) Reference values from EO, (b) measured filter efficiencies, (c) measured filter efficiencies with noisy data modified.

The fluctuations in the light level between each measurement was then investigated by plotting the datasets without filters, as shown in Figure 5.3. It can be seen that the integrating sphere and the blue sky are both very stable, while the light varies significantly with the cloudy sky. It can also be seen that the light sources are slightly different. The peak of the integrating sphere spectrum is around 600 nm, while the Sun spectrum peaks around 500 nm. The data captured out the window also contains Fraunhofer lines and absorption lines from the atmosphere, while the integrating sphere spectrum is very smooth.

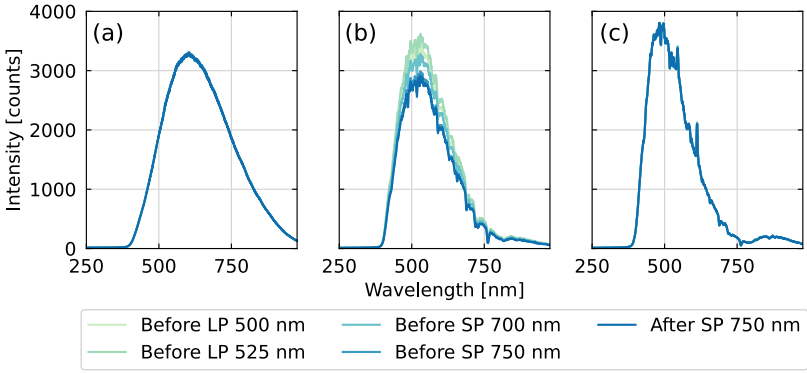

Figure 5.3: Measurements without filter, to observe variations in the light level. (a) Radiometric calibration source, (b) cloudy sky, (c) blue sky.

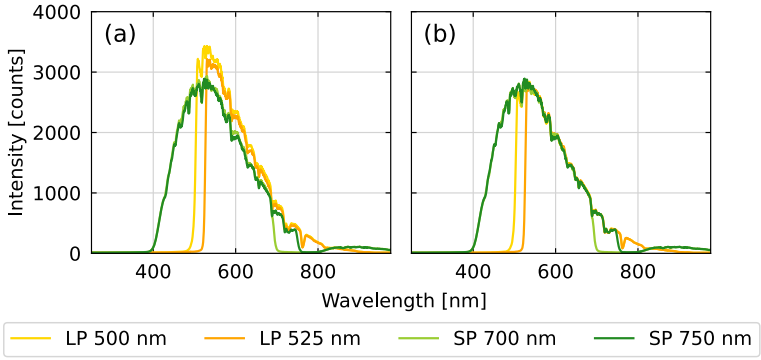

Figure 5.4: Finding the scale factor for cloud measurements. (a) Original data captured with each filter, (b) data with scaling factors (0.83 for the SP 500 nm filter, 0.87 for the SP 525 nm filter, 0.98 for the LP 700 nm filter and 1 for the LP 750 nm filter) applied.

The images captured with filters were normalized by dividing by the corresponding filter efficiency curves (Figure 5.2). For the SP filters, data above the cut-off wavelength was kept untouched, as this signal is from the second order effects that are being investigated. To adjust for the varying signal strength in the cloud measurements, a scaling factor was found manually for each cloud measurement. These were found to be 0.83 for the SP 500 nm filter, 0.87 for the SP 525 nm filter, 0.98 for the LP 700 nm filter and 1 for the LP 750 nm filter. The original and corrected cloud measurements are shown in Figure 5.4, and it can be seen that they follow each other nicely as expected after scaling.

The normalized data from all three sets are shown in Figure 5.5. It can be seen that the filter data mostly follows the no filter lines, with some exceptions. The most noticeable and interesting area is above 750 nm, where the signals start to disperse. For the LP filters, since no light below the cut-off wavelengths enters the instrument, no second order effects can be seen, and there is little to no signal above 800 nm. For the SP filters, on the other hand, ideally there should be zero signal above their cut-off wavelengths. But since the shorter wavelengths (400 nm to 500 nm) enter the instrument, the second order light of these wavelengths becomes visible on the sensor above 800 nm.

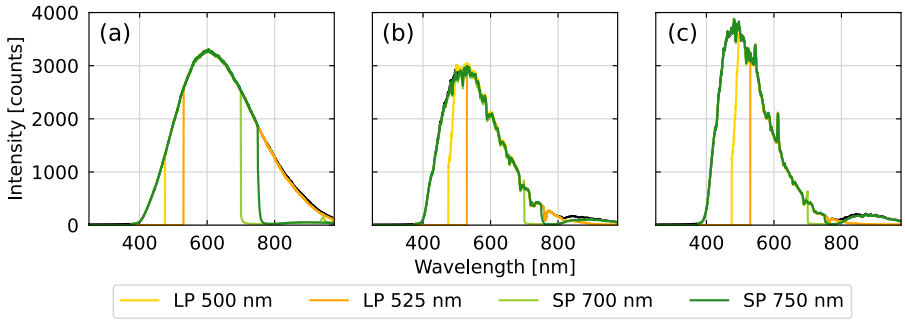

Figure 5.5: The normalized datasets. (a) Radiometric calibration source, (b) cloudy sky (scaled), (c) blue sky.

Using the two different types of filters gives, as mentioned, two independent ways of measuring the same second order light. With the LP filters the second order light can be estimated by subtracting the first order light from the total signal (first and second order together which is present in the no filter data), while with the SP filters the second order light is measured directly. A zoomed in view of the estimated second order light from the different filters is shown in Figure 5.6. For the radiometric calibration source data (Figure 5.5a) very little second order light in the 800 to 900 nm range is present due to little light below 450 nm from the calibration source. The second order light found here, specially with the LP filters, is therefore very noisy. The peak from the SP 700 nm filter efficiency curve is also visible here due to strong intensity in the radiometric source at longer wavelengths. This suggests that this filter should not be used when measuring the second order effects above 930 nm. For the cloudy and sunny sky data, however, the second order light measured by the SP filters and estimated with the LP filters coincides nicely. It can also be noted that the LP data has lower and more noisy signal below 800 nm than the SP filter data.

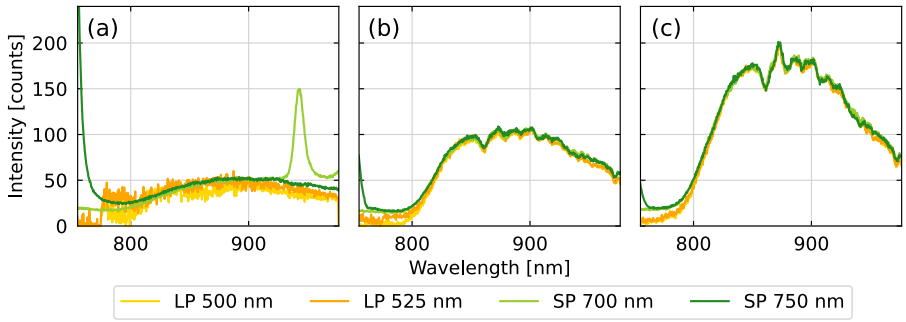

Figure 5.6: Measured and estimated second order light. (a) Radiometric calibration source, (b) cloudy sky, (c) blue sky.

From these results, the SP filters seems to measure the second order light with less noise. The SP filters also measures it directly instead of being dependent on a second measurement with no filter attached as the LP filters do. It is, however, important that the filters block all light of the longer wavelengths, so that the results are not affected by artifacts such as the peak at 930 nm for the SP 700 nm filter. It is also beneficial to use the Sun as a light source over the radiometric calibration source used here, as it provides more light with shorter wavelengths which again gives more second order light, so that the SNR of the second order light is higher when using these signals for further analysis and corrections.

5.2.2 Second order efficiency

To use the filter measurements for correction, the second order light efficiency, A_λ, was first calculated. This describes the amount of second order light that is produced by the different first order wavelengths, and is calculated as

$$A_\lambda = \frac{C_{\lambda\,\text{(second order)}}}{C_{\lambda/2\,\text{(first order)}}}, \tag{5.2}$$

where $C_{\lambda\,\text{(second order)}}$ is the second order signal appearing at a given wavelength λ, while $C_{\lambda/2\,\text{(first order)}}$ is the first order signal of the same wavelength.

The calculated second order light efficiency for all three data sets with all four filters are shown in Figure 5.7. It can be seen that the LP data is generally noisier than data from the SP filter, especially below 800 nm. This is as expected when looking at the second

order light in Figure 5.6, as they have lower intensities below 800 nm. It can also be seen that the estimated second order efficiency diverges below approximately 810 nm. This is mostly due to the first order signal from around 400 nm having very low signal strength with relatively high levels of noise. The results in this region are therefore expected to be less accurate. Above 850 nm, however, the curves have similar values both across filter types and light source, suggesting that these values are more reliable. Again, it can be noted that the peak from the SP 700 nm filter is visible in the radiometric calibration source plot, which is an artifact of the filter and not the correct second order efficiency. The curves were then smoothed by a Bartlett window to reduce noise before they were used further for corrections.

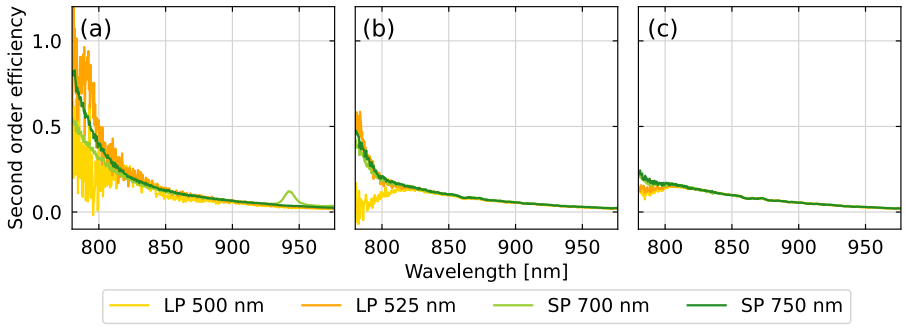

Figure 5.7: Estimated second order efficiency. (a) Radiometric calibration source, (b) cloudy sky, (c) blue sky.

5.2.3 Correction with second order efficiency

Correction can then be done by applying

$$C_{\lambda,\,\mathrm{corr}} = C_{\lambda} - C_{\lambda/2} A_{\lambda}, \tag{5.3}$$

where $C_{\lambda,\,\mathrm{corr}}$ is the corrected signal at wavelength λ (for example at 800 nm, without any second order light present), C_{λ} represents the number of measured counts at wavelength λ (the signal recorded at 800 nm before correction), $C_{\lambda/2}$ is the number of measured counts at wavelength $\lambda/2$ where the second order light originates from (the measured light at 400 nm), and A_{λ} is the calculated efficiency describing the amount of generated second order effects expected to occur at wavelength λ based on the amount of signal at wavelength $\lambda/2$.

An example of how the correction works on the test data is shown in Figure 5.8 (corrected with the second order efficiency from the sunny sky dataset with the SP 750 filter). Filter data (using the LP 500 nm filter) from the test dataset is also shown for reference. The goal is that the corrected signal follows the original signal until the second order effects appear, and then follows the filter data where the second order effects are filtered out. The figure shows that the corrected signal behaves as expected.

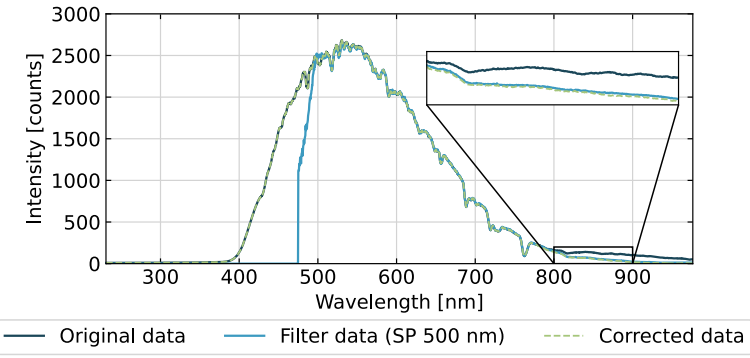

Figure 5.8: Example of second order correction by filter (here using the SP 750 nm filter). Additional filter data is shown as reference of data without second order light. Zoomed in inlet shows that the corrected signal (dashed) follows the reference signal nicely.

The correction applied to the same test dataset using all the calculated second order light efficiencies (four filters, three light sources) are shown in Figure 5.9. It can be seen that the correction based on the radiometric calibration dataset performs worst, as the corrected signals deviate from the reference filter data. This is most likely due to the low amounts of second order light in the original dataset, with high levels of noise, resulting in a poorer estimate of the second order efficiency. And again, the peak from the SP 700 nm filter can be seen, this time as a dip at 930 nm after the correction with values close to negative 150 counts. This shows that filter artifacts can greatly disturb the correction, and filters with such peaks and dips in their transmission curves should not be used. The corrections based on the datasets when observing the sky, however, shows better performance. They both estimate a bit too much second order light, resulting in slightly lower signal after correction than what the reference filter data shows. The cloudy sky dataset gives on average a signal that is 14% below the reference, while the blue sky data is on average 11% below. Even though the test dataset is also looking at a cloudy sky, the correction based on the blue sky datasets performs better, suggesting that a stable light source is beneficial when collecting the filter data measurements.

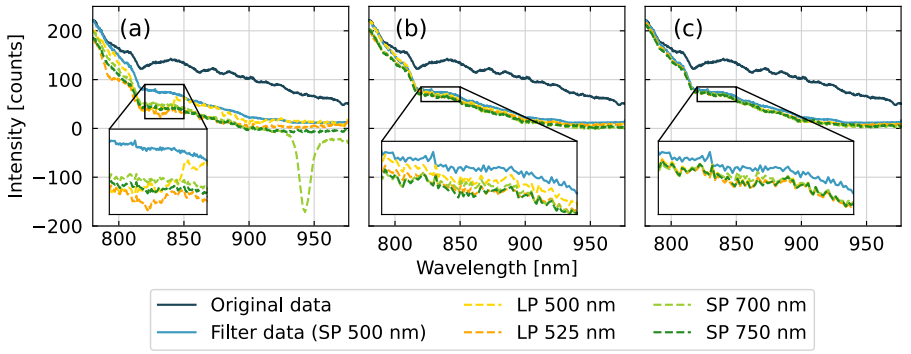

Figure 5.9: Second order correction applied to the test data, using the second order efficiency calculated by all four filters with all three light sources. (a) Radiometric calibration source, (b) cloudy sky, (c) blue sky.

5.3 Monochromator method

Measurements of second order light with a monochromator, following the outline presented in Section 5.1.2, were also conducted. The monochromator set-up itself is described in Section 4.1.2, and in greater detail in publications by Sigernes et al. [143, 144]. In this section, only the second order light measurements and results are presented.

5.3.1 Measurements

Again, the HSI V6 was used for the experiments. The HSI was placed in front of the monochromator, as seen in Figure 5.10. Images were then captured with light in the range of 390 nm to 495 nm with 5 nm steps on the output of the monochromator. However, due to noisy data, only the measurement points from 400 nm to 485 nm were further used.

It should be noted that this monochromator set-up was initially built for very sensitive aurora instruments, and therefore has very low output light intensity. To compensate for this, high exposure times (4 seconds, which was the upper limit of the HSI V6 capture software at the time of the experiment) and gain were used when collecting the data. The background noise level and hot pixels that occurred (as more of these occur with longer exposure times and higher gain) was estimated with separate dark datasets, and removed from the collected datasets.

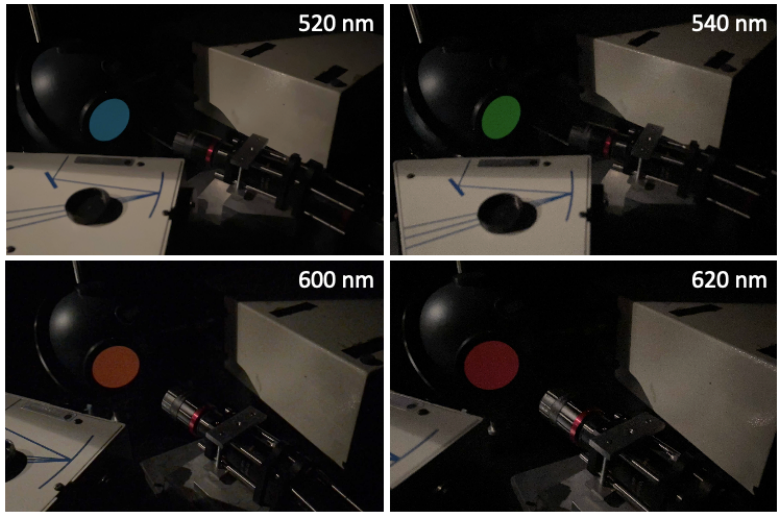

Figure 5.10: The HSI V6 in front of the monochromator set-up set at 520 nm, 540 nm, 600 nm and 620 nm, showing different colors on the output light.

The gain was compensated for by the use of a gain factor function estimated from a radiometric calibration dataset captured with different gain settings. The compensation was found to be

$$C_{\text{no gain}} = \frac{C_{\text{with gain}}}{10^{\frac{0.275 \cdot G}{20}}}, \tag{5.4}$$

where $C_{\text{with gain}}$ is the signal captured with a gain factor G, $C_{\text{no gain}}$ is the corresponding signal with no gain, and 0.275 is the factor found for the relation between gain in [dB] to gain setting in the range of 0-100 relation used in the software.

The data was also normalized before use, as scaling the dataset does not affect the ratio between the first and second order light in the same signal. The final dataset is shown in Figure 5.11. It can be seen that the shorter wavelengths, such as 400 nm, has higher noise levels, which is as expected since the signal before normalization is also lower at these wavelengths. The second order peaks also clearly show up in the dataset, and are decreasing with longer wavelengths.

5.3.2 Second order efficiency

The data collected with the monochromator was further used to calculate the second order efficiency as described in Equation (5.2), as done for the filter data in Section 5.2.2.

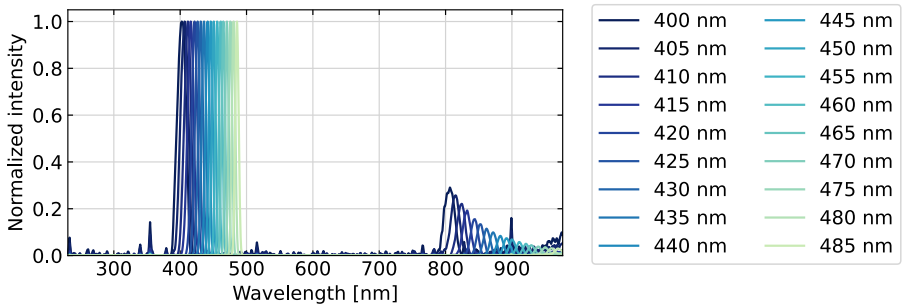

Figure 5.11: Data collected with monochromator set-up in the 400 nm to 485 nm range with 5 nm steps, after noise level and hot pixel correction, gain compensation and normalization.

The efficiency was calculated for the detected peaks (crosses), and a third order polynomial fit (green line) was made to the data points, as shown in Figure 5.12. It can be seen that the calculated efficiency is slightly higher than for the filters for all wavelengths above 825 nm. Below 825 nm the filter curves varies quite a lot, and the estimated monochromater line looks like a reasonable line in between the filter measurements.

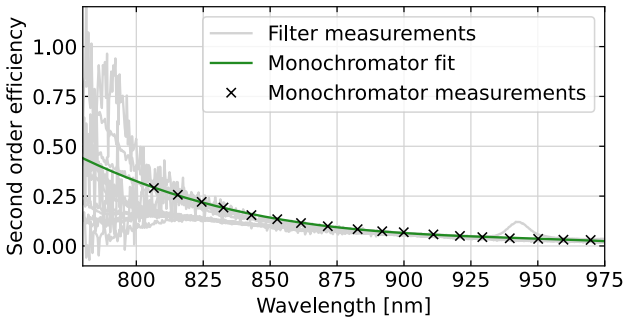

Figure 5.12: Second order efficiency from monochromator data (green) compared to those calculated from filter data (gray).

5.3.3 Correction with second order efficiency

The correction in Equation (5.3) was applied to the test dataset. The resulting corrected signal is shown in Figure 5.13, together with the corrected lines from the filter data (Figure 5.9) for comparison. It can be seen that the correction based on the monochromator data overestimates the amounts of second order light, so that the corrected signal is significantly lower than it should be when comparing with the

reference filter data where the second order light has been filtered out. This could be due to the light source in the monochromator having a different spectrum than the sky, as the results are similar to what was seen when using the radiometric calibration source in the filter measurements.

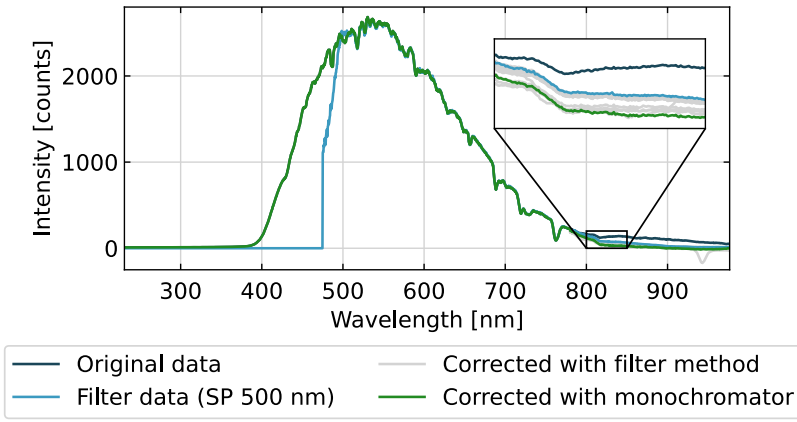

Figure 5.13: Correction with second order efficiency calculated from monochromator data (green) compared to the filter method (gray).

5.3.4 Spectral stray light matrix (Zong method)

The monochromator dataset was then used to calculate the spectral stray light matrix from Zong et al. [116], as described in Section 5.1.2. The method, sometimes referred to as the Zong method in the literature, is based on using LSFs obtained from the monochromator dataset to calculate a Spectral Stray Light Signal Distribution Function (SDF) matrix, **D**, which is further used to calculate a correction matrix, **C**, that can be applied to the dataset by simple matrix multiplication.

First, the In-Band (IB) region (the first order peak response as defined in Zong et al. [116]) was isolated for each LSF. The sum of the IB region was then used to normalize the LSF, and the values in the IB region set to zero to obtain the SDF. Since the monochromator dataset contained some noise, the second order region was also isolated and the values outside this region set to zero here. This compromises the SDF to some extent, as some spectral stray light might also be removed from the SDF, and thereby not be corrected for at a later stage. For the second order correction purposes, however, this was seen as an acceptable trade-off to reduce the amounts of noise in the collected data.

From the measured LSFs, a model describing the second order peak as a Gaussian distribution with a given position, height and width of the peak based on the first order peak was made. This was further used to estimate the SDF for each wavelength (pixel) in the HSI spectrogram line. The measured LSFs and the Guassian fits are shown in Figure 5.14. The SDFs were then all combined to one SDF matrix, **D**, with one SDF (for each pixel in a row of the spectrogram) on each row in the matrix.

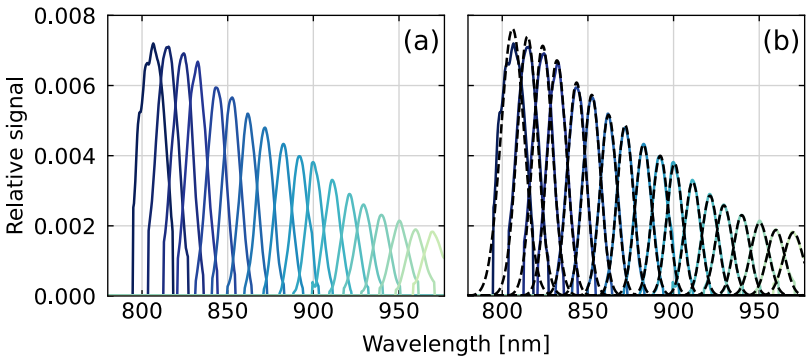

Figure 5.14: (a) Measured LSFs, (b) Gaussian fit (black dashed line) to the measured LSFs.

5.3.5 Correction with spectral stray light matrix (Zong method)

Following the steps from Zong et al. [116], the correction matrix was then calculated as

$$\mathbf{Corr} = (\mathbf{I} + \mathbf{D})^{-1}, \tag{5.5}$$

where **I** is the identity matrix. The correction matrix can then be used to correct for spectral stray light, or like here mainly second order effects, by simple matrix multiplication

$$S_{\text{corrected}} = \mathbf{Corr} \cdot S_{\text{measured}}, \tag{5.6}$$

where S_{measured} is a measured line in the image (since only the middle line is used here), and $S_{\text{corrected}}$ is the corrected line. The extend this correction to the full spectrogram, an SDF matrix and correction matrix should be made for each line to account for differences in the spectral stray light response and smile effects.

The correction was then tested on the test data, and compared to that of the filter method and monochromator second order efficiency correction in Figure 5.15. It can be seen that the correction performs well for the wavelengths up to 850 nm, even better than all filters

from the filter method. Above 900 nm however, the amounts of second order light is overestimated, and the corrected signal far below the measured reference signal (filter data from the SP 500 nm filter in the figure). In Figure 5.14 it can be seen that the relative signal of the longer wavelengths (900 nm and above) are low. The correct height of these peaks (which affects the correction) could be affected by the noisy data and therefore be slightly erroneous, causing a poorer correction. A monochromator dataset with a stronger signal should be tested to improve the quality of the data, which might further improve the quality the correction. The method does, however, seem promising based on the results shown here.

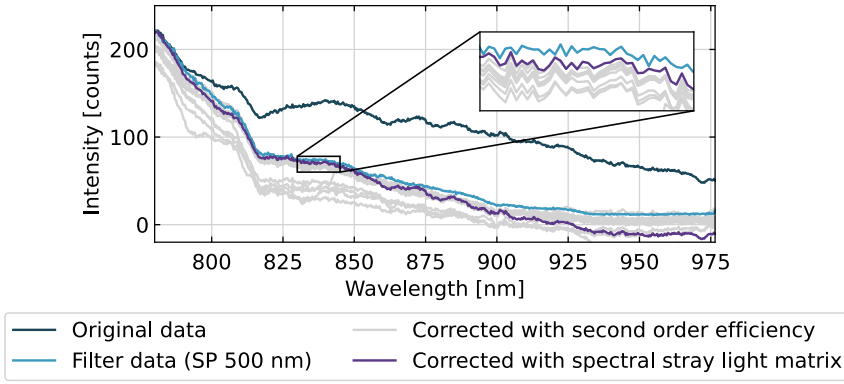

Figure 5.15: Correction with spectral stray light matrix (Zong method) calculated from monochromator data (purple) compared to correction with second order efficiency calculated from filter and monochromator data (gray).

5.4 Visual example of second order light correction

A visual example of second order light and correction in the HSI V6 data is shown in Figure 5.16, which shows parts of a hyperspectral datacube of Adventdalen recorded on 09-09-2019. Figure 5.16b shows a "normal" RGB image made using the wavelengths 660 nm, 540 nm and 480 nm as red, green and blue channels, and Figure 5.16a shows a reference image taken simultaneously with a mobile phone. Figure 5.16c shows an RGB image using a red channel closer to NIR, of 780 nm which results in a more teal-looking image. This is as expected since the snow and sky reflects less light closer to NIR, contributing to less light in the red channel. The vegetation in the mountainside and on the ground appears red since vegetation reflects light at NIR wavelengths, thereby contributing to more signal in the red channel.

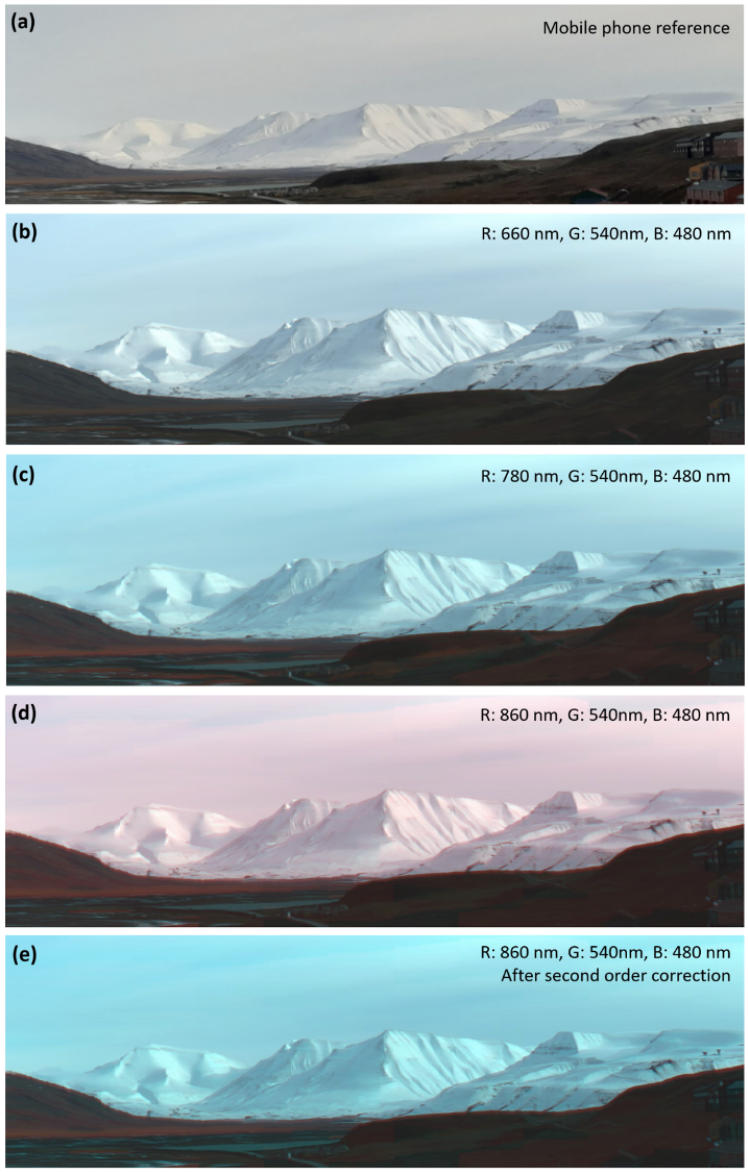

Figure 5.16: Adventdalen, 09-09-2019. (a) Mobile phone image, for reference. (b)-(e) RGB images generated from the hyperspectral datacube using the wavelengths (b) 660 nm, 540 nm and 480 nm, (c) 780 nm, 540 nm and 480 nm, (d) 860 nm, 540 nm and 480 nm, (e) 860 nm, 540 nm and 480 nm after second order correction. Data from Hazendonk et al. [139].

When changing the red component to a wavelength above 800 nm, however, second order effects become apparent, as seen in Figure 5.16d where the red channel is set to 860 nm. Red color from the vegetation on ground is expected, but the pink hue seen in the sky and on the snowy mountains are not since the signal should be lower at 860 nm than for 780 nm, thereby creating an even more teal color than in Figure 5.16c. The extra signal in the 860 nm channel is due to the second order light.

The second order light was corrected by the filter method, using a cut-off filter with zero transmission below 575 nm. The second order corrected image is shown in Figure 5.16e. The color of the sky has changed from pink to teal, which is the expected outcome of the correction. The vegetation on ground is still visible with red color, which is also as expected. The corrected image looks similar to the RGB image created using 780 nm in Figure 5.16c, but has slightly more teal color which is reasonable as they are both in the NIR range. As long as it is kept in mind which colors to expect in the images (such as more teal color when changing the red channel to a longer wavelengths), Figure 5.16 gives a nice visual view on how the correction affects the data.

5.5 Future work and recommendations

These experiments have given some insight in how second order light can be measured and corrected. However, the different methods should be further tested and the errors and uncertainties related to the corrections better estimated before further use.

For the filter method, LP filters seem easier to use as they measure the second order light directly, while SP filters are useful for validation of the correction as the first order light is measured directly with these filters. The filter efficiencies should be measured with a stable light source, such as a calibration lamp, before use. The filter efficiency should also not contain any sharp artifacts that might disturb the correction (such as the peak in transmission in the SP 700 nm filter at 930 nm). The light used for the filter measurements should be stable in intensity (such as for the blue skies compared to the cloudy skies) if second order effects are estimated from SP filters. For LP filters, however, this is not as important since the second order light is measured directly. Finally, it seems beneficial to use a light source with a similar spectrum to what will be used during in-flight measurements, such as the Sun directly or a solar simulator.

For future monochromator measurements, a monochromator with stronger output light should be used. The HSI (or other instrument used for measurements) should use the

same settings (such as exposure time and gain) for all measurements, and preferably use short exposure time and low gain values to minimize noise. In Zong et al. [118] it was suggested to use an instrument with at least 15-bit resolution. The HSI V6 has a 12-bit sensor, which is already lower than what was recommended. One way to achieve higher intensity resolution (dynamic range) with a 12-bit sensor could be to use a bracketing technique/stacking. Data is then captured at a set of different exposure times, capturing from well exposed to overexposed images, and combined to expand the dynamic range (as more information from the dark areas becomes available in the overexposed images). This technique was, however, not used here as the maximum exposure time of 4 seconds did not lead to overexposure, and the technique could therefore not be used. If a better dataset gathered with shorter exposure times and less noise could be acquired, testing the full spectral stray light correction matrix (without setting all values except the second order peaks to zero) could be tested, which might improve the correction. Uncertainties from this method should also be estimated, and since they depend on the uncertainties of the measured LSFs, the uncertainties of these measurements should also be estimated.

Finally, even with a noisy dataset, the monochromator data with the Zong stray light correction method shows promising results for the wavelengths below 850 nm. It would therefore be interesting to see what results could be achieved with a better dataset. No matter which method is used, investigations should be done to estimate the quality of the correction before further use.

Part II

The HYPSO CubeSat Mission

From building the payload to receiving data from space

6 | Assembly, integration, and testing

The HYPSO-1 HSI payload was developed from 2019, and several models were built for testing before launch. The Engineering Model (EM) was used as a preliminary test model, with different components in the early design phases to verify their performance. The Qualification Model (QM) was built as similar to the Flight Model (FM) as possible, and underwent the main environmental tests like shock, vibration, and TVAC tests, to minimize stress on the FM. Finally, the FM was built in the end of 2020, calibrated and sent to KNA to be integrated into the satellite bus. Final testing was performed with KNA in the fall of 2021, before the launch of the satellite in 13 January 2022.

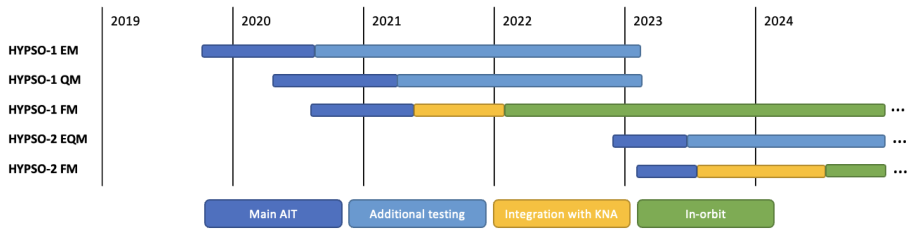

Figure 6.1: Timeline showing the development and use of the different HYPSO HSI models.

For HYPSO-2, the HSI payload is similar to the one of HYPSO-1, so both the HYPSO-1 EM and QM were used for preliminary testing. A dedicated test model, the Engineering-Qualification Model (EQM), was built in the end of 2022 for HYPSO-2 to test the new components, such as a modified slit tube and a new RGB camera, which also required minor changes to the payload platform. The HYPSO-2 FM was finally built in the spring of 2023, and calibrated then shipped to KNA in August 2023. A timeline summarizing when the different models were built and used is shown in Figure 6.1.

In this chapter, the AIT process of the HYPSO-1 and HYPSO-2 HSI payloads are first briefly described. The following sections focus on the optical characterization and optical effects observed before, during and after the environmental tests. Other details of the assembly process, the full test reports and additional experiments can be found in the references.

6.1 Building the HYPSO HSI payloads

Both the HYPSO-1 and HYPSO-2 HSI payloads consist of the HSI, a supporting RGB camera, and an electronics stack (called picoBoB) with an embedded computer that controls the instruments. Only the HSI is in focus in this thesis.

The HSI is based on the HSI V6 presented in Chapter 3. Some components had to be modified for use in space, as described for HYPSO-1 in detail by Prentice et al. in [36]. The main modifications are custom apertures inside the lens objectives (instead of variable apertures), a custom slit tube in aluminum (instead of multiple parts with COTS slit tube and adapter rings), a custom platform and platform brackets in aluminum (instead of rods and cage plates, to make sure no components in the optical train move during launch). The 3D printed parts, such as the grating cassette and sensor housing, were machined in aluminum instead of being 3D printed with PLA filaments. In addition, all parts went through a cleaning step before assembly. Specially important was the cleaning of the lens objectives to make sure that no grease would be present in vacuum (as this can cause outgassing).

All of the aluminum parts in the optical train were anodized before testing and launch. An exploded view showing the main components in the HYPSO-1 HSI is shown in Figure 6.2 The HYPSO-2 HSI was made almost identical, with minor changes as described in Section 6.1.2.

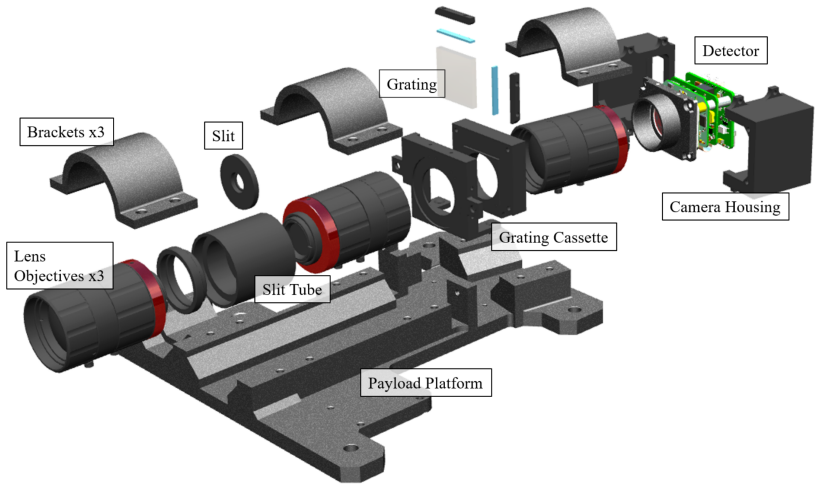

Figure 6.2: An exploded view showing the main components of the HYPSO-1 HSI [36]. The lens objectives, slit, grating and detector are the same as the ones used for the HSI V6, while the other parts are machined from aluminum.

6.1.1 HYPSO-1 HSI payload

For HYPSO-1, three HSI payload models were built, the EM, QM and the FM, as seen in Figure 6.3. The models are close to identical, the main difference being the version of

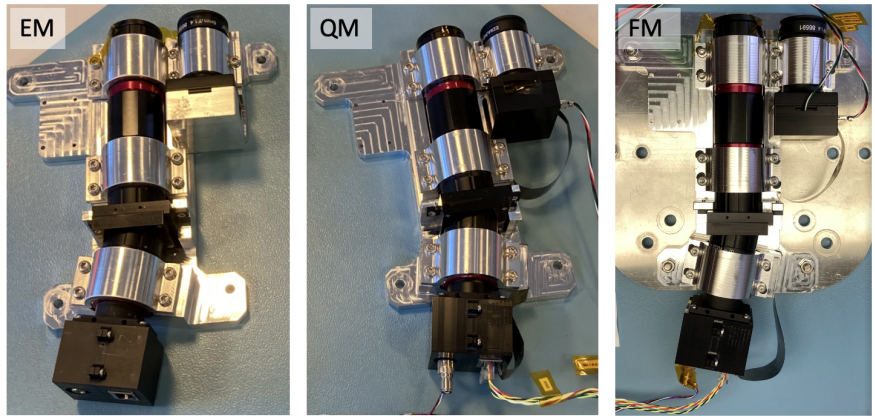

Figure 6.3: HYPSO-1 HSI payload models. In each image, the HSI is to the left, and the RGB to the right (electronics stack is not included in the images). The mounting plate under FM is not a part of the payload.

the slit tube that is used with each model, and that the EM is not equipped with thermal straps. Detailed descriptions of how the FM was built can be found in publications by Prentice et al. [32, 36] (**Paper 4**). Here, only details from the assembly phase that are important for the final optical performance of the imagers are presented.

Slit tube

The length of the slit tube is important for focusing the instrument. The lens objectives themselves should all have focus set to infinity, and the distance between the slit and the objectives are then required to be 17.526 mm, as described in Section 3.3. Achieving the exact length of the slit tube that is needed is hard when machining the parts due to machining tolerances. The later versions were therefore made about 0.5-1 mm shorter, so that the length could be adjusted by adding spacer rings. In addition, aligning the slit inside the slit tube was found to be a cumbersome process. Modifications to the design of the outer part of the tube was therefore made iteratively to improve this process. This resulted in the EM having a slightly different slit tube, compared to the QM and FM, as it used one of the earlier versions of the slit tube. This is an important detail to remember when seeing optical test results for the different models during thermal tests, as discussed further in Section 6.2.2.

FM spectral focus

During the finalization of the HYPSO-1 FM, the spectral focus (investigated by looking at the FWHM) was not within the expected requirements. When looking at argon and mercury lines from spectral calibration, the FWHM of the peaks ranged from 3.61 nm to 9.48 nm, with an average value of 6.31 nm, while the requirement states that the spectral resolution should be better than 5 nm. After some considerations, it was suspected that the wider spectral peaks might originate from an incorrect distance between the lens objectives and the slit in the slit tube.

An experiment to investigate this idea was performed with the EM, adding length to the slit tube by adding spacer rings between the slit tube and the collimating objective in steps of 0.1 mm. The EM was then placed in front of the integrating sphere with the argon spectral lamp as a light source, with the results shown in Figure 6.4. The change in spectral focus can easily be seen in the images, as the spectral lines get broader, weaker and more blurry for the larger distances, indicating worse spectral focus.

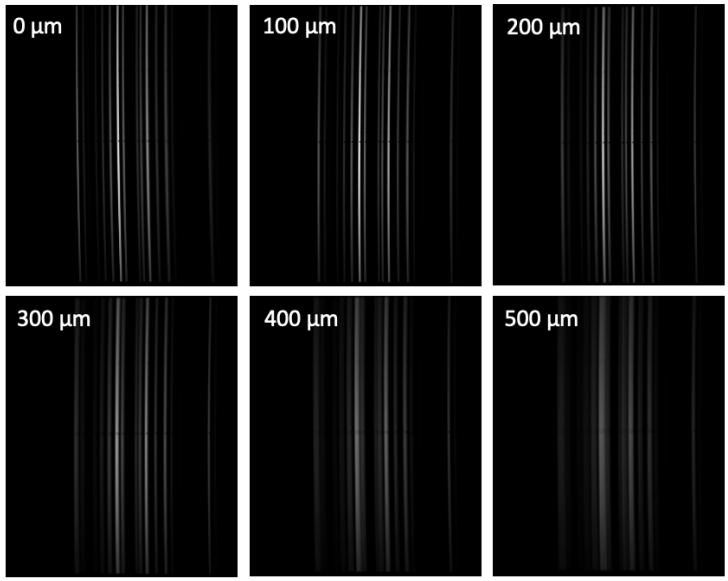

Figure 6.4: Zoomed in spectrograms from the EM, covering about 600 to 950 nm (x-axis) and the full slit height (y-axis), at different slit tube lengths. Note: spectral tilt (as seen for 0 μm) is due to the slit tube being slightly rotated, and is not a result of the difference in the length of the slit tube.

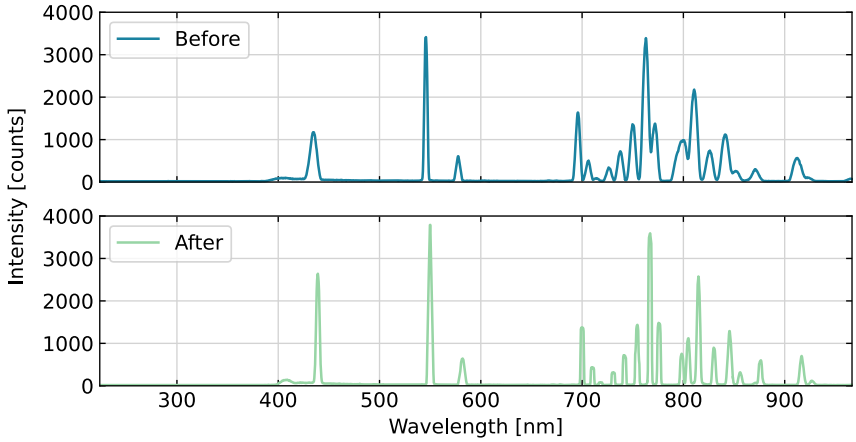

Figure 6.5: Spectral lines of argon and mercury calibration lamps taken with the HYPSO-1 FM, before and after the spacer ring was added to slightly increase the slit tube length.

After the investigations with the EM, a 0.25 mm spacer ring was added to the FM between the slit tube and the collimating (middle) objective. This improved the spectral focus as seen in Figure 6.5, where the spectral peaks are noticeably more narrow after the spacer ring was added than before. The FWHM of the argon and mercury peaks ranged from 3.63 nm to 5.00 nm, with an average value of 4.05 nm, after the ring was added, which is just within the requirement of 5 nm for all the peaks investigated. This shows how sensitive the instrument is to changes in position of the optical components, and that it is important to verify the optical performance during assembly of the instrument.

6.1.2 HYPSO-2 HSI payload

For HYPSO-2, two HSI payload models were built, the EQM and the FM, shown in Figure 6.6. The models are close to identical. However, the payload platforms are slightly different, as a late change was made to the design to accommodate a change in position of the star tracker inside the satellite bus in the early spring of 2023. The change was minor, and only affected the flat part of the platform to the left of the HSI, and is not expected to affect the environmental test results. A detailed description on how the EQM and FM were built can be found in the reports "HYPSO2-DR-009 Building HYPSO-2 EQM" [163] and "HYPSO2-RP-015 HYPSO-2 Flight Model As-Built" [164], respectively.

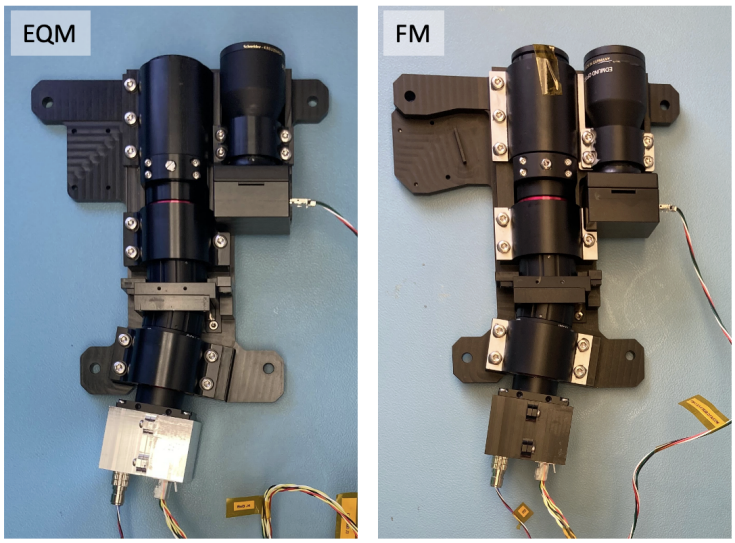

Figure 6.6: HYPSO-2 HSI payload models.

This section describes the differences in the design from HYPSO-1, and parts of the assembly of the FM, focusing on adjusting the spectral and spatial focus of the instrument. Since the FM was built at the very end of the project period of this thesis, only data from the assembly is described. The results from the full HYPSO-2 FM calibration was not completed at the time of writing, and are therefore not included in this thesis.

Design changes from HYPSO-1

The changes that were made between the HYPSO-1 and HYPSO-2 HSI payloads can be summarized as follows:

- **New slit tube**: The design of the new slit tube was made by a group of bachelor's students in the spring of 2022, described in their thesis [165]. A prototype was made, and initial tests completed before the design was accepted. The final test that confirmed that the new slit tube design would be used was the shock and vibration test, which was later completed with the HYPSO-2 EQM, as described in Section 6.2.3. The new slit tube makes it easier to adjust the orientation of the slit after assembly.

- **New RGB camera**: Both the RGB sensor and RGB lens were changed to different components. The sensor had the same physical size, and the same RGB housing could therefore be used. The lens, however, was longer, and an UV/IR filter was added as well, making the lens assembly even longer. The payload platform therefore had to be modified (see next bullet point).

- **Modifications to the payload platform**: Changes were made to accommodate for changes in RGB payload (the lens being longer) and to movement of the star tracker (FM platform only). The brackets holding the HSI and RGB front lenses were also modified due to the longer RGB lens.

- **No thermal straps**: It was decided to not use thermal straps on HYPSO-2 since they are cumbersome to work with, and simulations showed that they did not really dissipate much heat for HYPSO-1.

- **Anodizing all machined parts**: All machined aluminum parts were anodized (except for certain areas for electrical connection), not only parts in the optical train as done for HYPSO-1.

In addition, there were minor changes between the HYPSO-2 EQM and FM. For the apertures (used inside the HSI objectives), 0.5 mm thick aluminum sheets were used to make the apertures for the FM instead of 0.25 mm sheets (used both for HYPSO-1 models and HYPSO-2 EQM) to improve the smoothness of the edges when cutting them. The last modifications to the payload platform, regarding the position of the star tracker, was not made until after the EQM was machined, meaning that the EQM had an older version of the payload platform than what was used for the FM. This should not, however, affect the test results. Lastly, the HSI detector housing for the EQM was not anodized (as seen in the pictures of the payloads). None of these changes should affect the test results when comparing the performance of EQM to the expected performance of FM.

FM spectral focus

From HYPSO-1, it was learned that checking the focus properly before final assembly (and before epoxying the screws) is important. These procedures were therefore improved for the assembly HYPSO-2. Ideally, the spectral calibration lamps should be used to assess spectral focus. However, these were not available in the SmallSat Lab where the assembly took place. A fluorescent lamp was therefore used instead, illuminating a white sheet of paper, giving a fairly uniform target with spectral lines when observed by the HSI.

To adjust the spectral focus, the distance between the slit tube and the middle/collimating objective was increased. As previously mentioned, the slit tube is made shorter than necessary by design, so that any inaccuracies after machining should require adding length to the tube (and not making it shorter), which is done by adding spacer rings. A set of spacer rings were used, and an image taken with the HSI with each spacer ring. The resulting normalized line plot of the middle row (center of slit image) of each image is shown in Figure 6.7. The lines were normalized by dividing by the maximum value for easier comparison. From this, and additional analysis (not shown here), it was found that a distance of 0.75 mm gave the most narrow lines in the center of the image (around wavelength 600 nm), indicating best focus. Spacer rings of 0.5 mm and 0.25 mm were therefore added to the FM.

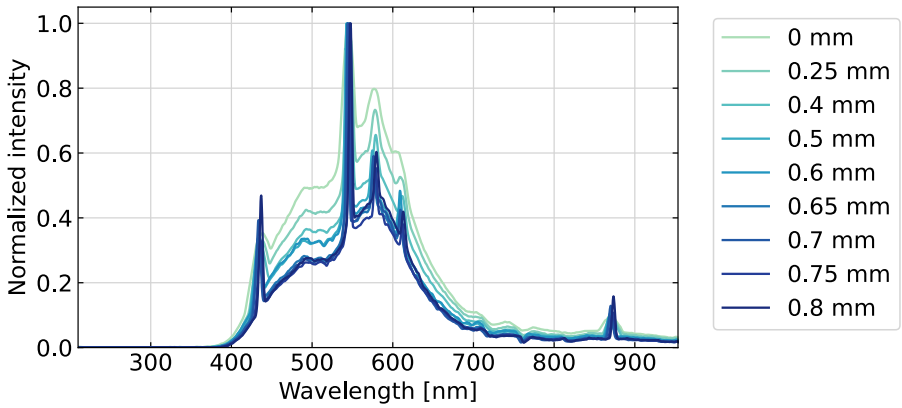

Figure 6.7: HYPSO-2 FM spectral focus. Showing the normalized center line in spectrograms of the fluorescent light spectrum and light from the flow bench. Different images/colors with different distances between the slit and the middle objective.

FM spatial focus

In addition to checking the spectral focus during assembly, the spatial focus was also investigated during the assembly process. To adjust the spatial focus, the distance between the front objective and the slit tube was increased. To see spatial features in the image, the collimator lens and 3D printed striped pattern were used, placed in front of the HSI. The HSI was then pointed towards a white sheet of paper illuminated by a broadband light source (the Thorlabs QTH10/M lamp), providing light at all wavelengths in the visible spectrum.

Again, a set of spacer rings were used to find the sharpest lines in the center of the image (middle row, center of slit image). The line plot of the middle column (about 600 nm) for the images taken with each spacer ring can be seen in Figure 6.8. The best focus is found when the lines in the image are shaped like a box, with sharp edges and a flat top. The exact position of the stripes in the image differs due small movement in the optical train between each step, since the objective is removed and re-attached each time a spacer ring is added. When having a closer look at the data, the distance of 0.35 mm was found to give the best response. Spacer rings of 0.1 mm and 0.25 mm were therefore chosen and added to the FM. For future assemblies, both this method and the method for adjusting the spectral focus can be improved by detecting the sharpest lines automatically. For the spatial focus, it would also be beneficial to investigate the focus at several wavelengths, and not only at the center wavelength as done here.

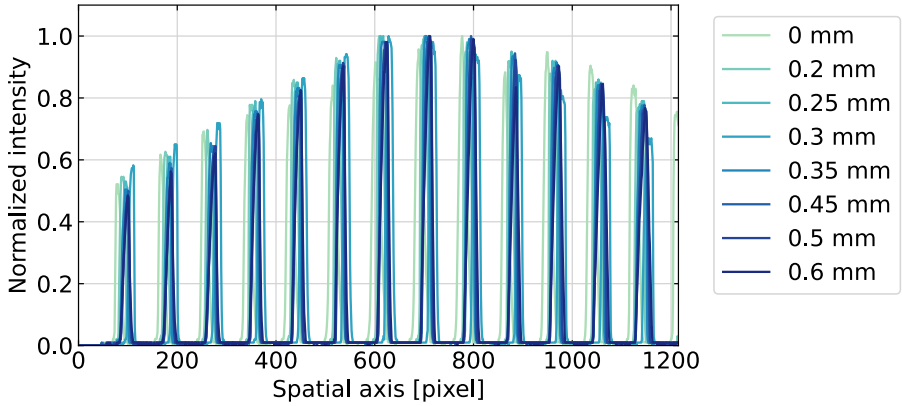

Figure 6.8: HYPSO-2 EQM spatial focus. HYPSO-2 FM spatial focus. Showing the center line in spectrograms of the broadband source, with the collimator and striped pattern in front of the HSI. Different images/colors with different distances between the slit and the front objective.

6.2 Optical performance after environmental tests

The HSI payloads for both HYPSO-1 and HYPSO-2 went through a number of environmental tests before launch, such as being exposed to vacuum, radiation, shock, vibration and temperature changes both in and out of vacuum. Since the HYPSO-2 HSI payload was a continuation of the HYPSO-1 HSI payload design and using the same COTS components, not as many environmental tests were required for HYPSO-2 as for HYPSO-1. However, the new components such as the slit tube and the RGB camera had to pass both TVAC and shock and vibration tests before the final design was accepted. The environmental tests were mostly performed by other HYPSO team members. However, since the focus of this thesis is on the optical performance of the hyperspectral instruments, the author was involved in setting up the optical validation set-ups and analyzing the hyperspectral data before and after testing. The results from the optical validation during the environmental tests are presented and discussed here.

6.2.1 Optical validation set-up

Several set-ups and configurations were used for optical validation throughout the project, and the set-ups were improved and re-configured as needed for the different tests. The main optical validation set-up used consisted of a white sheet of paper illuminated by

either a fluorescent lamp (Osram Dulux, 15W, 900lm, 2700K) or a stable quartz-halogen lamp (Thorlabs QTH10/M), covered by a cardboard box that was painted black on the inside to block out external light sources. The fluorescent lamp was used to provide spectral lines in the HSI images to investigate spectral shifts or changes in spectral focus, while the quartz-halogen lamp was used to provide illumination at all wavelengths to investigate changes in transmission or spatial shift of the slit or image sensor.

An example of the optical validation set-up used during radiation testing of HYPSO-1, showing the quartz-halogen lamp illuminating the white sheet of paper is shown in Figure 6.9a. The set-up used during focus testing of the HYPSO-2 EQM in the Smallsat lab, showing the white paper being illuminated by the fluorescent lamp can be seen in Figure 6.9b. Normally, the cardboard box would be placed over the set-up in Figure 6.9a and the lights in the room turned off. When using the fluorescent lamp in Figure 6.9b it would normally be placed in an inlet in the cardboard box, and the box placed over the set-up. However, during tests when the exact spectral response or intensities are not that important, the cardboard box was not used.

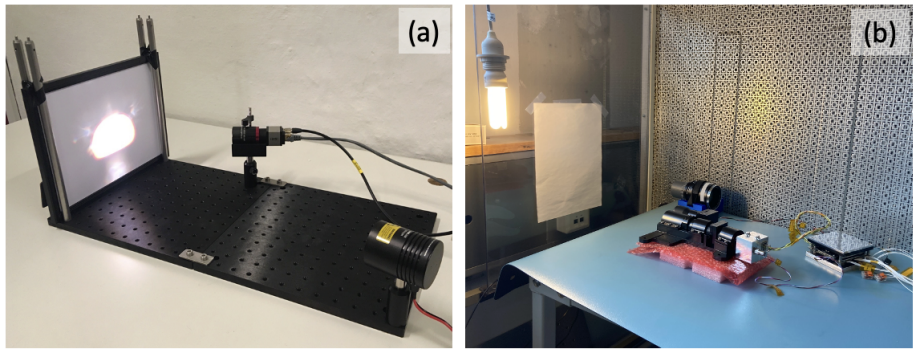

Figure 6.9: Example of optical validation set-ups. (a) Quartz-halogen lamp illuminating white sheet of paper (without cardboard box), from HYPSO-1 component radiation testing, (b) fluorescent lamp illuminating white sheet of paper (normally lamp would be placed in the cardboard box), from HYPSO-2 EQM focus testing.

6.2.2 HYPSO-1 environmental tests

The full AIT process of HYPSO-1 is described in detail in **Paper 4**: "Pre-Launch Assembly, Integration, and Testing Strategy of a Hyperspectral Imaging CubeSat, HYPSO-1" [32]. Here, only a short overview of the tests will be given, followed by the results from the optical characterization done before, during and after the tests.

*Table 6.1: Test overview (summary of Table 4 in [32] (**Paper 4**)). HSI means a prototype of the payload. $g = 9.8$ m/s (standard acceleration of gravity).*

Date	Test	Components	Details
2019-02-08	Vacuum	HSI objective, HSI sensor	Vacuum level 1.9×10^{-2} Pa for 60 min. Observed internal grease condensed on the lenses.
2019-03-26	Radiation	HSI objective, HSI sensor	Gamma radiation (Cobalt-60), 5-150 Gy. Observed about 10% loss in transmissivity after tests.
2019-05-25	Shock & vibration	HSI objective	20-2000 Hz, 6.7g RMS, 70g for 2 ms. No damage observed.
2019-07-24	Thermal	HSI	Temperature range from -40°C to 70°C. Noticeable spectral shift observed.
2019-10-03	Vacuum	HSI objective	Vacuum level 2.95 Pa for 60 min. No damage observed.
2019-10-31	Thermal	HSI	Temperature range from -40°C to 50°C. Noticeable spectral shift observed.
2019-11-12	Vacuum	HSI objective	Vacuum level 5.8×10^{-2} Pa for 45 min. No damage observed.
2020-01-28	Vacuum	RGB objective, RGB sensor	Vacuum level 2.6×10^{-2} Pa for 60 min. No damage observed.
2020-03-05	Thermal	HSI	Temperature range from -40°C to 50°C. Noticeable spectral shift observed.
2020-05-28	Shock & vibration	EM	20-2000 Hz, 5.48g RMS, 300g for 2 ms. Some screws loosened, after this proper torque was applied and epoxy used to secure screws.
2020-09-24	Shock & vibration	QM	20-2000 Hz, 5.48g RMS, 300g for 2 ms. No damage observed.
2020-11-06	Bakeout	QM	Temperature 50°C for 72 hours at vacuum level less than 1.33×10^{-3} Pa. No damage observed
2021-01-18	TVAC	QM	Vacuum level 3×10^{-4} Pa, temperature range from -30°C to 60°C (non-operational) and -20°C to 50°C (operational). Noticeable spectral shift observed.
2021-09-20	Vibration	FM	20-2000 Hz, 5.13g RMS. No damage observed.
2021-10-27	TVAC	FM	Vacuum level 3×10^{-4} Pa, temperature range from -30°C to 60°C (non-operational) and -20°C to 50°C (operational). No damage observed, spectral shift not investigated.

An overview of the environmental tests performed on the HYPSO-1 components and models can be seen in Table 6.1. Preliminary tests were done with some of the COTS components in 2019, to see if any of the components had to be modified before being used in space. Most noticeable outcome from these tests was the need for disassembling the HSI lens objectives and clean the parts to remove grease that would condense on the lenses in vacuum. Further, a prototype (denoted only HSI in the table) was used for initial testing of the instrument at different temperatures. A spectral shift was observed, which will be discussed in the next sections. The EM then underwent shock and vibration tests, where some of the screws loosened. After this, proper torque was applied and the screws epoxied to properly secure the screws on the other models. The QM was then tested both with shock and vibration tests, then bakeout followed by a TVAC test. No new issues were found during these tests. Then, after integration with the satellite, the FM also underwent vibration and TVAC tests, which both passed, before it was launched.

Radiation test of components

One of the first tests the HSI objective and HSI sensor were subject to, was a radiation test to investigate the level of degradation of the components that could be expected when exposed to radiation. Glass substrates typically darken when exposed to radiation [166, 167], while an increase in dark signal and dark current, less uniform distribution of the dark current and increased Random Telegraph Signals (RTSs) are some of the effects that can be expected for the image sensor [168]. The components were tested in a gamma radiation chamber with a Cobalt-60 source at the Technical University of Denmark (DTU), and were cumulatively radiated by 5, 10, 20, 30, 40, 60, 80, 100 and 140 Gy. Cobalt-60 gamma radiation is often used to simulate the natural space radiation environment, even though other types of radiation are also present in space. Higher energy radiation does, however, not cause as much damage, which makes Cobalt-60 reliable for worst case simulation of the space environment [169].

Between each dose the components were brought out of the radiation chamber and tested in front of a light source in combination with non-irradiated components (as seen in Figure 6.9a). The irradiated objective was tested with a non-irradiated sensor, the irradiated sensor with a non-irradiated objective, and the non-irradiated components tested together for reference. The cameras (sensor and objective) were placed in front of the white sheet of paper, at a set distance and in the same position each time, that was illuminated by the stable quartz-halogen lamp (Figure 6.9a). In addition, dark images was taken with the HSI sensor to investigate changes in noise in the sensor.

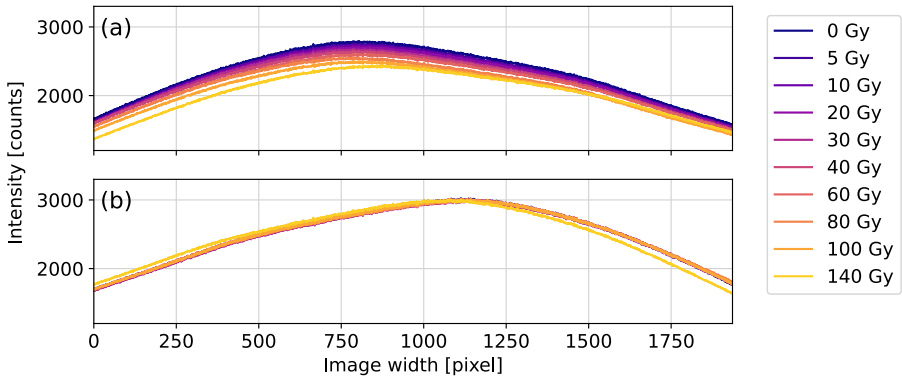

Figure 6.10: HSI objective and camera sensor after each radiation dosage. (a) Irradiated objective and non-irradiated sensor, (b) non-irradiated objective and sensor for reference.

A decrease in the transmitted light through the irradiated lens objective can be seen in Figure 6.10. The response in the non-irradiated lens objective stays the same, however, showing that the measurement set-up is stable. The exception is a small jump in the signal decrease that can be seen in the 140 Gy curve for both curves, which is due to a small movement in the set-up for this measurement. About 10% of the light was lost after the objective was exposed to 100 Gy, and the lenses were visually more brown in color after the experiments, as seen in Figure 6.11. The irradiated and non-irradiated objectives were

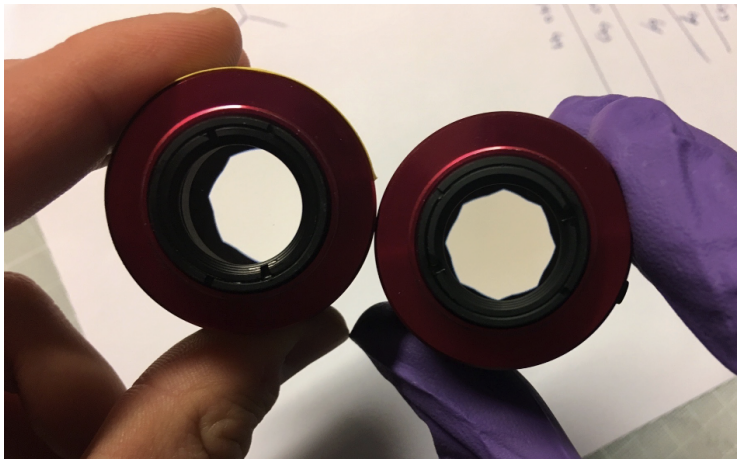

Figure 6.11: Non-irradiated objective (to the left), next to the irradiated objective (to the right). The irradiated objective is visually more brown in color.

also tested as the front lens in a HSI assembly. The same type of measurements, looking at a white sheet of paper illuminated by the stable light source, were then repeated. It could be seen that less light was recorded for all wavelengths with the irradiated objective, and that the largest decrease was found around 500 to 600 nm. These wavelengths correspond to green, yellow and red light, and explains the brown color seen in the glass after the radiation experiments.

Figure 6.12 shows the values in the dark images with the irradiated and non-irradiated sensor. A higher value in some pixels can be observed in the irradiated sensor, with more of these pixels appearing with the higher radiation doses. The non-irradiated sensor, however, has a stable background value of about 8 pixels, with no clear difference with each measurement. This indicates that the higher values seen in the irradiated sensor are due to the radiation it has been exposed to, and not other external sources.

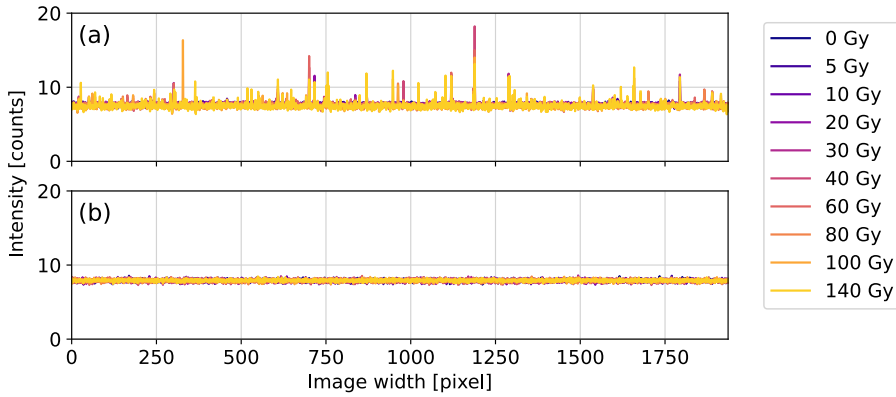

Figure 6.12: HSI camera sensor before and after radiation test. (a) Irradiated sensor, (b) non-irradiated sensor for reference.

Shock and vibration test of QM

The payload is exposed to vibrations during the launch of the satellite, and shock when the satellite is separated from the launch vehicle. Shock and vibration tests were therefore performed at the Norwegian Defense Research Establishment (FFI) to check that the payload could handle these events. The HYPSO-1 QM was mounted inside a mass model of the satellite bus and secured to the shock and vibration table. The shock and vibration test were then performed, and repeated for the X-, Y- and Z-axis (see Figure 1.6). Sine sweeps of 5-200 Hz with amplitude of 0.4g (g=9.8 m/s, standard acceleration of gravity)

sweeping two octaves per minute were done before and after each random vibration and shock test. The test procedure started with a sine sweep, then was followed by random vibrations, sine sweep, shock and ended with a sine sweep. For shock, a 300g Shock Response Spectrum (SRS) for 2 ms was used. Further details on the test are described in the test report "HYPSO-TPR-VIB-003 HYPSO-1 QM Shock, Resonance, and Vibration Test Report" [170].

Before and after the test in each axis, images were taken with the HSI of the white sheet of paper illuminated by the fluorescent lamp inside the cardboard box. The recorded spectra before and after the shock and vibration testing in the Y-axis are shown in Figure 6.13, as the largest changes in the images were found after testing in this configuration. In the figure it can be seen that the recorded spectrum after the tests has slightly lower peaks, which indicates either less light through the system or a broadening in the peaks which make them lower and wider. It could, however, also be due to uneven illumination with extra light entering the box. No large spectral shifts were observed.

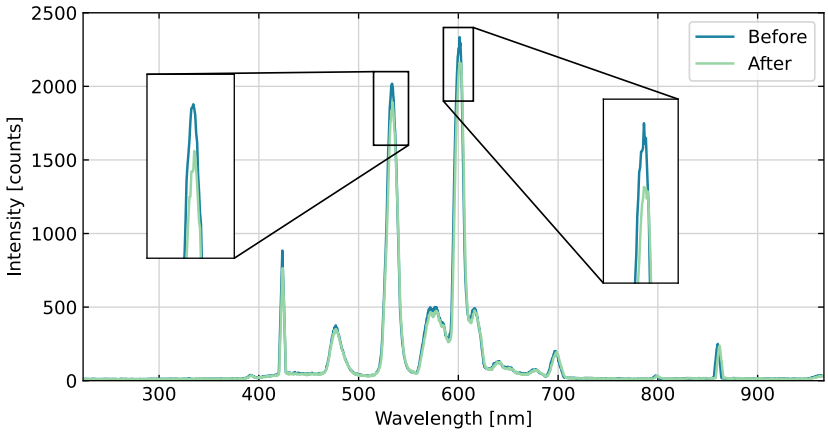

Figure 6.13: Fluorescent light spectrum captured by the HYPSO-1 QM before and after shock and vibration tests in the Y-axis.

The images taken by the HSI were also analyzed along the spatial axis, looking at a column in the image (one band) instead of a row (spectrum). This is done with the same image in Figure 6.14, for the column/band corresponding to 600 nm in the image. That the recorded light is slightly weaker in the images after the tests can again be observed, and the uneven light intensity along the spatial axis is due to vignetting effects in the optics, as the images used here are not calibrated. The sharp edge around spatial pixel 45 shows the edge of the slit. When zooming in, as done in the figure, it can be seen that the edge

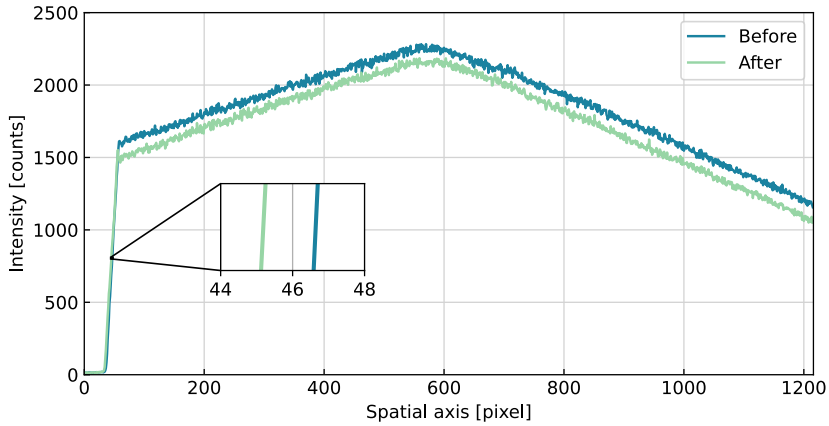

Figure 6.14: Recorded light at column (along the slit) corresponding to 600 nm in the fluorescent light spectrum captured by the HYPSO-1 QM before and after vibration test (Y-axis) shown in Figure 6.13. The sharp edge at spatial pixel 45 is the edge of the slit.

of the slit has moved slightly towards the left after the tests. The average shift between the lines in the intensity range from 500 to 1000 counts is 1.5 pixels, indicating a small shift after this vibration test. The same calculations were performed on the images from the X- and Z-axis tests as well, which showed a shift of -0.15 and 0.28 pixels, respectively. From these results it can be noted that the slit might change position slightly, but no large changes in placement would be expected when launching the satellite into space.

Thermal Vacuum test of QM

After bakeout, a TVAC test of the QM was performed, as described in further detail in "HYPSO-TRP-TVAC-003 HYPSO-1 QM TVAC Test Report" [171]. A vacuum level of 3×10^{-4} Pa was kept, and the temperature cycled first from -30°C to 60°C to emulate non-operational temperature that the payload might encounter during launch etc., followed by a temperature cycle from -20°C to 50°C to emulate the temperature expected in worst case operating conditions. The temperature cycles were done in steps of 10°C. Images were taken with the HSI both before and after the tests outside the chamber, and inside the chamber during the test with the operational temperature cycle.

When images were acquired by the HSI inside the chamber, light from the fluorescent lamp entered the chamber through a window. Since a white sheet of paper (or other suitable targets) could not be placed inside the chamber, the metallic chamber wall was

used as target. The resulting spectra for each temperature are shown in Figure 6.15. For higher temperatures, the whole spectrum shifts towards the left (shorter wavelengths), and the peaks get lower and wider, as seen in the zoomed in box plots of two of the peaks. The lowest peaks are found for 30°C, while at 40°C and 50°C the peak height increases again. The widest peaks are, however, found for the highest temperatures. This suggests that the performance declines for higher temperatures, as the FWHM increases, resulting in worse spectral resolution.

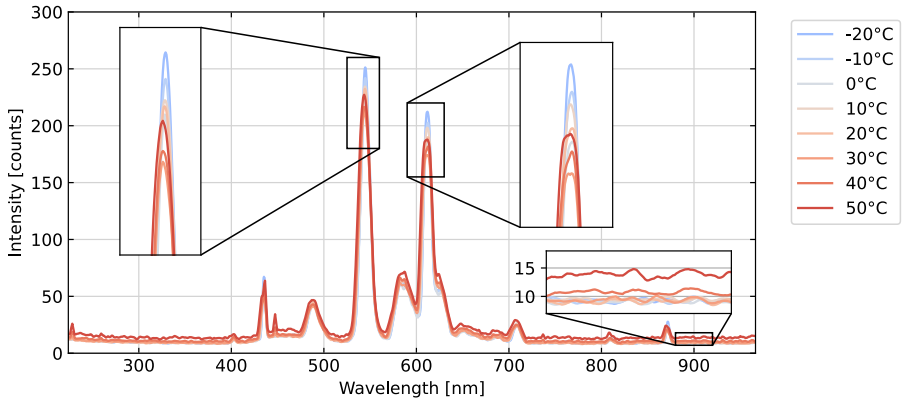

Figure 6.15: Fluorescent light spectrum captured by the HYPSO-1 QM during TVAC test (inside the chamber). The spectra are smoothed to minimize noise due to low light level.

The inside of the chamber was quite dark, even when illuminated by the fluorescent lamp, which results in noisy data. The spectra were therefore smoothed to easier observe the shape of the spectra. It can also be noted that the intensity (sensor counts) are much lower here, due to the darker environment. The background level of about 10 counts is also visible, since the y-axis only goes to 300 counts (of 4095 counts possible). It can also be seen that the background level increases slightly for higher temperatures, which is as expected. At 40°C the background level raises to about 11 counts, while for 50°C it jumps to almost 15 counts. The increase in the peak heights for higher temperatures could also be related to the increase in noise and background level.

The fluorescent lamp illuminating the white sheet of paper inside the cardboard box was once again used to acquire images before and after the test outside the chamber. The resulting spectra can be seen in Figure 6.16. The spectrum after the tests seems to have shifted towards the right (longer wavelengths), so the opposite of what was seen when going from low to high temperatures inside the chamber. The shift is consistent for the

full spectrum, and is of about 8 pixels, which corresponds to about 3 nm. This is quite a large shift, and it was decided that this should be investigated further, together with the shifts and broadening of the peaks seen during the TVAC test.

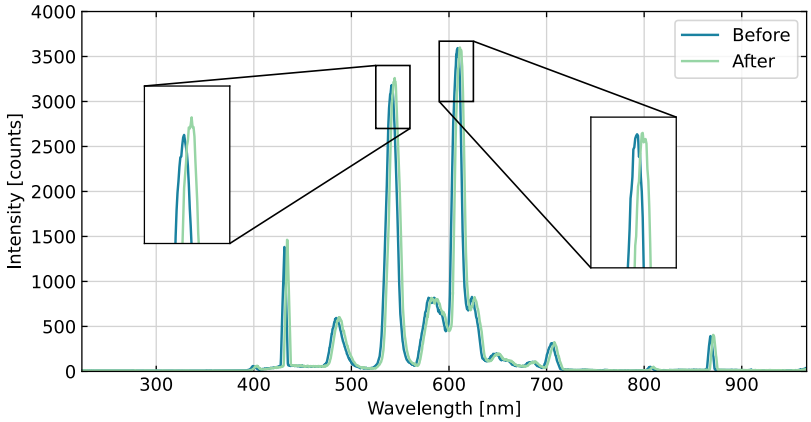

Figure 6.16: Shift seen in fluorescent light spectrum captured by the HYPSO-1 QM before and after TVAC test (outside the chamber).

Additional thermal characterization of EM

To further investigate the changes in spectral response occurring during TVAC testing, an additional test was set up with the HYPSO-1 EM. The results presented here are based on the experiments performed in **Paper 3**: "Characterizing Spectral Response in Thermal Environments, the HYPSO-1 Hyperspectral Imager" [172].

For these experiments, a Vötsch VT 4011 (Vötsch Industrietechnik GmbH, Germany) thermal chamber (no vacuum) was used. Temperatures from -40°C to 70 °C were cycled through with 10°C steps, as done during the TVAC testing of QM. The thermal chamber had an outlet port for cables, which was large enough for the HSI to look through. The white sheet of paper illuminated by the fluorescent lamp and covered with the cardboard box was again used, and placed in front of the chamber outlet as a target for the HSI. Images were taken at each temperature step both when ramping up (from lower to higher temperatures) and when ramping down (from higher to lower temperatures). The results are slightly different in terms of peak intensities at each step, but the trends are the same. Therefore, only the latter case is shown here.

In Figure 6.17 the results from the ramping down test can be seen, and shows that the peaks get higher and more narrow for higher temperatures. For the peak around 546 nm, a double peak even gets visible for the highest temperatures, while for the lower temperatures these two peaks are fully merged. It can also be seen that for the temperatures below 0°C the recorded signal is very weak. During the experiments there was no humidity control, and condensation (freezing for the lowest temperatures) was observed on the front lens, which might explain why less light was recorded.

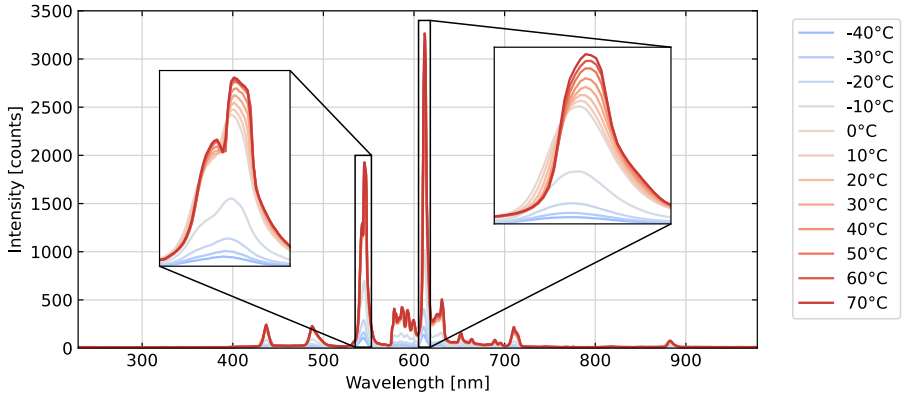

Figure 6.17: Fluorescent light spectrum captured by the HYPSO-1 EM during the thermal experiments cycling from higher to lower temperatures (ramp down) .

Sharper peaks for higher temperatures is the opposite effect of what was seen for the QM during TVAC testing. As mentioned, the EM has an older version of the slit tube than the QM. The exact length of the two slit tubes might also differ. The aluminum in the slit tube expands with higher temperatures, following the thermal expansion coefficient. If the EM slit tube was shorter than the ideal length, expansion of the slit tube would mean a longer distance between the slit and the objectives, thereby improving the focus. This would explain the sharper peaks at higher temperatures that can be observed. For the QM slit tube, however, the focus gets worse with higher temperatures. If the slit tube was at the correct length in the beginning, expansion of the slit tube with higher temperatures would make the focus worse, which would explain the results seen during the TVAC tests.

Since both tests were done with two different models, and not in vacuum, the conclusion was that further investigations in a TVAC chamber would be needed. Additional experiments were therefore set up by Navarro-Medina and Oudijk with the HYPSO-1 QM, as described in **SP 3**: "Experimental set-up of a thermal-vacuum chamber for

thermal model in-house correlation and characterization of the HYPSO hyperspectral imager" [173] and **SP 4**: "Structural Thermal Optical Performance (STOP) analysis and experimental verification of the HYPSO hyperspectral imager" [174]. These experiments are not described in further detail in this thesis. However, the reader is encouraged to read the publications if models, simulations and further experiments on the optical response with temperature in vacuum is of interest.

6.2.3 HYPSO-2 environmental tests

The AIT of HYPSO-2 followed the AIT of HYPSO-1 closely. Testing of the new components (the slit tube and the RGB camera) was in focus when testing the EQM, and they both had to pass these tests before the design was set for FM. The list of environmental tests conducted for HYPSO-2 can be seen in Table 6.2.

A preliminary TVAC test of the RGB was done to ensure that the components would survive the changes in temperature and pressure without any major issues. Further, two TVAC tests were done, the first one without any light in the chamber (since light through a chamber window was not available at the time), and later with light so that images could be taken at the different temperature steps. Vibration and TVAC tests of the FM will be conducted after integration with the satellite bus in the winter of 2023/2024.

Shock and vibration test of EQM

The HYPSO-2 HSI payload EQM was also shock and vibration tested to ensure that the new slit tube and the new RGB camera would survive the launch, as described in the report "HYPSO2-TRP-SHK-001 HYPSO-2 EQM Shock, Resonance, and Vibration Test Report" [175]. The testing was again performed at the testing facilities at FFI. The EQM was mounted inside the mass model of the satellite bus (same as for HYPSO-1), and secured to the shock and vibration table. The same testing parameters and scheme as for HYPSO-1 were used (sine sweeps of 5-200 Hz with amplitude $0.4g$ sweeping two octaves per minute, random vibrations and shock with a $300g$ SRS used). The tests procedure started with a sine sweep, followed by random vibrations, sine sweep, shock and then a sine sweep again, and this was repeated for the X-, Z- and lastly the Y-axis.

For optical validation before and after the test in each axis, images were acquired of the white sheet of paper illuminated by the fluorescent lamp covered with the cardboard box, by the quartz-halogen lamp (no box used), and with the collimator and the striped pattern

Table 6.2: Overview of environmental tests for the HYPSO-2 HSI payload. Text marked in cursive denotes tests that have not yet been completed at the time of writing. $g = 9.8$ m/s (standard acceleration of gravity).

Date	Test	Components	Details
2023-02-06	Vacuum	RGB	Vacuum level 7.72×10^{-6} mBar, duration of 23 hours. No damage observed.
2023-02-15	Shock & vibration	EQM	20-2000 Hz, 5.48g RMS, 300g for 2 ms. No damage observed.
2023-03-15	Bakeout	EQM	Temperature 50°C for 24 hours at vacuum level of 1.4×10^{-5} mBar. No damage observed.
2023-03-23	TVAC (dark)	EQM	Vacuum level 3×10^{-7} mBar to 1×10^{-6} mBar, temperature range from -30°C to 60°C (non-operational) and -30°C to 50°C (operational). No damage observed.
2023-04-24	TVAC	EQM	Vacuum level 3×10^{-7} mBar to 1×10^{-6} mBar, temperature range from -30°C to 60°C (non-operational) and -20°C to 50°C (operational). No damage observed.
2023-xx-xx	*Vibration*	*FM*	*Planned, but not completed at the time of writing.*
2023-xx-xx	*TVAC*	*FM*	*Planned, but not completed at the time of writing.*

between the HSI and the white paper. The fluorescent lamp was used to investigate any spectral shifts, as seen in Figure 6.18, while the quartz-halogen lamp was used to investigate any spatial shifts in Figure 6.19. The data with striped pattern and collimator could also be used to assess spatial shifts, but were not used here.

For the spectral response in Figure 6.18, the images before and after the full test are compared, and shows no spectral shift detected. The images between the tests were also investigated, and show the same results. In Figure 6.19 the response before and after the test in Y-axis (last test) are plotted as an example. The edge of the slit is visible as a sharp edge in all images, and stays within the same 1-2 pixels for all images. This small shift could mean that either the slit or image sensor has moved slightly during the tests, as observed for HYPSO-1 as well. However, since no larger shifts were seen, the test was marked as successful and the components passed the test.

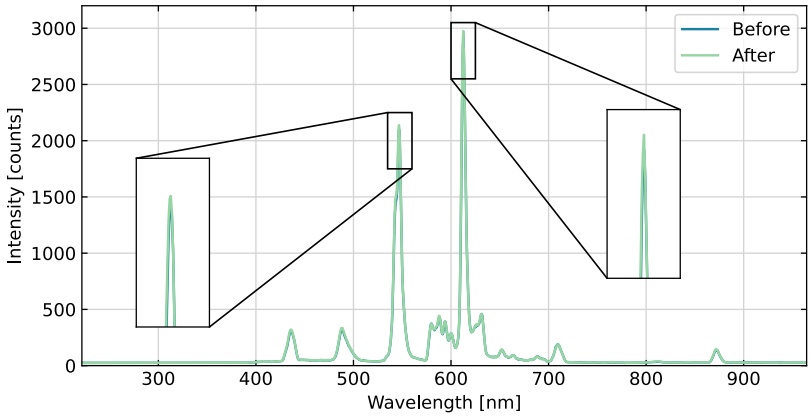

Figure 6.18: Fluorescent light spectrum captured by the HYPSO-2 EQM before and after shock and vibration tests.

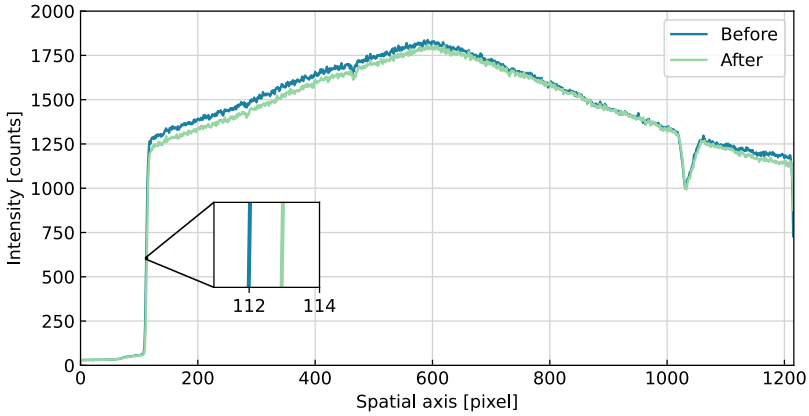

Figure 6.19: Quartz halogen lamp spectrum captured by the HYPSO-2 EQM before and after shock and vibration tests in the Y-axis.

Thermal Vacuum test of EQM

Two TVAC tests were performed with the EQM, one where the inside of the chamber was dark and one with fluorescent light entering a window in the TVAC chamber, thereby illuminating the inside of the chamber. The vacuum level was at 3×10^{-7} mBar to 1×10^{-6} mBar, and temperature cycles were run from -30°C to 60°C with 10°C steps. Five full frame spectrograms without binning were acquired with the HSI at the steps

between -30°C to 50°C. Both tests are further described in the report "HYPSO2-TRP-002 HYPSO-2 EQM TVAC Test Report" [176].

Data from the TVAC test in the dark is shown in Figure 6.20. The figure shows histogram plots of the recorded pixel values, and shows that for colder temperatures most pixels have a value of 8-10 counts (coinciding with previous measurements), while the values and number of pixels with higher values increase significantly with higher temperatures. Not seen in the plot are values higher than 180 counts, which were only found for the highest temperatures. For the 50°C step as shown in the plot, 17-18 pixels had values above 180 counts in the five recorded images, reaching 2000-3500 counts. It is clear that the pixels values increase with increasing temperature, as is also seen for HYPSO-1 and normal for camera sensors.

Data from the TVAC test with the window and fluorescent lights is shown in Figure 6.21. The background level can be seen to be generally high and reaching almost 20 counts (also seen in the dark data). When looking at the spectral lines, focus seems clearest at around 30°C, with the highest and most narrow peak. This suggests that the slit tube length is most correct at this temperature, and most likely slightly too short and too long at the other temperatures. The performance is as expected, and coincides with what is seen in the other tests for the HYPSO-1 HSI in terms of the response changing slightly with temperature.

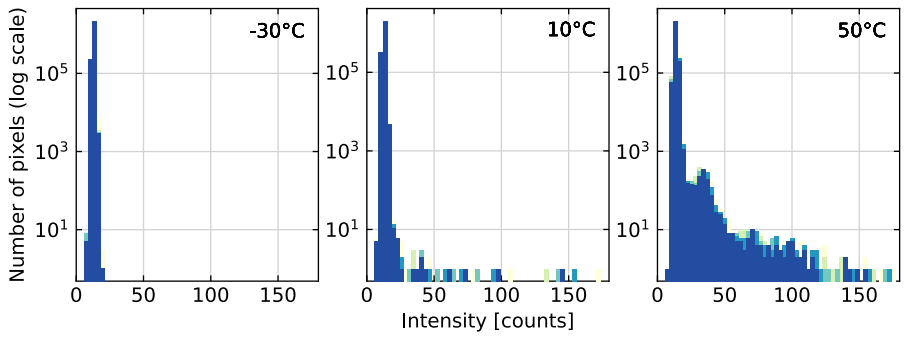

Figure 6.20: Distribution of the recorded pixel values in HYPSO-2 EQM during TVAC test in the dark (no light entering the chamber).

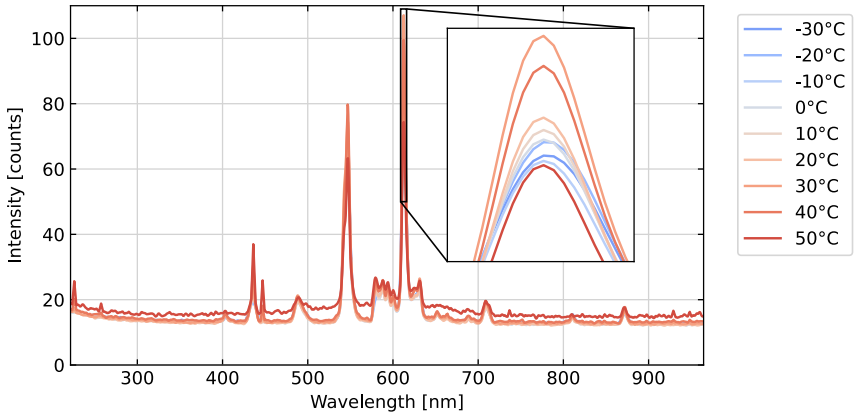

Figure 6.21: Fluorescent light spectrum captured by the HYPSO-2 EQM during TVAC test (inside the chamber). The spectra are smoothed to minimize noise.

6.3 Conclusions

Five HSI models, in addition to some prototypes, were built during the project period of this thesis (2019-2023). Three models for HYPSO-1 (EM, QM and FM) and two models for HYPSO-2 (EQM, FM). The design was iteratively improved. In addition, the assembly process, quality assurance (in terms of procedures) and quality control (the tests during assembly) were also improved throughout the project. HYPSO-1 launched successfully in January 2022, and HYPSO-2 is scheduled for launch summer 2024.

From the environmental tests of both HYPSO-1 and HYPSO-2, small shifts of 1-2 pixels were seen during the shock and vibration tests. As discussed in the HYPSO-2 test report "HYPSO2-TRP-SHK-001 HYPSO-2 EQM Shock, Resonance, and Vibration Test Report" [175], the weakest component is the HSI sensor. This should be taken into consideration when designing new instruments. From the TVAC tests and additional thermal experiments, it is clear that the spectral response changes slightly with temperature. Whether this is a problem for the HYPSO mission should be assessed. The temperatures inside the satellite in-orbit are, however, expected to be stable and stay within 15-25°C. The optical performance should therefore not change too much in-orbit due to temperature changes.

7 | HYPSO-1 pre-launch calibration

After the AIT process, the HYPSO-1 FM was delivered to KNA for integration with the satellite bus and final testing was performed. Then it was shipped to the launchpad and finally, launched into space. Before this, however, the instrument went through a laboratory calibration campaign to characterize the instrument and investigate the final data quality achieved prior to launch.

In Skauli et al. [83], a list of about thirty characteristics suggested for HSI specification is presented. A large calibration campaign can, however, be both time consuming and expensive to perform. As discussed in Section 2.3, Bowles et al. [85] suggested that the calibration cost should be consistent with the cost and need of the instrument and its application. As the HYPSO-1 HSI is a small instrument built with COTS components in a university environment, a smaller calibration campaign focused on verifying a set of the HYPSO-1 payload requirements was therefore planned. As the laboratory facilities, equipment and time were limited, known issues such as smile and keystone

characterization were prioritized over, for example, characterizing the PSF or doing detailed stray light characterization.

This chapter is based on **Paper 2**: "Pre-Launch Calibration of the HYPSO-1 Cubesat Hyperspectral Imager" [148], which describes the pre-launch calibration performed, shows the results from these tests and compare the calibration results to the requirements. Since the HYPSO-1 mission focuses on the spectral range of 400 to 800 nm, and uses a selected AoI of the sensor during nominal operations, the analysis performed is focused in this spectral range and inside this selected AoI (spectral pixel 428:1508, spatial pixel 266:950).

7.1 Wavelength calibration

For the wavelength calibration, the argon and mercury-argon spectral lamps were used in combination with the integrating sphere in the calibration lab at NTNU. The spectral lamps were mounted in a small input port of the sphere to ensure even illumination. The HSI was placed in front of the sphere outlet and 10 images were taken for each lamp with an exposure time that let the strongest peak in the image approach saturation. A combined image (full frame), with both the argon and the mercury lines, is shown in Figure 7.1. The full frame is used here instead of the selected AoI, to use as many spectral

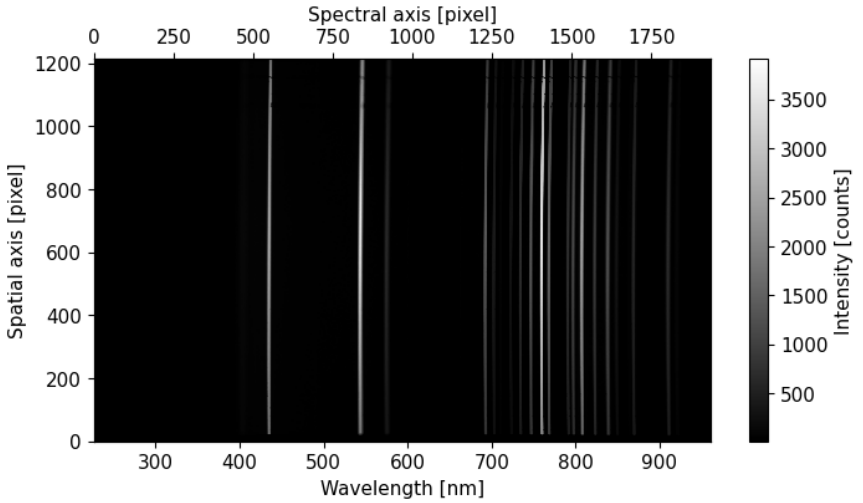

Figure 7.1: Spectral calibration frame, with both the argon and mercury emission lines.

lines as possible during calibration. In the figure it can be seen that the sharpest lines are found for the longer wavelengths (above 700 nm), indicating best spectral focus at these wavelengths (further discussed in Section 7.4).

For the wavelength-pixel relation, or wavelength calibration, different order polynomials were fit to the data. The spectral pixel position of each peak in the center row of the image (center of slit) was detected and compared to the known positions of the peaks to estimate the polynomial coefficients. The RMSE was calculated for each polynomial to determine the fit, as shown in Table 7.1. The third order polynomial was chosen to describe the wavelength-pixel relation since it minimized the RMSE without increasing complexity.

Table 7.1: RMSE of polynomial fits of different orders.

Order	RMSE
1	0.98
2	0.16
3	0.10
4	0.08

The third order polynomial fit is described by

$$\lambda \approx a_0 + a_1 \cdot p + a_2 \cdot p^2 + a_3 \cdot p^3, \tag{7.1}$$

where λ is the wavelength, p is the spectral pixel index and a_0, a_1, a_2 and a_3 are the spectral calibration coefficients. The calculated values of the coefficients are shown in Table 7.2.

Table 7.2: Spectral calibration coefficients.

Coefficient	Value
a_0	2.24e+02
a_1	3.84e-01
a_2	4.75e-06
a_3	-3.21e-09

From the spectral calibration coefficients the full spectral range on the image sensor was found to be 224 to 962 nm. The chosen wavelength range of 400 to 800 nm is located between spectral pixel 456 and 1502 on the sensor, which is within the pre-selected AoI.

7.1.1 Spectral calibration matrix

The pre-launch wavelength calibration was later expanded to calculate the wavelength-to-pixel relationship in all rows (also outside the nominal AoI), resulting in a spectral calibration matrix. This matrix is the same size as a full frame, and holds the correct wavelength for each pixel in the frame within the corresponding pixel in the spectral calibration matrix. When plotting some of the columns in the spectral calibration matrix, smile (also calculated simultaneously with keystone in Section 7.5) becomes visible, as shown in Figure 7.2.

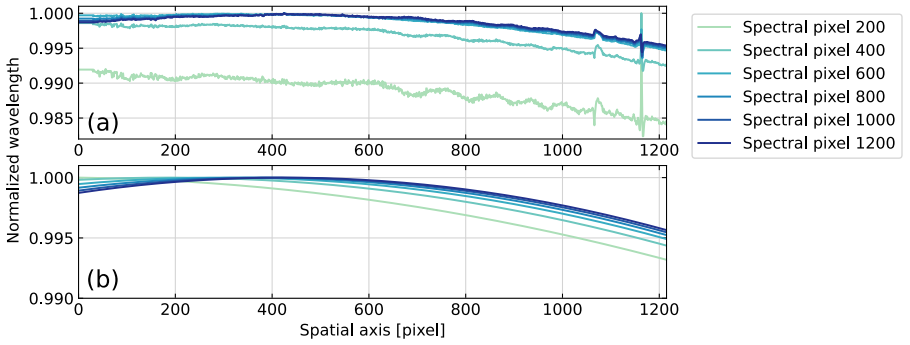

Figure 7.2: Selected columns in the spectral calibration matrix. (a) Original, and (b) corrected by normalizing and applying a second order polynomial fit (bottom).

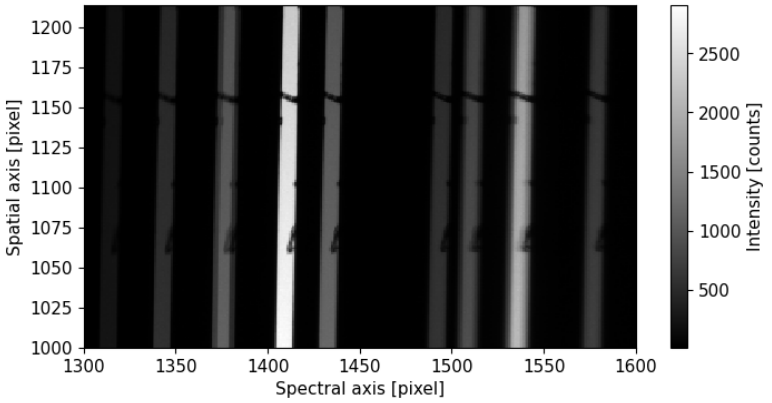

Figure 7.3: Zoomed in area, spectral pixel 1300:1600 and spatial pixel 1000:1216 (top of image), of the spectral calibration frame (Figure 7.1), showing particles/dust on the slit.

It can be noticed in Figure 7.2a that the lines look noisy and some spikes appear for the higher spatial pixels. When having a closer look at the calibration frame, Figure 7.3, it can be seen that there are particles of some sort on the slit in these spatial pixels disturbing the signal, which disturbs the peak detection. Since the lines in Figure 7.2a are expected to be curved (due to smile), a second order polynomial fit is applied to each column to correct for the noise and spikes, which is shown in Figure 7.2b.

7.2 Radiometric calibration

Radiometric calibration data was collected using the integrating sphere in the calibration lab at NTNU with the HSI placed in front of the sphere outlet. The HSI was set at 25 ms exposure time and 10 images were captured. A set of dark images were also taken using the same exposure time, but with the lens cap on the camera and all light sources in the room turned off. The dark images were used to estimate the average background signal in the images, which is described in Section 7.3.

The normalized signal in a frame, S [counts/sec], was estimated by averaging the 10 captured frames to reduce random fluctuations, removing the estimated background signal, and scaling the image by the exposure time. The radiometric calibration coefficient K was then calculated as

$$K = \frac{L}{S}, \tag{7.2}$$

where L is the absolute radiance value [mW/(m^2 nm sr)] known from the integrating sphere lamp. K is different for each pixel, and therefore also corrects for any inter-pixel variations, also known as Photo Response Nonuniformity (PRNU) [177]. The K matrix is visualized in Figure 7.4. The brighter areas, such as for wavelengths close to 400 nm and above 700 nm, indicate that a larger value is needed to convert from counts to radiance. This can lead to higher radiometric uncertainties after calibration for the shorter and longer wavelengths.

The uncertainty of the radiometric calibration coefficients was estimated by radiometrically calibrating a single frame, subtracting it from a reference frame, and dividing the difference by the reference values to obtain the percentage difference. The uncertainties for the center line in the spectrogram, and the mean radiometric uncertainty (calculated as the mean of the columns, as the target was uniform), are shown in Figure 7.5. The center line shows that noise fluctuations increase uncertainty for all wavelengths. The mean radiometric uncertainty shows higher uncertainty for

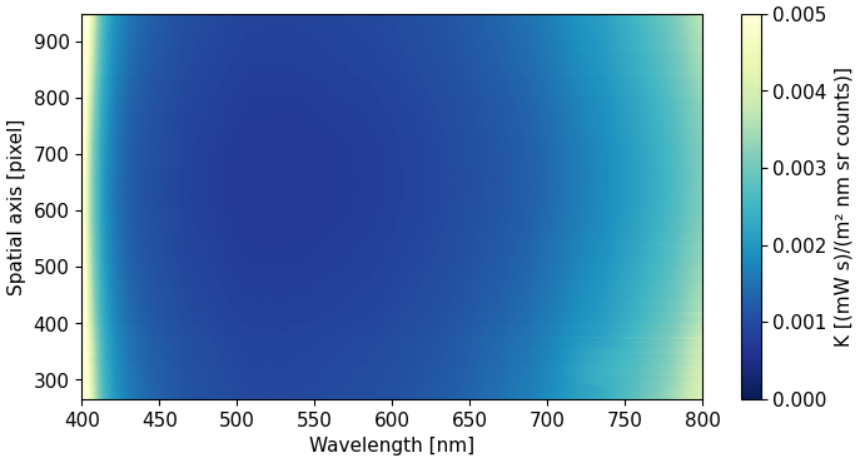

Figure 7.4: Radiometric calibration coefficients.

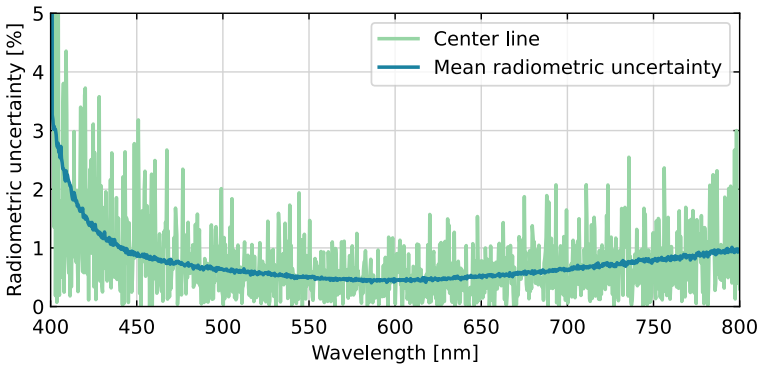

Figure 7.5: Radiometric uncertainty of calibration coefficients.

wavelengths below 450 nm and lowest uncertainty of around 0.5% between 500 nm and 600 nm. To estimate the full radiometric uncertainty of the final data, other factors should be included, such as linearity of the sensor response (both with increasing light intensity and exposure time), polarization sensitivity and uncertainties of the calibration source.

7.3 Sensor characteristics

Data from radiometric calibration (including dark images) and a set of images of the integrating sphere captured at different exposure times were used further to investigate the sensor characteristics. Average numbers are given throughout this section as the mean ± Standard Deviation (SD).

7.3.1 Sensor noise characterization

The background signal in the sensor was estimated by using the dataset of dark images. A single dark frame, Figure 7.6, shows that the distribution of background signal is mostly uniform across the sensor and has no significant discrepancies. The average value overall was found to be 8.01±0.8 counts out of a total of 4095 counts (12-bit image).

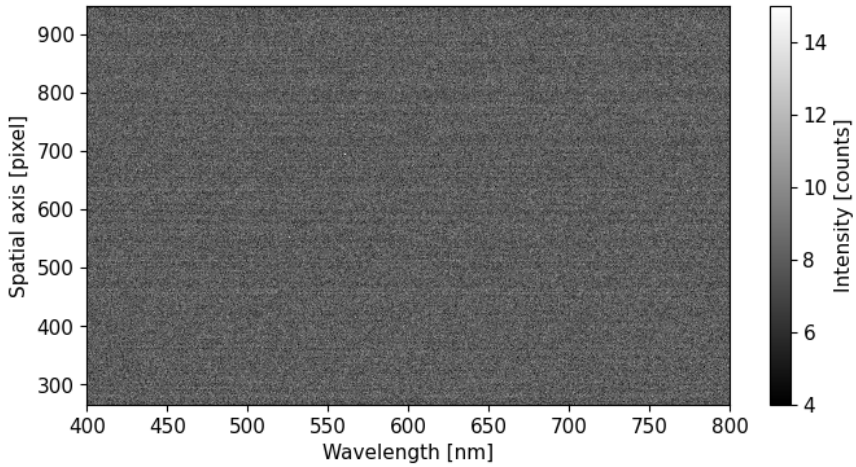

Figure 7.6: Single dark frame.

An average dark frame was calculated from the set of images, with an average value of 8.02±0.27 counts. This confirms that averaging the set of images reduces the noise fluctuations, and that the average background value in the frames is about 8 counts.

The same calculations were repeated for datasets of different exposure times. The increase in the average background value was found to be less than 0.2 counts from exposure times 5 ms to 500 ms. The increase in noise fluctuations with exposure time was also found to be negligible.

7.3.2 Radiometric response

The radiometric calibration data was also used to investigate the radiometric response. First, an example of the raw counts from a radiometric calibration frame can be seen in Figure 7.7. It shows that a vignetting effect is visible, making the center of the image brighter (meaning a stronger signal) and the edges darker. It also shows that no strong dust stripes or other optical deficiencies are immediately visible in the image.

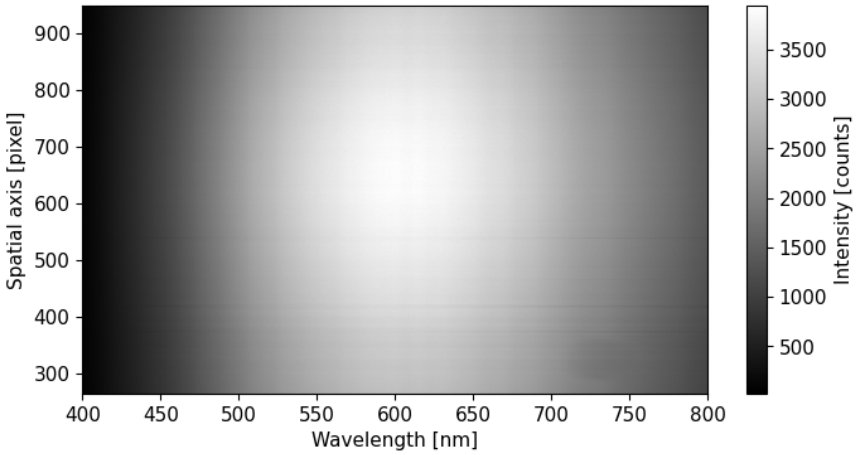

Figure 7.7: Radiometric calibration frame.

The absolute radiometric response was calculated as the average pixel response for each wavelength by taking the mean of the columns in the radiometric image. The smile effect was ignored as the absolute radiometric response was only used for visual inspection. The resulting absolute radiometric response is shown in Figure 7.8, together with the reference signal from the integrating sphere lamp, and the sensor and grating QEs. The absolute radiometric response near 400 nm is very weak, which is mostly due to low light level from the integrating sphere lamp at shorter wavelengths. The decrease in absolute radiometric response above 600 nm is mainly due to decreasing QE in the sensor and grating.

The relative radiometric response was calculated as the radiometric response divided by the absolute radiometric response, as described in Lenhard et al. [111], and is shown in Figure 7.9. This can be used to investigate the relative sensitivity of each spectral channel. The relative response shows a smudge at approximately 710 to 750 nm for pixels 300 to 400 on the spatial axis. The smudge causes a decrease in recorded signal, and might also

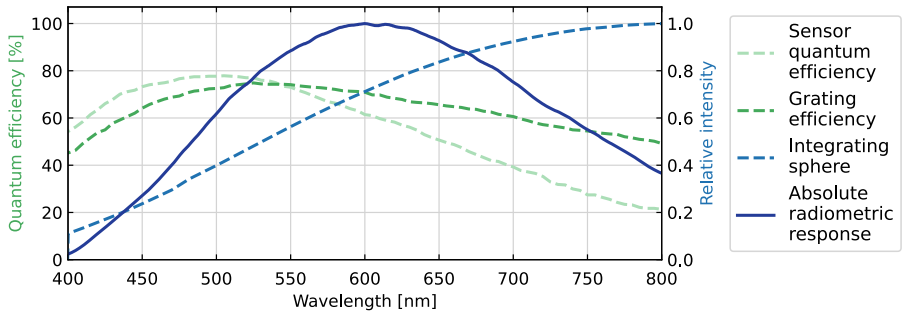

Figure 7.8: Absolute radiometric response, reference radiance from the integrating sphere tungsten halogen lamp and the QE of the sensor and the grating.

cause other distortions as the signal is smeared out. The signal decrease is compensated for by the radiometric calibration. It is worth noting its presence, however, as that area will have lower radiometric accuracy from the lower signal level, and possible unwanted effects from the smear. The brighter area in the center of the spatial axis comes from the vignetting effect, while the narrow horizontal stripes can indicate small dust particles on the slit.

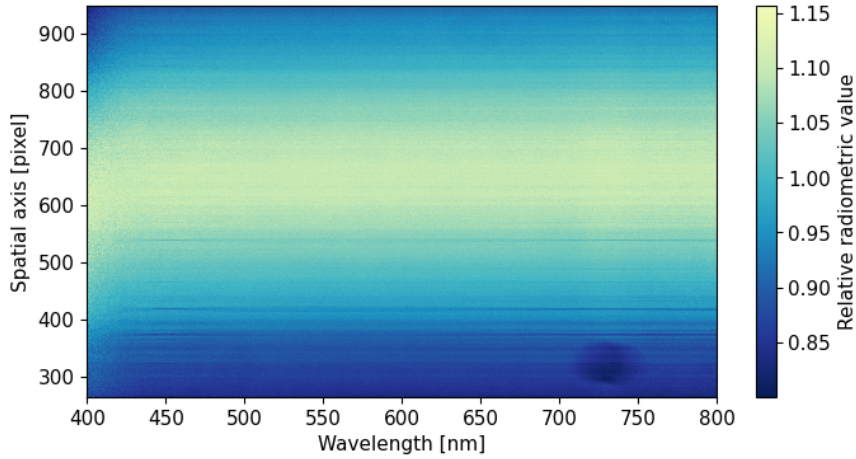

Figure 7.9: Relative radiometric response (radiometric response divided by absolute response). A smudge can be seen between 710 and 750 nm for pixels 300 to 400 on the spatial axis.

7.3.3 Photon noise

The photon noise was investigated using the center line in the set of images from radiometric calibration. The measured noise, shown in Figure 7.10, was estimated as the SD of each pixel in the line, and sorted according to signal strength (varying for different wavelengths).

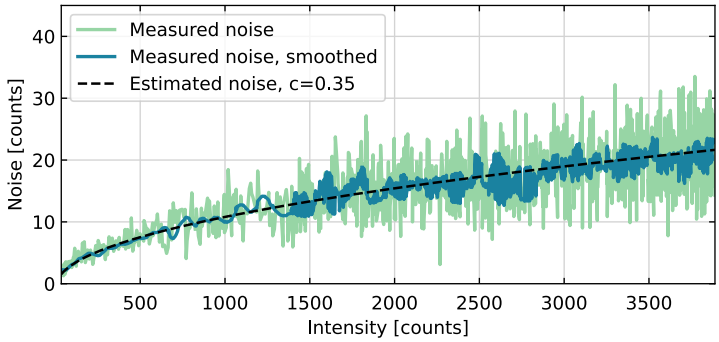

Figure 7.10: Photon noise, measured and estimated.

The theoretical photon noise was also calculated as the square root of the signal, S, and scaled with a proportionality constant c, following the relation

$$n_{\text{photon}} = c\sqrt{S}. \tag{7.3}$$

Choosing $c = 0.35$ gave the estimated noise to follow the measured noise, as shown in Figure 7.10. The measured noise was also smoothed (using a Bartlett window function) to make an easier comparison with the estimated noise.

7.3.4 Linearity of sensor response

The linearity of the sensor response with exposure time was examined using the set of images of the integrating sphere captured at different exposure times. First, a pixel that was nearly saturated in the highest exposed image was found. The value of this pixel was then plotted for each exposure time, as seen in Figure 7.11. It can be seen that measured points follows the linear fit, meaning that the assumption of a linear sensor response with exposure time holds.

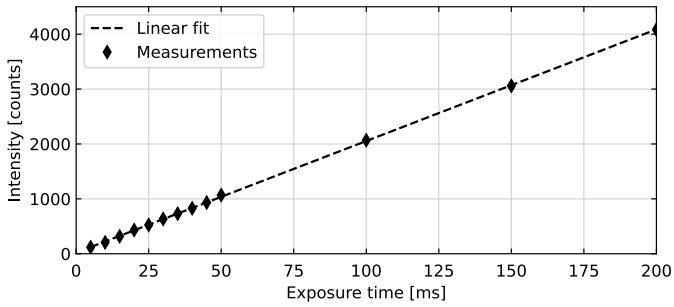

Figure 7.11: Linearity of sensor response with exposure time.

A nonlinear behavior is expected for low exposure times (less than 10 ms), where readout noise and dark noise fluctuations are expected to dominate. To explore this behavior, however, more measurements in this region are needed. For higher exposure times (more than 10 ms) the sensor response is expected to behave linearly, which is confirmed by the measurements.

7.4 Full width at half maximum

The FWHM was calculated using the argon and mercury-argon spectral calibration data. The peaks were identified, and the width at half maximum of each was found for several positions along the spatial axis. These include the mercury emission lines 435.85 nm and 546.07 nm, and the argon lines 696.54 nm, 706.72 nm, 738.40 nm, and 763.51 nm (other detected peaks known to be double peaks were excluded).

The resulting FWHM values are shown in Figure 7.12. It can be seen that they vary between approximately 3.5 and 4.5 nm in the desired spectral range. The average FWHM for the selected wavelengths along the spatial axis (different slit height positions) was calculated to be 3.93 ± 0.30 nm.

Figure 7.12 also shows that it is the shorter wavelengths that have the broadest peaks, while the peaks close to 700 nm are narrowest. This suggests that the optimal focus was set in favor of the longer wavelengths, and coincides with the visual impression from the spectral calibration frame in Figure 7.1. Most wavelengths follow a trend where the FWHM is lower at the edges of the spectrogram (low and high spatial pixels), while the line at 546.07 nm shows the opposite behavior. All values are below 4.5 nm, which is within the set requirement of 5 nm spectral resolution for the HYPSO-1 mission.

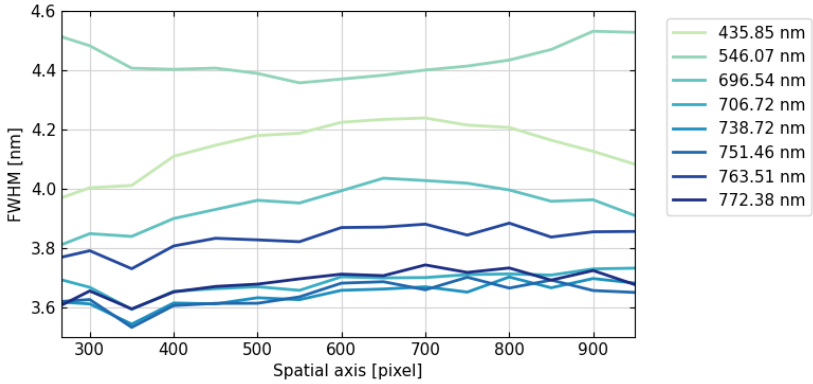

Figure 7.12: FWHM for argon and mercury spectral lines as a function of slit height.

7.5 Smile and keystone

As previously discussed, smile is the change of central wavelength as a function of field position, while keystone is change in magnification as a function of wavelength. Together, they create a warping effect on the recorded image. This can be measured by creating a set of control points on a grid recorded by the HSI. The points can then be mapped to a straight reference grid to unwarp the image. The map that is created can be further used to correct for smile and keystone in other images [104]. For the smile and keystone characterization, the Zeiss lens objective was used in combination with the striped pattern and the argon and mercury-argon spectral lamps to provide points (GCPs) in focus in the spectrogram at a close distance to the target, as described in Section 4.2.4. The location of the points were detected and used to make a two-dimensional quadratic polynomial distortion model. The model coefficients were then used to correct the spectrograms by mapping the pixels to the correct position and estimating new values with interpolation for non-integer pixel positions.

The pixel shift caused by smile before and after correction is shown in Figure 7.13. The curve before correction is not symmetric, which is due to spectral tilt as the slit was not aligned perfectly straight during assembly. Both smile and spectral tilt are reduced by the correction. The amount of smile was calculated as the difference between the minimum and maximum pixel positions for each of the spectral lines, and the average value was found to be 3.58 pixels before correction and 0.38 pixels after correction. The maximum smile was found to be 4.05 pixels and 1.05 pixels before and after correction, respectively.

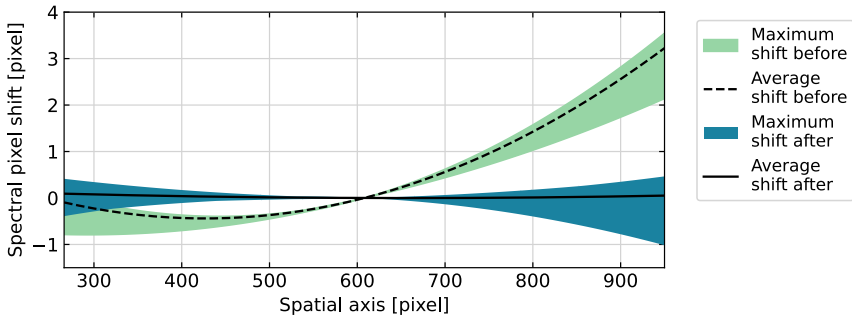

Figure 7.13: Pixel shift due to smile before and after correction. The maximum values (green and blue) shows the most extreme smile effects detected.

The maximum pixel shift due to keystone is shown in Figure 7.14. The keystone effect is less apparent than smile, but is also reduced by the correction. The amount of keystone was calculated as the maximum shift of the horizontal lines in the image. It was found to be 1.72 pixels before correction and 0.56 pixels after correction.

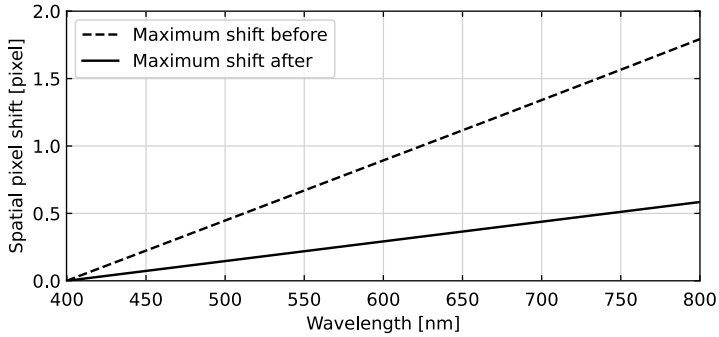

Figure 7.14: Maximum pixel shift detected due to keystone before and after correction.

The requirements for both smile and keystone after correction are less than 1 pixel shifted due to the distortion. The average smile effect after correction of 0.38 pixels is within the required value, while the maximum smile of 1.05 pixels is just above the requirement. Keystone is within the requirement with the maximum value of 0.56 pixels shifted after the correction.

Figure 7.15 shows the characterization data used before and after correction, which illustrates the effect of the correction. The full spatial axis, exceeding the AoI, is used and

the spectral axis is cropped to focus on a smaller set of wavelengths to better visualize the effect. Smile in the data before correction can be seen as the curved lines, while keystone is not as apparent. After correction, the curved lines appear straight, indicating less smile in the data.

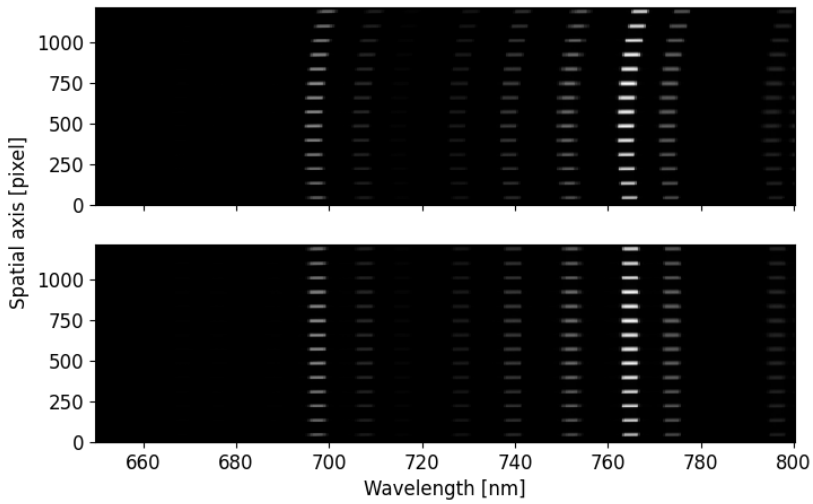

Figure 7.15: Cropped area of smile and keystone characterization data before (top) and after (bottom) correction. Note that the spatial axis is not cropped to AOI, showing a larger area than for intended use.

7.6 Polarization sensitivity

For polarization sensitivity analysis a linear glass polarizing filter (#46-574, Edmund Optics) was used. Polarization sensitivity was measured using the EM to limit unnecessary wear on the FM. The polarizing filter was mounted in front of the HSI observing the integrating sphere used for radiometric calibration. The filter was then rotated in steps of 15 degrees, in a range from 0 to 180 degrees. Sets of 10 spectrograms were acquired at each step, and averaged images from these sets used to estimate the final polarization sensitivity.

The measured signal, averaged for all pixels in the AoI varying with the polarizer angle is shown as crosses in Figure 7.16, together with a sinusoidal fit made to the data points. Some of the crosses deviate slightly from the sinusoidal shape, which is likely a result of the filter being rotated by hand.

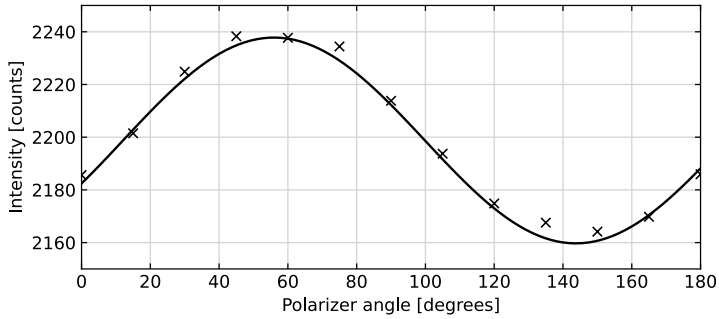

Figure 7.16: Sinusoidal fit (line) of averaged data points to polarization angle (crosses).

The polarization sensitivity, $P_{\text{sensitivity}}$, was then calculated as

$$P_{\text{sensitivity}} = \frac{P_{\text{max}} - P_{\text{min}}}{P_{\text{max}} + P_{\text{min}}},$$

where P_{max} is the maximum value [counts] and P_{min} the minimum value [counts] in each pixel for all polarization angles, as defined in the IOCCG report no. 13 [42]. The calculated polarization sensitivity for each wavelength is plotted in Figure 7.17, and shows that all wavelengths over 410 nm have a polarization sensitivity below 5%. The uncertainty of the polarization sensitivity was also estimated, as seen in Figure 7.18, using the SD of the polarization sensitivity calculated with the different datasets. The calculation showed an uncertainty below the required 0.2% in the range of 500 nm to 700 nm. Below 500 nm, and especially below 450 nm, the uncertainty increases substantially, and this should be taken into consideration if using these wavelengths for analysis. Above 700 nm it increases to about 0.25%, which is above the requirement of 0.2%, but still close to the required value.

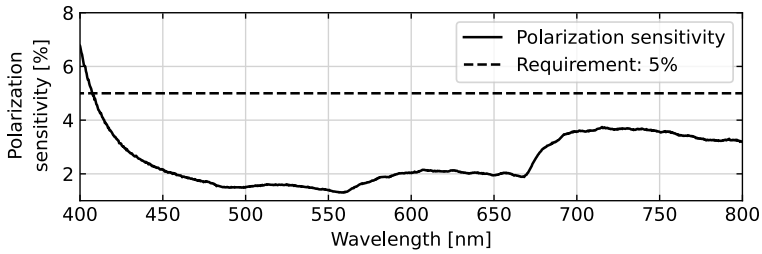

Figure 7.17: Calculated polarization sensitivity.

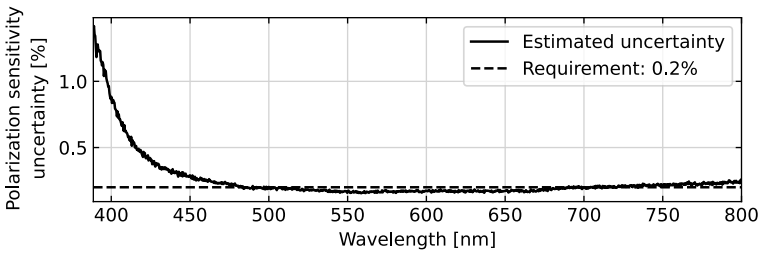

Figure 7.18: Uncertainty estimate of the calculated polarization sensitivity.

7.7 Spatial focus test

A simple test was done to initially investigate any large amounts of unexpected stray light in the system. A sharp transition from a bright to dark area was used as a target. This is commonly used for Earth observation instruments to simulate transitions from bright clouds to dark ocean [115]. The target was created using the halfmoon pattern (an enclosed black 3D printed target cap) illuminated by a light source. The dynamic range between the bright and dark area (ratio of bright to dark) was only about 100, suggesting that an improved set-up would be needed to properly investigate stray light. The data did, however, prove useful to inspect the spatial focus of the instrument.

The 3D printed halfmoon pattern is formed as a cylinder with the opening in one end half-closed, creating a sharp transition edge between the dark (closed) and bright (open) area. It was covered with black matte tape inside after printing to reduce internal reflections. The Zeiss lens objective was again used as the collimating unit with the 3D print fastened to one end. The length of the 3D print was made so that the sharp edge was in focus when attached to the collimating objective. The integrating sphere in the calibration lab at NTNU was used as the stable light source to minimize light fluctuations.

The resulting spectrogram is shown in Figure 7.19. The bright to dark transition can be seen at approximately spatial pixel 700. For the shorter and longer wavelengths at the edges of the spectrogram, the transition line becomes more blurry. This could be due to optical effects of the lenses since the sharpest response is expected to be in the center of the lens and more aberrations are expected at the edges. This should be kept in mind when analyzing the final data and using the shorter and longer wavelengths as it will affect the spatial resolution per wavelength.

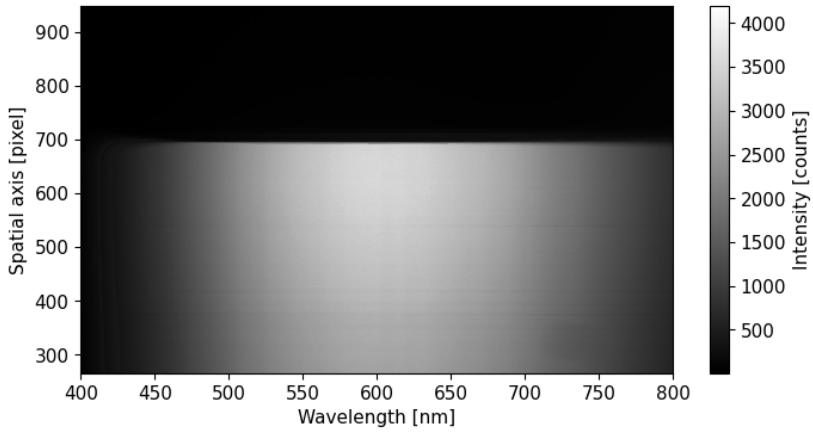

Figure 7.19: Captured frame of the black and white scene.

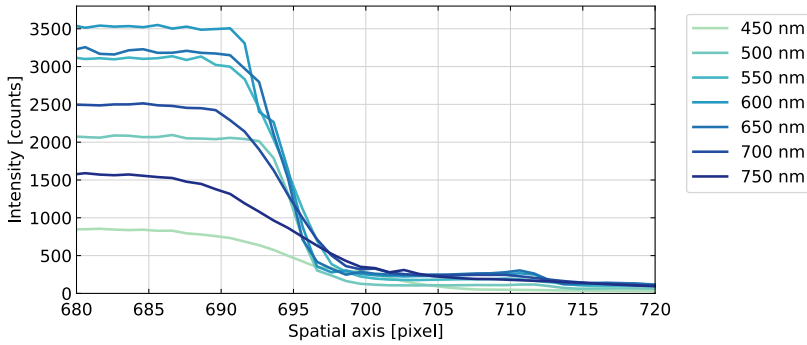

Figure 7.20: Lines showing defocus at shorter and longer wavelengths in the area close to the edge on the spatial axis.

Figure 7.20 shows a cropped view of the transition line for a set of wavelengths to better investigate how the steepness of the bright to dark transition varies with wavelength. The sharpest edge was found at 600 nm, which is the designed center wavelength, closely followed by the lines at 550 nm and 650 nm. For the shorter and longer wavelengths, such as 450 nm and 750 nm, however, the transition is more gradual and covers more than 10 pixels from the bright to the dark transition. This suggests that a sharp edge in the image is smeared out and results in poorer spatial resolution for the wavelengths considered. Simulations done with ray tracing software (Zemax) show the same trends (not shown here). The smallest spot size is at 600 nm and larger spot sizes at 400 nm and 800 nm.

In Figure 7.20 a small bump can also be seen for some of the wavelengths at approximately spatial pixel 710 nm. This could be caused by irregularities in the 3D printed part. A higher quality black and white scene is suggested to investigate this further. It is also worth noting that the Zeiss objective used as the collimating unit could also contribute to aberrations since the objective itself is not perfect. The test confirms that the design is optimized for 600 nm, and that more aberrations are expected at shorter and longer wavelengths than the center wavelength.

7.8 Summary of HYPSO-1 pre-launch calibration

The HYPSO hyperspectral imaging payload was calibrated and characterized prior to launch. The spectral and radiometric calibration coefficients and uncertainties were determined. The full spectral range available at the sensor was found to be 224 to 962 nm, and the desired spectral range of 400 to 800 nm was shown to be within the chosen AoI. The FWHM was found to be between 3.5 to 4.5 nm for all wavelengths, which allows spectral binning of 9 pixels to increase SNR without losing spectral resolution [29]. Sensor characteristics, such as background signal and noise in dark images, photon noise and linearity of the sensor response, were identified and the values found were as expected. A summary of the selected HSI requirements and the corresponding measured values is shown in Table 7.3, and shows that most values are within the requirements.

Table 7.3: Comparison of the selected HSI requirements and the measured values.

Parameter	**Requirement**	**Measured value**
Sensor response	Linear	Linear
FWHM	< 5 nm	Between 3.5 nm and 4.5 nm (3.93 nm on average)
Smile after correction	< 1 pixel	0.38 pixels (average), 1.05 pixels (maximum)
Keystone after correction	< 1 pixel	0.56 pixels
Polarization sensitivity	$< 5\%$	$< 5\%$ above 410 nm
Uncertainty of polarization sensitivity	$< 0.2\%$	$< 0.2\%$ in the range 500 to 700 nm

8 | HYPSO-1 in-orbit data

On Thursday January 13 2022 at 15:25 (UTC), the HYPSO-1 satellite launched into space with the SpaceX Transporter-3 rideshare mission together with 104 other small satellites [178]. At 16:28 (UTC) the same day the separation was confirmed, and on January 28 at 11:01 (UTC) the HYPSO team got the first contact with the satellite from the ground station at NTNU, and the room was filled with joy. The following months consisted of payload commissioning and testing, in parallel with further development of the satellite operations scheme, imaging campaigns and payload calibration and validation activities. A selection of images captured by HYPSO-1 during the first year can be seen in Fig. 8.1. The RGB composites show off the visual aspects of the images nicely. However, it only shows 3 of the available bands in each pixel, where the full spectral signature is available. In this chapter, data from the first (and following) months are presented, focusing on assessing the performance of the HSI using the in-orbit data.

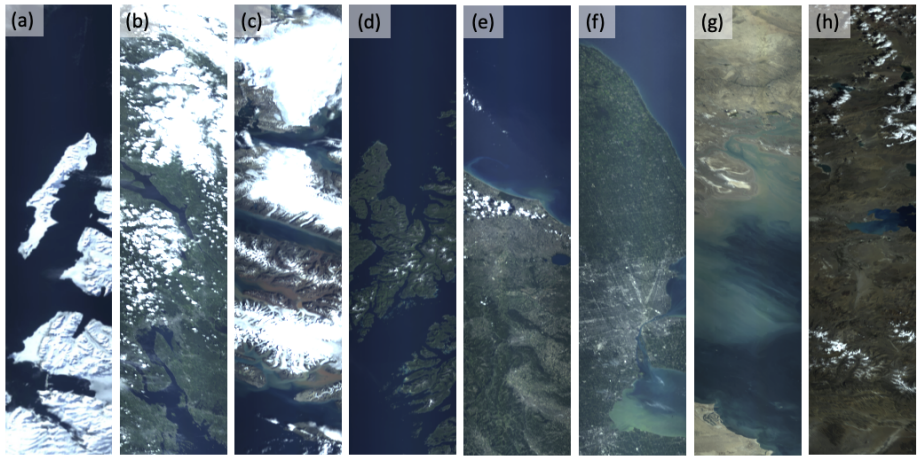

Figure 8.1: Panel of images taken by HYPSO-1, RGB representation of the hyperspectral cubes using wavelengths R=630 nm, G=550 nm and B=480 nm, with bandpass of 5 nm. (a) 2022-05-24 Svalbard, (b) 2022-07-08 Mjøsa, (c) 2022-07-18 Svalbard, (d) 2022-07-31 Andøya, (e) 2022-08-27 Erie, (f) 2022-09-12 Rome, (g) 2022-09-26 Kuwait, and (h) 2022-09-29 Tibet.

8.1 Comparing pre- and post-launch images

During the first months of operations, several datasets were captured by the HYPSO-1 HSI to assess different aspects of the optical performance. Some of the data was compared to data from the pre-launch calibration, to see if any differences between the pre- and post-launch data could be seen. Both the investigations done and their results are presented here. This section is mainly based on **Paper 6**: "Comparing pre- and post-launch images from the HYPSO-1 cubesat hyperspectral image" [179], and the spectral resolution analysis based on parts of **Paper 7**: "HYPSO-1 CubeSat: First Images and In-Orbit Characterization" [28].

An overview of the datasets used for this analysis is shown in Table 8.1. Dataset 0 is from the pre-launch calibration, and is used for comparison. Dataset 1 contains dark data collected by HYPSO-1 in-orbit both pointing up towards outer space and down towards the dark oceans. Dataset 2 is captured from above the Sahara desert, while dataset 3 is captured when pointing towards the moon. Datasets containing a frame denotes that only one frame/spectrogram was used, while a cube means that the full hyperspectral cube was used in the analysis. The cubes are normally following the HYPSO-1 nominal operations format, which only uses a selected AoI of the sensor (spectral pixel 428:1508,

spatial pixel 266:950) and a binning factor of 9 (binning by summation). The exception is dataset 3 of the moon, which is denoted as a full frame cube, meaning the full sensor (all pixels) and no binning was used.

Table 8.1: Overview of HYPSO-1 datasets.

Dataset	Date(s)	Description
0a	2022-03-18	Dark frame from pre-launch calibration
0b	2022-03-18	Radiometric calibration frame from pre-launch calibration
1a-1	2022-06-20	Dark cube, pointing up towards outer space
1a-2	2022-06-20	Dark cube, pointing up towards outer space
1b-1	2022-05-14	Dark cube, pointing down towards dark ocean
1b-2	2022-06-23	Dark cube, pointing down towards dark ocean
1b-3	2022-05-04	Dark cube, pointing down towards dark ocean
2a	2022-02-01	Sahara cube
2b	2022-02-01	Sahara frame
3	2022-10-11	Moon cube (full frame)

8.1.1 Dark images

Dark signal, here also referred as background values, is the signal recorded by the sensor when no light is present, and is mostly caused by thermally generated electrons collected by the sensor. Shifts in the mean dark signal can lead to systematic errors if not accounted for. The values depend on the residence time of the signals in the sensor and are also typically increasing with increasing temperature [180].

Several dark data cubes have been captured by HYPSO-1, both pointing up towards outer space and down towards the ocean during night time. Different exposure times have been used, as different exposure times are often used for observations. Other camera settings such as frames per second, number of frames etc. have been kept constant. The dark cubes captured only cover the AoI and are spectrally binned. For the comparison with dark pre-launch calibration data, the dark frame was also cropped to AoI and spectrally binned prior to the analysis. To investigate dark signal in the datasets, a histogram showing the distribution of pixel values in the frame is plotted, as seen in Figure 8.2. For the pre-launch dark calibration frame (dataset 0a), only 1 frame was used, while for the data cubes both the first and last frames (frame 0 and frame 955) in the cube are plotted.

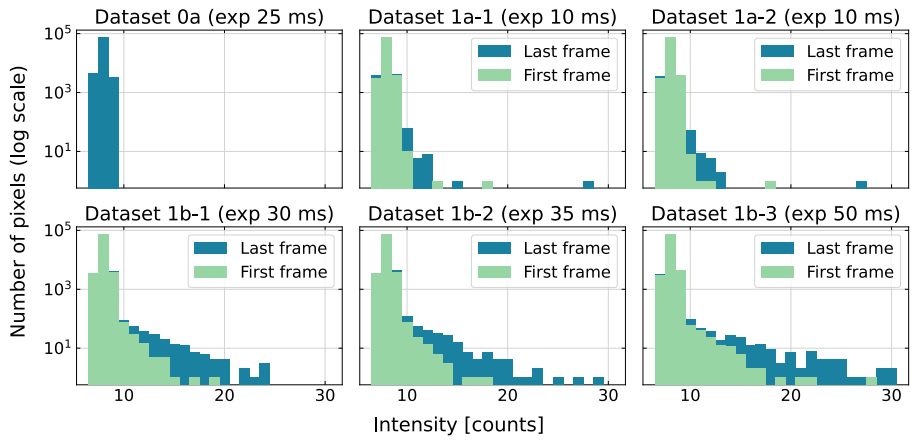

Figure 8.2: Distribution of the recorded raw values in the dark datasets (described in Table 8.1).

During a capture, power is consumed and heat is generated and released. Logs show that the temperature typically increases from 16 to 22 degrees Celsius while capturing a hyperspectral data cube with exposure time of 30 ms. It can be seen in Figure 8.2 that the last frame contains higher maximum values, and a larger amount of higher values than the first frame for all data cubes. This is consistent with background values increasing with increasing temperature. In addition, it can be noted that the data cubes with longer exposure times show higher values in both the first and last frames, suggesting that the mean dark signal also increases with exposure time. It is also worth noting that the dark images captured in-orbit might also contain signal from stars etc., contaminating the dataset.

Hot pixels

Hot pixels are pixels that record higher values than what is expected from the incoming light. An investigation of hot pixels in the HYPSO-1 data was done using the dark data cubes. A pixel value of two times the average value in the first frame was used as a threshold, and all pixels with values above this threshold here counted as hot pixels.

Hot pixels were marked in every frame in the data cube, and the number of hot pixels counted are shown in Table 8.2. Case 1 is the number of pixels in the cube that registered a hot pixel value in any frame, case 2 is the number of pixels that registered a hot pixel value in more than half of the frames in the cube, while case 3 is the number of pixels

that registered a hot pixel value in all frames in the cube. Since only one frame was used from the pre-launch calibrated data, it is only shown for case 1. In addition, the pixel location of the hot pixels were marked so that they could be compared between different datasets. As seen in the table, no pixels recorded hot pixel values in all of the data cubes.

Table 8.2: Hot pixels counted in dark datasets. Case 1 is all hot pixels counted in any frame in the cube, case 2 is all hot pixels counted in more than half of the frames in the cube, and case 3 is all the hot pixels counted in every frame in the cube. The datasets are described in Table 8.1.

Dataset	Case 1: # hot pixels in any frame	Case 2: # hot pixels in half of the frame	Case 3: # hot pixels in all frame
0a	0	-	-
1a-1	2	1	1
1a-2	4	3	1
1b-1	46	18	2
1b-2	41	17	2
1b-3	98	45	6
All	0	0	0

The results in Table 8.2 suggest that number of hot pixels increases with temperature and exposure time, and that some hot pixels are random while others last for the whole capture, but that they are all reset between each capture. That there are more hot pixels appearing for half of the frames than for all the frames in the cube suggests that some of the hot pixel values are not constant, but randomly jumping, known as RTSs [180]. That the hot pixels are not consistent and recorded in the same location every time makes it harder to correct pixels with a hot pixel mask or similar, since a new mask would have to be created for each capture.

8.1.2 Spectrogram artifacts

Some artifacts, such as a blob/smudge and dust stripes, were observed in the spectrogram before launch, as seen in Figure 8.3a, which shows the full frame spectrogram from radiometric calibration in the lab (presented in Section 7.3.2). Vignetting is, as previously mentioned, visible at the edges. Two dust stripes can be seen in the top of the image at spatial pixel 1050 and 1140, and a small smudge can be seen at spatial pixel 300 and spectral pixel 1300 (wavelength 720 nm). This smudge is more prominent in Figure 8.3b which shows the relative response of the calibration frame, zooming in on the location with the smudge in the box. The relative response is calculated by dividing the full

frame by the absolute response, where the absolute response is the average signal per wavelength (average row in the frame), as described in Section 7.3.2. In the bottom of both images a darker edge can be seen, which marks the lower edge of the slit. The slit is not centered perfectly, which results in the lower edge being visible in the spectrogram.

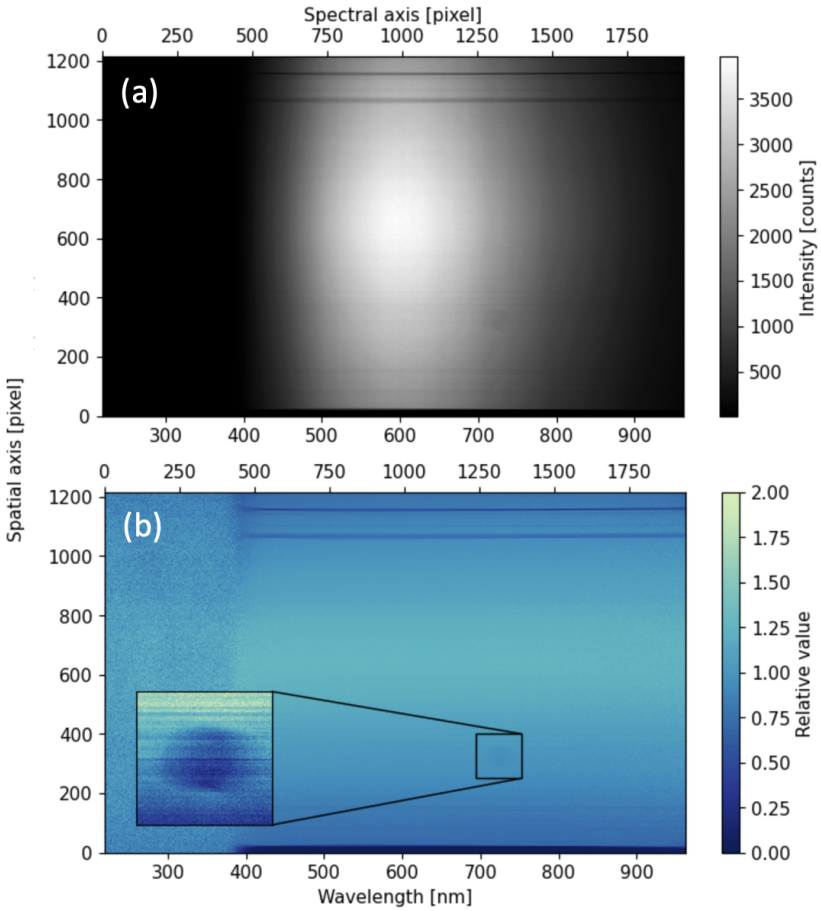

Figure 8.3: (a) Radiometric calibration frame from pre-launch calibration (dataset 0b). (b) Relative response of radiometric calibration frame. Smudge can be seen at spatial pixels 250:400 and spectral pixels 1240:1390

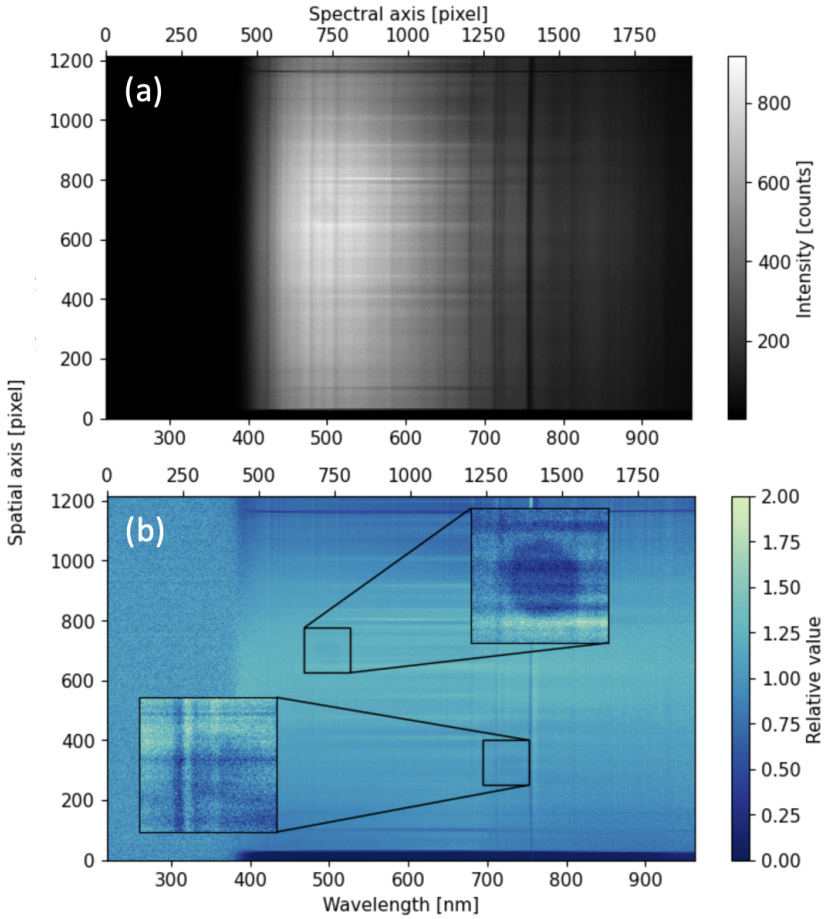

Figure 8.4: (a) Sahara frame (dataset 2b). (b) Relative response of Sahara frame. The first smudge can be seen at spatial pixels 250:400 and spectral pixels 1240:1390, and the second smudge at spatial pixels 625:775 and spectral pixels 650:800.

HYPSO-1 acquired images of the Sahara Desert, to provide data from a nearly uniformly illuminated scene for comparison to the ground calibration data. Figure 8.4a shows one of these full frame spectrograms of the Sahara Desert. The surface of the desert is quite bright and uniform, however, as it is not perfectly uniform some features are present. This makes the signal vary slightly across the slit, which appears as horizontal features in the spectrogram. Atmospheric features, which are also visible in the data, cause absorption lines which can be seen as vertical stripes in the frame.

Overall, the intensity in the captured image is lower in the Sahara image than in the pre-launch calibration image, giving lower SNR, meaning that noise might be more apparent in the data. One horizontal dust stripe is visible at spatial pixel 1150, while the second stripe seen in the calibration data is not as apparent. Either it has disappeared, or it might be mixed with the features seen across the slit. A smudge appears, but this time around spatial pixel 700 and spectral pixel 700 (wavelength 500 nm). The first smudge seen in the calibration data is not as distinguishable in the Sahara frame. This might be due to the lower light level, so that the smudge feature disappears in the noise, or it might no longer be present. Zoomed in boxes on both locations are marked in Figure 8.4b, which shows the relative response of the Sahara frame.

8.1.3 Spectral shift

During the pre-launch calibration, spectral calibration coefficients were found to determine the wavelength corresponding to each pixel element on the sensor. Since the payload must endure strong forces during launch, and small movements of components can affect the optical path, any spectral shift that can be observed after launch should be reported and used to correct the spectral calibration. For this, Fraunhofer lines can be useful. These are known absorption lines from the Sun spectrum, as seen in Figure 8.5. Since these absorption lines appear at known wavelengths, they can be used to assess the spectral calibration post launch, and detect potential spectral shifts in the spectrogram.

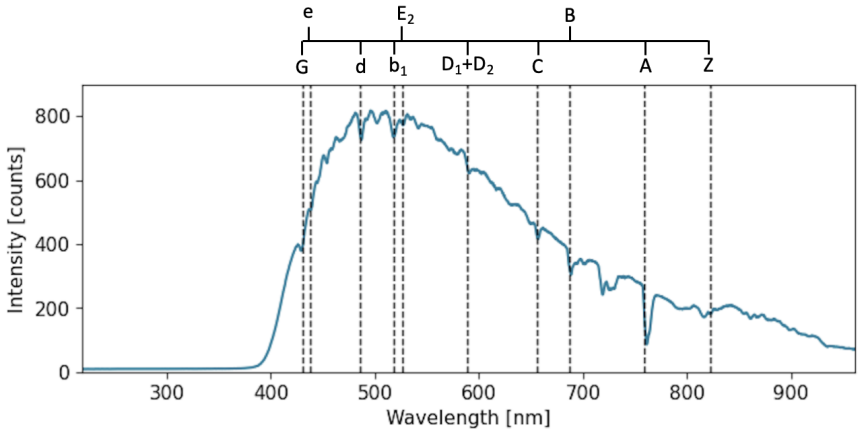

Figure 8.5: Center row/spectrum in the Sahara full frame (dataset 2b), with the Fraunhofer lines marked with dashed black lines in the plot.

A spectral shift can also be estimated by monitoring the oxygen A-band, with center wavelength at 759.37 nm [181, 182]. To determine the shift post launch, the difference of the center position of the band is calculated. When comparing with pre-launch data, however, the wavelength location must be used, since HYPSO-1 did not acquire any data with atmospheric absorption lines prior to launch.

The Sahara frame (dataset 2b) is again used to investigate the spectral response. The center of the spectrogram is used to minimize smile effects, and 50 rows are averaged to minimize noise. The spectrum, plotted together with known Fraunhofer lines, is shown in Figure 8.5. The dips in the recorded spectrum were detected and compared with the Fraunhofer lines, presented in Table 8.3. The largest difference can be found at the oxygen A-band, where the reference value is 759.37 nm and the recorded value 761.6 nm. The oxygen absorption lines come from absorption in the Earth's atmosphere, and varies as a function of height/pressure [183]. This leads to varying center wavelength of the bands, which can explain some of the variation seen here. There is no clear trend in the calculated differences, they are both positive and negative, and vary across the spectrum. This suggests that no clear spectral shift is detected.

Table 8.3: Spectral shift, detected dips compared with known Fraunhofer lines.

Designated letter	**Fraunhofer wavelength [nm]**	**Recorded wavelength [nm]**	**Difference [nm]**
G[a]	430.8	429.2	1.6
e	438.4	438.3	0.1
d	486.1	487.0	-0.9
b_1	518.4	518.1	0.3
E_2	527.0	527.2	-0.2
D_1+D_2	589.3	590.6	-1.3
C	656.3	657.0	-0.7
B	686.7	688.7	-2.0
A	759.4	761.6	-2.2
Z	822.7	822.4	0.3

[a] Average value of G(Ca) 430.774 nm and G(Fe) 430.790 nm.

From the lines investigated, the RMSE value is 1.21, which is quite large compared to the spectral calibration RMSE values reported in [148] (**Paper 2**). Spectral calibration coefficients of second order were applied to the data, as suggested in [150] (**Paper 3**), which may introduce some inaccuracies. However, errors might also come from noise, making it hard to detect the exact location of the absorption lines, specially for

wavelengths with low SNR. Higher variation in the in-orbit data may also be caused by variations in the atmosphere, or from features of the Sahara Desert in the dataset.

8.1.4 Smile

The Sahara frame (dataset 2b) was also used to investigate smile in the in-orbit data. Five absorption lines, the Fraunhofer lines (marked in in Figure 8.5) G (429 nm), B (688 nm), A (761 nm) and Z (815 nm), and one line between the B- and A-band (719 nm), were detected

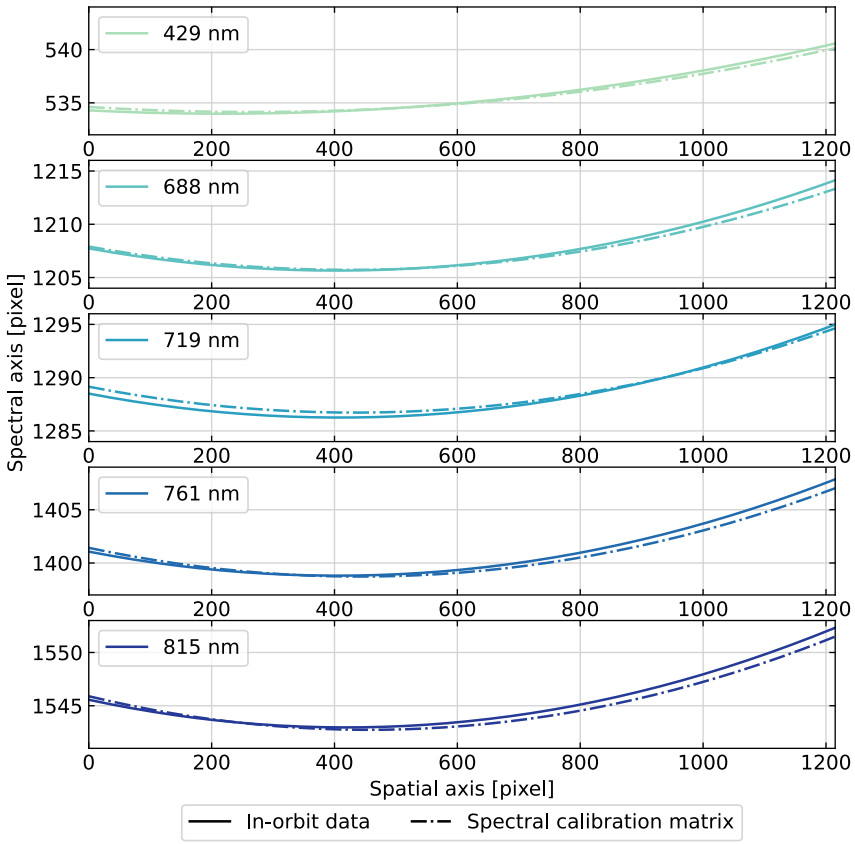

Figure 8.6: Smile in five absorption bands from the Sahara frame (dataset 2b) (solid lines) and corresponding wavelengths in the spectral calibration matrix (dashed lines). The absorption lines are Fraunhofer lines G (429 nm), B (688 nm), A (761 nm) and Z (815 nm) and one line between the B- and A-band (719 nm).

in each row. Smoothing was used to reduce noise and the spectrum was inverted to detect position of the peaks instead of dips/valleys. A second order polynomial fit was made to the spectral pixel position for each peak across the slit (spatial axis), and plotted as a solid line in Figure 8.6. The pixel positions of the same wavelength in the spectral calibration matrix is plotted in a dashed line for comparison.

It can be seen that the lines follow each other closely, meaning that the smile is similar before and after launch. There are small deviations however, such as for the first spatial pixels for 719 nm and the last spatial pixels for 815 nm. This could either suggest that there are minor differences before or after launch, or come from other effects such as vacuum in space in the in-orbit data, or from the polynomial fits of the smile curve in post processing. Here, smile for the full spatial axis is shown, and is between 8 to 10 pixels for the full range. Within the selected AoI (spatial pixel 266 to 959) smile is about 4 pixels. This is comparable values to the detected smile found from the pre-launch data (Section 7.5), where the maximum value was reported to be 4.05 pixels within the AoI, and to smile values of about 10 pixels later shown in Section 8.2.2.

8.1.5 Spectral resolution

Spectral resolution of an HSI is typically measured in the laboratory prior to launch, as described in Chapter 7 for HYPSO-1. A method to estimate spectral resolution in-orbit is to compare the recorded spectrum with a reference spectrum [184]. The reference spectrum is convolved with a simulated instrument response at different spectral resolutions to produce a simulated spectrum for each spectral resolution. These spectra are further compared to the recorded spectrum by HYPSO-1, and the most similar one gives an indication of which spectral resolution HYPSO-1 achieves.

Here, the Solar spectrum (1985 Wehrli Standard Extraterrestrial Solar Irradiance Spectrum) with known Fraunhofer lines is used as the reference spectrum, while the recorded spectrum is reflected light off the Moon (dataset 3). The spectral range from 430 nm to 780 nm is investigated due to low amounts of recorded signal below 430 nm, and to avoid second order effects appearing above 780 nm. The instrument response is simulated as a perfect instrument response, represented by a triangular function of different half-widths to represent different spectral resolutions. The solar spectrum convolved with a set of instrument responses is shown in Figure 8.7. For wider triangular functions the peaks that are close together get merged. This is easily observed in the 10 nm resolution response (dark blue line) in the figure.

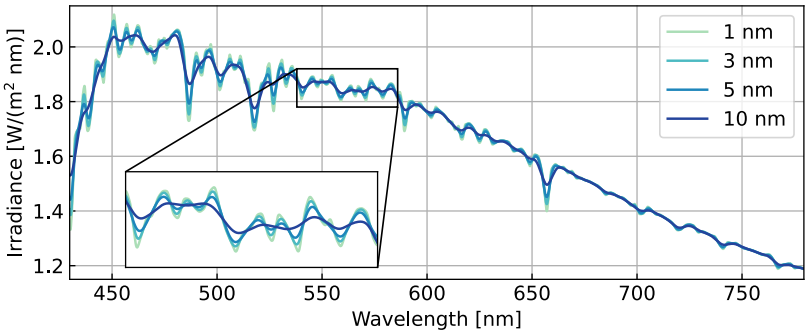

Figure 8.7: Convolved reference spectra. Solar irradiance spectrum at 1 nm resolution convolved with a set of instrument responses to obtain simulated solar irradiance spectrum at different spectral resolutions.

HYPSO-1 can capture data with and without binning. During nominal operations, binning of 9 spectral pixels by summation is applied. Binning data reduces noise and data size. However, binning spectral pixels can also affect the spectral resolution. The spectral resolution is therefore estimated for both full resolution data (image of the Moon, dataset 3), and the same dataset with binning applied. Another method to reduce noise when imaging uniform areas is to average the signal from consecutive frames. 10 frames are therefore averaged and compared to the original and binned data in Figure 8.8. Only the center of the slit image is used to avoid smile effects. It can be seen that 1 full resolution

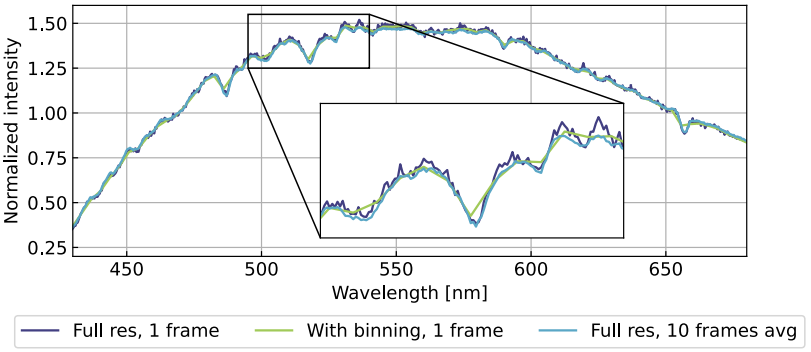

Figure 8.8: Raw spectrum of the Moon captured by HYPSO-1, with and without binning (spectrally binning 9 pixels). Reducing noise by averaging 10 frames (without binning) is shown in light green. Normalized intensity is recorded digital counts divided by the mean value.

frame has more noise fluctuations than both the 10 frames average and the binned data, and that the binned data is slightly worse at resolving the curves in the spectrum due to less datapoints.

For further analysis, a low-pass filter was applied to smooth the full resolution data to reduce noise, and a high-pass filter applied to both the HYPSO-1 data and the reference data to remove slow intensity changes. The datasets are then normalized by scaling with their maximum values. The resulting filtered and normalized responses of the reference spectrum and full resolution data (1 frame) are shown in Figure 8.9, showing comparable features from the Fraunhofer lines in the datasets.

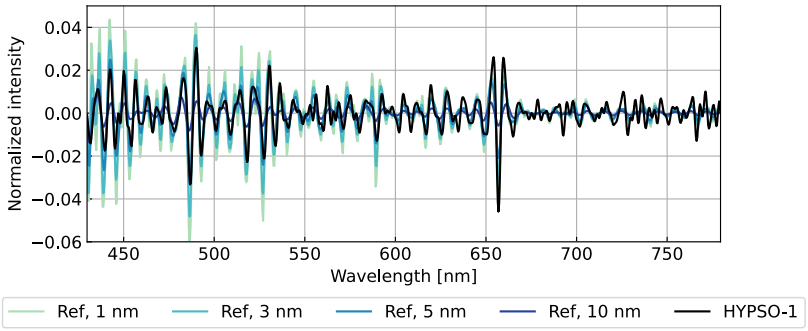

Figure 8.9: Comparison with reference spectra. HYPSO-1 data (black) and solar spectrum at different simulated spectral resolutions (shades of blue), after filtering and normalization.

The solar spectrum was simulated at resolutions between 3.3 nm (theoretical limit of HYPSO-1) and 10 nm, with 0.1 nm steps. The spectra were compared by using RMSE between the HYPSO-1 spectrum and reference spectra, and best fit determined as the one with lowest RMSE value. The results are presented in Table 8.4. The solar spectrum with spectral resolution of 5.4 nm was found to be the best fit within the range of 430 nm to 780 nm for the full resolution data (1 frame) and 5.6 nm when 10 frames were averaged first. With binning, the same analysis gives the average spectral resolution over the same range to be 8.2 nm.

It is expected that the spectral resolution varies with wavelength, as shown in Section 7.4, where it was measured to be between 3.5 and 4.5 nm for HYPSO-1 prior to launch (for full resolution data). The best resolution was found above 700 nm, while wavelengths between 430 nm and 700 nm had resolution calculated to be roughly between 4 nm and 4.5 nm. The analysis here was therefore repeated for only parts of the spectra at the time (50 nm steps), with resulting best fit spectral resolution and RMSE of the fit also

presented in Table 8.4. The highest (lowest number) estimated spectral resolution of the full resolution data (both 1 frame and 10 frames average) is 3.4 nm, found between 630 nm and 680 nm and 730 nm and 780 nm, which is close to the theoretical limit of 3.3 nm. The lowest (highest number) for the full resolution data is 6.6 nm (1 frame) and 7.2 nm (10 frames average), which is found between 530 nm and 580 nm. This coincides with the trends seen in Section 7.4.

For the binned data, the highest spectral resolution is found at 730 to 780 nm, and is 4.0 nm, while the lowest is found at 430 to 480 nm to be 9.60 nm. Overall, the resolution is found to be best at the longer wavelengths (above 600 nm), and worse for the binned data. This also fits with what is presented Section 7.4, where the longer wavelengths have better spectral resolution. In the range 730 to 780 nm, the estimated spectral resolution is worse for the full resolution single frame than the binned data. This can be due to the high noise level in the data in this range. The signal recorded for short and long wavelengths is relatively low, as seen in Figure 8.8, resulting in more noise in this range.

Table 8.4: Estimated best fit of spectral resolutions in different parts of the spectral range, together with the corresponding RMSE value for full resolution and binned (9 pixels spectrally binned) data.

	Spectral resolution ± RMSE		
Spectral range	**Full resolution, 1 frame**	**Binned, 1 frame**	**Full resolution, 10 frames avg**
430-480 nm	5.9 ± 0.0047 nm	9.60 ± 0.0064 nm	6.0 ± 0.0030 nm
480-530 nm	5.0 ± 0.0052 nm	6.60 ± 0.0035 nm	5.2 ± 0.0038 nm
530-580 nm	6.6 ± 0.0042 nm	8.20 ± 0.0032 nm	7.2 ± 0.0018 nm
580-630 nm	5.4 ± 0.0028 nm	5.80 ± 0.0035 nm	5.4 ± 0.0028 nm
630-680 nm	3.4 ± 0.0058 nm	5.80 ± 0.0047 nm	3.4 ± 0.0041 nm
680-730 nm	3.9 ± 0.0035 nm	4.10 ± 0.0034 nm	4.2 ± 0.0018 nm
730-780 nm	5.7 ± 0.0053 nm	4.00 ± 0.0033 nm	3.4 ± 0.0027 nm
430-780 nm	5.4 ± 0.0045 nm	8.2 ± 0.0042 nm	5.6 ± 0.0033 nm

The RMSE value gives insight into how large deviation was found between the solar spectrum of estimated resolution and the measured HYPSO-1 spectra, with low RMSE values meaning similar spectra. However, mismatch between the spectra can also come from different intensities not being fully filtered out, leaving residue from the reflected light of the scene (the Moon), or from spectral shifts between the spectra. It is therefore important to make sure the spectra are properly filtered and aligned before the analysis. One reason for the RMSE varying between the different spectral ranges can be due to

different features at different locations in the spectrum, making some regions easier to match up than others. It can be noted that the 630 to 680 nm range has high RMSE compared to the other ranges, most likely due to few features being present in the Solar spectrum in this region. The values are also generally higher for the single full resolution frame than for the 10 frames average, indicating that averaging frames reduces noise and makes features in the spectrum more visible.

The estimated spectral resolution is overall slightly worse than what was found during pre-launch calibration. This can be due to the pre-launch measurements using spectral lamps, looking at few spectral lines at the time and estimating the spectral resolution by calculating the FWHM. The method used here, comparing the full recorded spectrum with simulated solar spectra of different resolutions, gives an indication of what spectral resolution can be achieved, but might not be as accurate as using spectral lamps and calculating the FWHM. The results presented here shows that a spectral resolution of about 5 nm is a realistic performance of the instrument in some spectral ranges, but further investigations should be done to estimate the exact spectral resolution as a function of wavelength with the in-orbit data.

8.1.6 Spatial shift

From pre-launch radiometric calibration (dataset 0b), shown in Figure 8.3, the edge of the slit is visible at the lower edge of the frame, and two horizontal stripes are visible at the top of the frame. In the Sahara full frame (dataset 2b) in Figure 8.4, the edge of the slit is again visible at the lower edge of the frame, while only one of the horizontal stripes are visible at the top. The exact spatial pixel location of the edge of the slit and the horizontal stripes are, however, not the same in the two frames.

The pixel location of both features (edge of slit and horizontal stripe) were investigated at spectral pixel 968 (corresponding to 600 nm), located approximately in the center of the spectrogram. The lines (column in the spectrogram) were normalized by the maximum value then smoothed, as shown in Figure 8.10. The solid lines show the lines before smoothing, while the dashed lines are smoothed. The areas around the features were isolated to better visualize the shifts. The shift was calculated as the difference in pixel location of 50% of the normalized intensity for the edge of the slit (left in Figure 8.10). While for the horizontal stripe which appears as a dip in the plotted line (right in Figure 8.10) the shift was estimated as the change in pixel location of the minimum value of the dip.

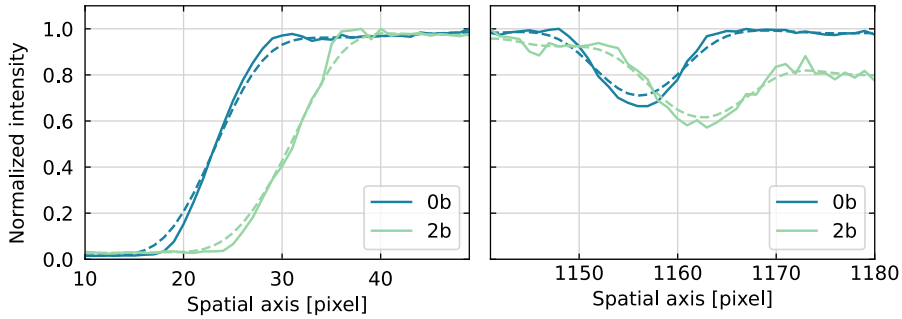

Figure 8.10: Spatial shift. Edge of the spectrogram from bottom of the spectrogram (left), and horizontal line from the top of the spectrogram (right). Solid lines are before smoothing while dashed lines are smoothed.

The shift was found to be 7 pixels for both the edge of the slit and the horizontal line. This was repeated for all wavelengths in the visible range (here 400 nm to 800 nm was used), and the average shift also found to be 7 pixels. Due to low signal at the edges of the spectrogram (below 400 nm and above 800 nm) the features and their shifts were disappearing in noise and therefore not detectable. That a shift of 7 pixels is observed both in the upper and lower part of the spectrogram for all wavelengths suggests that either the slit (assuming the horizontal line is dust on the slit) has moved, or the camera sensor has moved relative to the optical train. The slit used is a COTS component, mounted inside a disc with 0.1 mm extra space within the mount. It is therefore likely that the shift observed is caused by the slit having moved inside its casing during launch.

8.1.7 Summary of features seen in post-launch images

Overall, the hyperspectral data from HYPSO-1 appears as expected, except for the new smudge discovered at spatial pixel 700 and spectral pixel 700 (wavelength 500 nm) and the spatial shift of 7 pixels. The dark images show that most values are at around 8 counts, which is the estimated background value from pre-launch calibration. Higher background counts are detected when longer exposure times are used, which can be due to higher temperature increase induced with longer exposure times. When investigating hot pixels, some are recorded, and the higher numbers again found for the data captured with longer exposure times. Hot pixels in different datasets are, however, not located at the same pixels, which makes a general correction algorithm harder to provide.

No spectral shift was detected, but monitoring the spectral position of Fraunhofer lines or the oxygen A-band can be useful to ensure no spectral drift in-orbit. The spectral resolution was estimated to be around 5.5 nm on average for full resolution data, and 8.2 nm for binned data (binning of 9 pixels). This is slightly higher than recorded during pre-launch calibration, but that is most likely due to the method used. Corrections for the spatial shift can possibly be mitigated by shifting the calibration coefficients (which might affect the accuracy of the calibration, this must be assessed during correction), while the smudge should be characterized by performing radiometric calibration in-orbit. Adjusting the radiometric calibration in-orbit could also correct the spatial shift. This is addressed in the next section.

8.2 HYPSO-1 post-launch calibration and corrections

In this section, a test image captured by HYPSO-1 in-orbit is used to show how post-launch calibration and correction affects the HYPSO-1 data. The image used here is from a data cube captured outside of the Trondheim fjord (Frohavet) on 2022-05-07, as seen in Figure 8.11. The average frame of a selected number of frames (here 20 frames were used) in a uniform ocean area (marked in the white box in Figure 8.11) is used as the test image shown in Figure 8.12a).

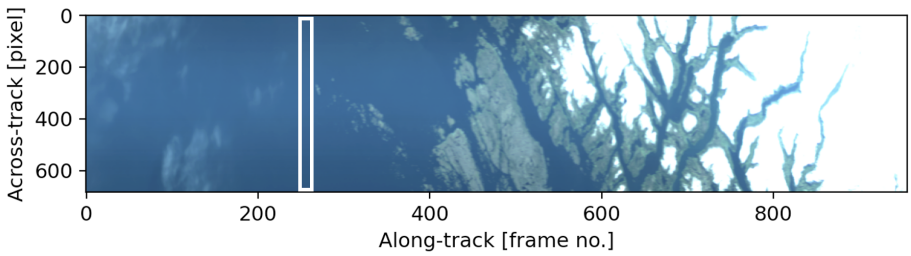

Figure 8.11: Raw data cube (not calibrated) from Frohavet, 2022-05-07. RGB representation using wavelengths R=630 nm, G=550 nm and B=480 nm, with bandpass of 5 nm. White box marks uniform ocean area (frame 240 to 260).

To further investigate features in the frame, the relative radiometric response is calculated (as described in Section 7.3.2). In short, the relative radiometric response is the radiometric response (the values in the image) divided by the absolute response (the average row in the image), leaving the differences in the response between the rows in focus. The test image (average frame of frame 240 to 260 in the data cube) is shown in Figure 8.12a, while the relative radiometric response of the frame is shown in Figure 8.12b.

The test image itself looks quite uniform, except looking slightly brighter in the upper right corner. This could be due to the ocean frames not being perfectly uniform, and is therefore taken into consideration when discussing the results further. One blob is barely visible and vignetting can be seen as this is uncalibrated data. Some vertical lines are visible, which is natural as the spectrum observed is from both the dark ocean and the atmosphere, leaving atmospheric features visible in the data. In the relative radiometric response, both blobs that were previously mentioned ([spatial pixel 700, wavelength 500 nm] and [spatial pixel 300, wavelength 730 nm]) are visible. Some horizontal stripes can now be seen, which are most likely from unevenness in the slit. The vertical lines (atmospheric features) looks doubled, which is due to the smile effect.

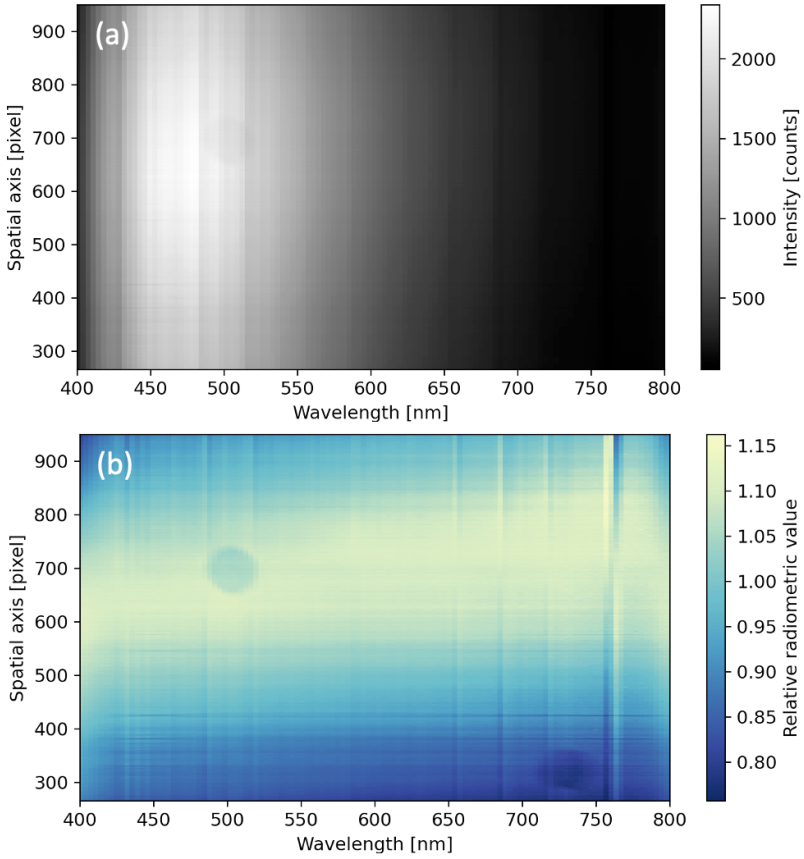

Figure 8.12: (a) Test image, the average frame of frame 240 to 260 in the Frohavet datacube, (b) relative radiometric response of test image.

8.2.1 Correction of spatial shift

The main consequence of the observed spatial shift of 7 pixels, as reported Section 8.1.6, is a mismatch between the captured data and the pre-launch calibration coefficients. This mismatch can be corrected by shifting the calibration coefficients 7 pixels. The effect of shifting the calibration coefficients can be seen in Figure 8.13, which shows the relative radiometric response in a uniform ocean frame after calibration with the original and shifted calibration coefficients have been applied.

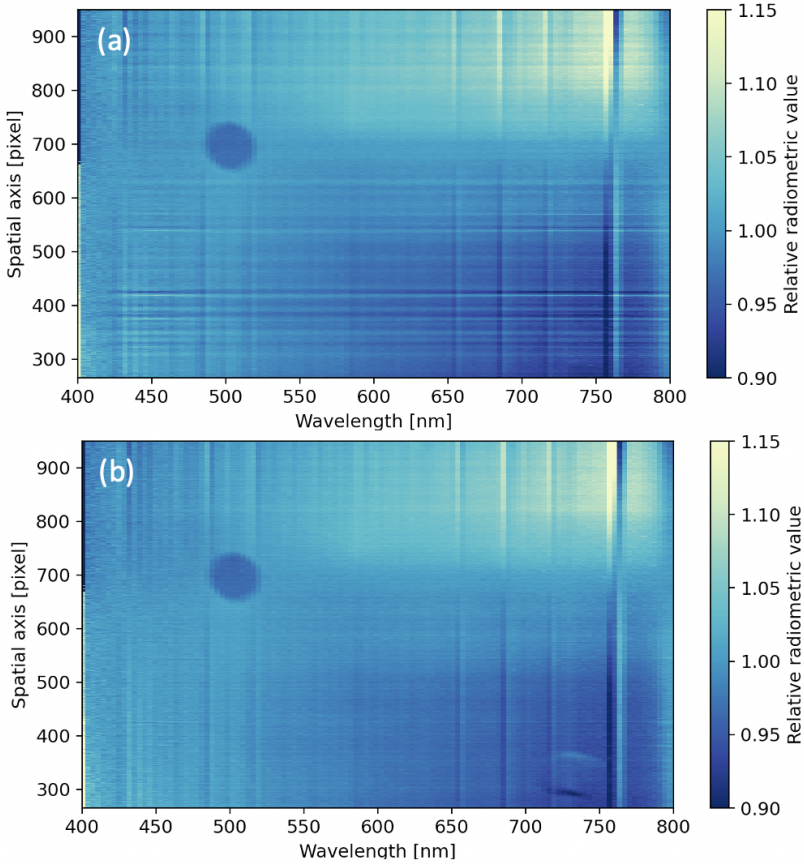

Figure 8.13: Relative response in calibrated ocean frame using (a) original calibration coefficients, (b) shifted calibration coefficients.

When using the original calibration coefficients (Figure 8.13a), horizontal stripes are still visible and now look doubled, meaning that this is an artifact from the data being shifted, giving a mismatch with the calibration coefficients. It can be seen that the horizontal stripes disappear when using the shifted calibration coefficients (Figure 8.13b). However, the second blob ([spatial pixel 300, wavelength 730 nm]) then becomes visible. This suggests that the blob did not shift after launch, like the rest of the image. This can be explained by the camera sensor moving during launch and thereby being the source of the shift, and the blob being dust or some other particle on the camera sensor, and therefore not moving with the rest of the image. The problem of the mismatch between the data and the calibration coefficients is therefore not fully solved by only shifting the calibration coefficients, and something must be done to remove the blobs. This will be further discussed in Section 8.2.3.

8.2.2 Correction of smile

Initially, smile and keystone characterization was done pre-launch to be able to correct the data for smile and keystone (Section 7.5). Whether or not this correction will still work without introducing errors when correcting the in-orbit data after shifts have appeared, is hard to verify. Therefore, it would be a safer choice to calculate new coefficients for smile and keystone correction from the post-launch data. This is, however, difficult. Since the data is mostly affected by smile distortions, smile correction is here prioritized over keystone correction, and another way of correcting smile will be compared to the pre-launch smile and keystone correction.

Comparison of smile corrections

The smile correction from the smile and keystone correction presented in Section 7.5 and only smile correction using the spectral calibration matrix (described in Section 7.1.1) are compared. Smile correction with the latter is performed by using the center row (center of the slit) in the calibration matrix as reference wavelengths, and for each row interpolating and resampling the values in the spectrum to these wavelengths. Smile is detected in the smile and keystone characterization frame (zoomed in version seen in Figure 7.15), before and after the smile corrections are applied, and the smile in this frame detected as described in Section 4.2.4. Since the smile and keystone characterization frame was acquired with argon and mercury calibration lamps, only wavelengths from these lamps are investigated here.

The results are shown in Figure 8.14. The colored areas show smile for all detected wavelengths, and the stippled lines show the average smile detected in the frames. It can be seen that there is a pixel shift about 10 pixels before correction, with larger deviations at the end of the spatial axis (top of the slit). After smile and keystone correction has been applied, the smile is reduced significantly, and is more centered around the mean. There are, however, some deviations seen on the edges. If applying the smile correction based on the spectral calibration matrix, the smile is reduced even further, and is again mostly centered around the mean. When looking closely one can see that the edges of the colored area have lower values at the beginning of the spatial axis (to the left), and higher values at the end of the spatial axis (to the right), meaning that some wavelengths probably are slightly tilted even after the correction.

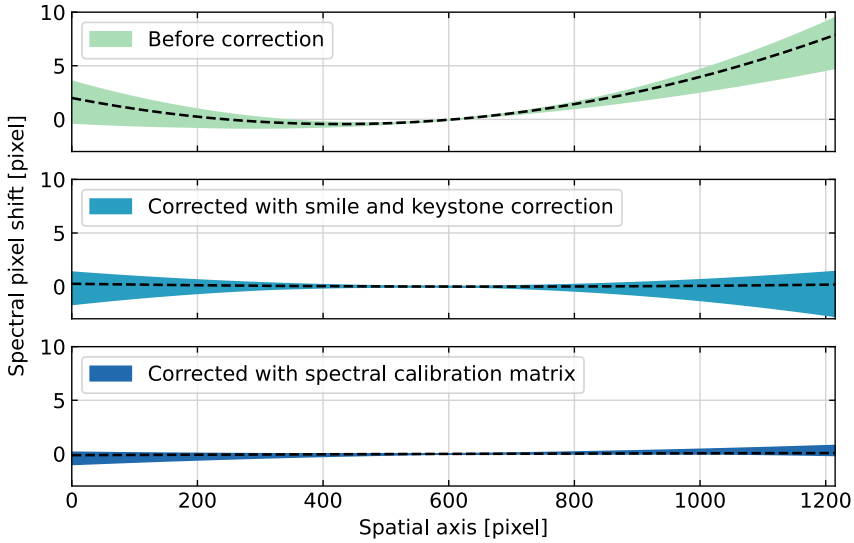

Figure 8.14: Smile detected in the smile and keystone characterization frame (seen in Figure 7.15) before and after smile correction. Colored areas show smile for all wavelengths, while the stippled line shows the average smile detected in the frame.

To easier compare the effects of the smile correction, the average and maximum values (pixel shift detected due to smile) before and after correction is shown in Table 8.5. Here it can be seen that both the average and maximum value is reduced after correction, and that correction with the spectral calibration matrix provides the better results. The table also shows detected keystone after correction. As expected, the keystone is improved when using the smile and keystone correction algorithm, while it has barely changed when only correcting smile with the spectral calibration matrix.

Table 8.5: Pixel shifts due to smile and keystone in smile and keystone characterization frame (seen in Figure 7.15) before and after smile correction has been applied.
Note: numbers are for the full frame.

Test frame	Smile, average shift [pixel]	Smile, maximum shift [pixel]	Keystone, average shift [pixel]	Keystone, maximum shift [pixel]
Before correction	8.36	9.83	1.75	3.32
After smile and keystone correction	1.05	2.82	0.48	1.08
After smile correction with spectral calibration matrix	0.23	1.14	1.62	3.35

In Section 8.1.4 it was shown that smile from the spectral calibration matrix (which has been shifted to match up with the data again after the spatial shift after launch) is comparable to smile seen in the in-orbit data. Smile correction should therefore be performed according to plans.

There is a trade-off regarding correcting of smile and keystone simultaneously or only correcting for the smile effect. The smile correction is better when being corrected alone. But this leaves keystone distortions affecting the data. However, Veglo showed in her master's thesis [185] that smile distortions affect the uncertainty of classification algorithms more than keystone. It is therefore of higher importance to correct the smile distortions properly, than attempting a combined correction yielding poorer results.

Since there is no easy way to test whether the pre-launch smile and keystone correction algorithm introduces unexpected errors or not, the smile correction performing better alone and the smile distortions being more critical to correct for, the safer choice is to use the smile only correction based on the spectral calibration matrix.

Smile correction on test image

The relative response in the test image (calibrated with shifted coefficients) using the pre-launch spectral calibration matrix can be seen in Figure 8.15. It can be seen that the vertical lines are less prominent after the smile correction.

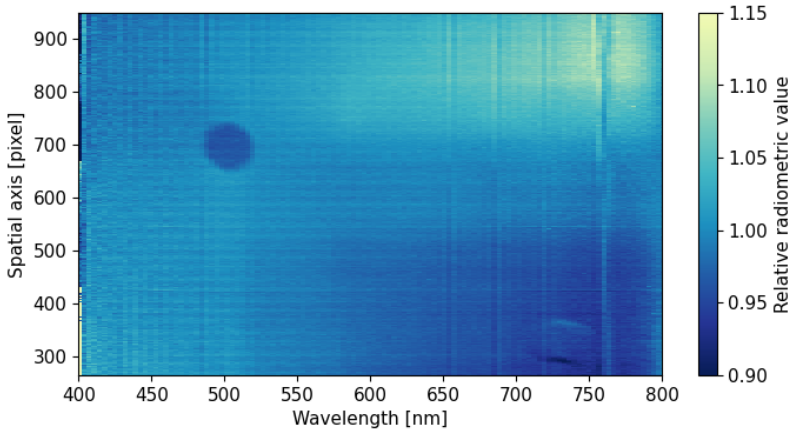

Figure 8.15: Relative response in smile corrected frame (calibrated with shifted components), using pre-launch spectral calibration data.

8.2.3 Correction of blobs

To remove the blobs, the destriping method described in Henriksen et al. [179] (**Paper 6**) can be used. Initially, this was used to correct for the stripes caused by the spatial shift. However, as the wavelengths are slightly affected by smile, it is more correct to shift the spectral and radiometric calibration coefficients 7 pixels first, and then do the destriping.

The destriping method essentially uses a uniform ocean frame with few spatial features (such as the test image used here), and uses the absolute response (average row in the image) to calculate the offset from the average row. The relative response of the test image, calibrated with shifted components, corrected after destriping can be seen in Figure 8.16.

The top image, Figure 8.16a, shows without smile correction applied, while Figure 8.16b shows the destriping applied after smile correction have been applied on the calibrated image. Double vertical lines appear in the upper image, which is due to smile. Since the smile curves the spectral lines, spectral features will not be in the same column for all rows, giving a difference between the rows and the average row, which is what the relative response plot shows. These double vertical lines are heavily reduced in the smile corrected image (lower image), proving that the smile correction helps. Some vertical lines are, however, still visible. Some could be from smaller smile distortions, while others could be due to noise.

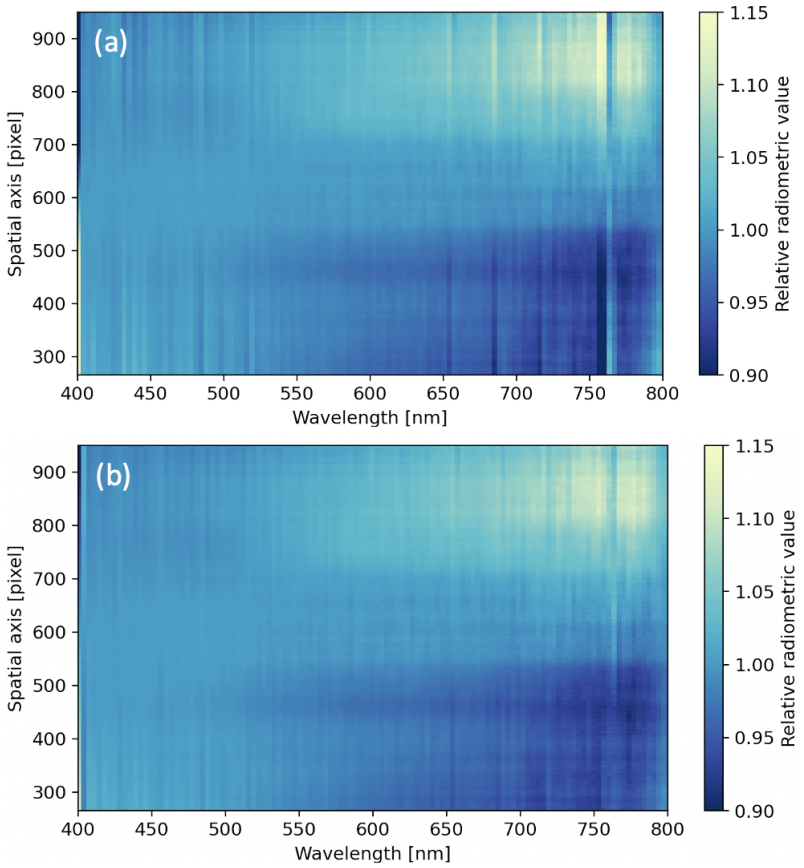

Figure 8.16: Relative response in destriped frame (calibrated with shifted components), (a) without smile correction) and (b) with smile correction applied before the destriping.

8.2.4 Future work

Further work should be done on the HYPSO-1 post-launch calibration. First of all, the background level (dark values) should be investigated in more detail both as a function of exposure time and sensor temperature. It should be discussed whether different background values should be used, or if it is sufficient to use the same background value for all captures. Further, how to treat the spatial shift (including the blob that has not been shifted), and the additional blob that appeared in the data after launch should be discussed. These deficiencies in the spectrogram affect the quality of the data, and should not be forgotten as the data is distributed to the users. The new blob should also

be monitored over time to check whether it move or not. The smile correction, both alone and combined with keystone correction, should be further investigated to see if any improvements can be made to this correction. If a better way of combined smile and keystone correction can be found, this could be re-applied to old datasets and improve the quality of the data. It is therefore worth continuing to develop these corrections. The quality of the correction must also be assessed. The destriping correction should also be further developed. Here, only destriping correction for the AoI have been presented. The correction for full frames must also be calculated. For this, an unbinned full frame capture over a uniform area is needed. The quality of the destriping correction must then also be assessed. In addition to improving the steps as already mentioned, correction of second order diffraction effects based on the in-orbit data can also be attempted, as done for HICO in Li et al. [65] (as described in Section 5.1.3). This would an interesting addition that would increase the usable range noticeably, as discussed in Chapter 5.

8.3 Suggestions for HYPSO-1 calibration pipeline

Before being passed to the users, the data should go through a minimum level of processing [84]. Typically, the data is prepared at different levels, as described in Table 2.1. For HYPSO-1, both raw (level 1a) and calibrated (level 1b) data will be available [186] (**SP 5**). In addition, reflectance (level 2) will also be available at a later time. Here, the main pre-processing steps both for working with the raw data and calculating the calibrated products are described.

8.3.1 Pre-processing steps

First, some of the details of the HYPSO-1 data are discussed, and the first steps needed to work with the raw data are presented. The data is assumed to be decompressed so that the datacube is on a .bip format.

Together with the datacube, an .ini-file containing metadata is attached. This file contains information about which pixels have been used (selected AoI) and other settings such as the binning factor, number of frames and exposure time. When importing the datacube into a data handling program, the dimensions, found in the .ini-file, are required as input.

When the HSI sensor was mounted, it was mounted upside-down to make the connectors on the camera head fit. This makes the spectrograms backwards when reading the raw files directly. The data should therefore be flipped (x-axis only) to sort the bands from

descending to ascending order. The same was done during the pre-flight calibration, so the calibration steps assume the x-axis has been flipped prior to calibration.

If binning is used, it bins by summation. This means that the values should be divided by the binning factor to convert back to 12-bit values before further use.

The pre-processing steps can be summarized as follows:

1. Read datacube and set correct dimensions.
2. Flip x-axis, sorting bands in ascending order instead of descending order to compensate for sensor being mounted upside-down.
3. Scale by binning factor.

8.3.2 Calibration and correction steps

Next are the calibration steps. As stated in Niro et al. [84], ensuring good level 1 data is the first fundamental step for tackling the issue of interoperability. Geometrical distortions in the spectrogram (such as smile and keystone) should be corrected to a sufficient level and intensity differences evened out by flat field correction (accomplished by radiometric calibration).

For spectral calibration, the pre-calculated wavelengths for each band (as stored in the spectral calibration matrix) can be used, or the spectral calibration coefficients can be applied to the pixels as described in Equation (7.1).

For the radiometric calibration, the first step is to remove the background value. For HYPSO-1 an average value of about 8 counts is used for all pixels, as described in Section 7.3.1. The radiometric calibration coefficients can then be applied, as described in Section 7.2. Note that the calibration coefficients must have been calculated on calibration data corrected in the same way as the data it will be applied to. If any of the correction steps prior to the radiometric calibration are changed, the calibration coefficients should be re-calculated accordingly. Here, it is suggested to use the spectral calibration matrix to provide the correct wavelength for every pixel, then perform smile and destriping corrections afterwards. No corrections should therefore have been applied to the calibration data before calculating the calibration coefficients. Both the spectral and radiometric calibration coefficients should, however, be shifted 7 pixels to correct for the spatial pixel shift (as described in Section 8.2.1). If the shift is not corrected, all pixels will be calibrated by the wrong gain. When the shift is corrected, however,

there are some pixels close to the blob [spatial pixel 300, wavelength 730 nm] that will be calibrated by the wrong gain instead. In-orbit radiometric calibration should therefore be performed in the future. Before the in-orbit calibration is ready, choosing to have only a few pixels calibrated with the wrong gain instead of all pixels seems like the better choice, so correcting for the spatial shift by shifting the calibration matrix is therefore recommended. The effect of the blob will anyways be evened out by the destriping step, described below.

Smile should be corrected by using the spectral calibration matrix as described in Section 8.2.2. Performing smile correction only, instead of smile and keystone correction, is here suggested since the smile correction was shown to perform better alone than in the combined correction. The smile effect is also more prominent in the data than keystone distortions, and as already mentioned, Veglo showed in her master's thesis [185] that smile distortions affect the uncertainty of classification algorithms more than keystone. Proper smile correction should therefore be prioritized over a combined smile and keystone correction which might give poorer results.

Destriping, as described in Section 8.2.3, should then be performed. Since the destriping correction is based on in-orbit data and will smooth out the response in the image, it should be applied after the radiometric calibration. Before this step is used in the calibration pipeline, further investigations should be done into how it affects the data, uncertainty estimates and accuracy of the calibrated values after the destriping correction. It does, however, seem promising, as it evens out the imperfect responses related to the blobs in the spectrogram (see Figure 8.13 for blobs and Figure 8.16 for no blobs after correction).

The suggested steps for calibration and correction in the calibration pipeline can be summarized as follows:

1. Wavelength calibration (read from file or calculate band wavelengths from spectral calibration coefficients).
2. Remove background value.
3. Apply radiometric calibration coefficients.
4. Apply smile correction (only) using the spectral calibration matrix.
5. Apply destriping correction.

In addition, other steps such as georeferencing of the whole cube and geometric distortions in the spatial-spatial domain should be corrected. Here, however, only

corrections in the spectral-spatial domain have been discussed as these are the ones most tightly connected to the optics (as the last spatial domain relies heavily on the movement and orientation of the platform during the scan).

8.3.3 Future work

The suggested order and steps of the calibration pipeline presented here should be reviewed and further developed to fit the need of HYPSO-1 users.

First and foremost, the uncertainty and accuracy of the different steps should be estimated and analyzed. The corrections applied (for smile and destriping especially) should be investigated in further detail to make sure that no artificial noise or defects are introduced in the data after correction. The destriping correction must also be expanded and calculated for all pixels in the unbinned full frames so that it can be used on all datasets. The effect of destriping on unbinned frames should also be investigated further.

The fully calibrated dataproduct (level 1b, ToA radiance) should be tested and validated against real-life measurements, or compared to in-orbit calibration. In-orbit calibration should anyways be performed and investigated to see whether pre-launch calibration with the corrections mentioned here or the in-orbit calibration yields more accurate results when it comes to the spatial shifts and blobs, as mentioned previously. A combined smile and keystone correction could also be attempted by using in-orbit data. A method must in that case be developed and tested prior to used.

Finally, level 2 data products should be developed. This includes applying atmospheric correction and retrieving the water leaving reflectance, as well as classification maps, Chl-a detection and Chl-a concentration estimates, among other things. This is, however, a huge task, and would be best achieved as a collaboration between HYPSO members and other users. It is also worth noting that there are often overexposed values in the datasets, typically from clouds or other bright areas such as deserts. The calibration is not valid for overexposed pixels as the amount of light collected is not recorded properly. A mask sorting out the overexposed pixels would also be useful to add with the distributed HYPSO data products, and could easily be created from the raw datasets by looking at the maximum recorded value out of the 12-bit available.

9 | Research campaigns and on-ground biological signatures

From the spring of 2022, the HYPSO-1 satellite has supported several research campaigns. These campaigns typically use other autonomous agents and/or manual methods to collect in-situ data to map and monitor an area. Acquiring satellite data of the same area gives useful support as larger areas can be mapped, and measurements can be taken on a regular basis without larger efforts when not denied by cloud cover. HYPSO-1 has therefore supported these campaigns from as early on as possible, even before the calibration and validation was completed. Moreover, the in-situ measurements acquired can also be useful to validate satellite products such as estimated Chl-a concentration. Some of the research campaigns HYPSO-1 has participated in are described in Section 9.1, with a research campaign in Kongsfjorden (outside of Ny-Ålesund) in May 2022 described in greater detail in Section 9.2. In addition to the space- and airborne systems, which has been the focus in this thesis, instruments and procedures to investigate in-situ data on ground is also being developed at NTNU. An example is the Autonomous Flowthrough Imaging (AFTI)-scope, which among other things uses a hyperspectral imager (currently the HSI V6) mounted on a microscope. Water flows through the microscope system and particles in the water are imaged with the HSI and an RGB camera (for reference) simultaneously. The hyperspectral data can then be used to easier classify and identify detected particles from the spectral signatures collected using machine vision. This set-up and some test data collected are further described in Section 9.3.

9.1 Research campaigns

The first research campaign HYPSO-1 supported was a joint mission with other remotely operated and autonomous agents run from Mausund (outside of Trondheim, Norway), focusing on the Mausund bank and the surrounding Frohavet, in April 2022. Details from this mission and an overview of all the data that was collected can be found in **SP 2**: "Campaign for Hyperspectral Data Validation in North Atlantic Coastal Water" [187]. An example of HYPSO-1 data collected from the area is shown in Figure 9.1a. The Mausund bank is a biodiversity-rich spot with nearly year-round high levels of primary production [188]. The high productivity makes the area important for eco-tourism, fishing and aquaculture-related business [189], which again drives an interest in monitoring the area, in particular Chl-a concentrations to detect algal blooms.

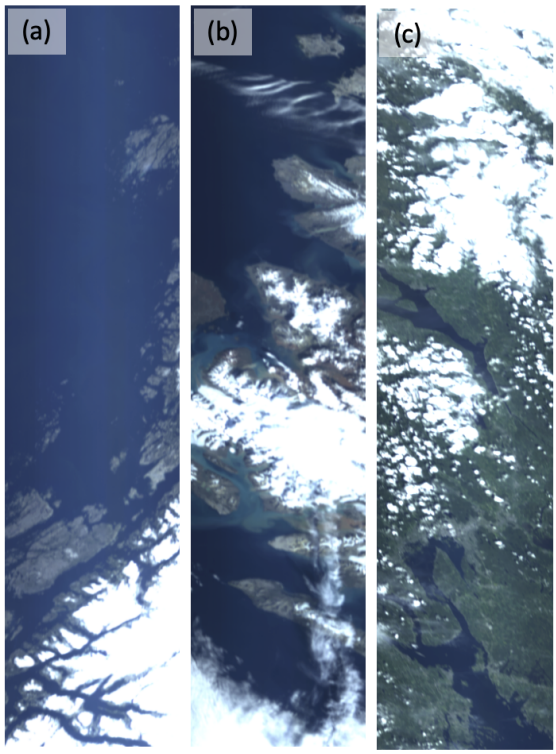

Figure 9.1: RGB representation of a hyperspectral datacubes from HYPSO-1 campaigns using wavelengths R=630 nm, G=550 nm and B=480 nm, with bandpass of 5 nm. (a) 2022-04-19 Frohavet, (b) 2022-07-16 Kongsfjorden, (c) 2022-07-08 Mjøsa.

For HYPSO-1, this was also a good opportunity to collect validation data for the satellite, as both radiometric ground measurements, an USV, an AUV, water sampling and two other HSIs mounted on drones would gather data in the same area at the same time, providing ground truth to the satellite data.

In May 2022, a joint mission to Kongsfjorden (Figure 9.1b) was conducted, which is described in greater detail in the next section. In the summer of 2022, Mjøsa (Figure 9.1c), the largest lake in Norway, was also monitored to look for indication of HABs and at the water quality. In addition to supporting research campaigns, HYPSO-1 gathers data over other areas of interests every day. Some of these datasets have been evaluated, calibrated and labeled, as presented in **SP 5**: "An Open Hyperspectral Dataset with Sea-Land-Cloud Ground-Truth from the HYPSO-1 Satellite" [186]. With this publication, calibrated and labeled datasets have been released and openly distributed, hopefully expanding the horizon of what HYPSO data can be used for.

9.2 Kongsfjorden campaign

Kongsfjorden is a glacial fjord located on the west coast of Spitsbergen in Svalbard. At the coordinates 78° 59' N, 11-12° E, it is surrounded by mountains, calving glaciers, rivers and the small town of Ny-Ålesund [190]. Normally, a spring bloom kicks off the biological production in April-May, which is why a joint research campaign was conducted there from 19 to 29 of May 2022 by NTNU AMOS and UNIS. The research campaign focused on detection and mapping of biological and environmental variables in the fjord using multiple sensor platforms such as UAVs, USVs, AUVs, Remotely Operated Vehicles (ROVs), water samples collected from boats and in-situ samples collected by divers, as envisioned with the observational pyramid (Figure 1.2). HYPSO-1 supported this research campaign by collecting hyperspectral data 2-4 times a day over Kongsfjorden during the main campaign period, and by continuing to monitor the area over the summer when cloud cover permits imaging. In total, more than 30 usable images were captured

First, some of the HYPSO-1 data from Kongsfjorden is presented, partly based on a section presented in **Paper 7**: "HYPSO-1 CubeSat: First Images and In-Orbit Characterization" [28], and in the conference presentation "HYPSO-1 cubesat with hyperspectral imager over Ny-Ålesund, Svalbard" [191, 192]. This is followed by data and analysis from the UNIS course AB-823, which focuses on the in-situ measurements conducted during the campaign and how this type of data can be useful for validation of the satellite data.

9.2.1 HYPSO-1 data over Kongsfjorden

The HYPSO-1 satellite acquired images over Kongsfjorden before, during and after the main campaign period. Cloudy weather affected many of the captures, making many of them useless. At the end of the campaign, however, the weather cleared up, and some images of the ground and sea could be taken. Since the campaign was during the first months of operations of the satellite, the captures were also affected by some pointing issues. This made the satellite point towards a target a few kilometers away from the original target. This was partly solved during the campaign by selecting a target a few kilometers away from Kongsfjorden, but due to different positions and angles of the satellite at the different passes, some captures still missed the target. Some images that did include Kongsfjorden during the campaign are shown in Figure 9.2. The exposure time was kept high (30-50 ms) to achieve high SNR in the ocean areas. This is visible in the RGB composites as the snow-covered land and clouds are overexposed. When closer inspecting the images, no major features or events such as algal blooms or river run-offs could be observed. There seems to be some river run-off starting to come off from the glaciers (Kronebreen and Kongsbreen) in the later captures, which coincides with what was observed at the end of the campaign period. Ice around Blomstrandhalvøya also seems to be melting from day to day, which was also observed on ground.

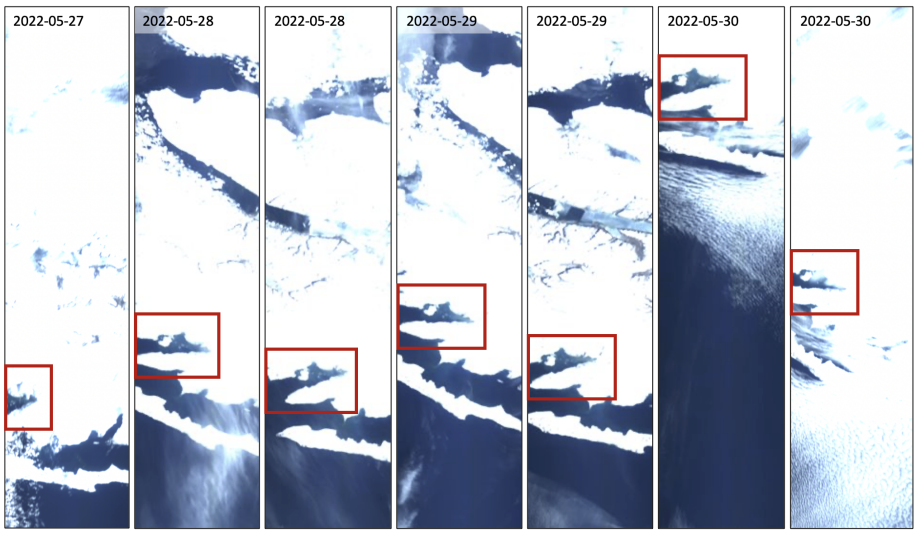

Figure 9.2: HYPSO-1 captures over Kongsfjorden from May 2022. RGB representation using wavelengths R=630 nm, G=550 nm and B=480 nm, with bandpass of 5 nm.

The area continued to be monitored by HYPSO-1 over the summer of 2022. On June 13, an image was captured around Prins Karls Forland (the island visible in the image), right outside of Kongsfjorden, shown in Figure 9.3a. Some features seemed visible in Forlandsundet (marked as point 2 in the image), and the image was therefore further investigated. A simple band ratio algorithm was used to enhance any Chl-a features in the image, and was calculated by dividing the ToA radiance at 549 nm by the ToA radiance at 663 nm. These wavelengths were chosen since Chl-a reflects most light around 549 nm (like several other pigments and constituents in the water) but absorbs light at 663 nm (as seen in Figure 2.2), thereby making it possible to distinguish Chl-a features to some extent. Ideally the ToA reflectance would be calculated by using information about the light field (the Sun and the satellite's position), and atmospheric correction to retrieve the water leaving radiance. Algorithms to estimate Chl-a concentration such as the one presented in Section 2.1.4 could then be used. Here, however, only a simplified band ratio algorithm is used on the ToA radiance data as a proof of concept.

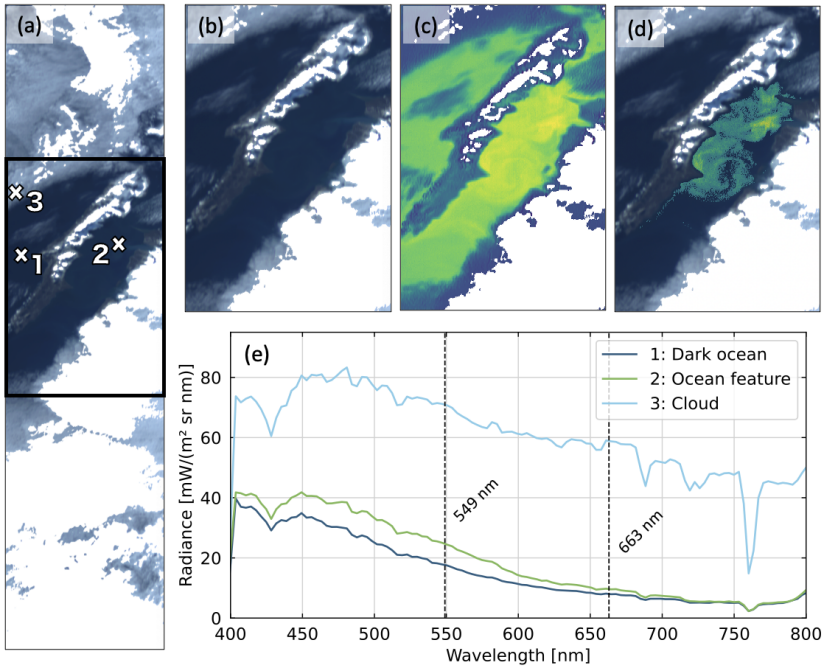

Figure 9.3: HYPSO-1 image captured over Prins Karls Forland on 13 June 2022. (a) RGB representation using wavelengths R=630 nm, G=550 nm and B=480 nm, with bandpass of 5 nm, (b) zoomed in view, (c) result of simple band ratio algorithm, (d) band ratio result with values above 2.35 laid over original image, (e) spectra of points marked in (a).

The result from the calculated band ratio is shown in Figure 9.3c, and the result with values above a set threshold laid on top of the original image in Figure 9.3d, showing a visual representation of the enhanced pattern. The swirls in the water can now easily be seen, and the brighter parts reveal where there might be more Chl-a present. Figure 9.3e shows the spectral signature of three pixels in Figure 9.3a, to look at the difference of the signal from dark ocean, the ocean area with features and clouds (not overexposed). As expected, the cloud pixel is brighter, and the ocean pixels quite dark. There is, however, a clear difference in the signal from the two ocean pixels. The ocean features reflect more light in most of the range below 700 nm, while they both reflect the same amount of light in the NIR. When inspecting the ratio of the signal from the ocean feature to the dark ocean signal, the peak of reflected light is around 550 nm, corresponding to green color. No clear absorption features from Chl-a are visible, but the reflection of green light is an indication that this can be Chl-a.

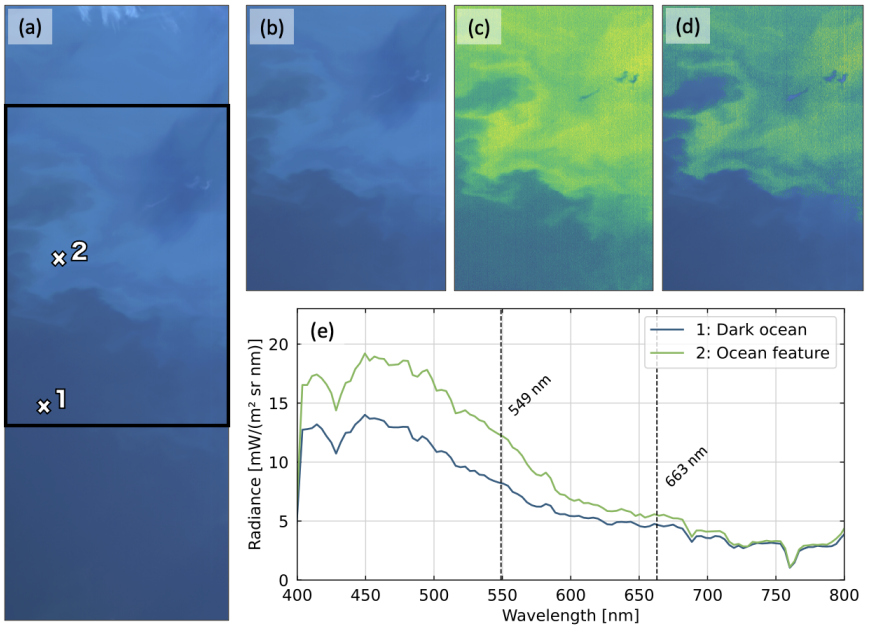

Figure 9.4: HYPSO-1 image captured over the Barents Sea during an algal bloom on 7 August 2023. (a) RGB representation using wavelengths R=630 nm, G=550 nm and B=480 nm, with bandpass of 5 nm, (b) zoomed in view, (c) result of simple band ratio algorithm, (d) band ratio result with values above 2 laid over original image, (e) spectra of points marked in (a).

For comparison, an image of an algal bloom in the Barents Sea captured on 7 August 2023, shown in Figure 9.4a, was also investigated. The features of the bloom are clearly visible in the image as swirling light blue features. The same band ratio algorithm was applied and laid over the original image in Figure 9.4c and Figure 9.4d. The spectral signatures of the darker ocean and the bloom feature are shown in Figure 9.4e. It can again be seen that the bloom pixel reflects more light between 400 nm and 700 nm, while the signals are similar in NIR, showing the same trends as the spectra seen in Figure 9.3e. Again, the peak difference is at 550 nm. This supports the belief that the features seen in the ocean in Figure 9.3a can be from Chl-a.

An example of three of the images captured over Kongsfjorden in July is shown in Figure 9.5. It can clearly be seen that the ocean features in the fjord change on a daily basis, which confirms the need to monitor such areas repeatedly to capture these dynamic events. In Kongsfjorden, the color of the water changes from a mix of green and weak brown to deep reddish brown in only a couple of days. This indicates run-off from rivers and/or glaciers of minerals with oxidized iron, likely originating from several rivers, such as the Bay River near Ny-Ålesund. Different colors indicate different minerals originating from different rivers, which might make it possible to trace them back to the river source [17]. In addition, the movement of turquoise patterns between Kongsfjorden and Krossfjorden, can indicate TSM from glacial run-off. There should be little CDOM present in the waters around Svalbard as there is no top soil. However, some Chl-a might be present in the water, contributing to a more greenish color as blue and red light would be absorbed by the Chl-a pigment.

Some of the pixels in the image captured on 18 July are investigated in more detail in Figure 9.6. The dark and green ocean pixels show again the same relationship, indicating Chl-a in the greenish water in the image. The brown ocean feature has a clearly different spectrum with less reflected light in the blue-green, and more reflected light in the red parts of the spectrum (600 nm to 700 nm especially). The light brown ocean features seems to be a mix of the brown and green, which seems plausible as it is most likely a mix between river run-off and Chl-a in the water. It would be interesting to investigate these images further after atmospheric correction has been applied and the water leaving radiance retrieved, to look at more details of the spectra leaving the water surface and investigate methods to retrieve which constituents are in the different water pixels.

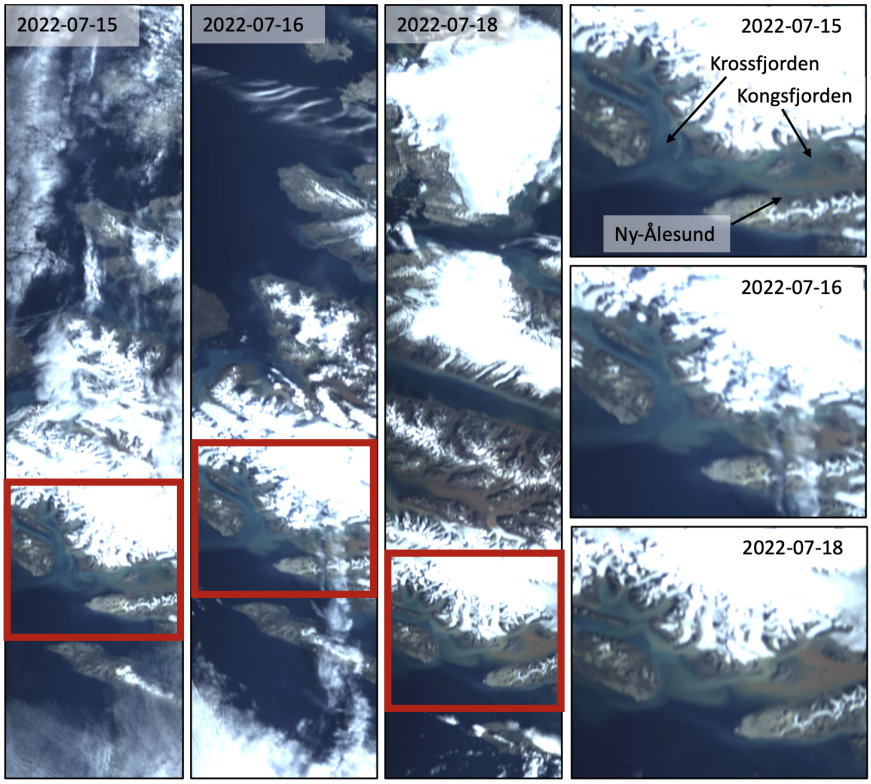

Figure 9.5: HYPSO-1 captures over Kongsfjorden from July 2022. RGB representation using wavelengths R=630 nm, G=550 nm and B=480 nm, with bandpass of 5 nm.

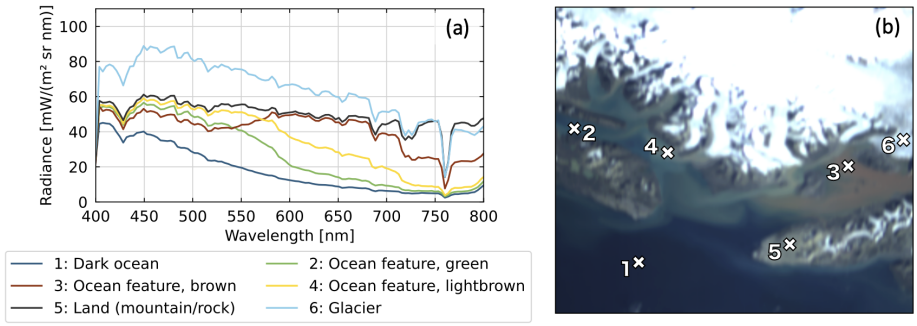

Figure 9.6: Further investigations of HYPSO-1 data over Kongsfjorden 18 July 2022. (a) Spectral signatures from selected pixels, (b) location of selected pixels in the image.

9.2.2 In-situ data from the AB-823 course

A group of 20 students participated in the UNIS course AB-823 "Light Climate and Primary Productivity in the Arctic" in the spring of 2022, the author being one of them. During the campaign, various in-situ samples were collected, and measurements were performed in the lab.

Among the samples collected were water samples (containing microalgae), phytoplankton collected with a phytoplankton net and macroalgal samples collected from the bay. Irradiance was recorded on land with the ArcLight observatory [193] and underwater in the bay with a spectroradiometer, together with an ECO Triplet measuring CDOM, TSM and Chl-a. Conductivity, Temperature, and Depth (CTD) transects were performed at different locations over several days, and an ROV was used to capture images and video of the seafloor to map macroalgae. In the lab, both reflectance and absorbance measurements were conducted with a spectrometer, and Pulse Amplitude Modulation (PAM) measurements were also performed on the micro- and macroalgal samples. Since the focus here is on hyperspectral data and spectral signatures, only the reflectance and absorbance measurements from the lab are presented here in further detail.

Collection of samples

Macroalgal samples were retrieved from the kelp forest in the bay close to the Marine lab in Ny-Ålesund, as seen in Figure 9.8. Specimens from four species were collected; *Alaria esculenta*, *Saccharina latissima*, *Palmaria palmata* and *Ulva sp.*, as shown in Figure 9.7.

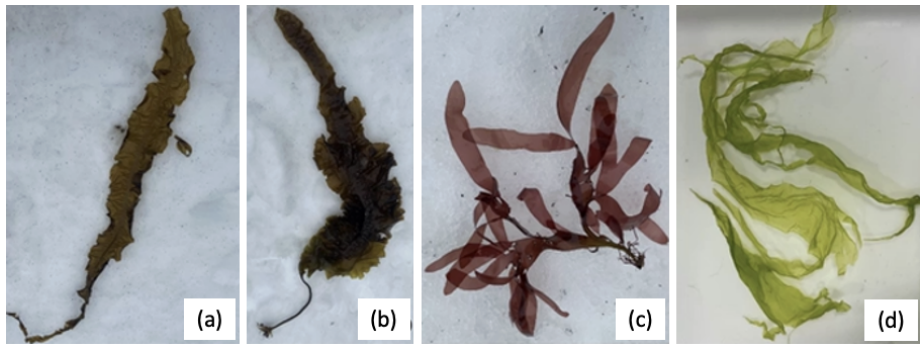

Figure 9.7: Specimens of the macroalgal species. (a) Alaria esculenta, (b) Saccharina latissima, (c) Palmaria palmata, (d) Ulva sp.

For the microalgal samples, water sampling was conducted with Niskin bottles at the surface of the water in the sampling point Kings Bay 3 (KB3), as seen in Figure 9.8. The water samples were filtered using a filtration machine and 25 mm diameter 0.2 μm fine Whatman glass microfiber filters. These samples were used for the reflectance measurements. In addition, microalgae was also collected with a phytoplankton net with mesh size of 10 μm at the surface of the water in KB3. These samples were further investigated in a microscope to determine which species were dominant in each sample.

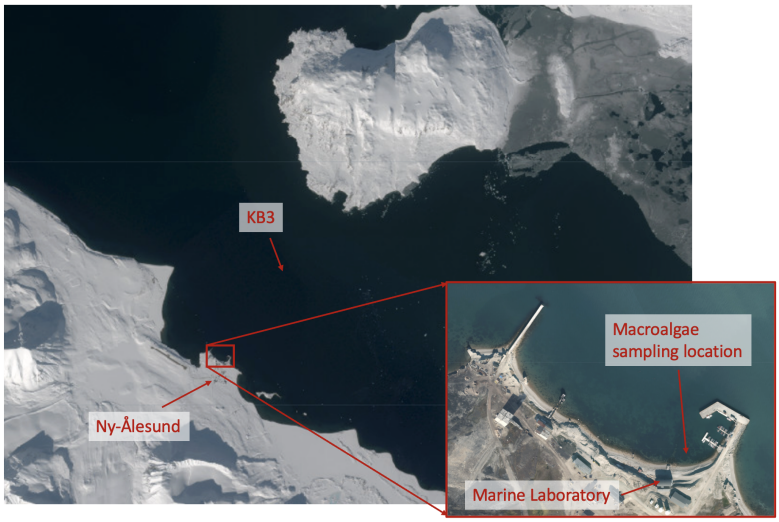

Figure 9.8: Sampling locations in Kongsfjorden (pictures from https://toposvalbard.npolar.no/).

Absorbance and reflectance measurements

Absorbance and reflectance measurements were performed using a QE Pro spectrometer, with a halogen lamp (HL-2000-FHSA). All measurements were done in a dark room to avoid light contamination. Each measurement was set to be the average of 3 scans, and before each measurement the background spectrum was recorded in order to calculate the normalized absorbance and reflectance spectra.

For the macroalgae samples, 3 samples from each of the 3 specimens of the 4 species were measured, resulting in 36 absorbance measurements and 36 reflectance measurements. For the absorbance measurements, the sample was placed in a cuvette which was placed in a holder so that light from a source fiber illuminated the sample from one side, and a

detection fiber recorded the transmitted light on the other side, as shown in Figure 9.9a. Reflectance was measured by placing the sample in a Petri dish on a white sheet of paper (for uniform background), and thereby placing the light source and detector on top, as seen in Figure 9.9b.

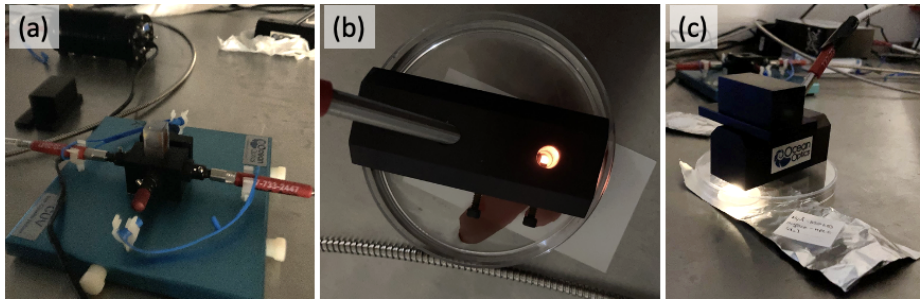

Figure 9.9: Absorbance and reflectance measurement set-ups with the QE Pro spectrometer. (a) Absorbance measurement of macroalgae, (b) reflectance measurement of macroalgae, (c) reflectance measurement of microalgae.

For the microalgal samples, only the reflectance was measured. The filter was placed in a Petri dish and aluminum foil used as the background, as seen in Figure 9.9c. The samples were then wrapped in this aluminum foil after the reflectance measurement was taken and stored in a freezer, to further undergo High-performance Liquid Chromatography (HPLC) analysis on the main land at a later time.

Analysis and results

The average absorbance and reflectance spectra of the macroalgae are shown in Figure 9.10. The spectra were scaled by dividing by the absorbance or reflectance value at 800 nm, to obtain the normalized absorbance or reflectance. It can be seen that the main features in both figures follow each other nicely, peaks in the absorbance spectra coincides with dips in the reflectance spectra, and visa versa, just as expected. The average reflectance spectra of the microalgae samples acquired on May 22 in the morning and in the afternoon at KB3 are shown in Figure 9.11. The spectra were also here scaled by the reflectance value at 800 nm to obtain relative reflectance. It can be seen that the morning sample here had a higher concentration of particles as it absorbs more light. Distinct dips and peaks are also more prominent in the morning sample.

The reflectance (or absorbance) spectra can then further be examined by comparison with known absorption wavelengths of pigments present in the samples. There are three

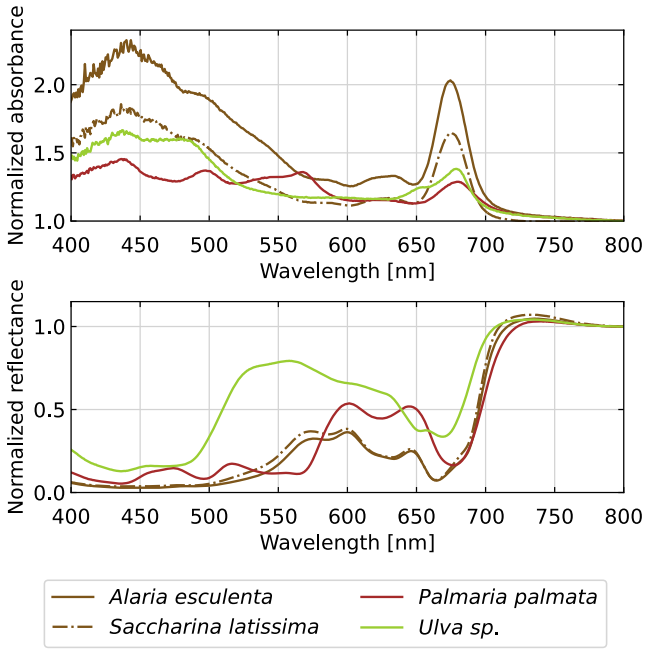

Figure 9.10: Macroalgae absorbance (top) and reflectance (bottom) spectra.

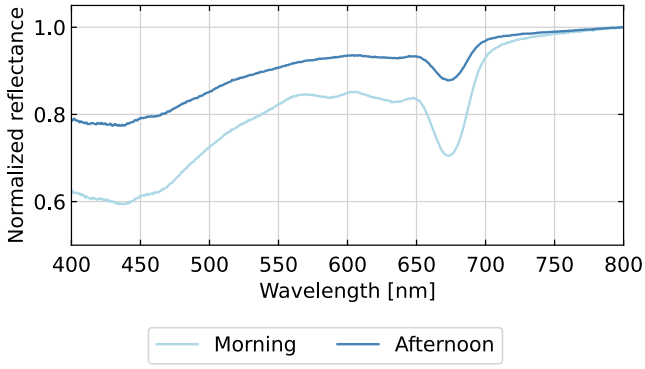

Figure 9.11: Microalgae reflectance spectra from water samples collected at KB3 in the morning and afternoon of May 22, after filtering.

main groups of photosynthetic pigments; chlorophylls (such as Chl-a, Chl-b and Chl-c), carotenoids (such as fucoxanthin and lutein) and phycibilins (such as phycobiliprotein). Macroalgae are mainly separated into brown, green and red algae, while microalgae

is divided into Chl-c containing microalgae (such as diatoms, dinoflagellates and haptophytes), Chl-b containing microalgae (such as chlorophytes), prochlorophytes or phycobiliprotein phytoplankton (such as cryptophytes and cyanobacteria). Chl-a is present in all groups, as discussed in Section 2.1.2, and is therefore not used as a discriminator between the groups [38].

The reference wavelengths for the pigments Chl-a (at 440, 630 and 675 nm), Chl-b (at 470, 600 and 650 nm), Chl-c (at 460, 585 and 635 nm), fucoxanthin (at 480 and 535 nm), lutein (at 460 and 485 nm) and phycobiliprotein (at 500, 540 and 568 nm) are shown together with the macroalgal species in Figure 9.12 and a selection of the pigments (Chl-a, Chl-c and fucoxanthin) for the microalgal samples in Figure 9.13.

For the macroalgal samples, the brown (*Alaria esculenta* and *Saccharina latissima*), red (*Palmaria palmata*) and green (*Ulva sp.*) algae are plotted separately in each sub plot in Figure 9.12, with their respective pigments as vertical dashed lines. There is a clear

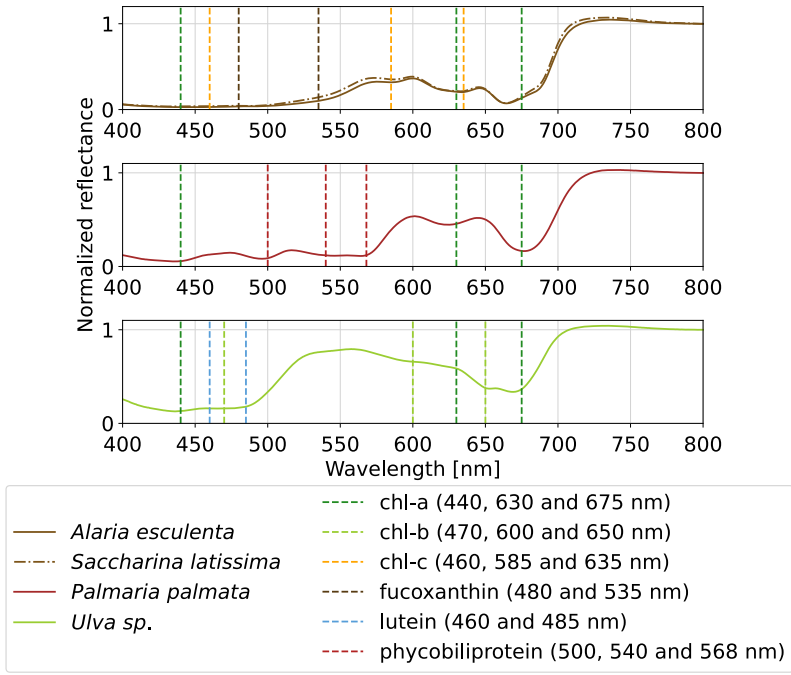

Figure 9.12: Macroalgae reflectance spectra, compared to the absorption wavelength of pigments present in the different species.

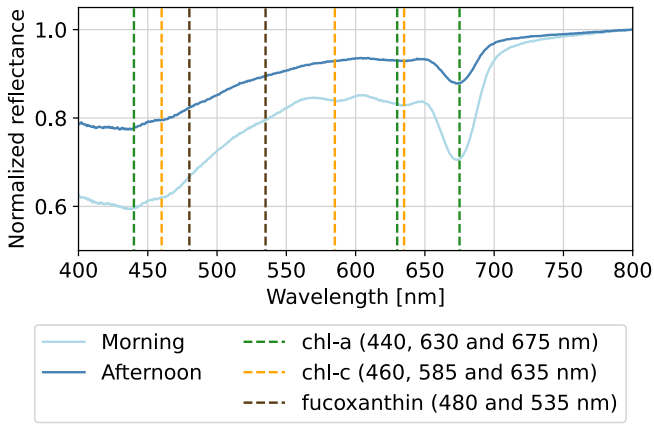

Figure 9.13: Microalgae reflectance spectra, compared to the absorption wavelength of pigments present in the different species.

difference in the spectra between the groups, and it can be seen that the reference absorption wavelengths of the pigments fit with where the samples absorb light. This is a good example on how different groups can easily be distinguished by their spectral signatures, and their spectra be explained by the pigments present in each group.

The spectra from the microalgal samples have a similar shape to that of the brown macroalgae. Absorption from Chl-a can easily be observed at 675 nm, and the two dips seen at around 585 nm and 635 nm, specially in the morning sample, fit well with absorption from Chl-c. From this, it can be deduced that Chl-c containing microalgae such as diatoms, dinoflagellates or haptophytes are present in the samples, specially in the morning sample. The exact microalgal species present are harder to determine as there can be several species mixed on the filter, and they may contain several of the same pigments but with slight differences in the exact location of the absorption wavelength based on different types within the pigment group (such as Chl-c1, Chl-c2 and Chl-c3), or different amount of the pigments being bound to different photosystems in the cells. The health of the cells also affects the spectra, which may give large variations to the spectra within one species.

The microplankton communities collected with the phytoplankton net, also at KB3, were observed in a microscope as shown in Figure 9.14, to determine which species that were dominant in the water samples. From these observations, *Phaeocystis pouchetii* and the diatom species *Chaetoceros socialis* were co-dominating in the water samples

both in the morning and afternoon of May 22. *Phaeocystis pouchetii* is a haptophyte, and the *Chaetoceros socialis* a diatom, which are both in the group of Chl-c containing microalgae. This coincides with what was seen in the microalgae reflectance spectra. The main difference between the two, in regards to their pigments and spectral signatures, is that haptophytes contain Chl-c2, Chl-c3, while diatoms contain Chl-c1, Chl-c2. From in-vitro measurements, it can be seen that Chl-c3 has an increased absorption peak at 584 nm. Chl-c2 has a peak at 580 nm, however, this is not as prominent [194]. Microalgae samples that are dominated by *Phaeocystis pouchetii* should therefore have an increased absorption peak at 584 nm from Chl-c3, while samples with more diatoms present will have less absorption at this wavelength. The spectra seen in Figure 9.13 do not have clear enough features to visually determine if it is *Phaeocystis pouchetii* or *Chaetoceros socialis* that are present, or the amount of each species. This shows how it can be hard to distinguish the species within similar groups, even with data from the hyperspectral imager. More advanced data-processing can, however, be used to extract features and classify different groups.

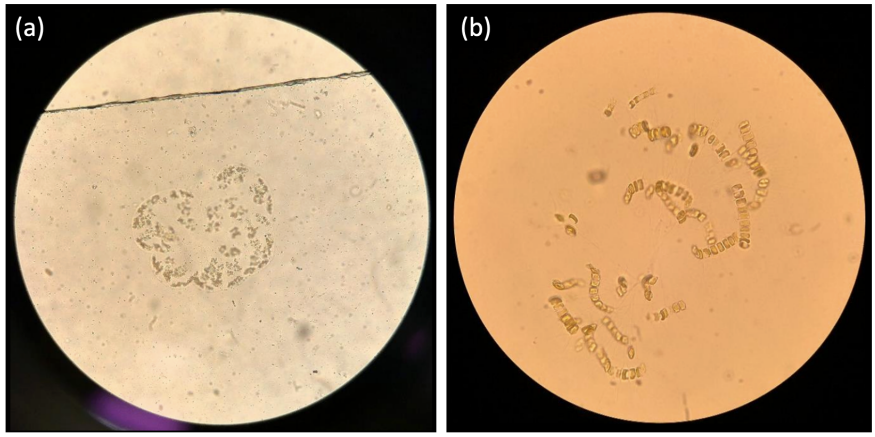

Figure 9.14: Microalgae observed in the microscope. (a) Phaeocystis sp., (b) Chaetoceros sp.

Since satellites can measure the remote sensing reflectance, it is sensitive to the absorption of light in the water by its constituents, such as Chl-a, CDOM and TSM. Comparing with the ground truth measurements gives value to both validating detection and classification algorithms in the data processing chain, and also validate estimated products such as Chl-a concentration from the data. If the spectral signatures are clear enough, absorption peaks can be used to determine which groups that may be present. However, determining species from the spectral signatures is hard, even from laboratory data. Unfortunately, no algal blooms were present during the research campaign period.

Detecting low Chl-a concentrations in satellite data is also hard due several factors, one of them being noise and general uncertainties. The collected in-situ data is, however, still valuable as it gives spectra that can be used for training of the satellite algorithms, and general knowledge on what spectra to expect from different types of micro- and macroalgae.

9.3 AFTI-scope

For hyperspectral in-situ measurements, the HSI V6 was connected to a microscope, as seen in Figure 9.15. The set-up is called the AFTI-scope, and consists of a microscope (Bresser Science TFM-301 Trino microscope), a peristaltic water pump (BOXER 29QQ) that pumps water through the system so that images can be taken of the flowing water, an RGB camera (from Delta Optical) taking reference photos, and the HSI V6 for acquiring hyperspectral images. This system can further be placed on an autonomous vehicle such

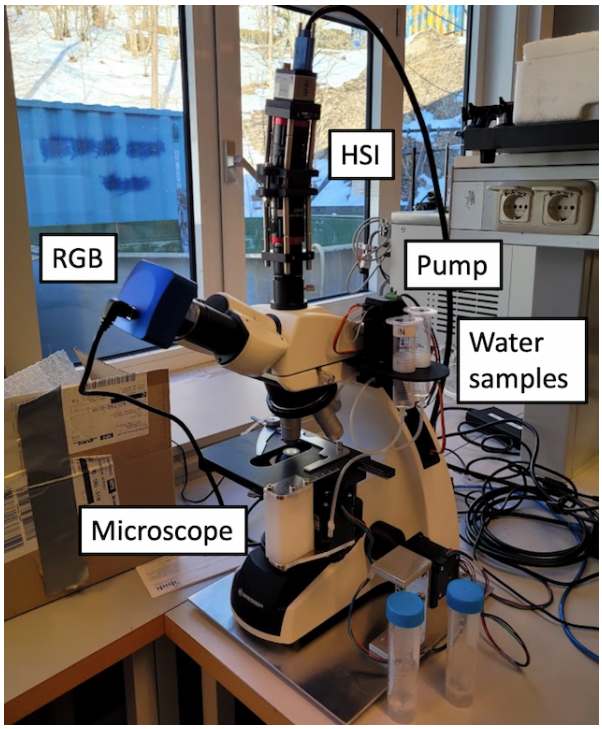

Figure 9.15: The AFTI-scope, set up for testing in the lab.

as a USV, and collect in-situ measurements in the ocean during campaigns, or be used in the lab for collection of spectral signatures for validation, as some examples. This section is based on parts of **Paper 8**: "Autonomous Flow-Through RGB and Hyperspectral Imaging for Unmanned Surface Vehicles" [137], where the full system is described. The parts included in this thesis focus on the hyperspectral data acquired during testing of the system.

The system was tested at Trondheim Biological Station (TBS) during the winter of 2022/2023. Fresh samples from the Trondheimsfjord were collected at the pier at TBS using a phytoplankton net with a mesh size of 20 μm. The water samples were then inserted and pumped through the system, so that the phytoplankton cells could flow through the channel located underneath the microscope objective and be imaged. The flow was stopped so that a hyperspectral image could be acquired by panning over an area, and a high resolution (2560×1922 pixels) RGB image taken of the same area for reference. The reference RGB image is shown in Figure 9.16, where several particles can be seen. Among these are some diatom chains that are clearly visible. To further investigate these particles, the hyperspectral data was used.

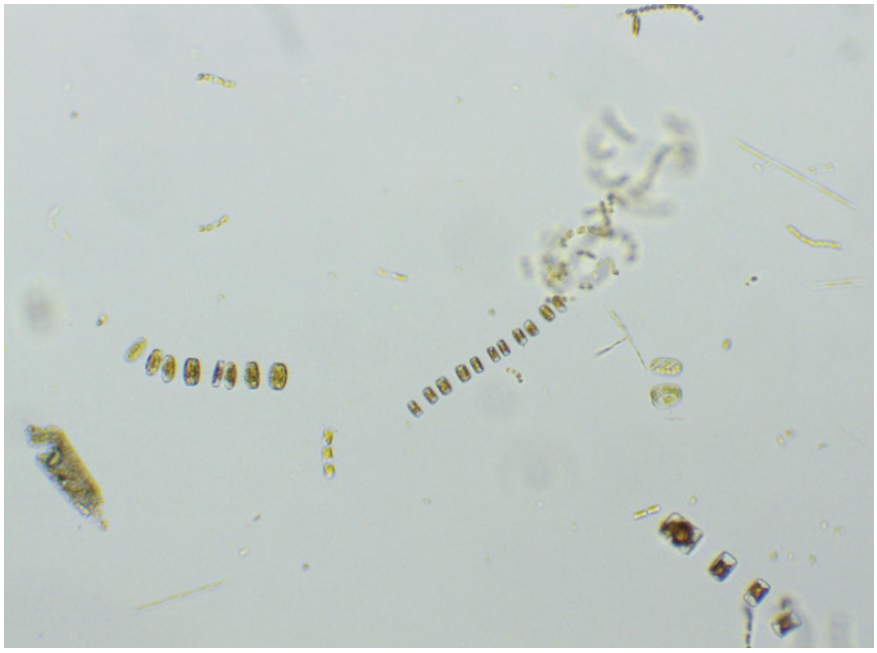

Figure 9.16: Reference image from the RGB camera connected to the AFTI-scope.

First, the spectral composition of the light source in the microscope was investigated. The average spectrum in a selection of pixels in the hyperspectral image where no particles were present (box 1 in Figure 9.18) in the 400 nm to 800 nm range was plotted and is shown in Figure 9.17. It shows that most light is available around 430 nm and between 500 nm to 650 nm, while light close to 400 nm, around 480 nm and above 700 nm is poorly represented. Where there is less light, reflectance and absorbance data will be more noisy, as the SNR will be considerable lower.

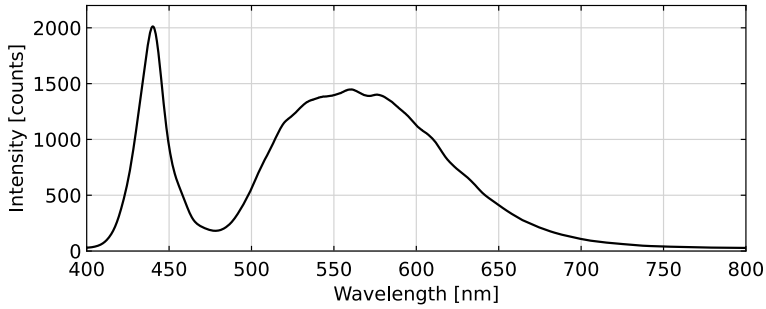

Figure 9.17: Spectral composition of the light source in the microscope.

An RGB representation of one of the hyperspectral datacubes can be seen in Figure 9.18, and the reference image from the RGB camera is shown in Figure 9.16. Several particles are visible in the image. A selection of the particles (and the background) is further investigated, as marked in red boxes and numbered in Figure 9.18. Box 1 shows the background area, particle 2, 3, 4 and 8 are most likely the diatom *Thalassiosira*, particle 5 looks like a fecal pellet, particle 6, 7 and 9 could be the diatom *Chaetoceros*, and particle 10 the diatom *Fragilariopsis*. The diatoms are all a part of the group haptophyta, which contains the pigments Chl-a, Chl-c and fucoxanthin [38]. To further look at the spectra of these particles, the background light was first removed from the raw data and the spectra normalized, then plotted as seen in Figure 9.19. The spectra can be compared to known spectra of phytoplankton, or to the typical reflectance or absorbance spectra of different pigments, such as the ones from [24] shown in Figure 2.2. For most spectra in Figure 9.19 the Chl-a peak at around 675 nm is easily visible, except for in the background (1) and the fecal pellet (5), which makes sense as the Chl-a pigment in the fecal pellet would be degraded. In the diatoms, the shape from carotenoids can be recognized specially in particles 2, 3, 4 and 5, and Chl-c seems also to be present, making the peak around 450 nm broader, and also peaking at around 580 nm and 640 nm. This is as expected, as diatoms contain the pigments Chl-a, Chl-c and the carotenoid fucoxanthin.

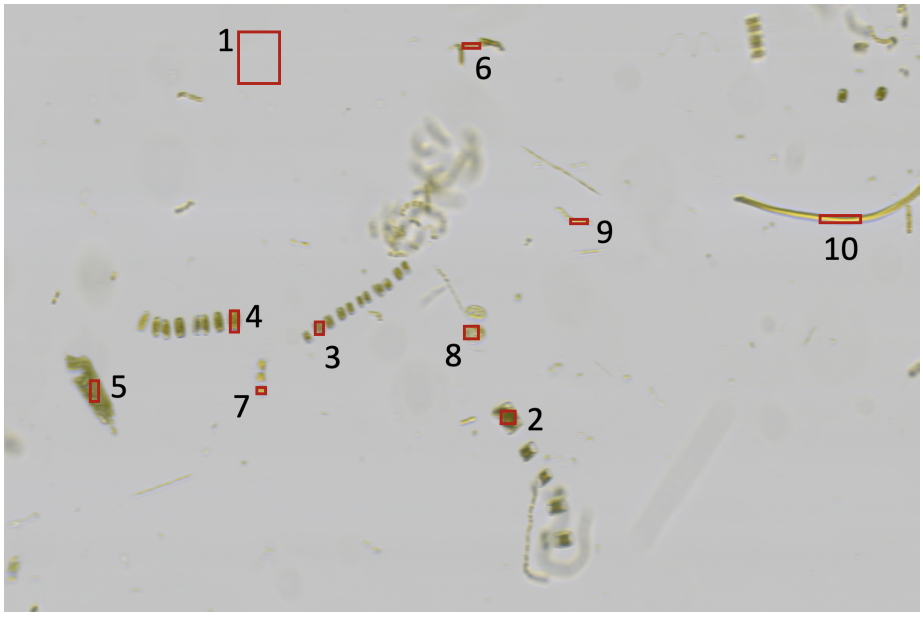

Figure 9.18: RGB representation of the hyperspectral datacube using wavelengths R=630 nm, G=550 nm and B=480 nm, with bandpass of 5 nm. (1) background area, (2, 3, 4, 8) diatom Thalassiosira, (6, 7, 9) diatom Chaetoceros and (10) diatom Fragilariopsis.

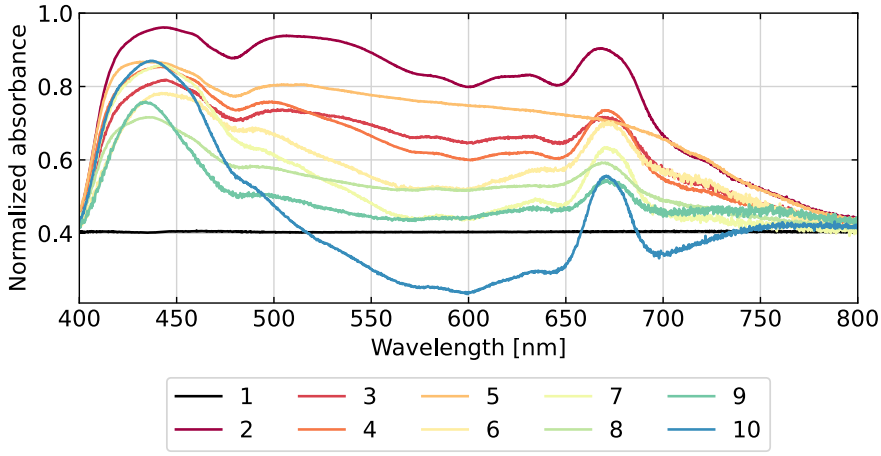

Figure 9.19: Spectra of the selected particles in Figure 9.18.

Further, one option is to use a spectral index such as the Normalized Difference Vegetation Index (NDVI) algorithm to separate pixels containing chlorophyll-a from the pixels without. This is often used in remote sensing applications such as in Kim et al. [195] and Song et al. [196]. The NDVI is calculated as

$$\frac{NIR - RED}{NIR + RED}, \tag{9.1}$$

where *RED* is a band in the red part of the spectrum and *NIR* a band in the near infrared. However, since the signal here is very noisy above 700 nm due to little light available, the index was modified to detect the Chl-a peak at 675 nm. The bands *RED*=675 nm and *NIR*=700 nm are therefore used, and the calculation applied to the image in Figure 9.18, with the result shown in Figure 9.20. A threshold value can be applied to create a mask of these particles. Choosing the threshold value to be 0.25 gives a mask as shown in Figure 9.21. This can be used to automatically detect particles in the samples. Furthermore, the spectra of the unmasked pixels can be investigated, and classification be used to sort the particles into different classes after a model has been trained, or classification could be applied to the whole unmasked images.

The results presented here shows only a small example on how the hyperspectral data can be used and analyzed. Further work should be done to improve the analysis and develop and test other and more complex algorithms to retrieve even more information from the pixels of interest in the images.

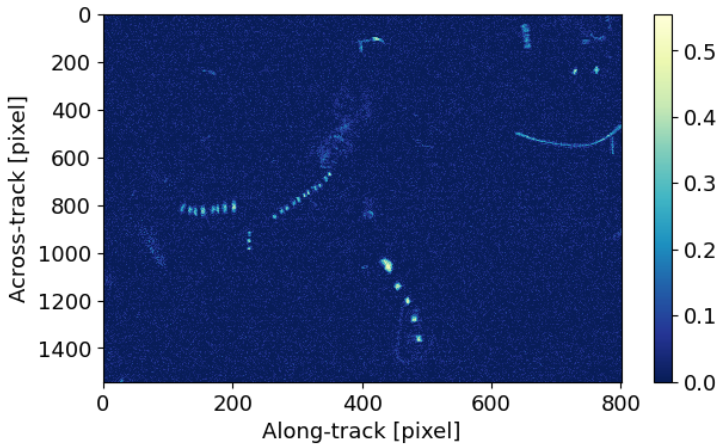

Figure 9.20: NDVI calculated using RED=675 nm and NIR=700 nm.

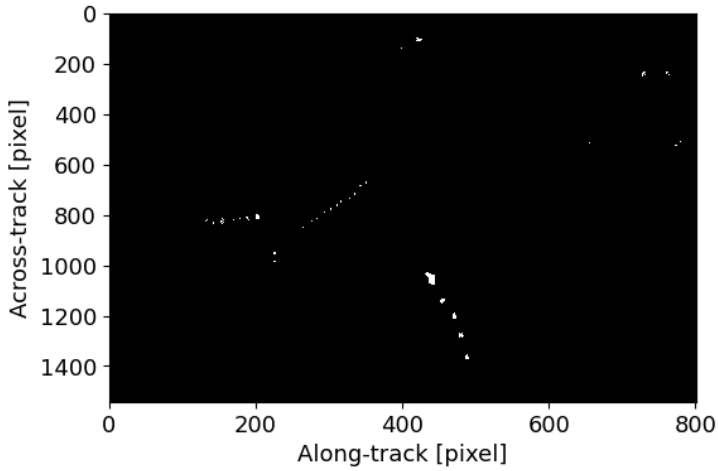

Figure 9.21: Mask created from the NDVI plot using a threshold value of 0.25.

Part III

Discussion and Conclusions

10 | Discussion

Most chapters in this thesis have a concluding section with summary, discussions, conclusions, and/or suggested further work for what is discussed within the chapter. The full content of these sections will not be repeated here. Instead, broader topics will be discussed in context of the research questions and the full thesis.

10.1 Optical design software and spot diagrams

For the design process of HSI V4 and HSI V6, no optical design software was used. In future projects, using an optical design software would be highly recommended. This could give insights into weaknesses in the design in the early stages. Other components could be tested to optimize the design, and the performance could be estimated before building the instrument.

One example on how this affected the current design can be found when looking at the spatial focus achieved at different wavelengths. For the HSI V4, a study was conducted to improve the performance in Mao et al. [158]. They modeled the instrument using the optical design software Zemax and simulated the spot diagrams (point response) for five different wavelengths (400 nm, 500 nm, 600 nm, 700 nm and 800 nm) at four different field positions, as seen in Figure 10.1. The response at 500 nm, which is close to the design wavelength at 550 nm, is pretty sharp, while the spot sizes at the other wavelengths

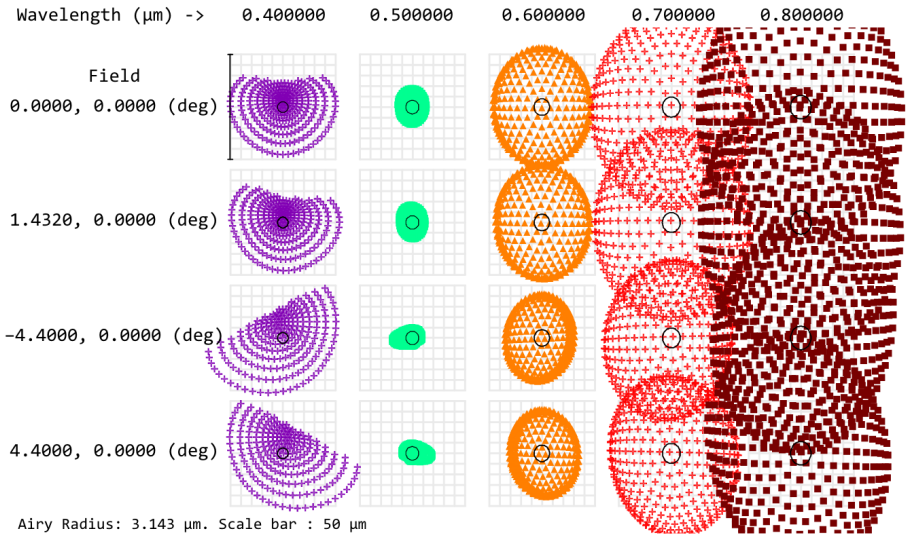

Figure 10.1: Spot diagram from Zemax simulations of the original HSI V4, from Mao et al. [158].

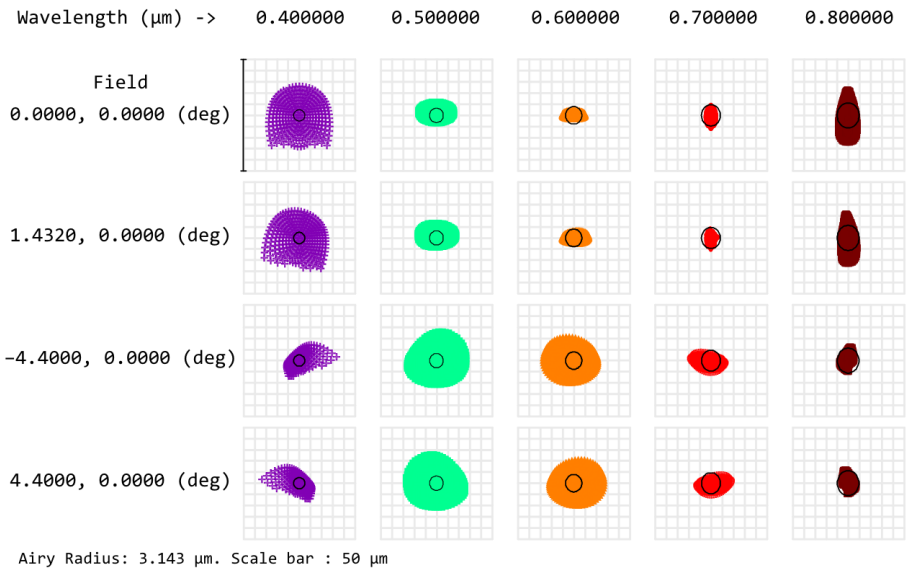

Figure 10.2: Spot diagram from Zemax simulations of the modified HSI V4 with achromatic field lens, from Mao et al. [158].

grow larger quite quickly. For larger spot sizes, the spatial resolution degrades. This effect comes from chromatic aberrations and can be improved by, for example, changing the primary lens in the collimator with an achromatic lens as done in Mao et al. [158]. This results in a spot diagram with more even spot sizes across the different wavelengths, as shown in Figure 10.2. This shows that the original design could be easily improved by the use of an optical design software, and achromatic lenses should be considered to be used in the design to reduce the amount of chromatic aberrations seen in the data.

A similar simulation was done at a later stage for the HSI V6 by Simon Strotmann (and later also by Adriënne E. Oudijk) in relation to the HYPSO-1 payload (not published). The spot diagrams for three selected wavelengths (405 nm, 600 nm and 800 nm) at two field positions (center and edge of FOV) are shown in Figure 10.3. Note the different scaling from Figure 10.1 and Figure 10.2 which are scaled to 50 μm, while the spot diagrams in Figure 10.3 are scaled to 1000 μm, 100 μm and 400 μm for the wavelengths 405 nm, 600 nm and 800 nm, respectively. A black line is added to the right in each spot diagram in the figure to show the length of 50 μm for easier comparison to the other figures. The HSI V6 is expected to show different spot sizes than HSI V4 due to the different optical elements and instrument specifications, but the same trends of broader spots for the shorter and longer wavelengths can be seen. This suggests that HSI V6 also suffers from chromatic aberrations, and that achromatic lenses should have been investigated in closer detail when developing the HSI V6.

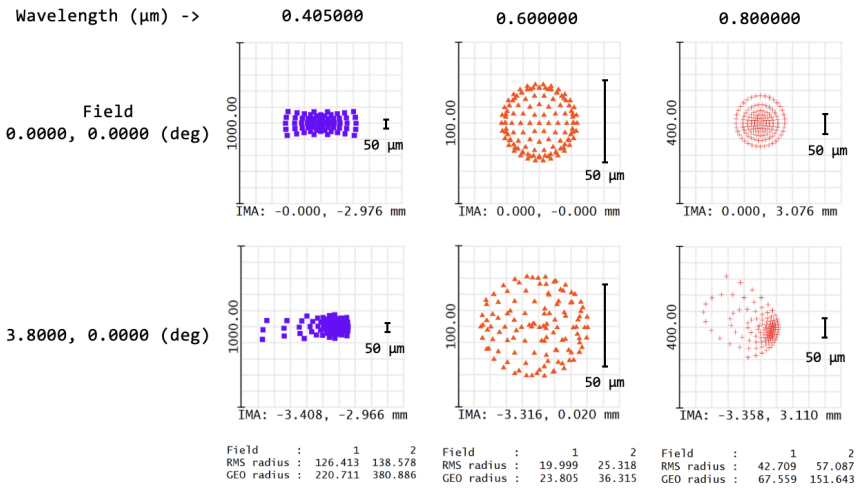

Figure 10.3: Spot diagram from Zemax simulations of the HSI V6, simulated by Simon Strotmann.

In closer detail, this effect is also noticeable in the spatial PSF measurements shown in Section 4.3.4 and visible in the spatial focus test done for HYPSO-1 in Section 7.7. In the PSF plots of both HSI V4 (Figure 4.17) and HSI V6 (Figure 4.18) chromatic aberrations can be seen, and it is clear that only a small part of the spectral range is in focus at the time. This affects the spatial resolution of the lower and higher wavelengths, which is of importance when discussing the optical performance of HYPSO-1, and the quality that can be expected of the data products in terms of spatial resolution across the spectral range.

The variation in spatial resolution with wavelength can be seen directly in the HYPSO-1 in-orbit data by investigating an area with clear spatial features. Figure 10.4, published in Bakken et al. [28] (**Paper 7**), shows how the spatial focus varies for different spectral bands by looking at roads and irrigation lines in an agricultural field near the Tigris-Euphrates estuary. The width of the lines running diagonally in the image are about 50 m across. For the bands with wavelengths between 500 nm and 600 nm these lines are visible, while for the lower and higher wavelengths the lines are completely blurred. To improve the performance of future versions of the instrument, further work should be done to improve the optical design of HSI V6 as well, as done for HSI V4 in Mao et al. [158].

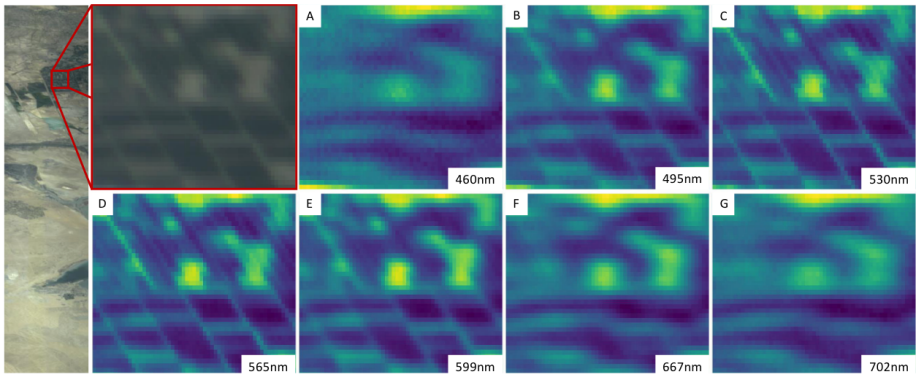

*Figure 10.4: Variation of spatial resolution with wavelength in HYPSO-1 data captured above an agricultural field near the Tigris-Euphrates estuary. To the left: RGB representation using wavelengths R=630 nm, G=550 nm and B=480 nm, with bandpass of 5 nm. (a)-(g) shows the zoomed in area at different wavelengths. From Bakken et al. [28] (**Paper 7**).*

10.2 Calibration methods

A visual example of how the radiometric calibration also includes flat field correction is shown in Figure 10.5. The figure shows two overlapping images captured by HYPSO-1 above Lake Urmia (Iran) before and after the radiometric calibration coefficients have been applied. It can be seen that the darker signal along the edges of the images that are caused by vignetting is removed, creating an even transition between the images.

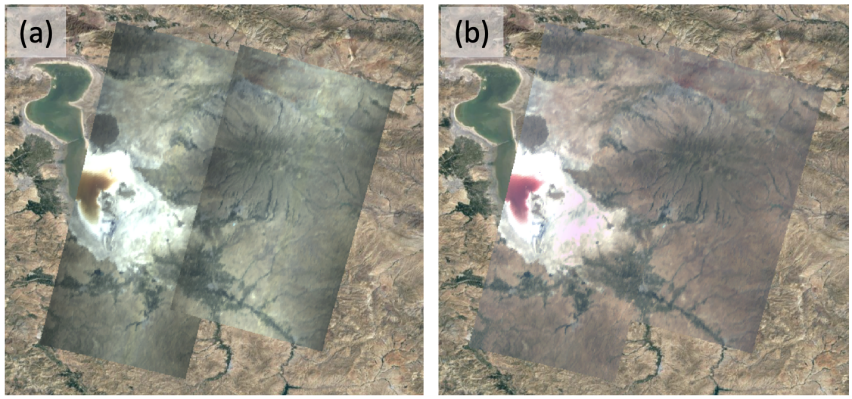

Figure 10.5: Example of flat field correction by radiometric calibration of HYPSO-1 data above Lake Urmia. RGB representation using wavelengths R=630 nm, G=550 nm and B=480 nm, with bandpass of 5 nm. (a) Before calibration with the edges of the images being darker (caused by vignetting), (b) after calibration with the vignetting removed. Overexposed areas are due to bright sand. Image credit: Dennis D. Langer.

The radiometric calibration can, however, be further developed and improved. During the calibration campaign, measurements should be acquired for different angular positions of the FOV to acquire information of the instrument's sensitivity to light from different angles. The linearity of the sensor response should also be investigated as a function of different light levels, not just as a function of exposure time. This can be achieved by adjusting the lamp intensity or using different Neutral Density (ND) filters in front of the instrument during measurements.

The 3D printed targets (striped and halfmoon patterns in Figure 4.2) could also be made better to improve the smile and keystone estimation and spatial focus investigations. One simple way to do this would be to use high precision laser cut slits such as the ones used in the instruments and the spatial PSF set-up, and attach this to the end of a tube of the correct length to replace the 3D printed parts. One thin slit could be used

for LSF measurements (as done when measuring the spatial PSF), or multiple slits in the same target could be used to create a pattern similar to the striped 3D printed pattern. The multiple stripes could measure the LSF at different field positions, and be used in combination with spectral lamps for the smile and keystone detection. For the halfmoon pattern, both a sharper and a higher contrast edge would be desirable. A sharper edge could be achieved by using a different material, like metal. A higher contrast could be accomplished by coating the inside of the tube with a very black material, such as Actar black coating, and let the bright part be illuminated by a very bright lamp.

10.2.1 Full width at half maximum on smoothed signal

When calculating the FWHM, a smoothed signal has been used to reduce the noise to make the peak positions easier to detect. Smoothing the signal does, however, also alter the shape of the peaks. Figure 10.6 shows the HYPSO-1 FM pre-launch spectral calibration data that was used to calculate the FWHM of HYPSO-1, before and after the signal was smoothed. It can be seen that the smoothed signal has lower peaks than the original signal, while the width of the peaks stay approximately the same. This affects the FWHM calculation as the width of the peaks are more narrow higher up, making the width at half maximum more narrow for the original signal than the smoothed signal.

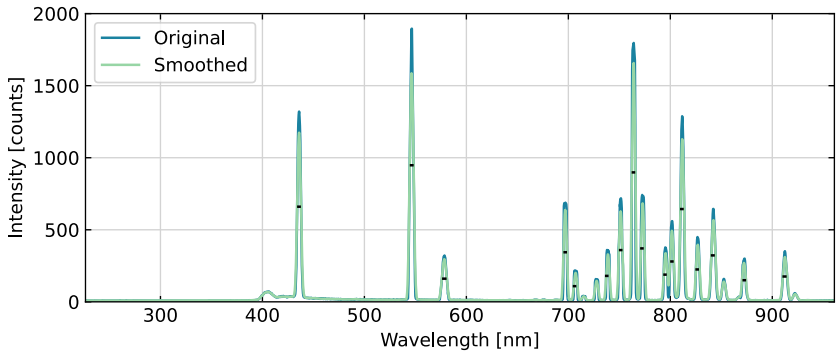

Figure 10.6: FWHM estimated on the center line (center of FOV) of HYPSO-1 pre-launch spectral calibration data, before (blue) and after (green) smoothing. Black vertical lines show the estimated FWHM of the peaks before smoothing.

How this affects the calculated FWHM values are shown in Table 10.1. The average FWHM is reduced from 4.04 nm to 3.68 nm when not smoothing the data. For every peak, the estimated value is lower for the original signal than for the smoothed signal. The

values are also closer to the theoretical FWHM of 3.33 nm when using the original data, showing that the performance of the instrument is actually better than first reported. This shows that the data should not be smoothed before calculating the FWHM values. To reduce noise, if needed, it is better practice to average or sum several images of the same target/lamp. The fluctuations in the signal will then be reduced while the height and shape of the peak are preserved, thereby not affecting the FWHM calculation.

Table 10.1: Calculated FWHM values from the HYPSO-1 pre-launch spectral calibration data before and after smoothing shown in Figure 10.6.

Wavelength [nm]	**FWHM original [nm]**	**FWHM smoothed [nm]**
435.83	3.73	4.22
546.07	3.78	4.37
576.96 / 579.02	4.43	5.01
696.54	3.53	3.70
706.72	3.48	3.65
738.40	3.54	3.66
750.39 / 751.46	3.55	3.83
763.51	3.52	3.70
772.37 / 772.42	3.52	3.69
794.82	3.44	-
800.62 / 801.48	3.47	3.82
810.37 / 811.53	3.66	4.06
826.45	3.53	3.91
840.81 / 842.46	3.93	4.43
871.68	3.56	4.01
912.30	4.12	4.58
Average	3.68	4.04

10.2.2 Estimation of uncertainty and accuracy

Estimating the uncertainties is important, but difficult. When looking at the full signal chain, all steps must be taken into account. Uncertainties from those relating to the equipment used (like the integrating sphere for radiometric calibration) to those of the correction algorithms, atmospheric correction and other post-processing steps, in addition to natural variation in the signal itself (of what is being observed), must be included. This is a challenge, but must not be overlooked when further working with this data.

The uncertainties related to the calibrated and corrected data products are of high importance, especially when used to estimate quantities like Chl-a concentration from data collected by satellite platforms. As discussed in Section 2.1.5, to achieve an accuracy of roughly 30% of the derived Chl-a data products, the water-leaving radiance needs to be determined with an accuracy of 5% (at 443 nm), which means that the ToA radiance must be determined with an accuracy of 0.5% (assuming 90% of the received signal comes from the atmosphere). To achieve these levels, however, both the accuracy and uncertainty of the calibration must be investigated to estimate realistic values. The methods and data should then be improved where possible, which can be a challenging task, as there are limits to the performance of both the instrument and equipment used.

An attempt of estimating the uncertainty of the radiometric calibration coefficients was done in Section 7.2 by looking at how the calibrated values in a single frame was affected by photon noise by comparing the measured values to the ideal reference values. This is, however, not enough, and better ways of estimating the uncertainties and accuracies of both the calibration methods, correction methods, and final data products should be developed.

10.3 The HYPSO-1 hyperspectral imager

The HYPSO-1 FM was built during the winter of 2020/2021, and much was learned both during the development phase and after the satellite was launched into space. Many of the lessons learned were incorporated into the AIT of HYPSO-2, such the as focusing adjustments which are discussed in further detail at the end of Section 10.3.1. Others lessons learned are yet to be implemented.

Here, some of the challenges and possible improvements to future HSI versions are discussed, and the performance of the HYPSO-1 HSI compared to the instrument requirements in Table 1.3.

10.3.1 Assembly, integration, and testing

The AIT process could probably be improved in many ways. The main focus here is, again, on steps that directly affect the optical performance of the instrument, as has been observed in the tests in Chapter 6.

Traceability and version control

First of all, one improvement that could be addressed in the future to help the AIT process could be to engrave the different machined parts with unique part numbers. This would make it easier to keep track of both different versions of the same component (such as the slit tube), as well as which versions and specific components that end up in each model. This would have been especially useful for the test models as they have been disassembled and re-assembled multiple times by different students, making it hard to keep track of which components have been used in each model at any given time. This does not affect the optical performance directly, but is crucial during testing. For example, when investigating variations with temperature with different test models, it is important to know which version of the slit tube that is used at the time of testing.

Spatial shift

One point that should be addressed in particular is the spatial shift seen in the post-launch data of the HYPSO-1 HSI. As discussed in Section 8.1.6, the image shifted 7 pixels in spatial direction after launch. Looking back to the shock and vibration tests performed on the HYPSO-1 QM (presented in Section 6.2.2), a spatial shift of 1-2 pixels was observed. This was, however, not thought to be of any importance, and the test was marked as successful. The post-launch spatial shift was first believed to be due to movement of the slit in the slit holder inside the slit tube. After shock and vibration tests performed on the HYPSO-2 EQM as described in Section 6.2.3, however, it was believed that the shift might be caused by movement of the sensor. It could be either movement of the sensor itself inside the sensor housing or that the full sensor housing moved relative to the optical train.

Heggelund discussed in both in the "HYPSO2-TRP-SHK-001 HYPSO-2 EQM Shock, Resonance, and Vibration Test Report" [175] and in his master's thesis [197] that the most critical component was found to be the HSI sensor, as the highest excitation during the tests was seen for this component. This was partly anticipated since it is only attached to the optical train via a threaded C-mount with no other structural support. It is, therefore, not unlikely that the image will shift during launch for HYPSO-2 as well. For future designs and payload developments this should be taken intro consideration. A stronger connection between the sensor and the optical train should be ensured to avoid similar shifts happening, by for example fixing the sensor head to the main mounting frame. The test results should also be discussed in greater details with experts that might help to catch these weaknesses earlier in the design phase.

Variations in spectral response with temperature

From the other environmental tests, the most noticeable feature found was the variation of spectral response (focus) with temperature, as discussed in Section 6.2.2. The temperature range investigated was between -40°C and 70°C, covering worst case temperatures in both ends. The expected temperature inside the HYPSO-1 satellite was simulated to be between -15°C and 30°C [172] (**Paper 3**). As seen in Figure 10.7, the typical temperature inside a KNA 6U CubeSat measured in orbit is between 10°C and 30°C, meaning that even less temperature fluctuations are experienced inside the satellite in-orbit. When looking at the TVAC test results, the variation in the signal between 10°C and 30°C is not very large. It should, therefore, not be crucial to correct for the slight variation in response with temperature. It should not be ignored, however, when estimating uncertainty and accuracy of the results.

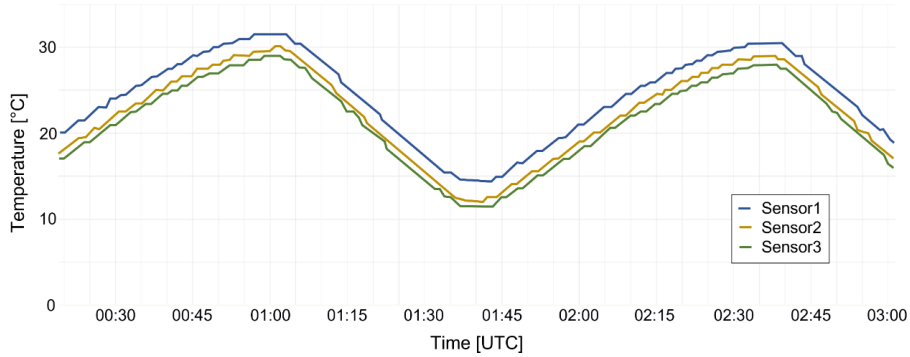

*Figure 10.7: Measured in-orbit temperature profiles from three temperature sensors located inside a KNA 6U CubeSat. Source: KNA via [172] (**Paper 3**).*

It is also worth noting the difference in background level with increasing temperature, as shown in both the HYPSO-1 in-orbit data (Section 8.1.1) and for TVAC testing of the HYPSO-2 EQM (Section 6.2.3). Even though the temperature inside the satellite bus does not vary much, the sensor itself heats up during a capture, which affects the noise and background level recorded by the sensor. It could therefore be beneficial to include a correction for this by adjusting the background value removed during radiometric calibration based on the sensor temperature during the capture. There is a temperature sensor close to the camera sensor inside the detector housing, which could be used both during characterization of the background value with sensor temperature in-orbit, and for input to the correction. This should be looked further into.

Another option which should be considered for future instruments (for satellite platforms specifically), is to perform the calibration in TVAC. Calibration coefficients would then be available for several temperatures, and the instrument response could be modeled as a function of temperature.

Focusing the instrument

For HYPSO-1, all procedures for AIT were made from scratch, and it was hard to know the importance of the different steps and which ones to prioritize. One of the steps that should have been prioritized even higher, is the methods of setting the focus correctly, both on the individual lens objectives and of the full instrument itself during assembly.

For HYPSO-1, the steps described for the HSI V6 in Section 3.3 were followed. Overall these methods work fine, but it was experienced that the lens objectives were difficult to adjust once the grease inside was removed (which it had to be, to avoid problems in vacuum). Fine-tuning the focus of each lens objective was therefore a difficult task in itself, and trying to focus on a target far away out the window with no clear metric on what is "good enough" was not optimal. Suggestions later came up, such as using patterns like a Bahtinov mask to focus the objectives, but not enough time has been spent on exploring such options.

The methods for focusing the full instrument were improved from HYPSO-1 to HYPSO-2 by adding separate checks for spectral and spatial focus during assembly when adding the spacer rings. The collimator-pattern-assembly has been a useful tool, but the method of selecting the correct spacer ring(s) to achieve optimal focus can still be improved. As already discussed, the focus can only be optimized for one wavelength (or a short spectral range) at the time. Using the center wavelength as the main wavelength to focus on is the most intuitive option. However, the blurring on the edges is not symmetric, so if the goal is to have the best focus across the full spectral range methods should be developed to estimate (or simulate beforehand) which option that is better for this.

All in all, the processing of focusing the lens objectives and instrument should be developed further to ensure that the instrument is focused properly, as this affects the quality of the data products significantly.

10.3.2 Performance compared to the requirements

The performance of the HYPSO-1 HSI compared to some of the requirements presented in Table 1.3 were shown in Table 7.3. The sensor response was shown to be linear (with different exposure times) and the FWHM estimated to be less than 5 nm for all wavelengths in the spectral range. For the smile and keystone correction, the maximum smile present after correction was just above the requirement of 1 pixel, while keystone was within the requirement. The distortions from smile would be improved by using the smile correction with the spectral calibration matrix, as shown in Figure 8.14 and discussed in Section 8.2.2. In addition, the spectral range has been shown to cover the 400 nm to 800 nm within the pre-selected AoI for nominal operations, and no large stray light effects have been detected.

The in-orbit SNR was investigated in Bakken et al. [28] (**Paper 7**) and shown to be about 100-400 in the 400 nm to 800 nm range. Since the requirement did not specify if an SNR above 400 was required at only one wavelength/band or the full range, one can choose to say that it is a pass. However, most bands have an SNR below the set requirement. The spectral resolution was also estimated using in-orbit data in Bakken et al. [28] (**Paper 7**), as presented in Section 8.1.5. No field data was acquired with the HYPSO-1 FM before launch. Data of atmospheric absorption lines, for example, could therefore not be compared directly before and after launch to investigate any changes in spectral resolution or detect any spectral shifts. The spectral resolution of HYPSO-1 in-orbit was, therefore, estimated by comparing with reference Fraunhofer lines. For the HYPSO-2 FM, a spectrum of the sky on a cloudy day was acquired. The spectrum is shown in Figure 10.8 together with a spectrum from a cloud pixel captured by HYPSO-1 in-orbit (since HYPSO-2 is not launched yet). It can be seen that features from the Fraunhofer lines and atmospheric absorption lines are present in both spectra, and will be useful for comparison of pre- and post-launch data of the HYPSO-2 FM when the time comes.

Overall, the performance of the HYPSO-1 HSI is mostly as expected. The spectral resolution estimated from in-orbit data is a bit worse than estimated from the pre-launch data, but this is more likely due to the different method used than changes in the instrument response itself. From Bakken et al. [28] (**Paper 7**) it should also be noticed that the spatial resolution was estimated. The ground resolvable distance was found to vary a lot across wavelengths, with the sharpest bands being around 550 nm. This coincides with was seen in the spatial focus test presented in Section 7.7. This makes it harder to reach the mission goal of a spatial resolution of 100 m per pixel, specially if one would try to reach this goal for all wavelengths in the 400 nm to 800 nm spectral range.

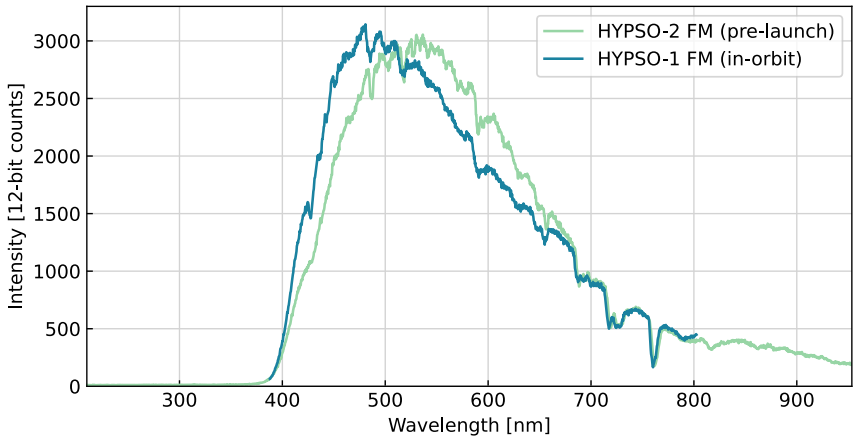

Figure 10.8: Cloud spectra by the HYPSO-2 FM pointing out the window in the lab, and by the HYPSO-1 FM from in-orbit, illustrating Fraunhofer lines and atmospheric absorption lines being visible for comparison in pre- and post-launch data. Note: the spectra might be different due to different scattering mechanisms. In addition, the spectrum by HYPSO-2 might be affected by looking through a window, and the spectrum from HYPSO-1 might be affected by ocean surface underneath the partly transparent clouds.

10.3.3 Validation of calibration and data products

HYPSO-1 data has been calibrated, producing ToA radiance values. To investigate these calibrated ToA radiance values, a selection of calibrated point spectra from HYPSO-1 in-orbit data were selected, as shown in Figure 10.9. It can be seen that the calibrated values are around 5-110 mW/(m^2 sr nm) across the full spectral range. The ocean signature is quite dark, while the cloud signature is the brightest, which is as expected. It can also be seen that the forest signal increases around 700 nm, which is as expected from vegetation.

When looking at ToA radiance values in the literature, simulated values of about 10-160 mW/(m^2 sr nm) [198, 199, 200] and measured values of 10-170 mW/(m^2 sr nm) [201] (converted from 1-17 μW/(cm^2 sr nm) as originally stated in the paper) can be found. This suggests that the HYPSO-1 calibration does indeed give reasonable results, as the values are close to the values found in the literature. However, validation in terms of checking the actual accuracy and uncertainty related to the calibrated values (as discussed in Section 2.3.9), in addition to any other derived data products, still remains and must be completed.

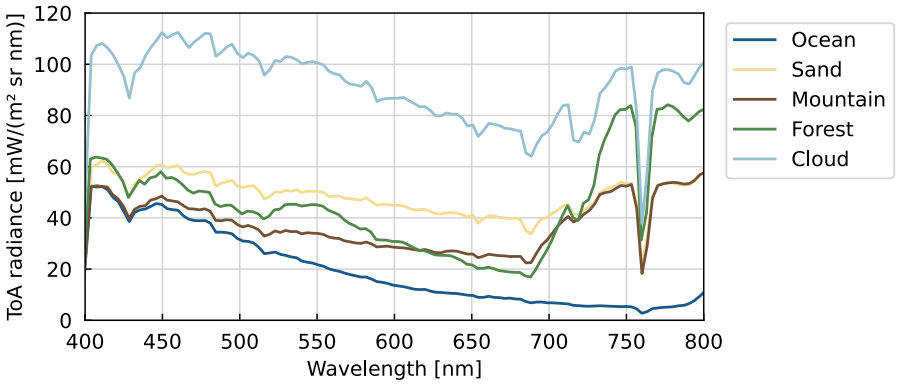

Figure 10.9: Calibrated spectra captured by HYPSO-1 in-orbit.

10.4 Research questions

The research in this thesis has been driven forward by the need of calibrated instruments for the HYPSO-1 and HYPSO-2 missions. On the way, research questions were defined to keep the exploration of different methods and techniques on track, and to make sure that the main questions related to the needs of the project were answered. Here, some discussion and answers to the research questions presented in Section 1.3.1 are presented.

RQ1:
What is a simple yet trustworthy method of performing wavelength calibration, and what must be taken into account to make sure it yields sufficient results?

This question is slightly vaguely formulated, mostly due to the uncertainties relating to whether or not any experiments could be designed to prove a better way of performing wavelength calibration with the available equipment (spectral lamps as described in Section 4.1.1). Several configurations (meaning combinations of different spectral lamps) were tested, and preliminary tests (not described here) were also performed when designing the experiments. Overall, the results did not confirm any specific method or spectral line selection that would give the best results. There were, however, several useful observations made on the way. That measurement points on the edges of the spectrogram are desirable is no surprise, but is useful information to have when selecting which spectral lamps to use in the calibration. The same goes for not needing points to be evenly distributed over the spectral range. This means that spectral lines at the edges should be prioritized over evenly distributed points in the spectrogram. It is also a useful

observation that removing the double peaks improves the results. For describing the pixel to wavelength relationship, no method was proven to be the best, but it was shown that both first, second and third order polynomials describe the relationship nicely, and that using theoretical knowledge such as including trigonometric relations can be beneficial and could be explored further. This is also useful knowledge, as the choice of which fit to use does not matter too much, and should not take up too many resources unless needed by strict spectral calibration requirements.

RQ2:
Which calibration and characterization procedures are needed to describe the performance of a low-cost HSI for ocean color applications?

The choice of which calibration and characterization procedures that should be performed is a tough challenge, as there are many characteristics that can describe the performance of a hyperspectral imager (as listed in Skauli [83]). As mentioned several times already, the cost of the calibration campaign should be consistent with the cost of the instrument [85]. It is therefore important to figure out which calibration and characterization steps that are most important for the instrument in question, specially for the low-cost ones. For the HSI used in this thesis, the smile distortion is quite prominent, which is why smile and keystone correction has been in focus since early development of the instrument. Other things, like stray light for example, has not been found to be a large issue, and has therefore not been prioritized. Wavelength and radiometric calibration are anyways essential calibrations that need to be performed to be able to convert the measurements to useful units. Further, from what has been explored in this thesis, it is worth setting up tests to characterize any features that are known problems, and characteristics that are needed to be able to estimate the quality of the data products. Performing characterizations where the results anyways will not be incorporated in any models or corrections, such as polarization sensitivity for HYPSO-1, should not be prioritized.

RQ3:
Which steps should be a part of the pre- and post-processing pipeline for the HYPSO-1 HSI?

One of the main things to figure out for the HYPSO HSIs is which calibration and correction steps to include in the data processing pipeline. The exact steps can not really be decided until the instrument has been launched, which is why this question focuses on HYPSO-1 only. From the work presented in Section 8.3 the answer to this research question is quite straight forward. For the HYPSO-1 HSI, the pre-processing

steps should be to set dimensions when reading the datacube, flip the x-axis and scale the data by the binning factor to obtain the 12-bit sensor counts. The wavelengths for each band should be calculated (if not already available in an existing file such as the spectral calibration matrix). Radiometric calibration should then be performed, by first subtracting the background value from the data, followed by applying the radiometric calibration coefficients. This should be followed by smile correction using the spectral calibration matrix. Finally, destriping should be performed to smooth out the response from blobs in the spectrogram. In addition to these steps, georeferencing and correction of geometric distortions in the spatial-spatial domain should also be performed on the data. Further, atmospheric correction can be applied and level 2 data products can be calculated.

RQ4:
Can a small HSI built out of COTS components be used to detect algae in the ocean?

From what has been presented in Chapter 9, the answer is yes. The spectral signature in each pixel can be used in combination with band ratio algorithms to enhance Chl-a features as shown in Figure 9.3 and Figure 9.4. In addition, the experiments with the AFTI-scope shows that different algal pigments can be recognized in spectra collected with the HSI V6. This is promising for further development of HYPSO-1 Chl-a detecting algorithms. Already, studies are being done to test algorithms and machine learning techniques to develop methods for Chl-a detection for HYPSO-1. One such example can be found in the master's thesis of Flores-Romero [202], which explores methods for Chl-a detection on atmospherically corrected HYPSO-1 reflectance data.

11 | Conclusions

In this thesis, the design, assembly, calibration, and optical performance of a pushbroom grating-based HSI for the 400 nm to 800 nm spectral range has been presented. The original assembly was made to fit as a drone payload. The design was then further developed for use in space, and models were made for the HYPSO-1 and HYPSO-2 CubeSats payloads. HYPSO-1 was launched in 2022 and has acquired data showing that the instrument works as expected and that the achieved performance is close to what was estimated from lab characterizations performed prior to launch. HYPSO-2 is scheduled for launch in 2024.

The focus in this thesis has been on calibration methods, characterization methods to estimate the optical performance, and ways of improving the optical performance of the HSIs used for both drones, HYPSO-1, and HYPSO-2. A study on wavelength calibration was performed to ensure that the correct wavelengths are mapped to each pixel, and investigations into correction of second order diffraction effects has been done in an attempt to make data from wavelengths longer than 800 nm available to the user.

The HYPSO-1 and HYPSO-2 HSI models have been thoroughly calibrated and characterized in the lab prior to launch, and methods for assembly have been improved by incorporating lessons learned along the way. The HYPSO-1 in-orbit calibration and validation is still ongoing, but the main steps for a calibration and correction pipeline has been outlined, and initial attempts to verify that the calibration products are reasonable have been performed successfully.

Using these HSIs for observation of algal blooms seems possible from the signatures seen in the lab by attaching the HSI to a microscope, and from the initial Chl-a maps calculated from the HYPSO-1 data. Algorithms for algal bloom detection are, however, still under development and should be finalized, tested, and validated before finally being implemented onboard the satellites.

List of abbreviations

AaSI Aalto Spectral Imager
AFTI Autonomous Flowthrough Imaging
AIT Assembly, Integration, and Testing
AMOS Centre for Autonomous Marine Operations and Systems
AoI Area of Interest
AOP Apparent Optical Property
ARF Along-Track Response Function
ASPECT Asteroid Spectral Imaging Mission
AUV Autonomous Underwater Vehicle

BOUSSOLE Buoy for the Acquisition of a Long-Term Optical Series

CAD Computer Aided Drafting
CDOM Colored Dissolved Organic Matter
CHB Calibration Home Base
CHIMA the Compact Hyperspectral Instrument for Monitoring the Atmosphere
CHIME the Copernicus Hyperspectral Imaging Mission for the Environment
Chl-a Chlorophyll-a
Chl-b Chlorophyll-b
Chl-c Chlorophyll-c
CMOS Complementary Metal Oxide Semiconductor
COTS Commercial-Off-The-Shelf
CRF Cross-Track Response Function
CSIMBA the Compact Smartspectral Imager for Monitoring Bio-agricultural Areas
CTD Conductivity, Temperature, and Depth
CubeSat Cube Satellite
CZCS Coastal Zone Color Scanner

DCC Deep Convective Cloud
DLR the German Aerospace Center
DTU the Technical University of Denmark

ELOIS the Enhanced Light Offner Imaging Spectrometer
EM Engineering Model
EnMAP the Environmental Mapping and Analysis Program
EO Edmund Optics
EQM Engineering-Qualification Model
ESA the European Space Agency
ESD Electrostatic Discharge
ESTEC the European Space Research and Technology Centre

FFI the Norwegian Defense Research Establishment
FLEX Fluorescence Explorer
FLORIS Fluorescence Imaging Spectrometer
FM Flight Model
FOV Field of View
FPI Fabry-Pérot Interferometer
FWHM Full-Width at Half-Maximum

GCP Ground Control Point

HAB Harmful Algal Bloom
HDR High Dynamic Range
HICO the Hyperspectral Imager for the Coastal Ocean
HPLC High-performance Liquid Chromatography
HSI Hyperspectral Imager
HYPSO Hyperspectral Small Satellite for Ocean Observation

IB In-Band
iDS Imaging Development Systems
IFOV Instantaneous Field of View
IOCCG International Ocean Colour Coordinating Group
IOP Inherent Optical Property
IR Infrared
ISS the International Space Station
ITK the Department of Engineering Cybernetics

KB3 Kings Bay 3
KNA Kongsberg NanoAvionics

LED Light-Emitting Diode

LEO Low Earth Orbit
LSF Line Spread Function
LVF Linear Variable Filter

M6P Multipurpose 6U Platform
MASSIVE Mission-oriented Autonomous Systems with Small Satellites for Maritime Sensing, Surveillance and Communication
MERIS the Medium Resolution Imaging Spectrometer
MISR Multi-Angle Imaging Spectroradiometer
MOBY the Marine Optical Buoy
MODIS the Moderate Resolution Imaging Spectroradiometer
MTF Modulation Transfer Function

NACHOS the Nano-satellite Atmospheric Chemistry Hyperspectral Observation System
NASA National Aeronautics and Space Administration
ND Neutral Density
NDVI Normalized Difference Vegetation Index
NIR Near-Infrared
NIST National Institute of Standards and Technology
NoSA the Norwegian Space Agency
NRC the Research Council of Norway
NTNU the Norwegian University of Science and Technology

OC Ocean Chlorophyll
OCI the Ocean Color Instrument
OCSF On-Chip Stepped Filter
OLCI the Ocean and Land Colour Instrument

PACE Plankton, Aerosol, Cloud, ocean Ecosystem
PAM Pulse Amplitude Modulation
Ph.D. Philosophiae Doctor
PicoBoB Pico Breakout Board
PICS Pseudo-Invariant Calibration Sites
PLA PolyLactic Acid
PNW Polar Night Week
POLDER Polarization and Directionality of the Earth's Reflectance
PRISMA the Hyperspectral Precursor of the Application Mission
PRNU Photo Response Nonuniformity
PRODEX Programme de Développement d'Expériences Scientifiques

PSF Point Spread Function

QE Quantum Efficiency
QM Qualification Model

RGB Red-Green-Blue
RMSE Root Mean Square Error
ROLO Robotic Lunar Observatory
ROV Remotely Operated Vehicle
RQ1 Research Question 1
RQ2 Research Question 2
RQ3 Research Question 3
RQ4 Research Question 4
RTM Radiative Transfer Model
RTS Random Telegraph Signal

SD Standard Deviation
SDF Spectral Stray Light Signal Distribution Function
SDR Software Defined Radio
SeaWiFS the Sea-viewing Wide Field-of-view Sensor
SI the International System of Units
SIOS Svalbard Integrated Arctic Earth Observing System
SiRF Spatial Response Function
SmallSat Small Satellite
SNR Signal-to-Noise Ratio
SP Supporting Paper
SRF Spectral Response Function
SRS Shock Response Spectrum
SSD Spatial Sampling Distance
SST Sea Surface Temperature

TBS Trondheim Biological Station
TMA Three-Mirror Anastigmat
ToA Top-of-Atmosphere
TROPOMI Tropospheric Monitoring Instrument
TSM Total Suspended Matter
TVAC Thermal Vacuum

UAV Unmanned Aerial Vehicle

UiO the University of Oslo
UNIS the University Centre in Svalbard
USV Unmanned Surface Vehicle
UV Ultraviolet

V4 Version 4
V6 Version 6
VIS Visible

WHISPERS the Workshop on Hyperspectral Image and Signal Processing: Evolution in Remote Sensing
WITSO the Workshop on Innovative Technologies for Space Optics

YGT Young Graduate Trainee

Bibliography

[1] IOCCG, *Why Ocean Colour? The Societal Benefits of Ocean-Colour Technology*, vol. No. 7 of *Reports of the International Ocean Colour Coordinating Group.* Dartmouth, Canada: IOCCG, 2008.

[2] IOCCG, *Remote Sensing of Ocean Colour in Coastal, and Other Optically-Complex, Waters*, vol. No. 3 of *Reports of the International Ocean Colour Coordinating Group.* Dartmouth, Canada: IOCCG, 2000.

[3] W. A. Hovis, D. K. Clark, F. Anderson, R. W. Austin, W. H. Wilson, E. T. Baker, D. Ball, H. R. Gordon, J. L. Mueller, S. Z. El-Sayed, B. Sturm, R. C. Wrigley, and C. S. Yentsch, "Nimbus-7 Coastal Zone Color Scanner: System Description and Initial Imagery," *Science*, vol. 210, no. 4465, pp. 60–63, 1980.

[4] P.-Y. Deschamps, F.-M. Breon, M. Leroy, A. Podaire, A. Bricaud, J.-C. Buriez, and G. Seze, "The POLDER mission: instrument characteristics and scientific objectives," *IEEE Transactions on Geoscience and Remote Sensing*, vol. 32, no. 3, pp. 598–615, 1994.

[5] S. B. Hooker and W. E. Esaias, "An overview of the SeaWiFS Project," *Eos, Transactions American Geophysical Union*, vol. 74, no. 21, pp. 241–246, 1993.

[6] C. R. McClain, G. C. Feldman, and S. B. Hooker, "An overview of the SeaWiFS project and strategies for producing a climate research quality global ocean bio-optical time series," *Deep Sea Research Part II: Topical Studies in Oceanography*, vol. 51, no. 1-3, pp. 5–42, 2004.

[7] W. Esaias, M. Abbott, I. Barton, O. Brown, J. Campbell, K. Carder, D. Clark, R. Evans, F. Hoge, H. Gordon, W. Balch, R. Letelier, and P. Minnett, "An overview of MODIS capabilities for ocean science observations," *IEEE Transactions on Geoscience and Remote Sensing*, vol. 36, no. 4, pp. 1250–1265, 1998.

[8] W. Barnes, T. Pagano, and V. Salomonson, "Prelaunch characteristics of the Moderate Resolution Imaging Spectroradiometer (MODIS) on EOS-AM1," *IEEE Transactions on Geoscience and Remote Sensing*, vol. 36, no. 4, pp. 1088–1100, 1998.

[9] M. Rast, J. L. Bézy, and S. Bruzzi, "The ESA Medium Resolution Imaging Spectrometer MERIS a review of the instrument and its mission," *International Journal of Remote Sensing*, vol. 20, no. 9, pp. 1681–1702, 1999.

[10] R. L. Lucke, M. Corson, N. R. McGlothlin, S. D. Butcher, D. L. Wood, D. R. Korwan, R. R. Li, W. A. Snyder, C. O. Davis, and D. T. Chen, "Hyperspectral Imager for the Coastal Ocean: instrument description and first images," *Applied Optics*, vol. 50, no. 11, pp. 1501–1516, 2011.

[11] "OLCI Instrument Description." Retrieved from `https://sentinels.copernicus.eu/web/sentinel/technical-guides/sentinel-3-olci/olci-instrument/description`. Accessed: 2023-04-20 .

[12] R. Loizzo, C. Ananasso, R. Guarini, E. Lopinto, L. Candela, and A. R. Pisani, "The PRISMA hyperspectral mission," in *Proc. Living Planet Symposium, ESA SP-740*, vol. SP-740, 2016.

[13] L. Guanter, H. Kaufmann, K. Segl, S. Foerster, C. Rogass, S. Chabrillat, T. Kuester, A. Hollstein, G. Rossner, C. Chlebek, C. Straif, S. Fischer, S. Schrader, T. Storch, U. Heiden, A. Mueller, M. Bachmann, H. Mühle, R. Müller, M. Habermeyer, A. Ohndorf, J. Hill, H. Buddenbaum, P. Hostert, S. Van Der Linden, P. J. Leitão, A. Rabe, R. Doerffer, H. Krasemann, H. Xi, W. Mauser, T. Hank, M. Locherer, M. Rast, K. Staenz, and B. Sang, "The EnMAP spaceborne imaging spectroscopy mission for earth observation," *Remote Sensing*, vol. 7, no. 7, pp. 8830–8857, 2015.

[14] S. Chabrillat, M. Brell, K. Segl, S. Foerster, L. Guanter, A. Schickling, T. Storch, H.-P. Honold, and S. Fischer, "The EnMAP Satellite - Mission Status and Science Preparatory Activities," in *IEEE International Geoscience and Remote Sensing Symposium (IGARSS)*, (Brussels, Belgium), pp. 123–125, 2021.

[15] P. J. Werdell, M. J. Behrenfeld, P. S. Bontempi, E. Boss, B. Cairns, G. T. Davis, B. A. Franz, U. B. Gliese, E. T. Gorman, O. Hasekamp, K. D. Knobelspiesse, A. Mannino, J. V. Martins, C. R. McClain, G. Meister, and L. A. Remer, "The Plankton, Aerosol, Cloud, Ocean Ecosystem Mission: Status, Science, Advances," *Bulletin of the American Meteorological Society*, vol. 100, no. 9, pp. 1775–1794, 2019.

[16] M. Rast, J. Nieke, J. Adams, C. Isola, and F. Gascon, "Copernicus Hyperspectral Imaging Mission for the Environment (CHIME)," in *IEEE International Geoscience and Remote Sensing Symposium (IGARSS)*, pp. 108–111, 2021.

[17] E. Sakshaug, G. Johnsen, and K. M. Kovacs, *Ecosystems Barents Sea.* Tapir Academic Press, 2009.

[18] "Phytoplankton bloom captured by Envisat." Retrieved from `https://www.esa.int/ESA_Multimedia/Images/2011/08/Phytoplankton_bloom_captured_by_Envisat`. Accessed: 2020-04-20.

[19] IOCCG, *Phytoplankton Functional Types from Space*, vol. No. 15 of *Reports of the International Ocean Colour Coordinating Group.* Dartmouth, Canada: IOCCG, 2014.

[20] IOCCG, *Observation of Harmful Algal Blooms with Ocean Colour Radiometry*, vol. No. 20 of *Reports of the International Ocean Colour Coordinating Group.* Dartmouth, Canada: IOCCG, 2021.

[21] C. Y. Kao, "Paralytic shellfish poisoning," in *Algal Toxins in Seafood and Drinking Water*, London: Academic Press, 1993.

[22] W. W. Carmichael, "Blue-Green Algae: An Overlooked Health Threat," *Health & Environment Digest*, vol. 5, no. 6, 1991.

[23] P. M. Gilbert, D. M. Anderson, P. Gentien, E. Granéli, and K. G. Sellner, "The Global Complex Phenomena of Harmful Algal Blooms," *Oceanography*, vol. 18, no. 2, pp. 136–147, 2005.

[24] S. Roy, C. A. Llewellyn, E. S. Egeland, and G. Johnsen, *Phytoplankton pigments: characterization, chemotaxonomy and applications in oceanography.* Cambridge University Press, 2011.

[25] S. Sathyendranath, L. Watts, E. Devred, T. Platt, C. Caverhill, and H. Maass, "Discrimination of diatoms from other phytoplankton using ocean-colour data," *Marine Ecology Progress Series*, vol. 272, pp. 59–68, 2004.

[26] H. M. Dierssen, S. G. Ackleson, K. E. Joyce, E. L. Hestir, A. Castagna, S. Lavender, and M. A. McManus, "Living up to the Hype of Hyperspectral Aquatic Remote Sensing: Science, Resources and Outlook," *Frontiers in Environmental Science*, vol. 9, 2021.

[27] M. Ludvigsen and A. J. Sørensen, "Towards integrated autonomous underwater operations for ocean mapping and monitoring," *Annual Reviews in Control*, vol. 42, no. 2016, pp. 145–157, 2016.

[28] S. Bakken, M. B. Henriksen, R. Birkeland, D. D. Langer, A. E. Oudijk, S. Berg, Y. Pursley, J. L. Garrett, F. Gran-Jansen, E. Honoré-Livermore, M. E. Grøtte, B. A. Kristiansen, M. Orlandic, P. Gader, A. J. Sørensen, F. Sigernes, G. Johnsen, and T. A. Johansen, "HYPSO-1 CubeSat: First Images and In-Orbit Characterization," *Remote Sensing*, vol. 15, no. 3, 2023.

[29] M. E. Grøtte, R. Birkeland, E. Honoré-Livermore, S. Bakken, J. L. Garrett, E. F. Prentice, F. Sigernes, M. Orlandić, J. T. Gravdahl, and T. A. Johansen, "Ocean color hyperspectral remote sensing with high resolution and low latency—the hypso-1 cubesat mission," *IEEE Transactions on Geoscience and Remote Sensing*, vol. 60, pp. 1–19, 2022.

[30] D. D. Langer, M. Orlandic, S. Bakken, R. Birkeland, J. L. Garrett, T. A. Johansen, and A. J. Sørensen, "Robust and Reconfigurable Hyperspectral Imaging Processing On-Board a Small Satellite," *Remote Sensing*, vol. 15, no. 5, 2023.

[31] E. Honoré-Livermore, R. Birkeland, S. Bakken, J. L. Garrett, and C. Haskins, "Digital Engineering Development in an Academic CubeSat Project," *Journal of Aerospace Information Systems*, vol. 19, no. 10, pp. 649–660, 2022.

[32] E. F. Prentice, E. Honoré-Livermore, S. Bakken, M. B. Henriksen, R. Birkeland, M. Hjertenæs, A. Gjersvik, T. A. Johansen, F. Aguado-Agelet, and F. Navarro-Medina, "Pre-Launch Assembly, Integration, and Testing Strategy of a Hyperspectral Imaging CubeSat, HYPSO-1," *Remote Sensing*, vol. 14, no. 18, p. 4584, 2022.

[33] R. Birkeland, G. Quintana-Diaz, E. Honore-Livermore, T. Ekman, F. A. Agelet, and T. A. Johansen, "Development of a multi-purpose SDR payload for the HYPSO-2 satellite," in *IEEE Aerospace Conference*, 2022.

[34] F. Sigernes, M. Syrjäsuo, R. Storvold, J. Fortuna, M. E. Grøtte, and T. A. Johansen, "Do it yourself hyperspectral imager for handheld to airborne operations," *Optics Express*, vol. 26, no. 5, pp. 6021–6035, 2018.

[35] M. B. Henriksen, E. F. Prentice, C. M. van Hazendonk, F. Sigernes, and T. A. Johansen, "Do-it-yourself VIS/NIR pushbroom hyperspectral imager with C-mount optics," *Optics Continuum*, vol. 1, no. 2, p. 427, 2022.

[36] E. F. Prentice, M. E. Grøtte, F. Sigernes, and T. A. Johansen, "Design of a hyperspectral imager using COTS optics for small satellite applications," in *Proc. SPIE 11852, International Conference on Space Optics – ICSO 2020, 1185258*, 2021.

[37] A. Morel and L. Prieur, "Analysis of variations in ocean color," *Limnology and Oceanography*, vol. 22, no. 4, pp. 709–722, 1977.

[38] J. Berge, G. Johnsen, and J. H. Cohen, *Polar Night Marine Ecology*. Springer, 2020.

[39] V. Stuart, S. Sathyendranath, T. Platt, H. Maass, and B. D. Irwin, "Pigments and species composition of natural phytoplankton populations: effect on the absorption spectra," *Journal of Plankton Research*, vol. 20, no. 2, pp. 187–217, 1998.

[40] C. Mobley, E. Boss, and C. Roesler, "Ocean Optics Web Book." Retrieved from `https://www.oceanopticsbook.info`. Accessed: 2023-04-21.

[41] R. Gordon, "Atmospheric correction of ocean color imagery in the Earth Observing System era," *Journal of Geophysical Research*, vol. 102, no. D14, pp. 17081–17106, 1997.

[42] IOCCG, *Mission Requirements for Future Ocean-Colour Sensors*, vol. No. 13 of *Reports of the International Ocean Colour Coordinating Group*. Dartmouth, Canada: IOCCG, 2012.

[43] J. E. O'Reilly and P. J. Werdell, "Chlorophyll algorithms for ocean color sensors - OC4, OC5 & OC6," *Remote Sensing of Environment*, vol. 229, pp. 32–47, 2019.

[44] P. J. Werdell, L. I. McKinna, E. Boss, S. G. Ackleson, S. E. Craig, W. W. Gregg, Z. Lee, S. Maritorena, C. S. Roesler, C. S. Rousseaux, D. Stramski, J. M. Sullivan, M. S. Twardowski, M. Tzortziou, and X. Zhang, "An overview of approaches and challenges for retrieving marine inherent optical properties from ocean color remote sensing," *Progress in Oceanography*, vol. 160, pp. 186–212, 2018.

[45] J. E. O'Reilly, S. Maritorena, B. G. Mitchell, D. A. Siegel, K. L. Carder, S. A. Garver, M. Kahru, and C. McClain, "Ocean color chlorophyll algorithms for SeaWiFS," *Journal of Geophysical Research*, vol. 103, no. C11, pp. 24937–24953, 1998.

[46] IOCCG, *Minimum Requirements for an Operational Ocean-Colour Sensor for the Open Ocean*, vol. No. 1 of *Reports of the International Ocean Colour Coordinating Group*. Dartmouth, Canada: IOCCG, 1998.

[47] K. R. Turpie, B. County, T. Bell, S. Barbara, and H. M. Dierssen, "Global Observations of Coastal And Inland Aquatic Habitats," tech. rep., 2016.

[48] F. E. Muller-Karger, E. Hestir, C. Ade, K. Turpie, D. A. Roberts, D. Siegel, R. J. Miller, D. Humm, N. Izenberg, M. Keller, F. Morgan, R. Frouin, A. G. Dekker, R. Gardner, J. Goodman, B. Schaeffer, B. A. Franz, N. Pahlevan, A. G. Mannino, J. A. Concha, S. G. Ackleson, K. C. Cavanaugh, A. Romanou, M. Tzortziou, E. S. Boss, R. Pavlick, A. Freeman, C. S. Rousseaux, J. Dunne, M. C. Long, E. Klein, G. A. McKinley, J. Goes, R. Letelier, M. Kavanaugh, M. Roffer, A. Bracher, K. R. Arrigo, H. Dierssen, X. Zhang, F. W. Davis, B. Best, R. Guralnick, J. Moisan, H. M. Sosik, R. Kudela, C. B. Mouw, A. H. Barnard, S. Palacios, C. Roesler, E. G. Drakou, W. Appeltans, and W. Jetz, "Satellite sensor requirements for monitoring essential biodiversity variables of coastal ecosystems," *Ecological Applications*, vol. 28, no. 3, pp. 749–760, 2018.

[49] L. Qi, Z. Lee, C. Hu, and M. Wang, "Requirement of minimal signal-to-noise ratios of ocean color sensors and uncertainties of ocean color products," *Journal of Geophysical Research: Oceans*, pp. 2017–2033, 2017.

[50] H. R. Gordon, "Radiometric considerations for ocean color remote sensors," *Applied Optics*, vol. 29, no. 22, 1990.

[51] R. M. Kudela, S. B. Hooker, H. F. Houskeeper, and M. McPherson, "The influence of signal to noise ratio of legacy airborne and satellite sensors for simulating next-generation coastal and inland water products," *Remote Sensing*, vol. 11, no. 18, 2019.

[52] IOCCG, *Atmospheric Correction for Remotely-Sensed Ocean-Colour Products*, vol. No. 10 of *Reports of the International Ocean Colour Coordinating Group*. Dartmouth, Canada: IOCCG, 2010.

[53] C. O. Davis, M. Kavanaugh, R. Letelier, W. P. Bissett, and D. Kohler, "Spatial and spectral resolution considerations for imaging coastal waters," *Coastal Ocean Remote Sensing*, vol. 6680, 2007.

[54] E. Herrala, J. T. Okkonen, T. S. Hyvarinen, M. Aikio, and J. Lammasniemi, "Imaging spectrometer for process industry applications," in *Proc. SPIE 2248, Optical Measurements and Sensors for the Process Industries*, 1994.

[55] F. Sigernes, D. A. Lorentzen, K. Heia, and T. Svenøe, "Multipurpose spectral imager," *Applied Optics*, vol. 39, no. 18, pp. 3143–3153, 2000.

[56] Z. Volent, G. Johnsen, and F. Signernes, "Kelp forest mapping by use of airborne hyperspectral imager," *Journal of Applied Remote Sensing*, vol. 1, 2007.

[57] S.-E. Qian, "Hyperspectral Satellites, Evolution, and Development History," *IEEE Journal of Selected Topics in Applied Earth Observations and Remote Sensing*, vol. 14, pp. 7032–7056, 2021.

[58] H. Saari, V.-V. Aallos, A. Akujärvi, T. Antila, C. Holmlund, U. Kantojärvi, J. Mäkynen, and J. Ollila, "Novel miniaturized hyperspectral sensor for UAV and space applications," in *Proc. SPIE 7474, Sensors, Systems, and Next-Generation Satellites XIII, 74741M*, 2009.

[59] H. Saari, I. Pellikka, L. Pesonen, S. Tuominen, J. Heikkilä, C. Holmlund, J. Mäkynen, K. Ojala, and T. Antila, "Unmanned Aerial Vehicle (UAV) operated spectral camera system for forest and agriculture applications," in *Proc. SPIE 8174, Remote Sensing for Agriculture, Ecosystems, and Hydrology XIII, 81740H*, 2011.

[60] E. Honkavaara, H. Saari, J. Kaivosoja, I. Pölönen, T. Hakala, P. Litkey, J. Mäkynen, and L. Pesonen, "Processing and assessment of spectrometric, stereoscopic imagery collected using a lightweight UAV spectral camera for precision agriculture," *Remote Sensing*, vol. 5, no. 10, pp. 5006–5039, 2013.

[61] J. G. Dwight, T. S. Tkaczyk, D. Alexander, M. E. Pawlowski, R.-I. Stoian, J. C. Luvall, P. F. Tatum, and G. J. Jedlovec, "Compact snapshot image mapping spectrometer for unmanned aerial vehicle hyperspectral imaging," *Journal of Applied Remote Sensing*, vol. 12, no. 04, 2018.

[62] N. Bedard, N. A. Hagen, L. Gao, and T. S. Tkaczyk, "Image mapping spectrometry: calibration and characterization," *Optical Engineering*, vol. 51, no. 11, p. 1, 2012.

[63] D. R. Korwan, R. L. Lucke, N. R. McGlothlin, S. D. Butcher, D. L. Wood, J. H. Bowles, M. Corson, W. A. Snyder, C. O. Davis, and D. T. Chen, "Laboratory characterization of the Hyperspectral Imager for the Coastal Ocean (HICO)," in *IEEE International Geoscience and Remote Sensing Symposium (IGARSS)*, 2009.

[64] B. C. Gao, R. R. Li, R. L. Lucke, C. O. Davis, R. M. Bevilacqua, D. R. Korwan, M. J. Montes, J. H. Bowles, and M. R. Corson, "Vicarious calibrations of HICO data acquired from the International Space Station," *Applied Optics*, vol. 51, no. 14, pp. 2559–2567, 2012.

[65] R. R. Li, R. Lucke, D. Korwan, and B. C. Gao, "A technique for removing second-order light effects from hyperspectral imaging data," *IEEE Transactions on Geoscience and Remote Sensing*, vol. 50, no. 3, pp. 824–830, 2012.

[66] J. Praks, A. Kestila, M. Hallikainen, H. Saari, J. Antila, P. Janhunen, and R. Vainio, "Aalto-1 - An experimental nanosatellite for hyperspectral remote sensing," in *IEEE International Geoscience and Remote Sensing Symposium (IGARSS)*, pp. 4367–4370, 2011.

[67] J. Praks, M. R. Mughal, R. Vainio, P. Janhunen, J. Envall, P. Oleynik, A. Näsilä, H. Leppinen, P. Niemelä, A. Slavinskis, J. Gieseler, P. Toivanen, T. Tikka, T. Peltola, A. Bosser, G. Schwarzkopf, N. Jovanovic, B. Riwanto, A. Kestilä, A. Punkkinen, R. Punkkinen, H.-P. Hedman, T. Säntti, J.-O. Lill, J. Slotte, H. Kettunen, and A. Virtanen, "Aalto-1, multi-payload CubeSat: Design, integration and launch," *Acta Astronautica*, vol. 187, pp. 370–383, 2021.

[68] M. R. Mughal, J. Praks, R. Vainio, P. Janhunen, J. Envall, A. Näsilä, P. Oleynik, P. Niemelä, S. Nyman, A. Slavinskis, J. Gieseler, N. Jovanovic, B. Riwanto, P. Toivanen, H. Leppinen, T. Tikka, A. Punkkinen, R. Punkkinen, H. P. Hedman, J. O. Lill, and J. M. Slotte, "Aalto-1, multi-payload CubeSat: In-orbit results and lessons learned," *Acta Astronautica*, vol. 187, pp. 557–568, 2021.

[69] S. S. Conticello, P. F. Manzillo, C. N. van Dijk, N. Vercruyssen, M. Esposito, M. Soukup, J. Gailis, D. Fantin, A. Jochemsen, C. Aas, P. J. Baeck, I. Benhadj, S. Livens, B. Delauré, M. Menenti, B. G. H. Gorte, S. E. H. Aria, M. D. Miranda, and S. K. Mahalik, "Hyperspectral Imaging for Real Time Land and Vegetation Inspection," in *Proc. Small Satellites, System & Services Symposium (4S)*, 2016.

[70] M. Esposito and A. Zuccaro Marchi, "In-orbit demonstration of the first hyperspectral imager for nanosatellites," in *International Conference on Space Optics (ICSO)*, vol. 11180, p. 71, 2018.

[71] M. Soukup, J. Gailis, D. Fantin, A. Jochemsen, C. Aas, P. J. Baeck, I. Benhadj, S. Livens, B. Delauré, M. Menenti, B. G. H. Gorte, S. E. Hosseini Aria, M. Esposito, and C. N. Van Dijk, "Hyperscout: Onboard processing of hyperspectral imaging data on a nanosatellite," in *Proc. Small Satellites, System & Services Symposium (4S)*, 2016.

[72] S. P. Love, L. A. Ott, K. W. Post, M. E. Dale, C. L. Safi, K. G. Boyd, H. D. Mohr, C. R. Ward, M. P. Caffrey, J. P. Theiler, B. R. Foy, M. P. Hehlen, C. G. Peterson, R. L. Hemphill, J. A. Wren, A. A. Guthrie, D. L. Graff, N. A. Dallmann, P. S. Stein, and M. K. Dubey, "NACHOS, a CubeSat-based high-resolution UV-Visible hyperspectral imager for remote sensing of trace gases: system overview and science objectives," in *CubeSats and SmallSats for Remote Sensing V* (C. D. Norton, T. S. Pagano, and S. R. Babu, eds.), p. 14, SPIE, 2021.

[73] K. W. Post, L. A. Ott, M. E. Dale, C. L. Safi, K. G. Boyd, H. D. Mohr, J. P. Theiler, B. R. Foy, M. P. Hehlen, C. R. Ward, M. P. Caffrey, C. G. Peterson, R. L. Hemphill, M. K. Dubey, and S. P. Love, "The NACHOS CubeSat-based hyperspectral imager: laboratory and field performance characterization," in *CubeSats and SmallSats for Remote Sensing V*, 2021.

[74] J. Blommaert, G. Habay, B. Delaure, S. Livens, D. Nuyts, K. Tack, A. Lambrechts, R. D. Paola, V. Moreau, E. Callut, L. Maresi, H. Strese, A. Z. Marchi, B. Deper, and M. Viitala, "CSIMBA: Towards a Smart-Spectral Cubesat Constellation," *IEEE International Geoscience and Remote Sensing Symposium (IGARSS)*, no. 1, 2019.

[75] S. Livens, B. Delauré, D. Nuyts, I. Benhadj, J. Blommaert, K. Tack, R. D. Paola, E. Callut, L. Maresi, H. Strese, and M. Viirala, "Advancing hyperspectral CubeSat monitoring with the CSIMBA IOD mission," in *Proc. of 13th IAA Symposium on Small Satellites for Earth Observation*, 2021.

[76] S. Livens, D. Nuyts, I. Benhadj, and J. Blommaert, "CSIMBA: Added Value of a Small Hyperspectral IOD Satellite Mission," in *12th Workshop on Hyperspectral Image and Signal Processing, Evolution in Remote Sensing (WHISPERS)*, 2022.

[77] T. Kohout, A. Näsilä, and T. Tikka, "Asteroid Spectral Imaging Mission (ASPECT) CubeSat to characterize resources on asteroid surfaces," *European Planetary Science Congress*, vol. 11, 2017.

[78] T. Kohout, A. Näsilä, T. Tikka, M. Granvik, A. Kestilä, A. Penttilä, J. Kuhno, K. Muinonen, K. Viherkanto, and E. Kallio, "Feasibility of asteroid exploration using CubeSats—ASPECT case study," *Advances in Space Research*, vol. 62, no. 8, pp. 2239–2244, 2018.

[79] A. Holmes, G. Feldman, J. Morrison, F. Patt, and S. Lee, "Hawkeye ocean color instrument: performance summary," in *CubeSats and NanoSats for Remote Sensing II*, p. 10, 2018.

[80] H. Strese and L. Maresi, "Technology developments and status of hyperspectral instruments at the European Space Agency," in *Proc. SPIE 11151, Sensors, Systems, and Next-Generation Satellites XXII, 111510T*, 2019.

[81] V. Moreau, L. Maresi, B. Borguet, A. Z. Marchi, and M. Miranda, "Freeform grating-based hyperspectral instruments : when SmallSat solutions benefit to big missions," in *Proceedings of the AIAA/USU Conference on Small Satellites, SSC19-VII-08*, 2019.

[82] R. U. Datla, J. P. Rice, K. R. Lykke, and B. C. Johnson, "Best practice guidelines for pre-launch characterization and calibration of instruments for passive optical remote sensing," *Journal of Research of the National Institute of Standards and Technology*, vol. 116, no. 2, pp. 621–646, 2011.

[83] T. Skauli, "Feasibility of a Standard for Full Specification of Spectral Imager Performance," *Proc. of SPIE: Hyperspectral Imaging Sensors: Innovative Applications and Sensor Standards*, vol. 10213, pp. 1–12, 2017.

[84] F. Niro, P. Goryl, S. Dransfeld, V. Boccia, F. Gascon, J. Adams, B. Themann, S. Scifoni, and G. Doxani, "European space agency (ESA) calibration/validation strategy for optical land-imaging satellites and pathway towards interoperability," *Remote Sensing*, vol. 13, no. 15, pp. 1–43, 2021.

[85] J. Bowles, M. Kappus, J. Antoniades, M. Baumback, M. Czarnaski, C. O. Davis, and J. Grossmann, "Calibration of inexpensive pushbroom imaging spectrometers," *Metrologia*, vol. 35, no. 4, pp. 657–661, 1998.

[86] R. O. Green, "Spectral calibration requirement for Earth-looking imaging spectrometers in the solar-reflected spectrum," *Applied Optics*, vol. 37, no. 4, pp. 683–690, 1998.

[87] X. Yu, Y. Sun, A. Fang, W. Qi, and C. Liu, "Laboratory Spectral Calibration and Radiometric Calibration of Hyper-spectral Imaging Spectrometer," in *2nd International Conference on Systems and Informatics, ICSAI 2014*, pp. 871–875, 2015.

[88] M. T. Eismann, *Hyperspectral Remote Sensing*. Bellingham, Washington DC: SPIE Press, 2012.

[89] K. Lenhard, A. Baumgartner, P. Gege, S. Nevas, S. Nowy, and A. Sperling, "Impact of Improved Calibration of a NEO HySpex VNIR-1600 Sensor on Remote Sensing of Water Depth," *IEEE Transactions on Geoscience and Remote Sensing*, vol. 53, no. 11, pp. 6085–6098, 2015.

[90] C. J. Bruegge, V. G. Duval, N. L. Chrien, R. P. Korechoff, B. J. Gaitley, and E. B. Hochberg, "MISR prelaunch instrument calibration and characterization results," *IEEE Transactions on Geoscience and Remote Sensing*, vol. 36, no. 4, pp. 1186–1198, 1998.

[91] G. Yang, J. Liu, C. Zhao, Z. Li, Y. Huang, H. Yu, B. Xu, X. Yang, D. Zhu, X. Zhang, R. Zhang, H. Feng, X. Zhao, Z. Li, H. Li, and H. Yang, "Unmanned aerial vehicle remote sensing for field-based crop phenotyping: current status and perspectives," *Frontiers in Plant Science*, vol. 8, 2017.

[92] R. A. Barnes, S. W. Brown, K. R. Lykke, B. Guenther, J. J. Butler, T. Schwarting, K. Turpie, D. Moyer, F. DeLuccia, and C. Moeller, "Comparison of two methodologies for calibrating satellite instruments in the visible and near-infrared," *Applied Optics*, vol. 54, no. 35, p. 10376, 2015.

[93] M. B. Henriksen, "Hyperspectral Imager Calibration and Image Correction," 2019. Master's thesis, Norwegian University of Science and Technology.

[94] A. J. den Dekker and A. van den Bos, "Resolution: a survey," *Journal of the Optical Society of America A*, vol. 14, no. 3, 1997.

[95] L. B. Moore and P. Mouroulis, "Tolerancing methods and metrics for imaging spectrometers," in *International Optical Design Conference 2017*, p. 67, 2017.

[96] P. Mouroulis, R. O. Green, and T. G. Chrien, "Design of Pushbroom Imaging Spectrometers for Optimum Recovery of Spectroscopic and Spatial Information," *Applied Optics*, vol. 39, no. 13, pp. 2210–2220, 2000.

[97] N. Yokoya, N. Miyamura, and A. Iwasaki, "Detection and Correction of Spectral and Spatial Misregistrations for Hyperspectral Data using Phase Correlation Method," *Applied Optics*, vol. 49, no. 24, pp. 4568–4575, 2010.

[98] G. Høye and A. Fridman, "Spatial misregistration in hyperspectral cameras: lab characterization and impact on data quality in real-world images," *Optical Engineering*, vol. 59, no. 08, 2020.

[99] L. Yuan, J. Xie, Z. He, Y. Wang, and J. Wang, "Optical design and evaluation of airborne prism-grating imaging spectrometer," *Optics Express*, vol. 27, no. 13, p. 17686, 2019.

[100] P. Mouroulis, R. O. Green, and D. W. Wilson, "Optical design of a coastal ocean imaging spectrometer," *Optics Express*, vol. 16, no. 12, p. 9087, 2008.

[101] A. Fridman, G. Høye, and T. Løke, "Resampling in Hyperspectral Cameras as an Alternative to Correcting Keystone in Hardware, with Focus on Benefits for Optical Design and Data Quality," *Optical Engineering*, vol. 53, no. 5, 2014.

[102] P. Mouroulis and M. M. McKerns, "Pushbroom imaging spectrometer with high spectroscopic data fidelity: experimental demonstration," *Optical Engineering*, vol. 39, no. 3, pp. 808–816, 2000.

[103] Y. Feng and Y. Xiang, "Mitigation of spectral mis-registration effects in imaging spectrometers via cubic spline interpolation," *Optics Express*, vol. 16, no. 20, pp. 15366–15374, 2008.

[104] K. C. Lawrence, B. Park, W. R. Windham, and C. Mao, "Calibration of a Pushbroom Hyperspectral Imaging System for Agricultural Inspection," *Transaction of the ASAE*, vol. 46, no. 2, pp. 513–521, 2003.

[105] R. A. Schowengerdt, *Remote Sensing - Models and Methods for Image Processing*. Elsevier Inc., 3 ed., 2007.

[106] J. F. Silny, "Resolution modeling of dispersive imaging spectrometers," *Optical Engineering*, vol. 56, no. 08, p. 1, 2017.

[107] H. A. Bender, P. Mouroulis, M. L. Eastwood, R. O. Green, S. Geier, and E. B. Hochberg, "Alignment and characterization of high uniformity imaging spectrometers," (San Diego, California, USA), p. 81580J, 2011.

[108] P. Mouroulis, B. Van Gorp, R. O. Green, H. Dierssen, D. W. Wilson, M. Eastwood, J. Boardman, B.-C. Gao, D. Cohen, B. Franklin, F. Loya, S. Lundeen, A. Mazer, I. McCubbin, D. Randall, B. Richardson, J. I. Rodriguez, C. Sarture, E. Urquiza, R. Vargas, V. White, and K. Yee, "Portable Remote Imaging Spectrometer coastal ocean sensor: design, characteristics, and first flight results," *Applied Optics*, vol. 53, no. 7, p. 1363, 2014.

[109] M. Kosec, M. Bürmen, D. Tomaževič, F. Pernuš, and B. Likar, "Characterization of a spectrograph based hyperspectral imaging system," *Optics Express*, vol. 21, no. 10, p. 12085, 2013.

[110] H. E. Torkildsen and T. Skauli, "Full Characterization of Spatial Coregistration Errors and Spatial Resolution in Spectral Imagers," *Optics Letters*, vol. 43, no. 16, pp. 3814–3817, 2018.

[111] K. Lenhard, A. Baumgartner, and T. Schwarzmaier, "Independent laboratory characterization of NEO HySpex imaging spectrometers VNIR-1600 and SWIR-320m-e," *IEEE Transactions on Geoscience and Remote Sensing*, vol. 53, no. 4, pp. 1828–1841, 2015.

[112] J. Jemec, F. Pernuš, B. Likar, and M. Bürmen, "Three-dimensional point spread function measurements of imaging spectrometers," *Journal of Optics*, vol. 19, no. 9, p. 095002, 2017.

[113] J. Jemec, F. Pernuš, B. Likar, and M. Bürmen, "2D Sub-pixel Point Spread Function Measurement Using a Virtual Point-Like Source," *International Journal of Computer Vision*, vol. 121, no. 3, pp. 391–402, 2017.

[114] T. Skauli, "An Upper-Bound Metric for Characterizing Spectral and Spatial Coregistration Errors in Spectral Imaging," *Optics Express*, vol. 20, no. 2, pp. 918–933, 2012.

[115] P. Coppo, A. Taiti, L. Pettinato, M. Francois, M. Taccola, and M. Drusch, "Fluorescence imaging spectrometer (FLORIS) for ESA FLEX mission," *Remote Sensing*, vol. 9, no. 649, 2017.

[116] Y. Zong, S. W. Brown, B. C. Johnson, K. R. Lykke, and Y. Ohno, "Simple spectral stray light correction method for array spectroradiometers," *Applied Optics*, vol. 45, no. 6, pp. 1111–1119, 2006.

[117] Y. Zong, S. W. Brown, G. Meister, R. A. Barnes, and K. R. Lykke, "Characterization and Correction of Stray Light in Optical Instruments," *Proc. of SPIE: Sensors, Systems, And Next-Generation Satellites XI*, vol. 6744, 2007.

[118] Y. Zong, "Uncertainty Analysis of Stray-Light Correction," *CIE Expert Symposium on Spectral and Imaging Methods for Photometry and Radiometry*, pp. 50–51, 2010.

[119] C. Schinke, M. Franke, K. Bothe, and S. Nevas, "Implementation and uncertainty evaluation of spectral stray light correction by Zong's method," *Applied Optics*, vol. 58, no. 36, 2019.

[120] P. J. Tol, T. A. Van Kempen, R. M. Van Hees, M. Krijger, S. Cadot, R. Snel, S. T. Persijn, I. Aben, and R. W. Hoogeveen, "Characterization and correction of stray light in TROPOMI-SWIR," *Atmospheric Measurement Techniques*, vol. 11, no. 7, pp. 4493–4507, 2018.

[121] IOCCG, *In-flight Calibration of Satellite Ocean-Colour Sensors*, vol. No. 14 of *Reports of the International Ocean Colour Coordinating Group.* Dartmouth, Canada: IOCCG, 2013.

[122] H. Cosnefroy, M. Leroy, and X. Briottet, "Selection and characterization of Saharan and Arabian desert sites forthe calibration of optical satellite sensors," *Remote Sensing of Environment*, vol. 58, no. 1, pp. 101–114, 1996.

[123] M. Bouvet, K. Thome, B. Berthelot, A. Bialek, J. Czapla-Myers, N. P. Fox, P. Goryl, P. Henry, L. Ma, S. Marcq, A. Meygret, B. N. Wenny, and E. R. Woolliams, "RadCalNet: A radiometric calibration network for earth observing imagers operating in the visible to shortwave infrared spectral range," *Remote Sensing*, vol. 11, no. 20, 2019.

[124] D. K. Clark, M. A. Yarbrough, M. Feinholz, S. Flora, W. Broenkow, Y. S. Kim, B. C. Johnson, S. W. Brown, M. Yuen, and J. L. Mueller, "MOBY, A Radiometric Buoy for Performance Monitoring and Vicarious Calibration of Satellite Ocean Color Sensors: Measurement and Data Analysis Protocols," in *Ocean Optics Protocols For Satellite Ocean Color Sensor Validation*, pp. 138–170, 2003.

[125] E. Ammannito, G. Filacchione, A. Coradini, F. Capaccioni, G. Piccioni, M. C. De Sanctis, M. Dami, and A. Barbis, "On-ground characterization of Rosetta/VIRTIS-M. I. Spectral and geometrical calibrations," *Review of Scientific Instruments*, vol. 77, no. 9, 2006.

[126] D. R. Doelling, D. Morstad, B. R. Scarino, R. Bhatt, and A. Gopalan, "The Characterization of Deep Convective Clouds as an Invariant Calibration Target and as a Visible Calibration Technique," *IEEE Transactions on Geoscience and Remote Sensing*, vol. 51, no. 3, pp. 1147–1159, 2013.

[127] T. C. Stone, "Radiometric calibration stability and inter-calibration of solar-band instruments in orbit using the moon," 2008.

[128] A. Meygret, C. Latry, A. Kelbert, and G. Blanchet, "PLEIADES high resolution optical sensors radiometric and spatial calibration based on stars," in *Earth Observing Systems XXIV*, p. 73, 2019.

[129] R. E. Eplee, Jr., J.-Q. Sun, G. Meister, F. S. Patt, X. Xiong, and C. R. McClain, "Cross calibration of SeaWiFS and MODIS using on-orbit observations of the Moon," *Applied Optics*, vol. 50, no. 2, 2011.

[130] C. Justice, A. Belward, J. Morisette, P. Lewis, J. Privette, and F. Baret, "Developments in the 'validation' of satellite sensor products for the study of the land surface," *International Journal of Remote Sensing*, vol. 21, no. 17, pp. 3383–3390, 2000.

[131] A. Loew, W. Bell, L. Brocca, C. E. Bulgin, J. Burdanowitz, X. Calbet, R. V. Donner, D. Ghent, A. Gruber, T. Kaminski, J. Kinzel, C. Klepp, J.-C. Lambert, G. Schaepman-Strub, M. Schröder, and T. Verhoelst, "Validation practices for satellite-based Earth observation data across communities: EO VALIDATION," *Reviews of Geophysics*, vol. 55, no. 3, pp. 779–817, 2017.

[132] F. J. Immler, J. Dykema, T. Gardiner, D. N. Whiteman, P. W. Thorne, and H. Vömel, "Reference Quality Upper-Air Measurements: guidance for developing GRUAN data products," *Atmospheric Measurement Techniques*, vol. 3, no. 5, pp. 1217–1231, 2010.

[133] F. Sigernes, *Basic Hyperspectral Imaging*. 2018.

[134] C. Palmer and E. Loewen, *Diffraction Grating Handbook*. Newport Corporation, 7 ed., 2014.

[135] J. M. Lerner and A. Thevenon, *The optics of spectroscopy, a tutorial v2.0*. Joblin Yvon Instruments SA, Inc., 1998.

[136] Z. Volent, G. Johnsen, and F. Sigernes, "Microscopic hyperspectral imaging used as a bio-optical taxonomic tool for micro- and macroalgae," *Applied Optics*, vol. 48, no. 21, pp. 4170–4176, 2009.

[137] M. Haugum, G. M. Fragoso, M. B. Henriksen, A. P. Zolich, and T. A. Johansen, "Autonomous Flow-Through RGB and Hyperspectral Imaging for Unmanned Surface Vehicles," in *Proc. OCEANS conference*, 2023.

[138] M. B. Henriksen, J. L. Garrett, E. F. Prentice, A. Stahl, and T. A. Johansen, "Real-time corrections for a low-cost hyperspectral instrument," in *10th Workshop on Hyperspectral Image and Signal Processing, Evolution in Remote Sensing (WHISPERS)*, 2019.

[139] C. M. van Hazendonk, "Calibration of hyperspectral imager," 2019. Tech. report, University Centre of Svalbard. Retrieved from `http://kho.unis.no/doc/Lotte_van_Hazendonk.pdf`. Accessed: 2021-03-24.

[140] J. L. Garrett, S. Bakken, E. F. Prentice, D. Langer, F. S. Leira, E. Honoré-Livermore, R. Birkeland, M. E. Grøtte, T. A. Johansen, and M. Orlandi, "Hyperspectral image processing pipelines on multiple platforms for coordinated oceanographic observation," in *11th Workshop on Hyperspectral Image and Signal Processing, Evolution in Remote Sensing (WHISPERS)*, 2021.

[141] M. Henriksen, "HYPSO2-TPL-OPT-004 Optical Validation Test Plan," tech. rep., 2023. Internal document.

[142] F. Sigernes, J. M. Holmes, M. Dyrland, D. A. Lorentzen, S. A. Chernous, T. Svinyu, J. Moen, and C. S. Deehr, "Absolute calibration of optical devices with a small field of view," *J. Opt. Technol.*, vol. 74, no. 10, pp. 669–674, 2007.

[143] F. Sigernes, J. M. Holmes, M. Dyrland, D. A. Lorentzen, T. Svenøe, K. Heia, T. Aso, S. Chernouss, and C. S. Deehr, "Sensitivity calibration of digital colour cameras for auroral imaging," *Optics Express*, vol. 16, no. 20, pp. 15623—-15632, 2008.

[144] F. Sigernes, M. Dyrland, N. Peters, D. A. Lorentzen, T. Svenøe, K. Heia, S. Chernouss, C. S. Deehr, and M. Kosch, "The absolute sensitivity of digital colour cameras," *Optics Express*, vol. 17, no. 22, p. 20211, 2009.

[145] G. M. Selnesaunet, M. B. Henriksen, and T. Skauli, "Imaging the point spread function of hyperspectral cameras - the full truth about coregistration error and resolution," in *Proc. SPIE Optics+Photonics*, 2023.

[146] H. Hovland, "Tomographic scanning imager," *Optics Express*, vol. 17, no. 14, p. 11371, 2009.

[147] K. A. Riihiaho, M. A. Eskelinen, and I. Pölönen, "A do-it-yourself hyperspectral imager brought to practice with open-source python," *Sensors*, vol. 21, no. 1072, 2021.

[148] M. B. Henriksen, E. F. Prentice, T. A. Johansen, and F. Sigernes, "Pre-Launch Calibration of the HYPSO-1 Cubesat Hyperspectral Imager," in *IEEE Aerospace Conference*, 2022.

[149] M. B. Henriksen, F. Sigernes, and T. A. Johansen, "Comparing filters for correction of second order diffraction effects in hyperspectral imagers," in *13th Workshop on Hyperspectral Image and Signal Processing, Evolution in Remote Sensing (WHISPERS)*, 2023. (accepted).

[150] M. B. Henriksen, F. Sigernes, and T. A. Johansen, "A Closer Look at a Spectrographic Wavelength Calibration," in *12th Workshop on Hyperspectral Image and Signal Processing, Evolution in Remote Sensing (WHISPERS)*, 2022.

[151] T. G. Chrien, R. O. Green, and M. L. Eastwood, "Accuracy of the spectral and radiometric laboratory calibration of the Airborne Visible/Infrared Imaging Spectrometer," in *Proc. SPIE 1298, Imaging Spectroscopy of the Terrestrial Environment*, 1990.

[152] S. Delwart, L. Bourg, R. Preusker, and R. Santer, "MERIS spectral calibration campaigns," *Sensors, Systems, and Next-Generation Satellites VIII*, vol. 5570, 2004.

[153] National Institute of Standards and Technology (NIST), "Strong lines of argon (ar)." Retrieved from `https://www.physics.nist.gov/PhysRefData/Handbook/Tables/argon table2.htm`. Accessed: 2022-03-05.

[154] National Institute of Standards and Technology (NIST), "Strong lines of mercury (hg)." Retrieved from `https://www.physics.nist.gov/PhysRefData/Handbook/Tables/mercury table2.htm`. Accessed: 2022-03-05.

[155] National Institute of Standards and Technology (NIST), "Strong lines of hydrogen (h)." Retrieved from `https://www.physics.nist.gov/PhysRefData/Handbook/Tables/hydrogen table2.htm`. Accessed: 2022-11-02.

[156] National Institute of Standards and Technology (NIST), "Strong lines of helium (he)." Retrieved from `https://www.physics.nist.gov/PhysRefData/Handbook/Tables/helium table2.htm`. Accessed: 2022-11-02.

[157] National Institute of Standards and Technology (NIST), "Strong lines of krypton (kr)." Retrieved from `https://www.physics.nist.gov/PhysRefData/Handbook/Tables/krypton table2.htm`. Accessed: 2022-11-02.

[158] Y. Mao, C. H. Betters, B. Evans, C. P. Artlett, S. G. Leon-Saval, S. Garske, I. H. Cairns, T. Cocks, R. Winter, and T. Dell, "OpenHSI: A Complete Open-Source Hyperspectral Imaging Solution for Everyone," *Remote Sensing*, vol. 14, no. 9, p. 2244, 2022.

[159] V. Stanishev, "Correcting second-order contamination in low-resolution spectra," *Astronomische Nachrichten*, vol. 328, no. 9, pp. 948–952, 2007.

[160] W. Lee, H. Lee, and J. W. Hahn, "Correction of spectral deformation by second-order diffraction overlap in a mid-infrared range grating spectrometer using a PbSe array detector," *Infrared Physics and Technology*, vol. 67, pp. 327–332, 2014.

[161] S. I. Bruchkouskaya, G. S. Litvinovich, I. I. Bruchkousky, and L. V. Katkovsky, "Algorithm for second-order diffraction correction in a concave diffraction grating spectrometer," *Journal of Applied Spectroscopy*, vol. 86, no. 4, pp. 671–677, 2019.

[162] Z. Xu and M. H. Brill, "Correction of second-order-diffraction errors in spectrophotometry," *Color Research and Application*, vol. 42, no. 2, pp. 189–192, 2017.

[163] S. E. Heggelund, E. Håland, M. B. Henriksen, and R. Birkeland, "HYPSO2-DR-009 Building HYPSO-2 EQM," tech. rep., 2023. Internal document.

[164] M. B. Henriksen, S. E. Heggelund, E. Håland, R. Birkeland, and A. Gjersvik, "HYPSO2-RP-015 HYPSO-2 Flight Model As-Built," tech. rep., 2023. Internal document.

[165] J. F. Tømmermo, H. H. Brovold, and T. Vitsø, "Mechanical Design Iteration of an Optical Slit Holder for Use in a Low Earth Orbit CubeSat Hyperspectral Imager," 2022. Bachelor's thesis, Norwegian University of Science and Technology.

[166] R. S. Barker, D. A. Richardson, E. A. G. McConkey, and R. Rimmer, "Gamma Irradiation of Lead Silicate Glass," *Nature*, vol. 187, no. 4732, pp. 135–136, 1960.

[167] W. Zdaniewski, T. Easler, and R. Bradt, "Gamma Radiation Effects on the Strength of a Borosilicate Glass," *Journal of the American Ceramic Society*, vol. 66, no. 5, pp. 311–313, 1983.

[168] A. Bardoux, A. Penquer, O. Gilard, R. Ecoffet, and M. Auvergne, "Radiation effects on image sensors," in *Proc. SPIE 10564, International Conference on Space Optics – ICSO 2012, 105640M*, (Ajaccio, Corsica, France), SPIE, 2017.

[169] H. Bao-Ping, Y. Zhi-Bin, and Z. Feng-Qi, "A comparison of ionizing radiation damage in CMOS devices from 60Co gamma rays, electrons and protons," *Chinese Physics C*, vol. 33, no. 6, pp. 436–439, 2009.

[170] M. Hjertenæs, E. Prentice, and T. Kaasa, "HYPSO-TRP-VIB-003 HYPSO-1 QM Shock, Resonance, and Vibration Test Report," tech. rep., 2021. Internal document.

[171] M. Hjertenæs, E. Prentice, T. Kaasa, and E. Honoré-Livermore, "HYPSO-TRP-TVAC-002 HYPSO-1 QM TVAC Test Report," tech. rep., 2021. Internal document.

[172] E. F. Prentice, M. B. Henriksen, T. A. Johansen, F. N. Medina, and A. G. San Juan, "Characterizing Spectral Response in Thermal Environments, the HYPSO-1 Hyperspectral Imager," in *IEEE Aerospace Conference*, 2022.

[173] F. Navarro-Medina, A. E. Oudijk, M. B. Henriksen, A. Gjersvik, F. S. Grønvold, and T. A. Johansen, "Experimental set-up of a thermal vacuum chamber for thermal model in-house correlation and characterization of the HYPSO hyperspectral imager," *CEAS Space Journal*, 2023.

[174] F. Navarro-Medina, A. E. Oudijk, M. B. Henriksen, U. Garcia-Luis, A. Gomez-San Juan, and T. A. Johansen, "Structural Thermal Optical Performance (STOP) analysis and experimental verification of the HYPSO hyperspectral imager," *Optics and Lasers in Engineering*, vol. 173, 2024.

[175] S. E. Heggelund and M. B. Henriksen, "HYPSO2-TRP-SHK-001 HYPSO-2 EQM Shock, Resonance, and Vibration Test Report," tech. rep., 2023. Internal document.

[176] E. S. Håland and M. B. Henriksen, "HYPSO2-TRP-002 HYPSO-2 EQM TVAC Test Report," tech. rep., 2023. Internal document.

[177] F. Ewald, T. Kölling, A. Baumgartner, T. Zinner, and B. Mayer, "Design and characterization of specMACS, a multipurpose hyperspectral cloud and sky imager," *Atmospheric Measurement Techniques*, vol. 9, no. 5, pp. 2015–2042, 2016.

[178] "SpaceX Transporter-3 Mission." Retrieved from `https://www.spacex.com/launches/transporter-3-mission/`. Accessed: 2022-12-09.

[179] M. B. Henriksen, J. L. Garrett, and T. A. Johansen, "Comparing pre- and post-launch images from the HYPSO-1 cubesat hyperspectral imager," in *73rd International Austronautical Congress (IAC)*, 2022.

[180] F. Weiler, T. Kanitz, D. Wernham, M. Rennie, D. Huber, M. Schillinger, O. Saint-Pe, R. Bell, T. Parrinello, and O. Reitebuch, "Characterization of dark current signal measurements of the ACCDs used on board the Aeolus satellite," *Atmospheric Measurement Techniques*, vol. 14, no. 7, pp. 5153–5177, 2021.

[181] P. Du Buisson, R. Borde, D. Dessailly, and R. Santer, "In-flight spectral calibration of the oxygen A-band channel of MERIS," *International Journal of Remote Sensing*, vol. 24, no. 5, pp. 1177–1182, 2003.

[182] D. A. Newnham and J. Ballard, "Visible absorption cross sections and integrated absorption intensities of molecular oxygen (O2 and O4)," *Journal of Geophysical Research Atmospheres*, vol. 103, no. D22, pp. 28801–28815, 1998.

[183] D. Q. Wark and D. M. Mercer, "Absorption in the Atmosphere by the Oxygen "A" Band," *Applied Optics*, vol. 4, no. 7, p. 839, 1965.

[184] V. N. Ostrikov, O. V. Plakhotnikov, and A. V. Kirienko, "Estimation of Spectral Resolution of Imaging Spectrometers from Fraunhofer Lines with the MODTRAN Atmospheric Model," *Atmospheric and Oceanic Optics*, vol. 32, no. 6, pp. 622–627, 2019.

[185] G. D. Veglo, "Uncertainty in Hyperspectral Remote Sensing: An Evaluation in Forest Monitoring," 2023. Master's thesis, Norwegian University of Science and Technology.

[186] J. A. Justo, J. L. Garrett, D. D. Langer, R. Ionescu, M. B. Henriksen, R. T. Ionsecu, and T. A. Johansen, "An Open Hyperspectral Dataset with Sea-Land.Cloud Ground-Truth from the HYPSO-1 Satellite," 2023. (submitted).

[187] A. E. Oudijk, O. Hasler, H. Øveraas, S. Marty, D. R. Williamson, T. Svendsen, S. Berg, R. Birkeland, D. O. Halvorsen, S. Bakken, M. B. Henriksen, M. O. Alver, G. Johnsen, T. A. Johansen, A. Stahl, P. Kvaløy, A. Dallalio, S. Majaneva, G. M. Fragoso, and J. L. Garrett, "Campaign for Hyperspectral Data Validation in North Atlantic Coastal Waters," in *12th Workshop on Hyperspectral Image and Signal Processing, Evolution in Remote Sensing (WHISPERS)*, 2022.

[188] R. Sætre, *The Norwegian coastal current: oceanography and climate*. Akademika Pub, 2007.

[189] H. Ervik, T. E. Finne, and B. Jenssen, "Toxic and essential elements in seafood from Mausund, Norway," *Environmental Science and Pollution Research*, vol. 25, no. 8, pp. 7409–7417, 2018.

[190] H. Hop and C. Wiencke, *The Ecosystem of Kongsfjorden, Svalbard*. Springer, 2019.

[191] M. B. Henriksen, "HYPSO-1 CubeSat with hyperspectral imager over Ny-Ålesund, Svalbard." SIOS online conference on Earth observation and remote sensing applications in Svalbard, 2022.

[192] M. B. Henriksen, "HYPSO-1 CubeSat with hyperspectral imager over Ny-Ålesund, Svalbard." Invited talk, SIOS Polar Night Week, 2023.

[193] G. Johnsen, A. Zolich, S. Grant, R. Bjørgum, J. H. Cohen, D. McKee, T. P. Kopec, D. Vogedes, and J. Berge, "All-sky camera system providing high temporal resolution annual time series of irradiance in the Arctic," *Applied Optics*, vol. 60, no. 22, p. 6456, 2021.

[194] L. A. Clementson and B. Wojtasiewicz, "Dataset on the absorption characteristics of extracted phytoplankton pigments," *Data in Brief*, vol. 24, 2019.

[195] E.-J. Kim, S.-H. Nam, J.-W. Koo, and T.-M. Hwang, "Hybrid Approach of Unmanned Aerial Vehicle and Unmanned Surface Vehicle for Assessment of Chlorophyll-a Imagery Using Spectral Indices in Stream, South Korea," *Water*, vol. 13, p. 1930, July 2021.

[196] B. Song and K. Park, "Detection of Aquatic Plants Using Multispectral UAV Imagery and Vegetation Index," *Remote Sensing*, vol. 12, no. 3, p. 387, 2020.

[197] S. E. Heggelund, "Design, Assembly and Testing of a Hyperspectral Imaging Payload for the HYPSO-2 CubeSat," 2023. Master's thesis, Norwegian University of Science and Technology.

[198] A. Mousivand, W. Verhoef, M. Menenti, and B. Gorte, "Modeling top of atmosphere radiance over heterogeneous non-Lambertian rugged terrain," *Remote Sensing*, vol. 7, no. 6, pp. 8019–8044, 2015.

[199] K. Stamnes, B. Hamre, S. Stamnes, N. Chen, Y. Fan, W. Li, Z. Lin, and J. Stamnes, "Progress in forward-inverse modeling based on radiative transfer tools for coupled atmosphere-snow/ice-ocean systems: A review and description of the AccuRT model," *Applied Sciences (Switzerland)*, vol. 8, no. 12, 2018.

[200] L. V. Katkovsky, A. O. Martinov, V. A. Siliuk, D. A. Ivanov, and A. A. Kokhanovsky, "Fast atmospheric correction method for hyperspectral data," *Remote Sensing*, vol. 10, no. 11, 2018.

[201] D. R. Thompson, J. W. Boardman, M. L. Eastwood, R. O. Green, J. M. Haag, P. Mouroulis, and B. Van Gorp, "Imaging spectrometer stray spectral response: In-flight characterization, correction, and validation," *Remote Sensing of Environment*, vol. 204, pp. 850–860, 2018.

[202] A. Flores-Romero, "Improving Ocean Chlorophyll Estimation in Satellite Hyperspectral Images Using Ensemble Machine Learning," 2023. Master's thesis, Norwegian University of Science and Technology.